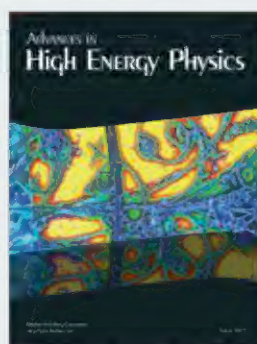
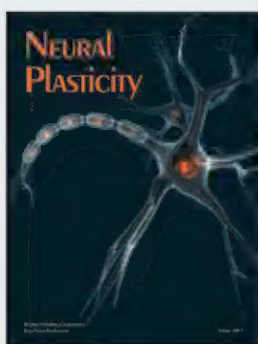
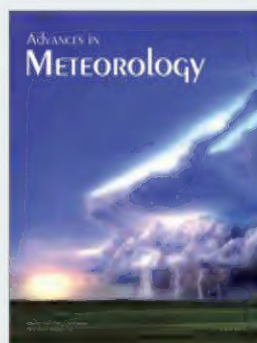
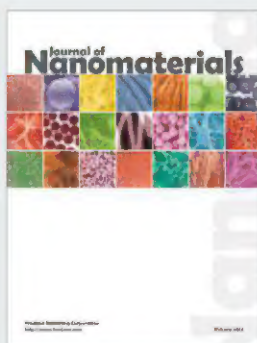
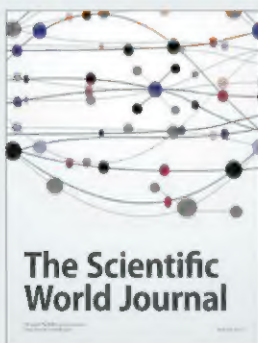
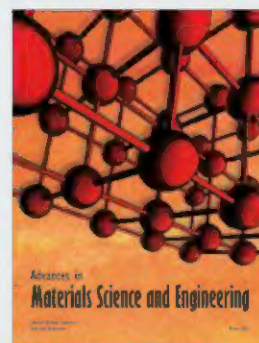
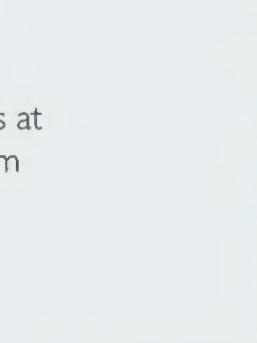
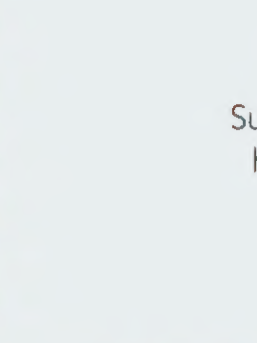
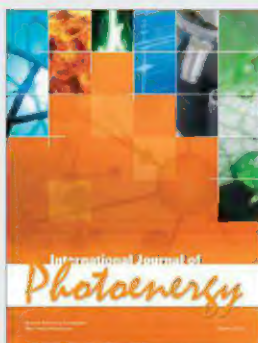
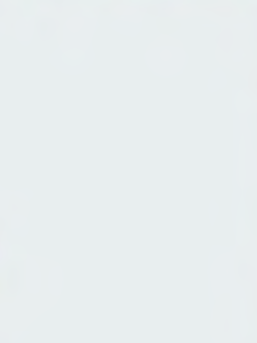
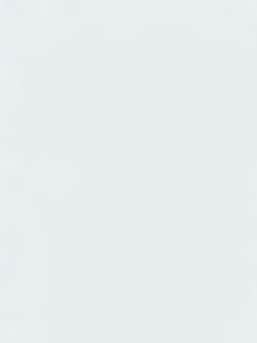
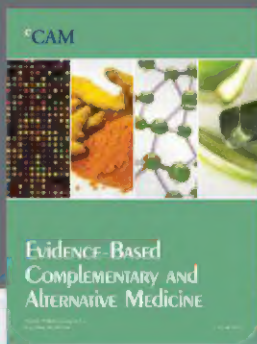
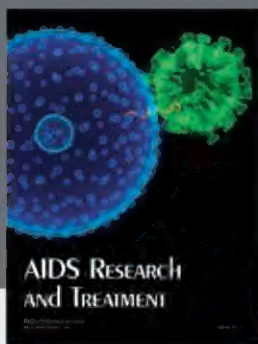




19 July 2013 | \$10

# Science







## EDITORIAL

- 215 Pathways for Conservation  
*Susan M. Haig et al.*

## NEWS OF THE WEEK

- 220 A roundup of the week's top stories

## NEWS & ANALYSIS

- 223 Tampered Data Cast Shadow on Drug Trial  
*>> Report p. 270*
- 224 Latest Skirmish Over Ancestral Violence Strikes Blow for Peace  
*>> Report p. 270*
- 225 Spain's Research Council Approaches Bankruptcy
- 226 Ever-Bigger Viruses Shake Tree of Life  
*>> Report p. 281*
- 227 Germany Debates How to Strengthen Universities
- 229 Mars Rover Plans Roll While Asteroid Acrimony Continues

## NEWS FOCUS

- 230 BIOGEOGRAPHY  
Battle for the Americas  
Salvage Paleontology on the Seaway  
*>> Science Podcast*
- 234 The Amazon in 4D

## LETTERS

- 236 Turkey Must End Violent Response to Protests  
*E. Altindis et al.*  
Optimizing Peer Review of Software Code  
*P. Sliz and A. Morin*  
Response  
*L. N. Joppa et al.*
- 237 CORRECTIONS AND CLARIFICATIONS
- 237 TECHNICAL COMMENT ABSTRACTS

## BOOKS ET AL.

- 238 Toms River  
*D. Fagin, reviewed by J. Tuomisto*
- 239 The Cost Disease  
*W. J. Baumol, reviewed by A. Chandra*

## EDUCATION FORUM

- 240 Crowdsourcing and Curating Online Education Resources  
*D. Porcello and S. Hsi*

## PERSPECTIVES

- 242 Trans-HSF1 Express  
*V. Gandin and I. Topisirovic*  
*>> Research Article p. 250*
- 243 Droplets Out of Equilibrium  
*T. M. Hermans et al.*  
*>> Report p. 253*
- 244 100 Years of Atomic Theory  
*D. C. Clary*
- 245 Enhancing Pluripotency and Lineage Specification  
*W. Xie and B. Ren*
- 247 Multiscale Design and Integration of Sustainable Building Functions  
*M. P. Gutierrez and L. P. Lee*  
*>> Science Podcast*

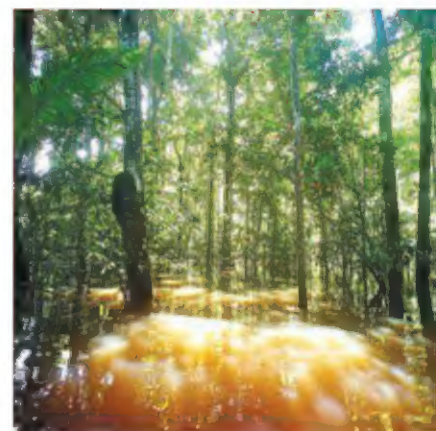
## REVIEW

- 249 Applications of Acceptorless Dehydrogenation and Related Transformations in Chemical Synthesis  
*C. Gunanathan and D. Milstein*  
*Review Summary; for full text:*  
<http://dx.doi.org/10.1126/science.1229712>

## RESEARCH ARTICLE

- 250 Tight Coordination of Protein Translation and HSF1 Activation Supports the Anabolic Malignant State  
*S. Santagata et al.*  
Chemical and genetic screening links ribosome activity levels and a transcriptional regulator in malignant cells.  
*Research Article Summary; for full text:*  
<http://dx.doi.org/10.1126/science.1238303>  
*>> Perspective p. 242*

CONTENTS continued >>



pages 230 & 234



page 240

## ON THE WEB THIS WEEK

### >> Science Podcast

Listen to stories on interdisciplinary buildings, measuring the martian atmosphere, an isthmus miracle, and more.

### >> Find More Online

Check out Science Express, our podcast, videos, daily news, our research journals, and Science Careers at [www.sciencemag.org](http://www.sciencemag.org).



## COVER

Enhanced transmission electron microscopy image of a "Pandoravirus" particle (length: 1.2 micrometers). Despite obeying all criteria to discriminate viruses from cells (no ribosome, no adenosine triphosphate production, no division), these Acanthamoeba viruses, unrelated to previously recognized virus families, exhibit genomes of up to 2.5 megabases, encoding more genes than some microsporidia. See pages 226 and 281.

Image: O. Poirat/Structural and Genomic Information Laboratory, CNRS Aix-Marseille Université

## DEPARTMENTS

- 214 This Week in Science  
216 Editors' Choice  
218 Science Staff  
299 New Products  
300 Science Careers



# BD Horizon™ Brilliant Violet™ Polymer Conjugates

Bright dyes help resolve rare and dim cell populations



For more discerning research.

Now you can resolve rare or dim cell populations with BD Horizon™ Brilliant Violet™ polymer conjugates from BD Biosciences.

Developed from pioneering polymer dye technology acquired from Sirigen Ltd., BD Horizon Brilliant Violet dyes are brighter than conventional dyes. Improved brightness enables you to identify cell populations with lower receptor density than was previously possible, resolving cell populations previously obscured.



Helping all people  
live healthy lives

The complete portfolio of BD conjugated antibodies can be used to explore cellular features and characterize cells through surface, intracellular, or secreted markers. To ensure you can use BD reagents across your entire multicolor panel, our portfolio contains a broad selection of fluorochrome-conjugated antibodies.

Request a free sample, or find out how you can use BD Horizon Brilliant Violet polymer conjugates with our expanded set of tools and information at [bdbiosciences.com/go/brilliant](http://bdbiosciences.com/go/brilliant).



## REPORTS

- 251 **Bright Hot Impacts by Erupted Fragments Falling Back on the Sun: A Template for Stellar Accretion**

*F. Reale et al.*

Analysis of plasma downflows after a solar eruption suggests that these events can be used to understand stellar accretion.

- 253 **Switchable Static and Dynamic Self-Assembly of Magnetic Droplets on Superhydrophobic Surfaces**

*J. V. I. Timonen et al.*

Magnetic droplets oscillate between static and dynamic self-assembly patterns in a magnetic field.

>> *Perspective p. 243*

- 257 **Ultrahigh Magnetoresistance at Room Temperature in Molecular Wires**

*R. N. Mahato et al.*

The conduction of molecular wires embedded in a zeolite host crystal is almost entirely blocked in small magnetic fields.

- 260 **Isotope Ratios of H, C, and O in CO<sub>2</sub> and H<sub>2</sub>O of the Martian Atmosphere**

*C. R. Webster et al.*

>> *Science Podcast*

- 263 **Abundance and Isotopic Composition of Gases in the Martian Atmosphere from the Curiosity Rover**

*P. R. Mahaffy et al.*

Data from the Curiosity rover provide a detailed account of the chemical and isotopic composition of Mars' atmosphere.

- 266 **Ice-Shelf Melting Around Antarctica**

*E. Rignot et al.*

Basal melting of Antarctic ice shelves accounts for as much mass loss as does icebergs calving.

- 270 **Lethal Aggression in Mobile Forager Bands and Implications for the Origins of War**

*D. P. Fry and P. Söderberg*

Nomadic foragers are less warlike than assumed, suggesting that war may not have been an early component of human behavior.

>> *News story p. 224*

- 273 **Interactions of Multisensory Components Perceptually Rescue Túngara Frog Mating Signals**

*R. C. Taylor and M. J. Ryan*

Mating signals that females find unattractive when presented singly become attractive when combined.

- 275 **Loss of Function of the Melanocortin 2 Receptor Accessory Protein 2 Is Associated with Mammalian Obesity**

*M. Asai et al.*

Disruption of a protein required for effective signaling by a melanocortin receptor causes severe obesity in mice.

- 278 **Developmental Control of the Melanocortin-4 Receptor by MRAP2 Proteins in Zebrafish**

*J. A. Sebag et al.*

A study in zebrafish sheds light on the signaling properties of a protein implicated in severe obesity in mice.

- 281 **Pandoraviruses: Amoeba Viruses with Genomes Up to 2.5 Mb Reaching That of Parasitic Eukaryotes**

*N. Philippe et al.*

Giant viruses that infect Southern Hemisphere *Acanthamoeba* and are visible under the light microscope have been identified.

>> *News story p. 226*

- 286 **Sept4/ARTS Regulates Stem Cell Apoptosis and Skin Regeneration**

*Y. Fuchs et al.*

Elimination of a proapoptotic gene increases hair follicle stem cells and improves skin regeneration and wound repair in mice.

- 290 **How the Red Queen Drives Terrestrial Mammals to Extinction**

*T. B. Quental and C. R. Marshall*

Loss of diversity among Cenozoic land mammals suggests a failure to keep pace with a deteriorating environment.

- 292 **Exceptional Convergence on the Macroevolutionary Landscape in Island Lizard Radiations**

*D. L. Mahler et al.*

A comparative study describes morphological evolution across the entire Greater Antillean anole lizard fauna.

- 295 **Predicting and Manipulating Cardiac Drug Inactivation by the Human Gut Bacterium *Eggerthella lenta***

*H. J. Haider et al.*

The heart drug digoxin can be inactivated by a strain of gut microbe bearing a cardiac glycoside reductase operon.



page 251

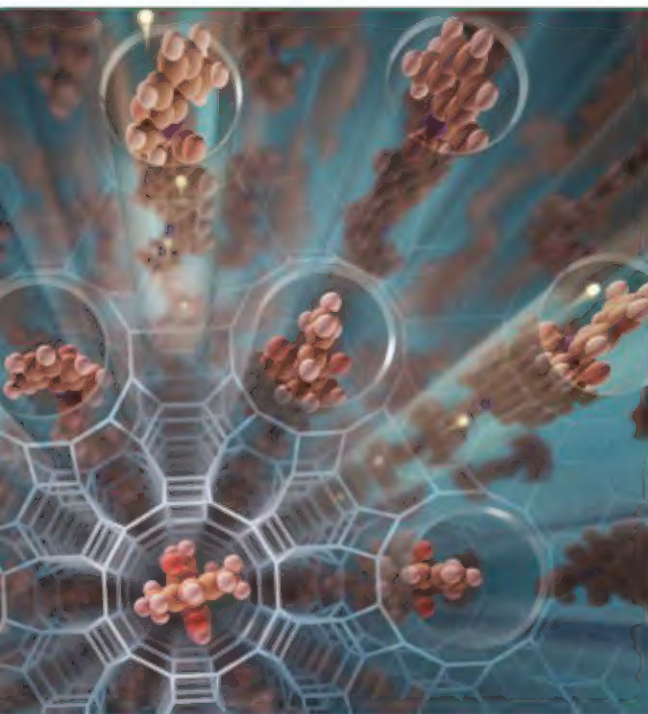


page 292

SCIENCE (ISSN 0036-8075) is published weekly on Friday, except the last week in December, by the American Association for the Advancement of Science, 1200 New York Avenue, NW, Washington, DC 20005. Periodicals Mail postage (publication No. 484460) paid at Washington, DC, and additional mailing offices. Copyright © 2013 by the American Association for the Advancement of Science. The title SCIENCE is a registered trademark of the AAAS. Domestic individual membership and subscription (S1 issues): \$149 (\$74 allocated to subscription). Domestic institutional subscription (S1 issues): \$990; Foreign postage extra: Mexico, Caribbean (surface mail) \$55; other countries (air assist delivery) \$85. First class, airmail, student, and emeritus rates on request. Canadian rates with GST available upon request, GST #1254 88122. Publications Mail Agreement Number 1069624. Printed in the U.S.A.

Change of address: Allow 4 weeks, giving old and new addresses and 8-digit account number. Postmaster: Send change of address to AAAS, P.O. Box 96178, Washington, DC 20090-6178. Single-copy sales: \$10.00 current issue, \$15.00 back issue prepaid includes surface postage; bulk rates on request. Authorization to photocopy material for internal or personal use under circumstances not falling within the fair use provisions of the Copyright Act is granted by AAAS to libraries and other users registered with the Copyright Clearance Center (CCC) Transactional Reporting Service, provided that \$30.00 per article is paid directly to CCC, 222 Rosewood Drive, Danvers, MA 01923. The identification code for Science is 0036-8075. Science is indexed in the Reader's Guide to Periodical Literature and in several specialized indexes.





## << More Magnetoresistance

When data is read off your computer's hard drive, chances are that the read head is using the phenomenon of magnetoresistance (MR)—the dependence of electrical resistance on applied magnetic field—to interpret the magnetic signature of the data on the disk. Devices that have the large MR necessary for such tasks are usually made of layers of magnetic materials. **Mahato *et al.*** (p. 257, published online 4 July) observed a large MR effect in a nonmagnetic material—organic molecules squeezed into a zeolite crystal. Importantly for potential future applications, the effect was observed at room temperature and at low magnetic fields.

## Accretion Analog

Mass flow from a circumstellar disk onto a young star's surface plays an important role in the final stages of star formation but the details of this complex process are not well understood.

**Reale *et al.*** (p. 251, published online 20 June) analyzed a solar flare that led to bright impacts of plasma onto the solar surface. Numerical simulations suggest that these events can be seen as analogs to accretion of matter onto stars and can thus be used to understand stellar accretion.

## Mars' Atmosphere from Curiosity

The Sample Analysis at Mars (SAM) instrument on the Curiosity rover that landed on Mars in August last year is designed to study the chemical and isotopic composition of the martian atmosphere. **Mahaffy *et al.*** (p. 263) present volume-mixing ratios of Mars' five major atmospheric constituents ( $\text{CO}_2$ , Ar,  $\text{N}_2$ ,  $\text{O}_2$ , and CO) and isotope measurements of  $^{40}\text{Ar}/^{36}\text{Ar}$  and C and O in  $\text{CO}_2$ , based on data from one of SAM's instruments, obtained between 31 August and 21 November 2012. **Webster *et al.*** (p. 260) used data from another of SAM's instruments obtained around the same period to determine isotope ratios of H, C, and O in atmospheric  $\text{CO}_2$  and  $\text{H}_2\text{O}$ . Agreement between the isotopic ratios measured by SAM with those of martian meteorites, measured in laboratories on Earth, confirms

the origin of these meteorites and implies that the current atmospheric reservoirs of  $\text{CO}_2$  and  $\text{H}_2\text{O}$  were largely established after the period of early atmospheric loss some 4 billion years ago.

## Major Meltdown

The ice shelves and floating ice tongues that surround Antarctica cover more than 1.5 million square kilometers—approximately the size of the entire Greenland Ice Sheet. Conventional wisdom has held that ice shelves around Antarctica lose mass mostly by iceberg calving, but recently it has become increasingly clear that melting by a warming ocean may also be important. **Rignot *et al.*** (p. 266, published 13 June) present detailed glaciological estimates of ice-shelf melting around the entire continent of Antarctica, which show that basal melting accounts for as much mass loss as does calving.

## Ancient Warriors or Murderers?

Some have suggested that the human predilection for war is ancient, perhaps dating back to the emergence of our species, while others maintain that evidence for such early warring is scant. Past studies that looked at nomadic foraging bands as models of early humans and their potential for conflict concluded that war is in our blood. **Fry and Söderberg** (p. 270),

however, reexamined the standard cross-cultural sample, the main repository for behavioral data on forage bands, and found little evidence for large-scale conflicts or wars. Instead, the majority of incidences of lethal aggression in these societies were homicides driven by a variety of factors relevant at the individual or family scale.

## Accessory to Obesity?

Melanocortin receptors are a family of cell membrane receptors that control diverse physiological functions. Mutations in the gene encoding melanocortin 4 receptor (MC4R) are a cause of familial early-onset obesity. **Asai *et al.*** (p. 275) studied the function of an accessory protein for MC4R signaling, MRAP2, and found that mice genetically deficient in MRAP2 develop severe obesity. Sequencing of MRAP2 in unrelated, severely obese humans revealed one individual with a clearly disruptive genetic variant, suggesting that MRAP2 mutations might also be a rare cause of human obesity. In a zebrafish model, **Sebag *et al.*** (p. 278) studied two paralogs of the MRAP2 accessory protein, one of which enhanced MC4R responsiveness to  $\alpha$ -melanocyte-stimulating hormone, which regulates feeding and growth.

## Romancing the Frog

In túngara frogs, auditory and visual components of mate calling do not naturally occur together. **Taylor and Ryan** (p. 273, published online 6 June) now show that two signals that are unattractive to female frogs when presented alone become highly attractive when presented together.



In a kind of "perceptual rescue," the unique combination of two signals increased the receiver's interest in the previously uninteresting signals.

## Stem Cells in Wound Healing

Although excessive numbers of stem cells (SCs) may increase the risk of cancer, elevated SC numbers may be desirable, at least transiently, for the promotion of tissue repair and regeneration. **Fuchs *et al.*** (p. 286, published online 20 June) found that mice deficient for the proapoptotic *Sept4/ARTS* gene have elevated numbers of apoptosis-resistant hair follicle SCs and display dramatic improvement in wound healing and regeneration. Inactivation of the caspase inhibitor XIAP, a direct target for the proapoptotic activity of ARTS, abrogated these phenotypes and impaired wound healing.



Susan M. Haig is a supervisory wildlife ecologist with the U.S. Geological Survey Forest and Rangeland Ecosystem Science Center, Corvallis, OR; a professor of wildlife ecology at Oregon State University, Corvallis, OR; and president of the American Ornithologists' Union, Washington, DC. E-mail: susan\_haig@usgs.gov.

Thomas E. Martin is a senior scientist with the U.S. Geological Survey Montana Cooperative Wildlife Research Unit, Missoula, MT; and a professor at the University of Montana, Missoula, MT. E-mail: tmartin@usgs.gov.

Charles van Riper III is a senior scientist and supervisory research ecologist with the U.S. Geological Survey at the University of Arizona, Tucson, AZ. E-mail: charles\_van\_riper@usgs.gov.

T. Douglas Beard Jr. is the chief of the U.S. Geological Survey National Climate Change and Wildlife Science Center, Reston, VA; and president of the World Council of Fisheries Societies, Bethesda, MD. E-mail: dbeard@usgs.gov.

## Pathways for Conservation

NEXT WEEK, CONSERVATION SCIENTISTS WILL GATHER AT THE INTERNATIONAL CONGRESS FOR Conservation Biology (ICCB) in Baltimore, Maryland, to grapple with the challenges of preserving our natural world in the face of a growing and increasingly consumptive human population. The natural world provides countless services, such as clean water, protection from flooding, and carbon sequestration, while offering opportunities for new medicines, foods, and energy production. Yet these valuable services and opportunities are disappearing along with the species and natural areas that supply them. The needs of a growing human population must be met while conserving the planet's natural systems. Accomplishing both will depend on making clearer connections between scientific results regarding issues such as biodiversity loss and the critical decisions that must be made about conditions that underlie change, such as greenhouse gas emissions and freshwater availability. The good news is that today's conservation scientists are developing innovative tools and strategies.

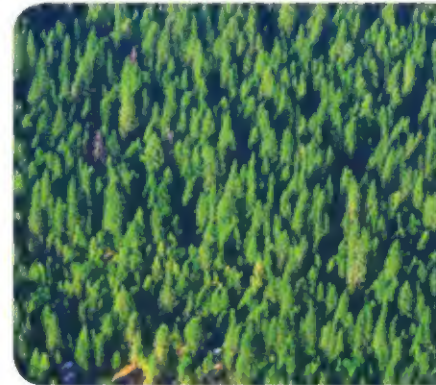
New technical concepts include applying electronic circuit theory to better understand how environmental features influence the genetic structure of multiple species in a particular landscape. This landscape genetics approach has provided guidance for decisions about timber management in the disappearing mature forests of the U.S. Pacific Northwest. Advances in automated wireless sensors, deployed by the thousands, will reduce the need for labor-intensive manual sampling of water, soil, air, vegetation, and wildlife, providing an unprecedented opportunity to track the effects of climate change. Likewise, identifying animal responses to environmental change throughout their life cycle will benefit from the use of unmanned aircraft. This effort will be greatly enhanced when a global animal tracking system operated from the International Space Station (called ICARUS) is launched and then expanded with the use of cell phone technology to monitor animal migratory connectivity. Even de-extinction technologies may be considered in future efforts.

Successful strategies for maximizing biodiversity while supporting human needs depend on understanding how species differ in their resilience and adaptability to broad environmental change. Those with little plasticity or genetic variance are at highest risk because of changing conditions; these include corals, amphibians, and island birds. Climate change may lead to completely new species assemblages, and conservation decision-makers must understand species responses so that responsible actions can be implemented. Another challenge is identifying the responses of invasive species, because they can so easily adapt to changing conditions and negatively alter biodiversity. This can be seen in the largely ineffective efforts to thwart loss of biodiversity in the U.S. Great Lakes as a result of a nonnative zebra mussel or in the loss of native plant diversity caused by invasive spotted knapweed.

Most importantly, conservation scientists must redouble efforts to communicate their research to the public, agencies, and policy-makers in ways that are easily understood and implemented. This approach is currently playing out in the California State Legislature as conservation scientists convey the negative effects of lead ammunition on wildlife and humans. A statewide ban on lead would also substantially boost recovery of the California condor and other scavenging birds and mammals. Overall, conservation decisions must be made by considering the fair-value impact on the ecosystem as well as the human need for the resource. If appropriately valued, nature and society should both benefit. The ICCB conference will continue this discussion to identify and address the most important of these challenges for preserving our natural world.

— Susan M. Haig, Thomas E. Martin, Charles van Riper III, T. Douglas Beard Jr.

10.1126/science.1242710





## ASTRONOMY

### Merger Relics

Massive galaxies are thought to form through a succession of mergers between smaller galaxies. These interactions are expected to be more frequent in regions where there are fewer galaxies; in high-density regions, galaxies move faster and mergers are less likely. However, a recent study has revealed that 38% of massive galaxies in heavy clusters of galaxies show features that are consistent with the merging of galaxies (such as tidal tails). To try to explain this unexpected result, Yi *et al.* ran a cosmological-volume simulation to derive the merger history of dark-matter halos, then constructed semi-analytical models of galaxies to populate those halos, and finally performed hydrodynamical simulations of galaxy-galaxy mergers to estimate the lifetime of merger features. Merger features are expected to last very long in clusters of galaxies. Thus, when observed there, they may not be the result of recent *in situ* mergers but relics from interactions that happened when the galaxies were in a different environment. — MJC

*Astron. Astrophys.* **554**, A122 (2013).

## SIGNAL TRANSDUCTION

### Minute Regulation

A more thorough understanding of cellular signaling mechanisms depends on resolving the spatial and temporal characteristics of such signals *in vivo*. During the third hour of development of the fruit fly embryo, formation of the membranes that partition the syncytium into individual cells occurs with such regularity that it can be used as a marker of developmental age of the embryo with an accuracy of about

on Cic, indicating that Cic degradation may be a consequence of an earlier signal. — LBR

*Proc. Natl. Acad. Sci. U.S.A.* **110**, 10330 (2013).

## CANCER

### Tumor Epigenetics

That human tumors display both genetic mutations and epigenetic alterations—for example, in DNA methylation—has been known for many years; with the completion of cancer genome sequencing projects, possible causal links between the two have come into sharper focus. The discovery of recurrent tumor-associated mutations in genes that encode chromatin-modifying enzymes or DNA methyltransferases represents a clear link between tumor genotype and “epigenotype.” Emerging evidence suggests that a link can be subtle, as illustrated by two studies describing consistent epigenetic alterations

in tumors with mutations in the gene encoding the metabolic enzyme succinate dehydrogenase (SDH). Killian *et al.* find that gastrointestinal stromal tumors harboring SDH mutations are characterized by dramatic and widespread DNA hypermethylation, whereas Letouzé *et al.* report that SDH-mutant paragangliomas display DNA hypermethylation that is associated with the silencing of genes involved in neuroendocrine

cell differentiation. Both groups hypothesize that the hypermethylation phenotype is due to the aberrant accumulation of an oncometabolite that inhibits DNA-demethylating enzymes, with succinate being a strong candidate. — PAK

*Cancer Discov.* **3**, 648 (2013);

*Cancer Cell* **23**, 739 (2013).

## EPIDEMIOLOGY

### Communicable Disease

In the United States, states have the authority to grant exemptions so that children can begin to attend school without having been vaccinated against childhood diseases. Medical exemptions can be granted when a child has a history of allergic reactions or is immunocompromised. However, there has been a noticeable increase in the numbers of unvaccinated children resulting from nonmedical exemptions, based on religious or philosophical grounds;

in 2011–2012, roughly 80% of all exemptions were nonmedical. Blank *et al.* have gathered information from public health officials, health departments, the Centers for Disease Control and Prevention, the National Conference of State Legislatures, and state legislature databases. Policies were characterized as easy, medium, or difficult, according to the level of effort they would pose for parents requesting exemptions. The lower the barrier, the more nonmedical exemptions were observed, with a twofold difference between the easiest and most difficult procedures. For 2011–2012, at least 21 bills were introduced at the state level to change the exemption procedures, and exemptions would have been made easier if bills in 10 states had passed. As of February 2013, three bills have been introduced in two states to tighten exemptions, and five bills have been introduced in four states to loosen them. The authors advocate social and policy efforts to promote parental education and to stem the spread of vaccine-preventable diseases. — BJ

*Health Affairs* **32**, 1282 (2013).

## OCEAN SCIENCE

### Heating the Deep Ocean

As greenhouse gas concentrations in the atmosphere increase, the resulting heat warms not only the atmosphere but also the oceans. However, temperature increases at the sea



1 min. Lim *et al.* analyzed the kinetics of the effects of the mitogen-activated protein kinase ERK on transcription in dozens of stained and fixed embryos oriented on microfluidics chips. Activated ERK was known to reduce the nuclear localization of the transcriptional repressor protein Cic, thus increasing Cic's degradation. However, these more refined measurements showed that ERK has a faster regulatory effect



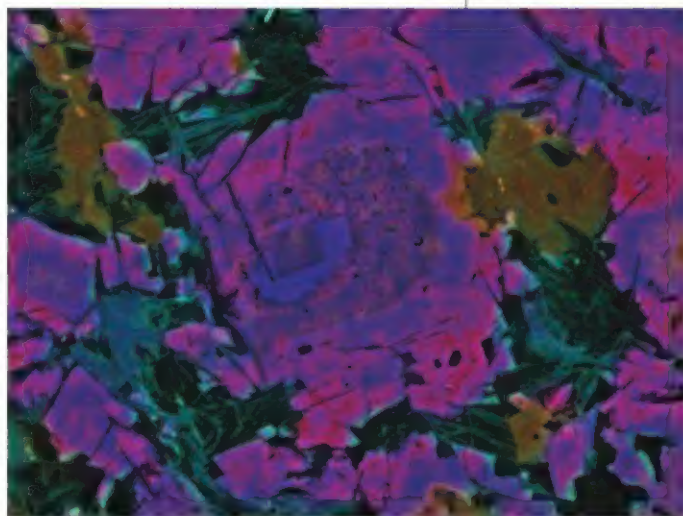
surface and in the upper ~700 m of the oceans stalled in the 2000s. Recent modeling and observational studies have suggested that the deep ocean has taken up the heat, particularly at depths between 700 and 2000 m. However, regular, spatially homogenous ocean temperature data are only available since 2003 from the Argo ocean observing system, complicating comparison with earlier data sets. Balmaseda *et al.* used a new observation-based reanalysis of the ocean to investigate how the heat content has changed over the period from 1958 to 2009. They provide evidence for an overall warming trend, punctuated by cooling episodes that can be attributed to volcanic eruptions. The massive 1997–1998 El Niño event also had a noticeable cooling impact. In the past decade, the deep ocean has continued to warm, whereas temperatures in the upper 300 m have stabilized; the ocean as a whole has continued to warm at an increasing rate. The qualitative warming patterns persisted when Argo data were removed. The authors attribute the changing heat distribution to changes in surface winds, particularly an intensification of the trade winds in subtropical gyres. — JFU

*Geophys. Res. Lett.* **40**, 1754 (2013).

## GEOCHEMISTRY

### Oxidation Before Oxygen

The emergence of oxygen-producing photosynthesis had a profound effect on Earth's surface environment. It eventually oxidized the oceans and atmosphere, paving the way for aerobic life.



Determining the timing of photosynthesis and the subsequent transformation of biogeochemical cycles relies on analyzing clues in ancient buried sediments. Johnson *et al.* analyzed the mineralogy and isotopic signatures of carbon

and sulfur in 2.4-billion-year-old drill cores from South Africa. Synchrotron-based x-ray absorption spectroscopy revealed that abundant Mn oxides were hosted in carbonate deposits, which were probably formed via oxidation of soluble Mn(II). Several lines of geochemical evidence based on redox-sensitive proxies, however, preclude oxygen as the primary oxidant acting on Mn. Moreover, because the rise of oxygen from oxygenic cyanobacteria would not occur for another 200 million years after the sediments were deposited, a primitive (or transitional) form of photosynthesis may have been responsible for forming the Mn oxides. In this scenario, the water-oxidizing complex in the early photosynthesizing enzyme machinery utilized Mn(II) as an electron donor. — NW

*Proc. Natl. Acad. Sci. U.S.A.* **110**, 11238 (2013).

## MATERIALS SCIENCE

### I Sense the Force

Although composite materials can show enhanced properties, understanding the way these materials deform and fail is not straightforward. Besides the individual properties of the matrix and the filler, one has to worry about the distribution of the filler particles, the strength of the interfacial bonding between the filler and matrix, and the way that the combined material will deform and debond. Raja *et al.* show that luminescent semiconductor nanocrystal tetrapods, composed of zinc-blend CdSe cores with epitaxially grown wurtzite CdS arms, can be used as stress sensors. The tetrapods were electrospun into a matrix

of poly L-lactic acid at weight fractions ranging from 3.6 to 40%. During extension of the composite fibers, both the elastic and plastic deformation regions could be tracked through shifts in the fluorescence of the nanocrystals. The authors note that because the particles tend to clump and because there is incomplete stress transfer from the polymer to the nanocrystals, they do not deform plastically when the polymer does, thus giving greater reversibility to the stress measurements, as seen in comparing the fluorescence observations with traditional tensile measurements. — MSL

*Nano Lett.* **10**, 1021/10.1021/nl401999t (2013).



## Join the Conversation!

Twitter is a great way to connect with AAAS members and staff about the issues that matter to you most. Be a part of the discussion while staying up-to-date on the latest news and information about your personal member benefits.

Follow us  
@AAASmember  
and join the  
conversation with  
#AAAS



MemberCentral.aaas.org







# Want to win a rather special prize in Stockholm, Sweden this December?



Winner's essay published in the journal *Science*  
\$25,000 dollars grand prize  
Awards held in Stockholm in December



This December a rather special prize will be awarded in Stockholm, Sweden. The journal *Science* and SciLifeLab have come together to recognize and celebrate excellence in PhD research. The *Science* and SciLifeLab Prize has been established to support young scientists at the start of their career.

*"Science has never been more exciting and, as leaders in science, we need to support and encourage young researchers today and tomorrow. This prize is a way of doing just that."*

*Professor Mathias Uhlen, Director SciLifeLab*

The grand prize winner of this major global award will have their essay published in the journal *Science* and receive \$25,000. Three runners up will receive a combined total of an additional \$10,000 in prize money.

The prizes will be presented in Stockholm, Sweden in the middle of December 2013.

#### To enter

You must be a recent Ph.D. graduate (awarded between January 1, 2011 and December 31, 2012).

Submissions must be in the form of a 1000 word essay, in English, on your thesis, highlighting the significance of its contribution and overall implications in the field. The four submission areas for this prize are: (1) Genomics / Proteomics / Systems Biology (2) Developmental Biology (3) Molecular and Cellular Biology (4) Environmental Life Science.

The deadline for submissions is August 15, 2013. The overall winning essay will be published in *Science*.

For further details and to enter, please go to: [www.sciencemag.org/scilifelabprize](http://www.sciencemag.org/scilifelabprize)

*For over 130 years the journal Science has been the world's leading journal of original scientific research, global news and commentary.*

*SciLifeLab is a collaboration between four universities in Stockholm and Uppsala, Sweden, and is a pioneering center for large-scale biosciences with a focus on health and environmental research.*

*With the kind support of the Knut and Alice Wallenberg Foundation*

*Knut och Alice  
Wallbergs  
Stiftelse*



SciLifeLab



## AROUND THE WORLD



Rome 1

## Rinderpest Research Poised For a Comeback

In 2011, rinderpest, a devastating cattle illness, became the second infectious disease after smallpox that humans have eradicated from nature. In June 2012, the U.N. Food and Agricultural Organization (FAO), in Rome, and the Paris-based World Organisation for Animal Health (OIE) banned research using live rinderpest virus, fearing

joint FAO-OIE expert committee that they can meet the new safety criteria. "We want to ensure [rinderpest research] is done in the safest possible environment," Lubroth says.

Bethesda, Maryland 2

## U.S. Senate Panel Gives NIH \$31 Billion in 2014

A U.S. Senate spending panel last week approved a bill giving the National Institutes of Health (NIH) \$31 billion in 2014, a 7% increase over this year's budget, which was depressed by the across-the-board federal budget cuts known as sequestration. The NIH funding level approved by the Senate Appropriations Committee is \$147 million below the president's request for 2014, but \$2 billion more than the \$28.9 billion that NIH has to spend this year.

Jennifer Zeitzer, legislative relations director for the Federation of American Societies for Experimental Biology, said that her group is "thrilled" with the figure. "It's far better than the current situation and it's a move in the right direction," she says. The bill now awaits a vote by the entire Senate. The House Appropriations Committee, which has a much smaller pot of money to fund NIH and other agencies, has not yet taken up its version of the bill.

Brussels 3

## E.C. Beefs Up Research Partnerships With Industry

The European Commission wants to double public money available for Joint Technology Initiatives (JTIs), five research programs that provide public support to private research and innovation, with industry matching E.U. funding. Together, the JTIs will receive €6.44 billion from the E.U. budget between

## Investing



**Double the money.** Geoghegan-Quinn announces new plans for Joint Technology Initiatives.

2014 and 2020, up from €3.12 billion in 2007 to 2013, research commissioner Maire Geoghegan-Quinn announced on 10 July. Industry says that it will put about €10 billion on the table for the next 7 years, up from €4.66 billion in the current period.

JTIs bring together academia, research organizations, and competing businesses in research areas considered complex or risky, such as aeronautics or pharmaceuticals. The initiatives have been slammed for having complex rules and procedures, but the funding boost is a testament to the participants' overall satisfaction with this collaborative model. Future incarnations will be more ambitious, cut down on red tape, and align disparate rules, a commission spokesman says.

The commission will release a detailed legal proposal early next week. The plans must then be signed off on by the European Parliament and member states before the programs are rolled out next year.

<http://scim.ag/EUJointTech>

Rome 4

## Scientists, Stem Cell Provider Meet to Discuss Trial

A panel of top science administrators and stem cell scientists met on 12 July with Davide Vannoni, president of the Stamina Foundation, which provides controversial stem cell treatments, to hash out details for a government-sponsored clinical trial of the therapy. Many stem cell scientists remain opposed to the study, saying there's little to suggest that the therapy—which is based on cultured mesenchymal stem cells but whose details remain unpublished—will work.

In May, the Italian Parliament ordered an 18-month clinical trial of the therapy and allocated €3 million to carry it out. But prior to the 12 July meeting, Vannoni had not yet provided the committee appointed to coordinate the study with protocols describing how his treatment works, because he says that he's still working on their standardization. The start of the trial has been delayed by at least

**Former scourge.** Cows dead from rinderpest in South Africa in 1896.



an accident could cause a resurgence. Now, research on the virus is set to resume following a 10 July decision by FAO and OIE to lift the moratorium. The two organizations used the hiatus to develop safety protocols and risk-versus-benefit criteria.

Juan Lubroth, FAO's chief veterinarian, says that there is interest in sequencing some of the hundreds of isolates that were collected over decades to understand how the virus changed over time. They also want to see if vaccines developed for peste des petits ruminants, a closely related disease, can protect cattle from rinderpest. If so, stores of rinderpest virus used to replenish vaccines could be destroyed, eliminating another potential source of accidental release. Researchers will have to convince a



a month. Vannoni has his own conditions, including that there can be no changes to his protocol and the cells need to be produced at one facility under the supervision of a Stamina biologist. Barring these, Vannoni says that he may move the research abroad. <http://scim.ag/Staminatrial>

Okuma, Japan 5

## Contaminated Water Likely Polluting Ocean From Reactors

Japanese and international groups monitoring Pacific Ocean waters near the Fukushima Daiichi Nuclear Power Plant have continued to find radioactive cesium at levels higher than expected, given the effects of dilution and radioactive decay. They have claimed that this suggests contaminated cooling water is leaking from the crippled reactors, though plant operator Tokyo Electric Power has long denied this possibility. At a press briefing on 10 July, Shunichi Tanaka, chair of Japan's new Nuclear Regulation Authority (NRA), sided with the experts, saying that the evidence suggests that radiological contamination of the ocean probably "has been continuing for the last 2 years." Tanaka added that it was important to take measures to minimize the leaks.

Also last week, four Japanese electric utilities applied for approval to restart 10 nuclear power plants that have been idled since shortly after the Fukushima accident. NRA will review the applications based on new safety standards unveiled last month. The process is expected to take at least 6 months. The utilities will also need the approval of local governments.

## NEWSMAKERS

### Origin-of-Everything Studies Nab Gruber Prize

Two physicists who made fundamental contributions to understanding how the universe evolved into its current structure have won the 2013 Gruber Cosmology Prize. **Viatcheslav Mukhanov**, a professor at Ludwig Maximilians University in Munich, Germany, and **Alexei Starobinsky**, a researcher at the Landau Institute for Theoretical Physics in Moscow, will share the \$500,000 award.

Starobinsky's calculations in the late 1970s showed that the universe could have

exploded in size in the first moments after the big bang. The work laid the foundations for the idea of an inflationary universe, a bedrock of modern cosmology.

Mukhanov's contribution dates back to 1981, when he was a researcher at the Moscow Physical Technical Institute. Along with a fellow scientist named G. V. Chibisov, Mukhanov showed that quantum fluctuations in the dense and tiny newborn universe could have served as the seeds of modern day cosmic structure. As the universe swelled, these fluctuations gave rise to the formation of galaxies and galaxy clusters.

## FINDINGS

### Cancer Knife Sniffs Out Tumor Cells

When cancer surgeons can't see the edges of a tumor, they often send some tissue to the pathology lab, which can take up to 30 minutes per analysis. Now, there's an alternative: The "intelligent knife," or iKnife. When tissue is seared by a standard electrosurgical scalpel, the iKnife sucks the resulting smoke into a modified mass spectrometry machine. The instrument aims to instantly detect whether cells are cancerous or healthy by analyzing this smoke for certain lipids, or fats, and comparing this profile to molecular signatures >>



Starobinsky



### Meet 'Big-Nose Horned-Face'

There's a new contender for wackiest-looking dinosaur: *Nasutoceratops*, which means, in Latin, "big-nose horned-face." The 5-meter-long dino had a giant schnoz and sharp, curved horns measuring nearly a meter long. *Nasutoceratops*, a distant relative of the famed *Triceratops*, was recently discovered by paleontologists digging in Utah's Grand Staircase-Escalante National Monument. As the team reports online this week in the *Proceedings of the Royal Society B*, the creature lived about 76 million years ago in a swampy, subtropical region that geologists call Laramidia, formed when an inland sea filled the center of North America and divided it in half. The dino's nose wasn't used for smelling; the scent organs of horned dinosaurs were further back in their heads, next to the brain. So why such a big honker? The researchers don't know, but suggest that the elaborate horns might have been used to attract females and fend off competing males.



## BY THE NUMBERS

**23.82 months** Average time from publication to retraction for articles published after 2002, according to a *PLOS ONE* analysis. Papers published between 1973 and 2002 took nearly 50 months before retraction, perhaps due in part to higher barriers to pulling papers.

**64%** Fraction of 455 women who experienced infertility after surviving childhood cancer and were eventually able to become pregnant, according to a report in *The Lancet Oncology*.

**8000 years ago** First known use of manure as fertilizer among Europe's first farmers—thousands of years earlier than thought—according to a study in the *Proceedings of the National Academy of Sciences*.

## &gt;&gt;FINDINGS

for various cancer types. When tested during 81 surgeries, the iKnife matched pathology results for cancerous and normal tissues for every single patient, the researchers report



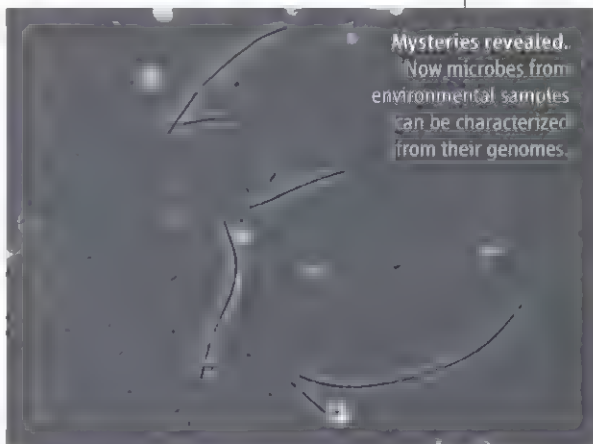
this week in *Science Translational Medicine*.

The iKnife provides “real-time information,” says its inventor Zoltán Takáts, a Hungarian chemist who collaborated with surgeon Jeremy Nicholson at Imperial College London to develop the tool. Their next step is to conduct clinical trials to find out

if using the iKnife helps patients develop fewer recurring tumors and live longer. <http://scim.ag/cancerknife>

## Shedding Light on Microbial ‘Dark Matter’

When researchers began sequencing DNA from environmental samples more than a decade ago, they discovered a vast, diverse world of microbes. But this microbial dark



matter has defied further description—and definitive placement on the tree of life—because so few kinds will grow in the lab.

That didn't stop microbiologist Tanja Woyke from the Department of Energy Joint Genome Institute in Walnut Creek, California. She and her colleagues used an approach that allowed them to sequence the DNA in individual cells (rather than requiring many copies of the cells). They characterized 200 new microbes from 29 largely uncharted phyla, then used the genomes to determine the microbes' phylogenetic relationships and to assess how each lives, naming 18 phyla

accordingly, the team reported online this week in *Nature*.

Novelties emerged: Some archaea possess genes previously thought to exist only in bacteria; some bacteria have archaeal genes. One group of microbes has even altered the three-base coding system for proteins.

In the future, single-cell sequencing could fill in more branches of the microbial tree of life. “It's an inflection point in environmental microbiology and microbiology in general,” says

Norman Pace, a microbiologist at the University of Colorado, Boulder.

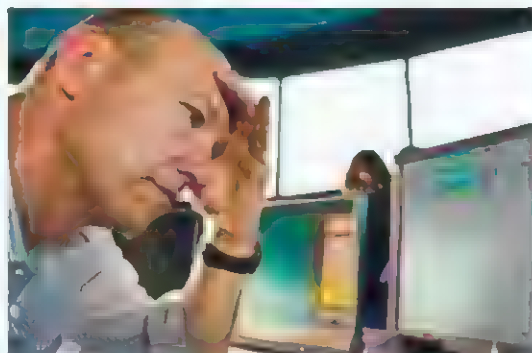
<http://scim.ag/microbedark>

## Random Sample

## Cool by the Numbers

When it comes to a hot, crowded room, hell really is other people. But once they exit, air-conditioning the empty room is an energy drain. The solution: a ventilation system that adjusts to the number of people in a room. Such a system could save three times as much energy as simply turning off the heat and air conditioning to empty rooms, computer models show. Installing people-counting sensors could save 18% of the energy used by a typical large office building in the United States, report researchers at the Department of Energy's (DOE's) Pacific Northwest National Laboratory (PNNL) in Richland, Washington. By comparison, turning off heating, ventilation, and air conditioning to empty rooms saves 6%, says PNNL engineer Guopeng Liu.

But building owners are likely to install such a system only if it's cheap and doesn't require rewiring the building, says Aravind Dasu, a computer scientist with the University of Southern California in Washington, D.C.: “If it's all wireless it's a game-changer.” James Freihaut, chief scientist at DOE's Energy Efficient Buildings hub in Philadelphia, Pennsylvania, notes that local building codes may also present a challenge, as many of them require constant ventilation within an occupied commercial structure.







JAPAN

## Tampered Data Cast Shadow on Drug Trial

**TOKYO**—In a scandal reverberating across Japan's biomedical research landscape, a university in Kyoto last week acknowledged data manipulation in a university-run clinical trial for a blockbuster hypertension drug, valsartan. Japanese media have turned the episode into a cause célèbre; the *Yomiuri Shimbun*, one of Japan's biggest newspapers, labeled it a "serious betrayal" for patients. Repercussions could extend beyond valsartan, marketed under the trade name Diovan by the Swiss pharmaceutical giant Novartis.

"This incident is causing a loss of confidence in Japan's research internationally and making Japanese patients skeptical [about treatments]," says Yoshiaki Yui, a medical doctor at Kyoto University. Health minister Norihisa Tamura has vowed to appoint a committee that would propose measures to prevent a recurrence.

Sold worldwide, valsartan was approved in Japan in 2000 and has become the country's best-selling drug, pulling in roughly \$1 billion last year, according to analysts. A clinical trial claiming that valsartan also reduces angina and stroke risk helped boost its popularity in Japan. That claim has fallen apart, in the process raising concerns about cozy ties between researchers and drug companies and about impediments to investigating research misconduct in Japan.

At the heart of the scandal are data from the Kyoto Heart Study, launched in 2003 by Hiroaki Matsubara, a cardiologist at Kyoto Prefectural University of Medicine (KPUM).

The 4-year study followed 3000 patients given valsartan or alternative medications. A main outcome, reported on 31 August 2009 in the *European Heart Journal*, was that valsartan, which reduces blood pressure by blocking the receptor for the hormone angiotensin, "prevented more cardiovascular events" in high-risk patients than did drugs that lower blood pressure through another mechanism.

In late 2011, bloggers started raising questions about alleged image manipulation in Matsubara's papers. Then, in an April 2012 letter to *The Lancet*, Yui expressed concerns about Kyoto Heart Study's statistics and conclusions, writing that the effectiveness in preventing angina was not seen in other trials of valsartanlike drugs or in clinical practice. Responding to requests from journals, KPUM started its own investigation. Matsubara resigned from KPUM in February, after the *European Heart Journal*, citing "[c]ritical problems ... with some of the data," retracted the heart study paper.

"Data were manipulated," KPUM President Toshikazu Yoshikawa bluntly stated at an 11 July press conference. According to the university's investigative report, which *Science* has obtained, in the Kyoto Heart Study there were 34 discrepancies between the clinical medical records and the data set used for analysis; these overstated adverse cardiovascular events in the nonvalsartan group and missed such events in the valsartan

**Chagrined.** KPUM President Toshikazu Yoshikawa (center) and other officials apologize after reporting fraud.

group. Once anomalous data were corrected, the claim that valsartan reduces the incidence of cardiovascular events such as angina or stroke by about half "is not supported," the report says. Eight papers authored by Matsubara have been retracted.

In an e-mail to *Science*, Matsubara writes that he "was not involved in and gave no instructions" for the event data analysis, which he said was the responsibility of a Novartis employee. Novartis headquarters in Basel declined to comment on KPUM's findings, stating in an e-mail to *Science* that "we are unfamiliar with how the university conducted its review." But the company has confirmed that employees of its Japanese subsidiary participated in the Kyoto Heart Study and several similar studies at other Japanese institutions without noting their affiliation on resulting papers. In a statement posted to its website on 12 July, Novartis blamed the disclosure failures on a lack of guidelines and a misunderstanding of the appropriate level of involvement in such trials. "Preventive and corrective measures have been implemented," the statement said.

The debacle raises troubling questions about research oversight. KPUM officials said that they could not probe more deeply into who manipulated data because they cannot compel cooperation from Novartis employees. Universities in Japan have no authority to question people outside their institution, says Tetsuya Tanimoto, a physician at the University of Tokyo who studies pharmaceutical regulatory issues. Japan needs something like the U.S. Office of Research Integrity, he says.

Japan's medical research establishment could come in for broad scrutiny. KPUM confirmed in an e-mail to

*Science* that since 2008, Matsubara received about \$1.4 million for his research from Novartis. Such grants to clinical researchers are not unusual, but they highlight inadequate public support for clinical research in Japan, Tanimoto says. The revelations could also erode public support for emerging plans to shake up medical research by establishing an outcome-focused version of the U.S. National Institutes of Health. In the wake of the scandal, the Japanese public may question whether the money will be well-spent and the results trustworthy.

—DENNIS NORMILE

**"Data were manipulated."**

—TOSHIKAZU YOSHIKAWA  
KPUM PRESIDENT





## ANTHROPOLOGY

# Latest Skirmish Over Ancestral Violence Strikes Blow for Peace

Are hunter-gatherer societies warlike? That question has sparked a war of its own among scientists. Some anthropologists see these traditional societies as largely peaceful, relying on trade networks with outsiders for survival, while other researchers cite frequent deadly clashes among neighboring groups. The question has implications beyond today's dwindling foraging peoples, because our ancestors lived as hunter-gatherers for most of prehistory. If war is a common feature of the foraging way of life, then perhaps it was a driving force in human evolution.

On page 270 of this issue, two researchers fire a salvo in support of peace. Using existing ethnographic data, Douglas Fry and Patrik Söderberg of Åbo Akademi University in Vasa, Finland, conclude that people living in mobile foraging societies, such as the !Kung of southern Africa and the Semang of the Malay Peninsula, today rarely engage in what most modern people call "war." Rather, two-thirds of killings in such societies occur among people of the same group, and most lethal events stem from personal disputes. "These findings imply that warfare was probably not very common before the advent of agriculture, when most if not all humans lived as nomadic foragers," says cultural anthropologist Kirk Endicott of Dartmouth College, who was not part of the study.

But those on the other side of the debate say that the paper lacks the numerical data to evaluate how common war and homicide actually are. "This is essentially a list of anecdotes—there's no real method in these eth-

nographies," says anthropologist Kim Hill of Arizona State University, Tempe, whose own detailed field studies found warfare in three South American groups. He and others cite recent work suggesting that ancient war was frequent enough to have influenced our evolution, for example by encouraging altruistic cooperation among warriors (*Science*, 5 June 2009, p. 1293).

Fry and Söderberg drew on data from the Standard Cross-Cultural Sample (SCCS), a respected ethnographic database set up by other anthropologists in the 1980s. The pair pulled out all mobile societies in which hunting, gathering, and fishing brought in 95% of the people's food—21 societies in all—then studied the oldest ethnographic descriptions that were highly rated by the SCCS scholars. "To be purists, we took only the oldest high-quality sources for each culture," says Fry, an anthropologist; he argues that the oldest studies best reflect a society's traditional ways.

The pair then scrutinized every instance of lethal aggression recounted in the ethnographies. They found that more than half of societies did not practice what they would call war on outside groups. Overall, 55% of cases had a single killer and single victim. Also, most killings were driven by personal motives, such as fights over women and revenge, and are better classified as homicides or sometimes feuds than as war, Fry says. Such societies are too small to wage wars, he notes, and groups rarely fight each other because group membership is flexible

**Play, not war.** !Kung men like these playing a traditional game in Namibia may attack other individuals, but they rarely gather to make war on other societies.

and blurred by intermarriage. "In my view the default for nomadic foragers is nonwarring."

The new study is "a very valuable contribution to the study of mobile foragers," says anthropologist Richard B. Lee of the University of Toronto in Canada, who has studied hunter-gatherers in the field for 40 years. Endicott agrees that the paper offers a "valuable corrective" to an "erroneous" view of mobile foragers as warlike.

However, critics find fault with Fry and Söderberg's selection of societies and their restricted samples and ask how well these societies represent the past. The descriptive data of the SCCS can't provide the key metric on how many people died in war compared with other causes of death, Hill says. He and economist Samuel Bowles of the Santa Fe Institute also argue that Fry should have included sedentary hunter-gatherers, such as warring fishing societies in British Columbia. And limiting the data to early ethnographies ignores a host of additional data—and deaths—says Harvard University anthropologist Richard Wrangham. "There is lots of evidence of war in some of the societies that they list as having no killings," he says. For example, the Andamanese Islanders are reported as having few killing events, but other researchers have documented additional killings there, often between groups.

Part of the dispute comes down to the definition of war. For Fry, war implies the killing of any outgroup member because they are in the outgroup; having a personal motive makes a homicide. His critics argue that personal motives may indeed spark "wars" in small-scale societies. "Feuds are warfare, revenge raiding is warfare," Hill says. Researchers on both sides caution against using living people as direct models of our ancestors.

Anthropologist Polly Wiessner of the University of Utah in Salt Lake City, who has studied both the relatively peaceful !Kung and the relatively violent Enga people of Papua New Guinea (*Science*, 28 September 2012, pp. 1593 and 1651), agrees that few mobile foragers often wage war today. But given that some foragers do fight fiercely, she hopes the battle lines among scientists will shift to asking what promotes and what inhibits warfare. "We should be asking how coalitionary aggression, which does appear in our phylogeny, was harnessed among our successful ancestors." —ELIZABETH CULOTTA

CREDIT: © K. M. WALKER/ROBERT HARDING WORLD. MAGERY/CORBIS



## SPAIN

# Spain's Research Council Approaches Bankruptcy

**BARCELONA, SPAIN**—Spain's flagship research agency is in deep trouble. The Spanish National Research Council (CSIC) has run massive deficits for several years. If the government—which has made drastic cuts in research funding the past few years—doesn't pick up the tab, it may go into bankruptcy before the year is over. At a press conference last week, CSIC President Emilio Lora-Tamayo warned of an impending "cataclysm" and said that without a cash injection, CSIC "wouldn't be able to go on."

On 28 June, the Spanish government agreed to give CSIC an extra €25 million, as part of an €104 million package for research; but CSIC says that it needs €75 million more. Meanwhile, Lora-Tamayo has issued a range of measures to stem the agency's financial hemorrhage, which scientists say is bringing research projects to a halt. CSIC's researchers are angry—particularly about the revelation that the agency has dipped into the savings accumulated by research groups. Some 140 researchers are considering taking legal action to get those funds back. "The situation is chaotic," says plant biologist José Pío Beltrán, who heads the office coordinating CSIC institutes in the Valencia region. CSIC researchers and trade unions held meetings this week to discuss the situation.

With some 6000 researchers in areas from biology and materials science to the humanities, CSIC is the largest research organization in Spain; its 125 institutes—more than 50 of them joint ventures with universities and other research bodies—account for 20% of the country's research output. The government provides roughly 60% of CSIC's budget; individual researchers raise the rest.

CSIC's revenues peaked at €879 million in 2008, when the agency still had a €26 million surplus. But since then, funding streams have declined much faster than expenditures, leading to annual deficits that have depleted reserves (see graphic). With a projected €101 million deficit in 2013, CSIC would go deeply into the red.

Part of the problem is that, in his first mandate between 2004 and 2008, Spanish president José Luis Rodríguez Zapatero "asked us to be really driving strongly the Spanish [research] system, so we started very ambitious programs to incorporate people," Beltrán says. When Spain's economy tanked and funds declined during Zapatero's second term, CSIC continued supporting those

people rather than laying them off, Beltrán explains. But a letter circulating among CSIC researchers to gauge their interest in legal action also blames "bad management" by successive CSIC governing bodies. (The CSIC presidency declined interview requests.)

Lora-Tamayo issued a directive on 2 July ordering CSIC directors and managers to slow down spending. Institutes were asked to prioritize salaries for staff members on short-term contracts and to finish research projects if not completing them by the end of the year would mean having to return funds. But for some institutes, the available money doesn't come close to even paying for short-term contracts, says Luis Sanz-Menéndez, director of the CSIC Institute of Public Goods and Policies in Madrid. As a result, researchers are barred from spending money and projects are grinding to a halt. "We can't pay ... laboratory expenses, bills for equipment that we have bought. ... We can't buy plane tickets" to go to meetings, says plant ecologist Fernando Valladares of the CSIC National Museum of Natural Sciences in Madrid.

Lora-Tamayo has also revealed that for years, CSIC has been using savings that research groups accumulated from past

competitive grants and industry contracts, without researchers' knowledge. Group leaders have traditionally used these stashes as emergency funds, to hire extra pairs of hands or bridge the gap between two contracts. Lora-Tamayo has said that CSIC intends to return the money "once the agency has been successfully stabilized."



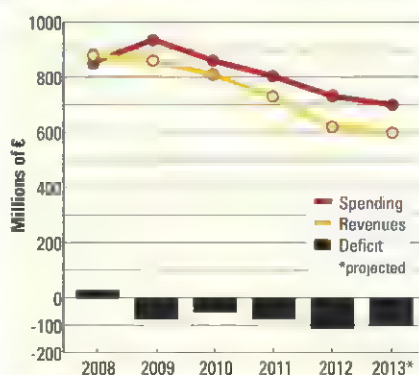
**Mad in Madrid.** Spanish researchers demonstrated against cuts in the science budget on 14 June. Their banner reads: "There is no future without science."

A petition launched on 10 July that drew 69,000 signatures in just 5 days urges Spain's state secretary for research Carmen Vela to "do whatever needs to be done so the CSIC doesn't die." Vela said last week that she would give CSIC an extra €50 million by September and find other solutions, if necessary. But Spain's fiscal situation is so dire that many researchers worry the money won't come. The prospect of losing the savings permanently is "spine-chilling," says Valladares, who says he's "still a little bit in a state of shock."

CSIC's woes aren't the only headache for Spanish science. The current government has slashed the national science budget, delayed competitive funding rounds, and failed to honor past commitments, causing "absolute bewilderment," says a 15 July statement by the Confederation of Spanish Scientific Societies, the Conference of Rectors of Spanish Universities, trade unions, and other associations. The entire scientific enterprise is affected, the letter says: "This strangulation of R&D is undermining a public research system that took more than 30 years to build."

—ELISABETH PAIN

## An Agency in Crisis



**Seeing red.** Since 2009, big deficits have depleted CSIC's reserves.



# Ever-Bigger Viruses Shake Tree of Life

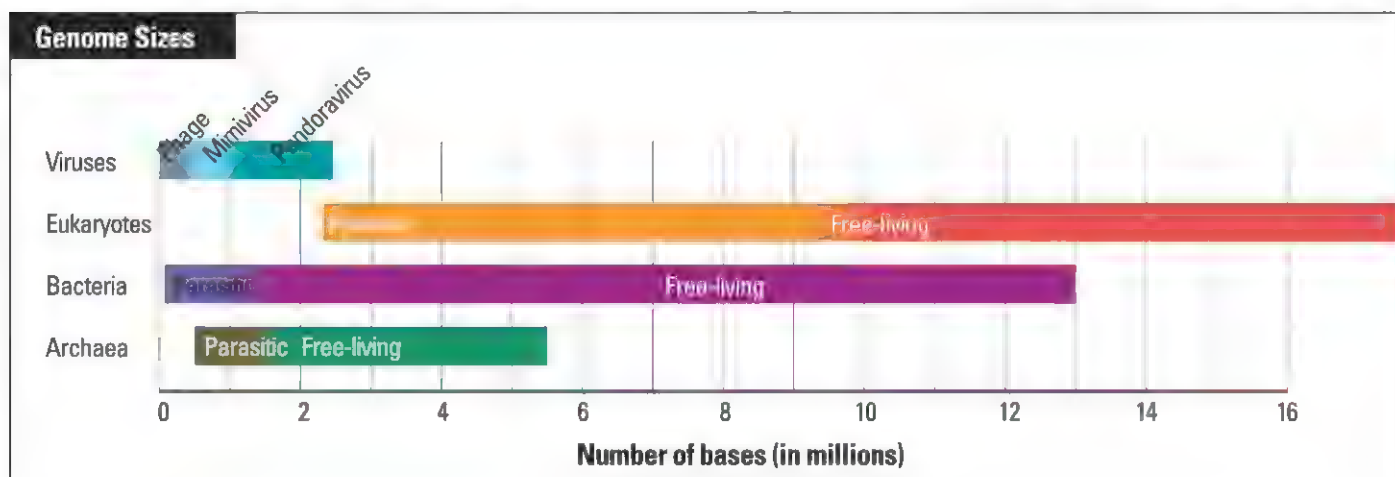
"It's like finding a sasquatch," says Elodie Ghedin, a virologist at the University of Pittsburgh in Pennsylvania. That's one of the amazed reactions to the discovery, reported on page 281, of two new viruses with by far the largest genomes ever seen in a virus, including one that's bigger than the genomes of some parasitic eukaryotes. The virologists in France who unearthed the massive viruses—the biggest one is 1 micron long, a hundred times the size of many viruses—suggest that their finds challenge the long-standing view that viruses don't qualify as life.

a cell and coax their host to replicate them, because they can't make their own proteins.

A decade ago, the discovery in an amoeba of a virus that rivals the size of a small bacterium prompted a rethinking of how viruses originated and what they could do. Didier Raoult, a microbiologist at the University of the Mediterranean in Marseille; Claverie; and their colleagues sequenced the genome of mimivirus, for "microbe mimicking virus." Its 1.18 million bases contained more than 900 putative genes, some closely resembling genes in non-

as mimivirus, plus a few more, and seems to represent an intermediate step between a free-living ancestor and mimivirus

Now, scans of the water and sediment samples that Claverie, Abergel, and other lab members gather whenever they travel have yielded the pandoraviruses. (The researchers inoculate amoeba with the samples to see if any viruses replicate and burst out). The one with the smaller genome came from mud in an Australian pond, while the new king of the viral genomes was in coastal sediments collected off Chile. "The fact that



"It is clear that the paradigm that viruses have small genomes and are relatively simple in comparison to cellular life has been overturned," says Curtis Suttle, a virologist at the University of British Columbia in Vancouver. The genome of one of the viruses is 1.91 million DNA bases long, while the other runs 2.47 million bases. That dwarfs some bacterial genomes and edges into the eukaryotic realm (see chart).

Jean-Michel Claverie and Chantal Abergel from CNRS, the French national research agency, at Aix-Marseille University in France, and their colleagues have dubbed the new viruses pandoraviruses because of their amphora shape and the surprises they may portend. They have strikingly different genes and physical appearances from other viruses. The finding "expands our view of the virus world," Ghedin says.

After their late 19th century discovery, viruses were quickly demoted to inert particles, too simple to belong to the realm of the living. Considered little more than a protein package of genetic material with no metabolic capabilities, viruses must get inside

viruses that are involved in protein production (*Science* 28 March 2003, p. 2033; 19 November 2004, p. 1344).

Mimivirus could have acquired those genes from its cellular hosts, but the mimivirus genes are so different from those of the host amoeba and other cells that Raoult and Claverie instead proposed that mimivirus descended from a free-living cell that gradually lost most of its other genes as it became a parasite. That mimivirus precursor, they suggested, represented a previously unknown branch of life, one predating the emergence of the three major branches, or domains, of life—bacteria, archaea, and eukaryotes.

This theory remains controversial, but it has motivated Claverie to keep hunting for viral giants. "According to this scenario, looking for even bigger viruses with bigger genomes was a way to go back in time, to take a closer, earlier look at this postulated ancestor," he says. He and other researchers have since come across several other giant viruses, including *Megavirus chilensis*, at 1.25 million bases the previous viral genome record-holder. It has many of the same genes

two of them were found almost simultaneously from very distant locations either indicates we were incredibly lucky or that they are not rare," Claverie says. "They are probably everywhere."

Because of their size, the pandoraviruses appeared bacterial-like at first. But using light and electron microscopy, the French group followed the newfound entities through a replication cycle, which proved virus-like. Instead of dividing in two like a typical bacterium or cell, they generated hundreds or more new viral particles, Claverie's team reports. Both pandoraviruses lack genes for energy production and can't actually produce a protein on their own, fulfilling the definition of virus. "The authors seem to have gone the proverbial extra mile to show that these agents are actually viruses rather than some sort of unusual bacteria," says Eugene Koonin, a computational evolutionary biologist at the National Center for Biotechnology Information in Bethesda, Maryland.

But unlike other viruses, the pandoraviruses lack the gene for the capsid protein that typically forms a capsule around a



-ELIZABETH PENNISI

their rightful place at the table where the story of the evolution of life is told."

## Germany Debates How to Strengthen Universities

Council Chair Wolfgang Marquardt says that the recommendations are affordable if Germany takes seriously the goal of spending 3.5% of gross domestic product on research and development. But others are more cautious. "There's still a huge gap between these proposals and the realities faced by politicians," says Wilhelm Krull, secretary general of the Volkswagen Foundation, a private research funder. —GRETCHEN VOGEL

www.sciencemag.org **SCIENCE** VOL 341 19 JULY 2013



Eppendorf Consumables—  
it's Your sample

## Future included

Eppendorf consumables are the result of 50 years constant improvement and development. With the new Eppendorf Tubes® 5.0 mL a new tube format in the medium volume range will complete the legendary Eppendorf Tubes family.

Laboratory processes will become easier and more convenient.

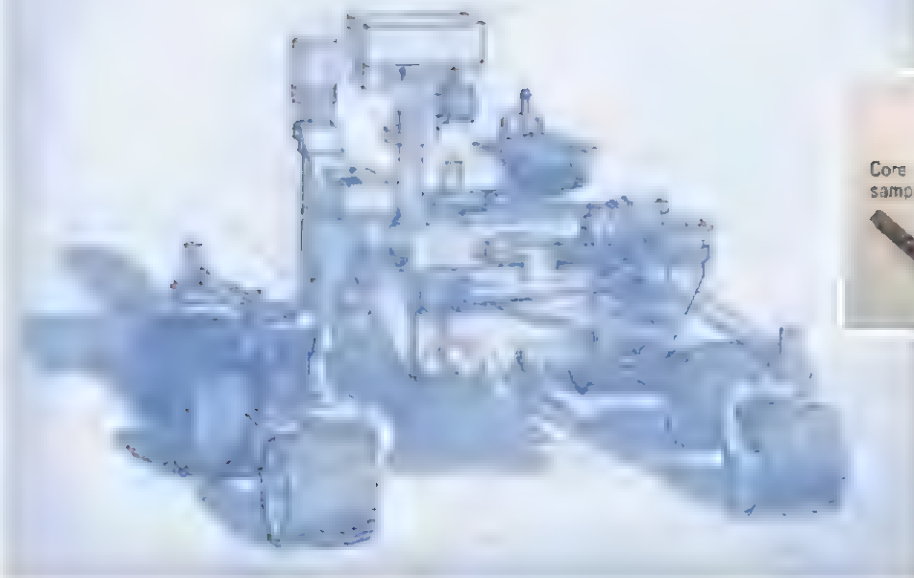
Purest assay results are no coincidence:

- > Unique features to make every day routines faster and easier
- > Minimized risk of chemical leaching from consumables
- > Purity grades tailored to even the highest requirements

[www.eppendorf.com/consumables](http://www.eppendorf.com/consumables)

Eppendorf®, the Eppendorf logo and Eppendorf Tubes® are registered Trademarks of Eppendorf AG, Germany. All rights reserved, including graphics and images. Copyright © 2013 by Eppendorf AG.





## SPACE SCIENCE

## Mars Rover Plans Roll While Asteroid Acrimony Continues

NASA officials are getting some contrasting messages about two of their boldest projects. An agency science panel last week gave a strong endorsement to sending a more capable robotic rover to Mars in 2020 that could cache samples for a later mission to pick up and return to Earth. But researchers and key members of Congress continued to raise serious doubts about the agency's proposal to capture a small asteroid and then land an astronaut on it.

The rover proposal, unveiled on 9 July by a NASA-appointed panel, buoyed the spirits of Mars scientists in the United States, who have been worried about NASA's commitment to exploring the Red Planet since it pulled out of a European-led effort in 2012 (*Science*, 24 February 2012, p. 900). The panel, led by planetary scientist John Mustard of Brown University, says that a 2020 rover should look a lot like Curiosity, the NASA robot now surveying Mars. But it would have a host of new capabilities. In addition to Curiosity-style instruments that take broad pictures of sites, for instance, it would also carry sensors that can make more detailed images of rocks and geological features. Other instruments would allow fine-scale mineralogy studies, especially of rocks through which water might have flowed in the past, and chemically detect and analyze organic carbon (a possible sign of life).

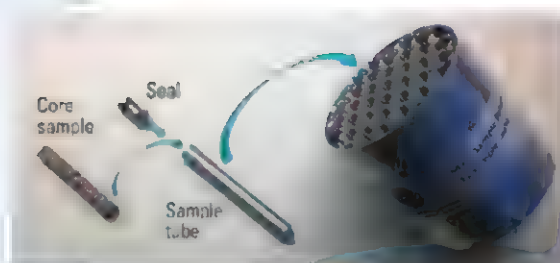
The biggest add-on, however, would be the capability to drill into rock sites chosen during the exploration and insert the cores into a container on the rover. Later missions would haul the container home. By analyzing

the samples in more capable laboratories on Earth, researchers should be able to address "an enormous number of science questions," Mustard says, including whether life ever existed on an earlier, damper Mars and how it evolved.

Although planetary scientists ranked Mars sample caching and return as a top priority in a 2010 decadal plan, the idea isn't devoid of controversy. Some scientists have argued that the time a rover spends caching rocks could be better spent collecting real-time data that could be beamed back to Earth. And some White House budget officials have been resistant to caching on the grounds that it would force NASA to commit to flying additional missions to retrieve the samples.

Ed Weiler, the former head of NASA science, hopes that the panel's unambiguous support for caching will end the debate. "The cache will last on Mars for many years," he says. "You can plan a sample return mission when money becomes available." There was "unanimous enthusiasm" for caching among the panelists, Mustard adds. "We said—Go big or go home. Are we going to do this or not?"

The caching capability will make it harder to estimate the rover's final cost, however, the panel says. NASA hopes to build it for less than \$1.5 billion, about \$1 billion less than Curiosity. It's not yet clear whether the White House and Congress will back that kind of spending, but NASA officials seem optimistic. Jim Green, head of NASA's planetary sciences division, said that the agency will soon take another step toward making



**Curiosity 2.0.** A blueprint for a more capable Mars rover includes instruments to enable the caching of samples (above).

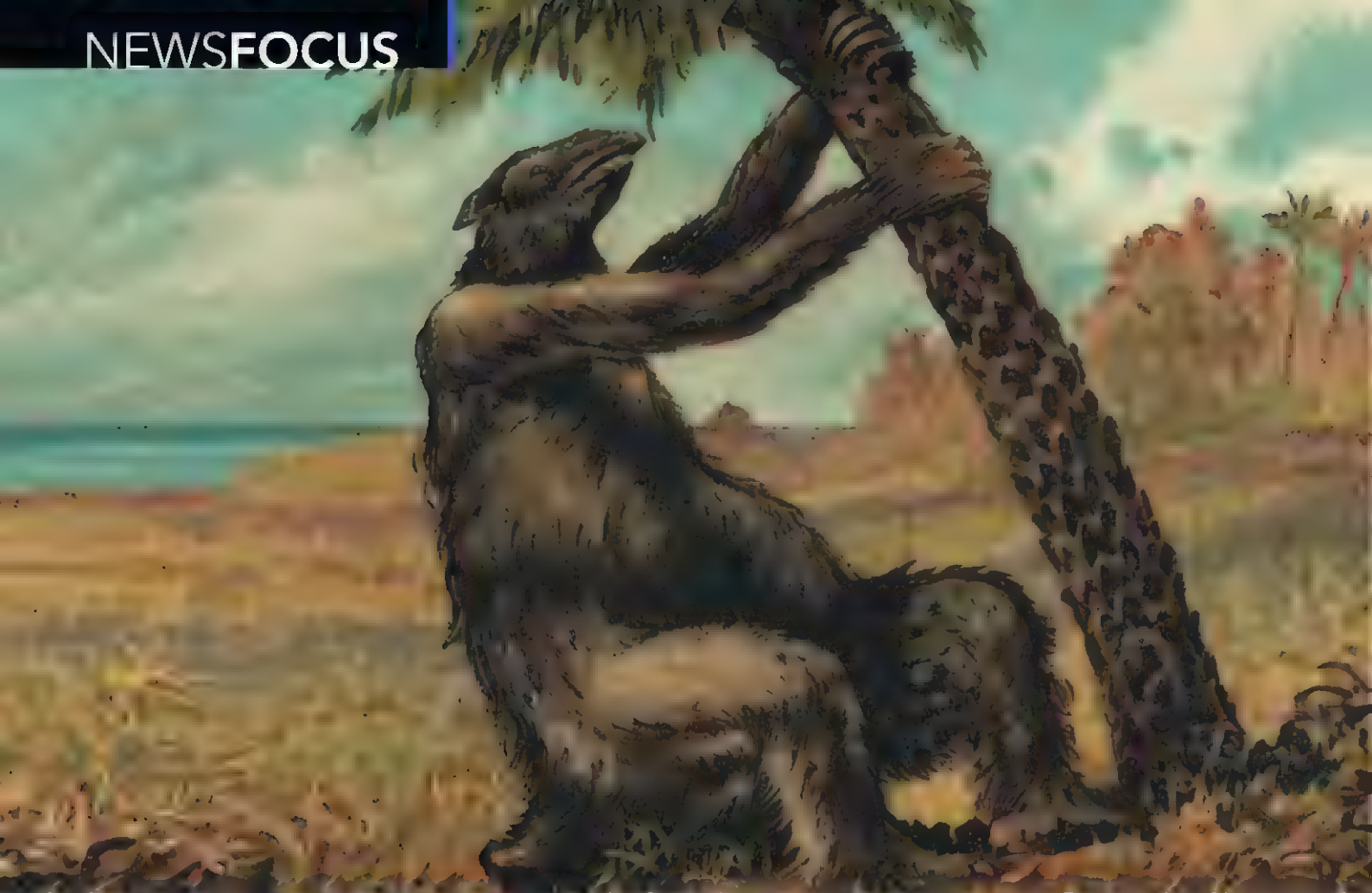
the rover a reality by issuing a call for proposals to design the science instruments.

The growing consensus around the Mars rover stands in stark contrast to the continuing acrimony surrounding NASA's asteroid capture plan. At a workshop held at the U.S. National Academies in Washington, D.C., on the same day that NASA released the rover blueprint, engineers and scientists questioned the fundamentals of the proposed Asteroid Retrieval Mission, which would involve identifying, capturing, and dragging a 500-tonne asteroid into lunar orbit and then sending astronauts to sample it in the early 2020s.

Organized by an independent group of planetary scientists, the meeting included presentations from NASA scientists and engineers. Many attendees, however, were not persuaded by the agency's explanation of the project's technical details or relatively short timeline, which calls for launching the capture spacecraft by 2018. A fatal flaw, according to some, is the difficulty of identifying an asteroid of suitable size. Another problem, according to engineers, is that NASA will not know how to design the equipment needed to capture the asteroid until it has determined the mass, spin, shape, and other characteristics of the object—which it won't be able to do without first getting close to it. The agency needs to take a deep breath and slow down, or risk technical delays and cost overruns, said Gentry Lee, chief engineer for solar system exploration at NASA's Jet Propulsion Laboratory in Pasadena, California.

Republicans in the U.S. House of Representatives are also sending that message. The House science committee this week is expected to approve a NASA authorization bill that would stop the agency from pursuing asteroid capture without further study. The Obama administration "has not been able to adequately justify the rationale or budget for such a mission," which could cost more than \$2 billion, panel chair Lamar Smith (R-TX) argued in *The Hill* newspaper on 9 July. The Senate has yet to offer its views on the mission. **—YUDHIJIT BHATTACHARJEE**  
With reporting by Richard Kerr.





# Battle for the Americas

**The formation of the Isthmus of Panama allowed the fauna of two continents to mingle, transforming biogeography. A radical new hypothesis holds that the land bridge formed millions of years earlier than scientists thought**

Panama, 3 million years ago. A narrow strip of land bridging the Americas turns into a migratory highway. Heading north is an assemblage of creatures isolated for tens of millions of years: porcupines and armadillos; the elephant-sized ground sloth *Megatherium*; opossums and other marsupials; and bizarre life forms like the terror bird, a flightless carnivore that reached 3 meters in height and sprinted like a cheetah. Beating a southward path are more familiar animals, including horses, cougars, and saber-toothed cats.

Alfred Russel Wallace, the father of biogeography, recognized the faunal melting pot created when the tip of Central America collided with South America and forged the Isthmus of Panama, and in 1876 he postulated what is now called the Great American

Biotic Interchange. The story has a dark ending: South American fauna compete poorly at home and away, and many species go extinct.

More intriguing is how the battle for the Americas got started. Decades ago the fossil record showed, indisputably, that intercontinental migrations exploded between 3 million to 2.5 million years ago—evidence to most scientists that the isthmus had just formed by then. Other studies have bolstered the idea, although it grew more nuanced as evidence accumulated of “herald” species moving from one continent to the other millions of years earlier. That led some to suggest that fragmentary marshes allowed some species to cross the gap early,

followed by others on a sturdy land bridge that formed 4 million to 3 million years ago.

A radical new model envisions a much earlier bridge, however. After dating the uplift of land masses born of volcanism in Central America and analyzing the geochemistry and magnetic alignment of rocks in the region, Camilo Montes of the University of the Andes in Bogotá; Carlos Jaramillo of the Smithsonian Tropical Research Institute (STRI) in Balboa, Panama; and colleagues argue that the land bridge was largely formed as early as 15 million years ago, with the last deep-water connection between the oceans closing at most 5 million years later. By then, “most of the

modern landscape was already uplifted,” Jaramillo says, although shallow links between the oceans persisted until full closure 4.2 million to 3.5 million years ago. The new model had its coming-out party at a feisty symposium at the annual meeting of the Geological

Society of America last November. Their scenario poses a number of conundrums, not least of which is why it took so long several million years—for the Great American Biotic Interchange to gain momentum.

## Online

**sciencemag.org**

**S** Podcast interview with author Richard Stone ([http://scim.ag/pod\\_6143](http://scim.ag/pod_6143)).



**Intercontinental interloper.** The elephant-sized ground sloth *Megatherium* made it as far north as Texas.

“Why did that vast diversity of land mammals stay penned up in their respective continents if there was a bridge to cross?” asks Jeremy Jackson, a STRI ecologist and paleontologist and former director of the Center for Marine Biodiversity and Conservation at the Scripps Institution of Oceanography in San Diego, California.

The timing of isthmus formation matters, Jackson says. “The joining of the continents and severing of ocean contacts stands as one of the most important and best documented events in earth system evolution,” he says. The new model, if correct, would force scientists to reinterpret dozens of studies—a prospect that delights Jaramillo. “We’re unraveling the whole story,” he says.

The debate is heating up. In April, geologists Anthony Coates of STRI and Robert Stallard of the U.S. Geological Survey in Boulder published a report online in the *Bulletin of Marine Science (BMS)* defending the standard model of late closure and offering an analogy for the late stages of closure: the Indonesian archipelago, where a narrow but deep strait between the islands of Bali and Lombok—identified in the 19th century by Wallace—is mostly impassable to animals moving south from mainland Asia. And two more papers in press marshal data from disparate disciplines supporting late closure, while acknowledging that the prelude to closure could have been messier—and more interesting—than thought.

### Oceans of evidence

While the first clues to a late closure of the isthmus came from fossils, the oceans on either side of the isthmus yielded more compelling evidence. In 1982, Lloyd Keigwin of the Woods Hole Oceanographic Institution published a seminal paper in *Science* comparing oxygen isotopes in the shells of bottom-dwelling foraminifera recovered from deep-sea drilling in the western Caribbean and the eastern Pacific. Keigwin found that oxygen isotopes on either side of Panama began to diverge about 4 million years ago, suggesting that the Caribbean’s salinity increased around that time—“possibly

in response to shoaling of the Panama isthmus,” he wrote. Combined with changes in carbon-13 enrichment, the oxygen isotope data suggested that modern ocean circulation patterns in the Caribbean and eastern Pacific developed about 3 million years ago. “It’s a brilliant paper,” Coates says. He credits Keigwin for “launching the standard model of isthmus closure.”

Over the next quarter century, a string of paleoceanographic studies have supported the standard model. For example,



**Across the divide.** Jeremy Jackson (top) says paleocean data are proof positive that a deep-water barrier between North and South America lasted until at least 4 million years ago. Geological data suggest the barrier vanished much earlier, says Carlos Jaramillo.

researchers found that carbonate began to pile up in the Caribbean sea floor from about 4.6 million years ago, pointing to more sluggish deep-ocean circulation. Then, about 3.5 million years ago, new kinds of carbonate-loving foraminifera and corals appear in the Caribbean’s fossil record, and molecular genetics data also back rapid diversification around this time. “It’s a classic Darwinian evolutionary experiment,” Coates says.

Another consequence of isthmus closure in the Caribbean was the collapse of upwelling, in which deeper, colder waters rise to the surface, bringing nutrients to shallower waters. Proxies of this collapse include local extinctions—seafloor organisms “withered on the vine,” Coates says—and a shift in the Caribbean from fast-growing oysters to slower-growing species about 3.5 million years ago.

The bottom line, Jackson says, is that until 4 million years or so ago, deep-ocean indicators in the Caribbean looked like those in the Eastern Pacific. “The ocean core data are the killer of the new hypothesis,” he says. “How could the two oceans have been so well mixed geochemically if there were a land barrier in between?”

### Putting the s in isthmus

Jaramillo and Montes’s journey into tectonic heresy began with a \$1 million grant from the Panama Canal Authority that Jaramillo landed to conduct geological studies along banks of the Panama Canal slated for obliteration to widen the waterway. “He started a fantastic project,” Coates says. A companion effort in rescue paleontology has netted thousands of specimens, including 10 species new to science (see sidebar, p. 232).

As part of the projects, Montes and Jaramillo used radioisotope, geochemical, and paleomagnetic analyses to date rocks and discern relationships between rock formations. They wanted more accurate timelines for recovered fossils, and they hoped that these would lead to a better understanding of how the link between the continents was forged. “When we started our study, we didn’t have any problem with 3 million years” as the date of isthmus formation, Montes says.

The gold standard for dating rock formations is a technique that relies on the radioactive decay of uranium-235 and uranium-238. The mineral zircon is chock full of these isotopes and their lead and thorium decay products. By measuring the proportions of these isotopes in a zircon crystal, researchers can determine the time since the crystal and surrounding rock hardened and cooled, as well as the exhumation, or exposure, of rock from tectonic processes. The team recovered zircon crystals, formed during the cooling of magma, from



## Salvage Paleontology on the Seaway

**PARAISO, PANAMA**—On an embankment hewn from the jungle during the construction of the Panama Canal a century ago, Jason Bourque sits hunched over a 19-million-year-old turtle. Under a broiling mid-day sun, Bourque spends a half hour patiently brushing away grit from a fractured black carapace the size of a dinner plate before covering it in a plaster bandage for removal. By the time he's finished, a dozen or so container ships, oil tankers, and other vessels steam past along the 77-kilometer-long seaway.

Bourque, a preparator at the Florida Museum of Natural History, is taking advantage of a fossil windfall. As part of a \$5.5 billion expansion of the canal that will move 152 million cubic meters of earth, the canal authority has opened up sections of the seaway to salvage paleontology: collecting fossils in newly exposed rock faces. "It's a once-in-century opportunity," says Bruce MacFadden, curator of vertebrate paleontology at the museum, run by the University of Florida in Gainesville, and director of the Panama Canal Project.

The project's geological studies have provided grist for a radical hypothesis that the Isthmus of Panama formed a land bridge several million years earlier than thought (see main story, p. 230). Its fossil finds are also revelatory: a menagerie of miniature horses and camels, gopherlike rodents, peccaries, and caimans, as well as weird creatures such as the giant bear-dog and the hippolike anthracothere. The assemblage recovered so far from the prehistoric rainforest suggests that the volcanic arc from which the isthmus formed was a "species

pump," MacFadden says, spawning new life forms that spread through North America.

The canal's construction in the early 20th century revealed a fossil trove, which scientists secured piecemeal over the years. The expansion is opening up whole new exposures. That's especially exciting because throughout the isthmus, lush forest has made it difficult to identify rich fossil sites, says Aaron Wood, a postdoc at the Florida Museum of Natural History. With the canal expansion slated for completion as early as next year, the window of opportunity for paleontologists is closing fast.



**Race against time.** Ongoing expansion of the Panama Canal has yielded a treasure trove of fossils. Jason Bourque (background) excavates a 19-million-year-old turtle.

Racing to gather up as many fossils as they can, MacFadden's crew over 4 years has hauled in more than 3000 specimens, among them 10 new species. A top fossil hunter on the team is Aldo Rincon, a Ph.D. student at the University of Florida, lead author on a report published in the *Journal of Vertebrate Paleontology* last March describing a new species of anthracothere. Rincon's favorite specimen, he says, is the fragile jawbone and teeth of a bat that he unearthed from the Cucaracha Formation, in the shadow of the Centennial Bridge, last year. "I rolled down the hill, I was so excited," he says.

The bat, descended from a South American species, is a rare example of a nonswimmer to have traversed the

deep-water gap that separated Colombia and Panama about 19 million years ago. (Crocodiles, turtles, and snakes crossed much earlier.) A view of life in this ancient cradle of biodiversity is coming into sharper focus. The Panama Canal, says Andrés Cárdenas, a postdoc at the Smithsonian Tropical Research Institute in Balboa, Panama, "has everything you need to tell the story."

—R. S.

the Azuero Peninsula west of the Panama Canal and from the San Blas mountains, a range to the east that extends into Colombia. The zircons revealed that a volcanic arc began forming about 70 million years ago in the gap between the two continents, with major exhumation events lifting up blocks of the arc about 47 million, 25 million, and 11 million years ago. By measuring the direction of the ancient magnetic fields frozen into the volcanic rocks, the researchers were able to reconstruct how tectonic forces had shifted and deformed the arc.

Piecing together the evidence, the researchers, with geologist David Farris of Florida State University in Tallahassee, proposed that the collision between South America's northern Andean blocks and the Central American volcanic arc began about 25 million years ago. Panama's 'S' shape, Montes points out, betrays the tremendous strain that the arc underwent. Around that time, the arc melded with the rest of Central America to

form a peninsula, allowing North American fauna to colonize it, as fossils found among the remnants of the arc testify. By then, possibly the final barrier to intercontinental movement was a deep-water gap between the peninsula and the coast of modern-day Colombia as it subducted under the arc.

"It's terrific work," Jackson says about the scenario, which Montes and Jaramillo published in the *Geological Society of America Bulletin* in January 2012 and in the *Journal of Geophysical Research: Solid Earth* that April. But he and others reject the headline-grabbing conclusion that Montes and Jaramillo arrived at: that by 10 million years ago, the geological shape-shifting they meticulously documented had squeezed away the last deep-sea connection between the oceans.

### Wallace would be proud

Coates himself accepts Montes and Jaramillo's account of the first stages of isthmus closure. "Our geological reconstructions

are stunningly similar," says Coates, referring to a pair of studies in the *Geological Society of America Bulletin* in 2003 and 2004. However, he argues, "There's no way you can tell from their data whether parts of the arc were still submerged" in the final stages of filling in. And the spatial resolution of their data is not fine enough, he says, to rule out deep-water gaps in the arc.

Coates and Stallard think that Indonesia may offer a modern-day analog of pre-isthmus Panama. Over millennia, Asian species have readily hopped or drifted between islands in the Sunda region, west of Bali. There, the migration mostly stopped at Bali. Lombok, the next major island to the east, is only 35 kilometers away, but the strait is several hundred meters deep and has an especially swift current, thwarting purposeful or accidental migration and forming a species barrier—Wallace's Line. Several hundred kilometers to the east is a similar species barrier: Lydekker's Line, the edge of the world for

marsupials and other creatures from the Sahul region, encompassing Australia and New Guinea. In between the Wallace and Lydekker lines is a collection of islands stretching from Borneo to New Guinea that biogeographers refer to as Wallacea for its unique faunal assemblage.

Coates and Stallard propose that deep-water gaps in the present-day Panama Canal Basin and between the volcanic arc and South America were equivalent to the Wallace and Lydekker lines. They argue that even as the isthmus was filling in, the path of migration was interrupted for 10 million years or more.

“Essentially, South America is a few million years ahead of Australia,” in that Indonesia’s volcanic arc and Australia should eventually form a contiguous land mass, says Coates, whose report with Stallard appeared online in *BMS* on 4 April. “It’s a very elegant analog,” says STRI paleobiologist Aaron O’Dea.

O’Dea and others who adhere to the late-formation thesis have also taken up the gantlet. In a paper in press at *BMS*, Jackson and O’Dea comprehensively review studies on the paleocean environment, dispersal of terrestrial and marine creatures, and molecular phylogeny of sea life, all pointing, they say, to closure of the isthmus about 3 million years ago.

One especially compelling find, presented at the geology meeting last November, is shark teeth and fish fossils such as otoliths recovered from 6-million-year-old sediments in the Chagres Formation in the Panama Canal Basin. The otoliths, or ear bones, are from marlins and bluefish: species that generally don’t ply shallow waters. STRI’s Carlos De Gracia and colleagues argue that the fossil assemblage points to waters between 100 and 700 meters deep. Coates calls the Chagres fossils a “smoking gun” for the existence of a deep-sea gap millions of years later than the closure envisioned by Jaramillo and Montes.

Yet, other pieces of the puzzle don’t fit the late closure thesis. Most troubling are the so-called herald animals. Biogeographers have long recognized that the Great American Biotic Interchange was never a stampede, as if a drawbridge were lowered over a moat. About 9 million years ago, well before the surge of migrations, two sloth species descended from South American ancestors appear in Flor-

ida and Texas. One gave rise to *Megalonyx*, a 1-ton sloth named by Thomas Jefferson, a fossil buff, who mistook a claw of the beast for that of a gigantic meat-eater. (Sloths are vegetarians.) The first emigrant from North America appears to have been the raccoon-like carnivore *Cyonasua*, fossils of which show up in Argentina 7.3 million years ago. Terror birds stormed Texas 5 million years ago, with giant armadillo-like pampatheriids hot on their heels.

Scientists have generally chalked up these early migrations to island-hopping or rafting. Modern sloths and raccoons are good swim-

by the Maya in Central America, arose in the Amazon; they reached Central America only after the isthmus formed. In 2011, STRI ecologist David Roubik, a specialist on bees, discovered two new, closely related stingless bee species: one in Colombia and one on Coiba Island, off the Pacific coast of Panama. The forest-dwelling bees are not accomplished fliers. “They can’t establish a new nest across more than a short stretch of open water,” Roubik says. It’s possible that rafts carried nests to Coiba, he says. But to Roubik, a simpler explanation is that a land bridge well before 3 million years ago paved the way for the bees. “My opinion is that there was something akin to a little isthmus around 6 to 12 million years ago,” he says, before portions of the volcanic arc were submerged again, only to reemerge about 3 million years ago.

That concept could be gaining traction. Most scientists accept that present-day Panama rose from the sea over millions of years as the volcanic arc and South America collided. In a paper in press at *Biological Reviews*, O’Dea; STRI ecologist Egbert Leigh; and Geerat Vermeij of the University of California, Davis, propose that about 10 million years ago, the shoaling resulted in a land bridge that was “briefly near-complete.” That would explain how key herald species, such as the sloths up north and the *Cyonasua* down south, pioneered new terrain long before the Great American Biota Interchange. By 7 million years ago, they propose, deep-water gaps in the emerging isthmus had disrupted the land bridge. “Multiple stages of isthmus formation are not inconsistent with the biological evidence,” Faris says.

That explanation may satisfy some researchers, but at STRI, where many of the debate’s antagonists are either based or spend time for research, the sparring continues. “I’ll see Carlos in the hall, and flash him three fingers. He flashes back

15,” says Coates, who calls Jaramillo “a very fine scientist” and says that their interactions “are always polite. This is the way science is supposed to be.”

Good manners can’t disguise the rift, however. “Both sides,” Montes says, “have entrenched positions.” For opponents in the debate, that means, for now, no closure.

—RICHARD STONE



**Elegant analog?** According to the standard model of isthmus formation (top), final closure occurred well after 6 million years ago. Deep-water gaps between the Panama Canal Basin and South America may have been equivalent to Wallace’s Line and Lydekker’s Line in present-day Indonesia.

mers, Jackson notes, while globally, the annals of biogeography are replete with accounts of accidental émigrés borne to distant lands on clumps of vegetation.

But some scientists find that explanation hard to swallow. And then there is the case of the stingless bees.

About 22 million years ago, ancestors of these honey bees, which were cultivated





## BIODIVERSITY

# The Amazon in 4D

An interdisciplinary team is linking data from field research in the Amazon into a comprehensive digital collection, aiming to map evolution in space and time

**NEW YORK CITY**—In a chilly specimen storage room on the sixth floor of the American Museum of Natural History (AMNH), Joel Cracraft opens a cabinet and slides out two trays filled with delicate, palm-sized songbirds, inhabitants of the Amazon rainforest. One tray holds a jumble of red-headed manakins—eyeless, boneless, and stuffed with cotton. The other holds their close relative, golden-headed manakins. The two species seem to differ only in the color of the males' crown feathers. But they are never found in the same place. Red-headed manakins live south of the Amazon River; golden-headed manakins live north of it.

How that pattern arose is a mystery, says Cracraft, the museum's curator of ornithology. Scientists don't know what drove the birds to evolve different colored crowns. They don't know when the two species began to diverge, or the precise age of the river that separates them—much less, when it became wide enough to deter birds from flying across. They don't know just how these birds, and the plants and animals living alongside them, may have adapted to the Amazonian climate, or exactly how that climate may have changed over time. In short, scientists don't know how the Amazon rainforest and its stunning biodiversity came to be.

"It's one of the great questions of all time," says Thomas Lovejoy, biodiversity chair of the Heinz Center in Washington, D.C., and an ecologist who has worked in the

Amazon for more than 45 years. Now, dozens of scientists from Brazil and the United States have teamed up across disciplines to try to find an answer. Called Dimensions of Amazonian Biodiversity, their project aims to create a "four-dimensional evolutionary atlas" of the Amazon. By combining data from a variety of fields such as geology, evolutionary biology, DNA analysis, and climate modeling, the team plans to track the region's biodiversity and environment through space and time to understand how they interacted and evolved.

### A volatile place

For many years, biologists took the Amazon's abundance of plant and animal species to mean that its rainforest was an old, stable ecosystem—a kind of ecological "museum" that has "had more time to accumulate more species," says botanist Lúcia Lohmann of the University of São Paulo in Brazil, who is, along with Cracraft, a principal investigator for Dimensions. But geological evidence points to a much more volatile history for the region, according to Lohmann and her collaborators. From at least 17 million to 11 million years ago, in the middle of an epoch known as the Miocene, the Amazon Basin was covered in an extensive system of wetlands that scientists refer to as Lake Pebas. At some point—exactly when is still disputed—the lake's water began flowing east, eventually breaking through into the

Atlantic and forming the beginnings of what is now the Amazon River.

As the wetlands drained and gave way to forest, the biodiversity that we see in today's Amazon began to take shape, Lohmann says. New evidence garnered from DNA sequencing and other evolutionary data point to an image of the region not as an environmental museum but as what Lohmann calls a biological "cradle" where large numbers of species have diversified fairly recently. As a result, says Alan Graham, a paleobotanist at the Missouri Botanical Garden in St. Louis, scientists now "need a whole new suite of explanatory factors" to account for the region's biodiversity. Dimensions, launched in September 2012 with a promise of \$2 million over 5 years from the U.S. government and an equivalent offer from the state of São Paulo in Brazil, aims to find them.

To untangle the Amazon's complicated history, scientists from many disciplines will need to work together, says Carina Hoorn, a geologist at the University of Amsterdam. Hoorn is involved in CLIM-AMAZON, a European-Brazilian collaboration begun in 2011 that is gleaning data on the region's climate and environmental history from sediments throughout the Amazon River Basin. It's not enough to focus on a single critical field, such as geology or evolutionary biology, she says. "You really have to see it in an integrated, interdisciplinary way."

Cracraft's manakins provide an example of how such a strategy might work. If you were studying Amazonian birds, he says, you might plot the location where each of AMNH's manakins was collected and see a sharp north-south separation between the golden-headed and red-headed species. But only if you overlaid the data on a map of the

CREDIT: KKE CALVO

**Uncharted.** The origins of Amazonia's stunning biodiversity aren't well understood.

region's waterways would it be clear that the barrier separating them is the Amazon River, the formation of which may have isolated two groups that evolved into separate species. Knowing precisely how long ago the two manakins split off from their common ancestor might give a good clue as to when the river became the major waterway that it is today. "This is one of the purposes of the grant, to try to tease apart that layered history of Amazonia and [its] biota in a way that can explain it all," Cracraft says. "Or at least most of it."

The team plans to go through a similar mapping process with all the region's birds, primates, and butterflies, as well as two families of plants. "To start with, we just want to understand general patterns of diversity and see how those relate to environmental features," Lohmann explains. A project like this is "long overdue," Lovejoy says.

### Finding hidden patterns

Although museum specimens are at the heart of the Dimensions project, much of the information that they contain is not easily accessible because it's not yet online. Improving digital archives is one of the project's main objectives. The team plans to create a comprehensive, freely available database, including details on when, where, and how specimens were acquired, which anyone will be able to use to analyze the region's biodiversity. "The key will be to make this information comparable so that we can combine stuff and analyze bigger data sets," Cracraft says. If this succeeds, "suddenly it will be possible to look at patterns and questions that have been hard to actually get at before," predicts Lovejoy, who is not involved in the Dimensions project.

In this first year of their grant, Dimensions researchers have been focusing on adding precise geographical coordinates to records of museum and herbarium specimens. Location is the common factor that runs through everything, from plants to birds to primates, and even "the paleo and geological data," says Barbara Thiers, director of the New York Botanical Garden's herbarium, which is contributing to the Dimensions project. "Collectors didn't routinely record [latitude and longitude] information on the specimens" until handheld GPS devices came along, she says. So the Dimensions team is reconstructing coordinates as best they can, trying

to match up places mentioned in collectors' original notes with the localities included in geographical directories called gazetteers, or by pulling out paper maps and retracing a collector's route.

Some patterns line up, like the distribution of plants and their pollinators, while others diverge in curious ways. Amazonian birds, for example, tend not to fly across rivers, meaning that scientists often find strikingly different species on either side of a waterway. Many plant species, however, "seem to cross rivers without any problems," Lohmann says. So while the formation of rivers might be a driving force behind bird evolution in the basin, researchers need



**Mapping manakins.** Dots represent related manakin species, including the golden-headed (red dots) and red-headed (green dots) species.

to come up with other ideas about how populations of plants might have become isolated and evolved into separate species.

The atlas coordinates should reveal not just how species are distributed but also where collectors in the past focused their efforts. Most fieldwork in the Amazon has been done along major rivers or near cities. But collecting in just a few areas, no matter how extensive, does not guarantee a representative sample of diversity—especially because Amazonian species tend to be very particular about where they live, even when barriers separating one area from another aren't yet clear to scientists. "People have basically been looking at nice, cute things at eye-height ... things that were easy to get at," says Alexandre Antonelli, an evolutionary biologist at the University of Gothenburg in Sweden.

This can skew conclusions and bias ongoing research, Lohmann agrees. "We often go back to the most collected areas as being the centers of diversity just because our data sets don't allow a very fair comparison throughout the area," she says. If the Dimensions

atlas can reveal which places and species are already well studied, it could help scientists target future fieldwork on undercollected areas.

Coordinating such a sprawling, interdisciplinary effort is not easy, and often requires getting "out of your comfort zone," Lohmann admits. As the Dimensions project progresses, it's "essential" that research leaders "be very closely attuned to other specialists, and especially those that have alternate viewpoints," agrees Graham, who is not involved in the

project. For example, the Dimensions and CLIM-AMAZON researchers disagree on some fundamental questions about the region, particularly the age of the Amazon River. Hoorn says that she welcomes the discussions. "The better people work together, the better the results will be," she says.

Although Dimensions focuses on Amazonia's history, it may help scientists and policymakers protect the increasingly at-risk ecosystem. The atlas, for example, may pinpoint areas where new species are likely

to evolve. Preserving those hotspots of biodiversity might give Amazonia's inhabitants a leg up in the race to adapt to Earth's changing climate, says George Gilchrist, the National Science Foundation (NSF) program director in charge of the Dimensions grant. "If we can't keep the full diversity of species there, can we keep the evolutionary potential that generated [it]?" he wonders.

Ultimately, scientists and NSF officials hope that Dimensions will serve as a model for interdisciplinary studies about the evolutionary history of all kinds of ecosystems. Cracraft, for one, seems to have already taken the Dimensions' strategy to heart. Outside the room where the AMNH manakins are stored, he calls to a group of museum employees about to go bird watching in Central Park, "Tell me what you see and where!"

—LIZZIE WADE



## LETTERS

edited by Jennifer Sills

## Turkey Must End Violent Response to Protests

THE TURKISH MEDICAL ASSOCIATION (TTB) REPORTED THAT 8121 PEOPLE WERE OFFICIALLY admitted to hospitals resulting from police violence between 31 May and 26 June (1). This number includes 5 deaths, 61 life-threatening injuries, 104 head traumas, and 11 ophthalmic injuries, one of which led to loss of an eye due to shots of tear gas canisters from short range

(1). Turkish police have used excessive amounts of tear gas (lachrymatory agents) in public (2) and confined spaces such as hospitals or infirmaries, according to international media reports and the TTB (1–4). Such use of asphyxiating gases in confined spaces is not only extremely dangerous for public health (5–8), but also strictly limited by international agreements, such as the Geneva Protocol (9), to which Turkey is a signatory. Security forces have used 130,000 tear-gas cartridges in 20 days, and Turkey is planning to buy 100,000 new cartridges (10). Doctors and nurses treating patients affected by tear gas and other police brutality, as well as the Istanbul Medical Chamber General Secretary, have been apprehended by police (11, 12), a clear violation of customary international and human rights

law (13). More than 4000 academics around the world have already signed a petition to protest the police brutality (14). We call upon the Turkish government to obey international law in the treatment of protesters and those providing medical treatment to them, and to start a good-faith dialogue with the protest movement.

EMRAH ALTINDIS,<sup>1\*</sup> M. ALI ALPAR,<sup>2</sup> EMRE AKSAY,<sup>3</sup> JONATHAN BECKWITH,<sup>4</sup> CHRISTIAN BÖKEL,<sup>4</sup> ROBERT F. CURL,<sup>5</sup> ROBERT B. DARNELL,<sup>6</sup> STEPHEN J. ELLEDGE,<sup>7</sup> BURAK ERMAN,<sup>8</sup> JENS FRAHM,<sup>9</sup> STEPHEN P. GOFF,<sup>10</sup> PAUL GREENGARD,<sup>6</sup> ROALD HOFFMANN,<sup>11</sup> BAYAZIT ILHAN,<sup>12</sup> JAN KASLIN,<sup>13</sup> STEVEN M. LIPKIN,<sup>3</sup> CORNELIA POULOPOULOU,<sup>14</sup> EREZ RAZ,<sup>15</sup> MARK A. RUBIN,<sup>3</sup> MEHMET SALTURK,<sup>16</sup> RICHARD R. SCHROCK,<sup>17</sup> ALAIN TRAUTMANN,<sup>18</sup> DERYA UNUTMAZ,<sup>19</sup> HAREL WEINSTEIN,<sup>3</sup> CAGHAN KIZIL<sup>14\*</sup>

<sup>1</sup>Harvard Medical School, Boston, MA 02115, USA. <sup>2</sup>The Science Academy (Bilim Akademisi), Istanbul, Turkey. <sup>3</sup>Weill Cornell Medical College of Cornell University, New York, NY 10065, USA. <sup>4</sup>Center for Regenerative Therapies Dresden, Technische Universität, 01307, Dresden, Germany. <sup>5</sup>Rice University, Houston, TX 77251, USA. <sup>6</sup>The Rockefeller University and The New York Genome Center, New York, NY 10065, USA. <sup>7</sup>Harvard Medical School, Brigham and Women's Hospital, Boston, MA 02115, USA. <sup>8</sup>Koc University, Istanbul, Turkey. <sup>9</sup>Max Planck Institute for Biophysical Chemistry, 37077, Göttingen, Germany. <sup>10</sup>Columbia University, NY 10027, USA. <sup>11</sup>Cornell University, Department of Chemistry and Chemical Biology, Ithaca, NY, 14853, USA. <sup>12</sup>Turkish Medical Association (TTB), Ankara, Turkey. <sup>13</sup>Monash University, Victoria, 3800, Australia. <sup>14</sup>University of Athens, Athens, 10679, Greece. <sup>15</sup>University of Münster, 48149, Münster, Germany. <sup>16</sup>University of Cologne, Cologne, 50923, Germany. <sup>17</sup>Massachusetts Institute of Technology, Cambridge, MA 02139, USA. <sup>18</sup>Centre National de la Recherche Scientifique (CNRS), 75794, Paris, France. <sup>19</sup>New York University, New York, NY 10012, USA.

\*Corresponding authors. E-mail: emrah\_altindis@hms.harvard.edu (E.A.); caghan.kizil@crt-dresden.de (C.K.)

## References

1. TTB Report ([www.ttb.org.tr/index.php/Haberler/venler-3842.html](http://www.ttb.org.tr/index.php/Haberler/venler-3842.html)).
2. Gas Burns Taksim Gezi Parkı 12.06.2013 ([www.youtube.com/watch?v=66e-jRqMEZg](http://www.youtube.com/watch?v=66e-jRqMEZg)).
3. A. O. Aktan, *Br. Med. J.* **346**, f3801 (2013).
4. Police Throwing Tear Gas into German Hospital Istanbul 16.06.13 2:57am #occupygezi ([www.youtube.com/watch?v=AL06wWNqTY4](http://www.youtube.com/watch?v=AL06wWNqTY4)).

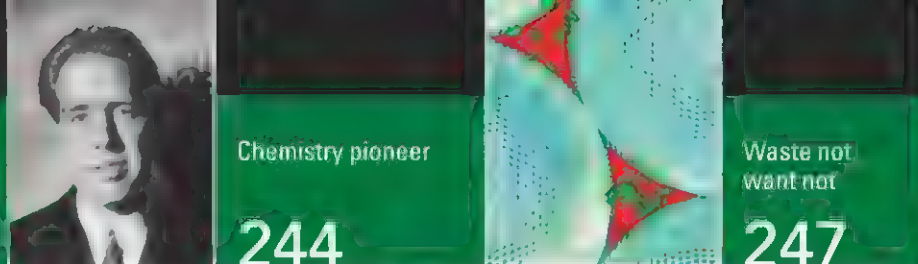
5. H. Hu, D. Christiani, *Lancet* **339**, 1535 (1992).
6. B. F. Bessac, S. E. Jordt, *Proc. Am. Thorac. Soc.* **7**, 269 (2010).
7. B. C. Howard, "The surprising history and science of tear gas," *National Geographic Daily News* (12 June 2013); <http://news.nationalgeographic.com/news/2013/06/130612-tear-gas-history-science-turkey-protests/>.
8. H. G. Atkinson, "Under the gun: Ongoing assaults on Bahrain's health system," *Physicians for Human Rights* (May, 2012); <http://physiciansforhumanrights.org/library/reports/under-the-gun-ongoing-assaults-on-bahrain-health-system.html>.
9. United Nations Geneva Protocol (1925); [www.icrc.org/eng/war-and-law/treaties-customary-law/geneva-conventions/index.jsp](http://www.icrc.org/eng/war-and-law/treaties-customary-law/geneva-conventions/index.jsp).
10. "Turkish police to buy 100,000 gas bomb cartridges," *Hürriyet Daily News* (19 June 2013); [www.hurriyetdailynews.com/turkish-police-to-buy-100000-gas-bomb-cartridges-.aspx?PageID=238&NID=49075&NewsCatID=341](http://www.hurriyetdailynews.com/turkish-police-to-buy-100000-gas-bomb-cartridges-.aspx?PageID=238&NID=49075&NewsCatID=341).
11. *Lancet* **381**, 2067 (2013).
12. E. Güne, "Police search houses of Gezi protests' starter group members," *Hürriyet Daily News* (9 July 2013); [www.hurriyetdailynews.com/police-search-houses-of-gezi-protests-starter-group-members.aspx?pageID=238&NID=50349&NewsCatID=339](http://www.hurriyetdailynews.com/police-search-houses-of-gezi-protests-starter-group-members.aspx?pageID=238&NID=50349&NewsCatID=339).
13. Convention (IV) Relative to the Protection of Civilian Persons in Time of War (Geneva, 1949); [www.icrc.org/applic/ihl/ihl.nsf/Treaty.xsp?documentId=AE2D398352C5B028C12563C0002D6B5C&action=openDocument](http://www.icrc.org/applic/ihl/ihl.nsf/Treaty.xsp?documentId=AE2D398352C5B028C12563C0002D6B5C&action=openDocument).
14. Academics for Gezi (<http://academicsforgezi.com/our-call/>).

## Optimizing Peer Review of Software Code

IN THEIR POLICY FORUM "TROUBLING TRENDS in scientific software use" (17 May, p. 814), L. N. Joppa *et al.* make a case for increased education of scientists in computer programming skills and requirements for peer review of scientific software code. We agree in principle but believe that some of the specific recommendations by Joppa *et al.* are unfeasible.

In particular, we believe that requiring prepublication peer review of computer source code by journal reviewers would place impossible strain on an already overburdened system. Many scientific journals currently have great difficulty finding sufficient numbers of qualified reviewers to evaluate submissions in a timely and construc-

CREDIT: OSMAN ORSAI/REUTERS



tive fashion. Requiring that reviewers be able to evaluate not only the scientific merit of a manuscript but also parse, understand, and evaluate what can be thousands or tens of thousands of lines of source code written in one or more of a variety of programming languages is impractical.

A more tenable solution for computer codes is postpublication peer review, where the release of source code is a requirement of publication (1) and interested and appropriately skilled members of the broader scientific community may download and evaluate the code at will. This would bring review of computer code in line with existing policies pertaining to data and materials availability already in place at most journals.

Increased dependence on postpublication review will require strengthening procedures and facilities for reporting corrections and retractions of published research articles, a course of action long advocated by those concerned over increasing rates of retraction, especially in the biomedical sciences (2).

PIOTR SLIZ\* AND ANDREW MORIN

BCMP, Harvard Medical School, Boston, MA 02115, USA.

\*Corresponding author. E-mail: piotr\_sliz@hms.harvard.edu

#### References

1. A. Morin *et al.*, *Science* **336**, 159 (2012).
2. Retraction Watch (<http://retractionwatch.wordpress.com/>)

## Response

SLIZ AND MORAN QUESTION THE FEASIBILITY of our recommendation to both peer-review computer code and release it, and they proffer an alternative: postpublication community review and stronger procedures and facilities for dealing with corrections and retractions of published results. These are not incompatible. Encouraging the broader scientific community to inspect computer code postpublication would help in identifying scientific errors currently unnoticed in the scientific literature. Improving the process of corrections and retractions would have positive benefits far beyond this issue. However, neither negates the need for prepublication review of code.

The scientific publishing process relies on prepublication peer review as a filter for robust results. This is so because, regard-

less of the strength of processes for dealing with corrections and retractions, putting "the genie back in the bottle" is always going to be a difficult task after a result has been reported in the literature. At a minimum, code needs to be available to reviewers should they choose to scrutinize it. Moreover, prepublication review of code need not necessarily rely on the current review system. Just as English-language editing services have emerged to ensure a minimum standard of accessibility of articles in many major journals, so might software-reviewing services provide a stamp of approval that code actually implements the algorithm reported in a paper. Indeed, in the commercial sector, software escrow providers routinely provide full verification services to companies purchasing (or investing in) business-critical software [e.g., (1)], and the approaches used by such companies might provide pointers for a new model for academic software verification services.

Of course, verification of software is just the first essential step in the process, with

by far the more challenging issue being software validation. Addressing this issue, together with the equally pressing issue of uncertainty quantification in complex [computational] models, has been the focus of intensive research efforts in other scientific disciplines (2). These efforts might provide a good starting point for equivalent efforts in the life sciences.

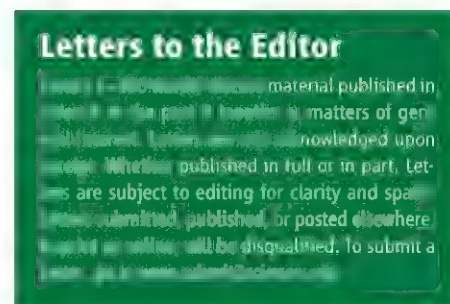
LUCAS N. JOPPA,<sup>1\*</sup> DAVID GAVAGHAN,<sup>2</sup> RICHARD HARPER,<sup>2</sup> KENJI TAKEDA,<sup>2</sup> STEPHEN EMMOTT<sup>1</sup>

<sup>1</sup>Microsoft Research, Cambridge, CB3 0FB, UK. <sup>2</sup>Department of Computer Science, University of Oxford, Oxford, OX1 3QD, UK.

\*Corresponding author. E-mail: lujoppa@microsoft.com

#### Reference

1. Iron Mountain, "How verification services fortify your software escrow solution" (Iron Mountain, 2011)
2. National Academies Press, *Assessing the Reliability of Complex Models: Mathematical and Statistical Foundations of Verification, Validation, and Uncertainty Quantification* (National Academies Press, Washington, DC, 2012).



## CORRECTIONS AND CLARIFICATIONS

**News & Analysis:** "NIH to phase out most chimp research" by J. Kaiser (5 July, p. 17). The article failed to note that Gabon has not banned biomedical research on chimpanzees. The HTML and PDF versions online have been corrected.

**Reports:** "A population of fast radio bursts at cosmological distances," by D. Thornton *et al.* (5 July, p. 53). A mistake in the script used to produce Table 1 caused the energy released ( $E$ ) values in the last row of the table to be off by  $10^6$ . The correct values are  $\sim 10^{33}$ ,  $\sim 10^{31}$ ,  $\sim 10^{32}$ , and  $\sim 10^{31}$ . The conclusions of the paper are unaffected. The HTML and PDF versions online have been corrected.

## TECHNICAL COMMENT ABSTRACTS

### Comment on "Can We Name Earth's Species Before They Go Extinct?"

Camilo Mora, Audrey Rollo, Derek P. Tittensor

Costello *et al.* (Review, 25 January 2013, p. 413) challenged the common view that many species are disappearing before being described. We suggest that their conclusion is overly optimistic because of a limited selection and interpretation of available evidence that tends to overestimate rates of species description and underestimate the number of species on Earth and their current extinction rate.

Full text at <http://dx.doi.org/10.1126/science.1237254>

### Response to Comment on "Can We Name Earth's Species Before They Go Extinct?"

Mark J. Costello, Robert M. May, Nigel E. Stork

Mora *et al.* disputed that most species will be discovered before they go extinct, but not our main recommendations to accelerate species' discoveries. We show that our conclusions would be unaltered by discoveries of more microscopic species and reinforce our estimates of species description and extinction rates, that taxonomic effort has never been greater, and that there are 2 million to 8 million species on Earth.

Full text at <http://dx.doi.org/10.1126/science.1237381>



## ENVIRONMENT

# A Saga of Industrial Pollution

Jouni Tuomisto

**T**oms River offers a fascinating, carefully written description of chemical industry malpractices during the past five decades and the subsequent actions of citizens, authorities, companies, employees, and lawyers. It helps us understand why chemical industry tends to produce health hazards, why that is happening in new areas (such as China) even today, and how these problems could be reduced.

In 1952, the Swiss company Ciba (later Ciba-Geigy and now Novartis) built a chemical factory for producing dyes and, later, other chemicals in sleepy Toms River, New Jersey. The town's enthusiastic welcome gradually turned into complaints and eventually outrage. Through illegal dumping of Union Carbide waste, Toms River came to host another hazardous site. The careless disposal of solid and liquid hazardous wastes at the two sites polluted the nearby river, soil, groundwater, and ocean and caused suspicion of a childhood cancer cluster. Both sites were included in the Superfund program, which identifies and attempts to clean up contaminated sites in the United States.

Describing in depth and with credible data what happened, the book also recounts who made the decisions and the reasons for and the outcomes of the actions. Dan Fagin (who teaches environmental journalism at New York University) lays out the practices through the different decades. He shows that many actions that readers may think of as outrageously stupid were at the time widely accepted standard practice and were based on rational although short-sighted thinking.

Fagin weaves his narrative from stories of individuals passionate about something—whether protecting children against cancer, finding methods to produce bright colors using

coal tar chemistry, or assembling elaborate patient studies to understand the development of cancer and other diseases. He presents dozens of key researchers from Paracelsus (in the 16th century) to Richard Doll (in the 20th) along with their contributions to the understanding and practices of what we now call environmental health sciences.

A similar case of drinking water contamination in Woburn, Massachusetts (1), became the basis of a 1998 feature film. The complexities Fagin presents suggest that the saga of Toms River could not be captured in a two-hour movie. However, it has the makings of a fine television series: numerous interesting characters, the spectacle of a growing industrial town with a complex social ecosystem, and a story spanning more than five decades (with flashbacks into even earlier history of chemistry and science). Indeed, *Toms River* synthesizes Fagin's extensive work. He interviewed 140 people and mentions more than twice that number.

Despite the huge amounts of detail and sometimes-difficult scientific concepts, the lucid text remains fairly easy to read. Fagin impressively discloses the web of contacts that stimulated the flow of ideas among

people who then applied their knowledge to new areas and challenges. Absorbing reading, the book also serves up excellent educational environmental case studies and stories. Although not a textbook (it contains no equations or chemical formulae), it provides

informative discussions of the limitations and opportunities of various methods. These should help readers understand the capabilities of environmental health.

Much of the regretful looking back in the book should not have been hindsight. Fagin convincingly demonstrates that in very many cases

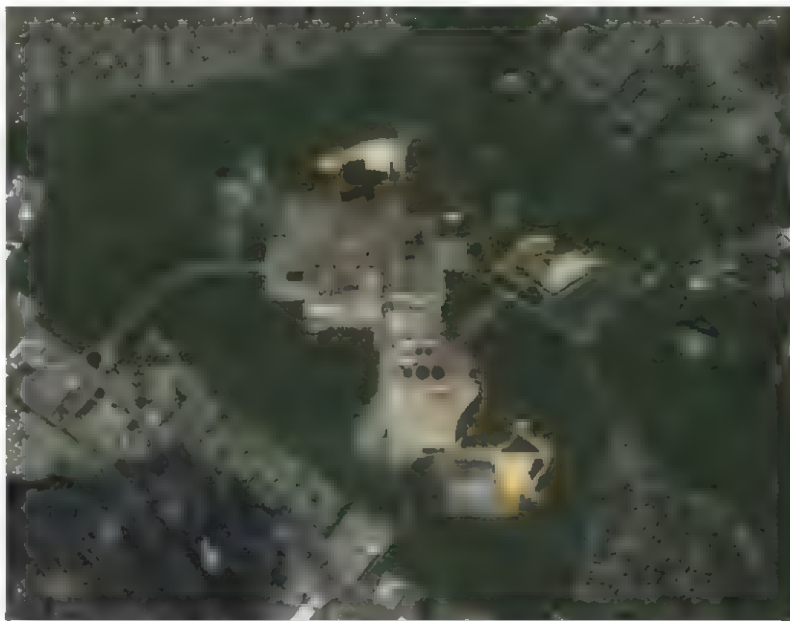
enough was known for people to have made better decisions. So why did the chemical companies go on dumping and the authorities keep ignoring future trouble? There seem to be two main reasons. Either the existing information did not reach the decision-makers, or the decision-makers' outlook prevented them from recognizing the hazards and opportunities. In other words, the business-as-usual approach seems to be such a strong default that even clear alternatives tend to go unnoticed. As the book shows, the approach was shared not only by the chemical industry and authorities but also by most researchers and citizens. Leaps of progress came only after a determined few succeeded in shaking the status quo.

This implies that we should systematically promote an open flow of environmental information, especially among people holding different views and different interpretations. In

Toms River, fear that open information would cause public outrage was repeatedly expressed. But the book shows that when at some point the information leaked out anyway, the largest outrage usually stemmed from the secrecy, not the bad news per se.

In the book's final part, Fagin describes how lawyer Jan Schlichtmann (who also was deeply involved in the Woburn case) pushed strongly for such a shared understanding about childhood cancer cases in Toms River. Not only did he succeed, his open approach was able to create trust and a feeling of understanding among the opposing

**Toms River**  
A Story of Science  
and Salvation  
by Dan Fagin  
Bantam, New York, 2013  
559 pp. \$28, C\$34  
ISBN 9780553806533



**Troubled environment.** The site of the Ciba chemical plant at Toms River, New Jersey.

The reviewer is at the Department of Environmental Health, National Institute for Health and Welfare (THL), Post Office Box 95, FI-70701 Kuopio, Finland. E-mail: jouni.tuomisto@thl.fi

CREDIT: GOOGLE EARTH

groups. That promising outcome supports claims that openness improves outcomes (2). Therefore, we seem to need more open assessments as early as possible. Once the damage is done, all we can do is estimate its scope and seek the culprits—as events played out in New Jersey.

A balanced book, *Toms River* does not push a political agenda, unlike Rachel Carson's *Silent Spring* (3). But both books offer many valuable lessons to those around the world who wish to improve environmental and occupational health.

#### References

1. J. Harr, *A Civil Action* (Vintage, New York, 1996).
2. M. V. Pohjola, J. T. Tuomisto, *Environ. Health* **10**, 58 (2011).
3. R. Carson, *Silent Spring* (Houghton Mifflin, Boston, 1962).

10.1126/science.1240379

## HEALTH ECONOMICS

# Can We Afford More Health Care?

Amitabh Chandra

William Baumol is among the most thoughtful economists of our time—over his prolific career he has covered everything from entrepreneurship to institutions to operations research. In the 1960s, he along with Princeton colleague William Bowen put together a clever thesis to explain the increasing share of incomes that go to relatively unproductive sectors. That thesis is now referred to as “Baumol’s cost disease,” and in *The Cost Disease*, Baumol applies his theory to the debate on health care spending.

Assume (as we economists are superb at doing) that there are two sectors in the economy that differ in the speed of innovation; call them fast and slow. In the fast lane, innovation is rapid. Wages grow because employees are more productive as a result of new technologies that allow them to do more for less. In the slow sector, where innovation is jaundiced, we might expect wages to stagnate and the industry to wither and ultimately disappear. This would be true if the two sectors compete with each other, as was the case of steamships and sailboats. But the cost-disease hypothesis posits that if the slow sector doesn’t compete

with the fast sector and the slow sector is necessary (as is the case with health care), then wages will rise in the slow sector in order to persuade people to enter it. The faster the growth of productivity in the fast lane, the faster wages will also rise in the slow lane. And so the rapid productivity growth that we have seen in computers and automobiles pulls up wages in health care, education, the arts, and garbage collection. The central claim in *The Cost Disease* is that the “crisis” of health care spending may not be a crisis at all: innovation in some sectors increases incomes (or reduces prices), allowing us to spend more on health care. In Baumol’s view, as long as there is a steady stream of innovation outside of health care—and he believes that there will continue to be—we’ll be able to spend even more on health care.

Baumol is careful not to argue that the health care system lacks wasteful spending, and he devotes a fair bit of space to noting the scope of that problem. His “however” is that the cost-disease hypothesis explains the rapid growth of health care spending but doesn’t defend the level of spending (which could be rife with waste). The distinction between the level of spending and the growth of spending is central. For Baumol, the waste lies in the level of spending, but the growth of spending simply reflects the lack of productivity growth in health care. Prices in health care rise in order for it to be produced. The same logic can be used to explain why the wages of barbers have increased over time, even though there has not been innovation in barbering (at least not since barbers stopped being surgeons and dentists).

*The Cost Disease* offers a fresh take on an important phenomenon. It uses tantalizingly simple ideas to illustrate the perils of curtailing the growth of health care spending. While Cassandras have sounded the alarm over the rapid growth of health care spending, Baumol tells us to keep calm and carry on. Who should one listen to?

There are four issues that one should think about in refereeing this debate. The first is to note that health care spending is the product of health care price and use. Baumol’s study focuses only on the rapid increase in prices and is silent on the quantity of health care that people receive. But we’re surely getting more done to us today—e.g., stents, cardiac computed tomography, visits to the intensive care unit, new oncology drugs, robots, and

proton-beam therapy. More things are constantly being discovered in health care (which pushes against the pokey view of health care innovation), and they have high prices because of market power, patents, or research and development costs.

In addition, several commentators have noted that the price of health care on a per-unit basis and adjusted for quality is actually falling. Quality in health care is admittedly difficult to measure, but at least for heart-attack treatments, a careful quality-adjusted evaluation shows falling prices (1). Connecting the dots to the first point about use, it’s possible for prices to

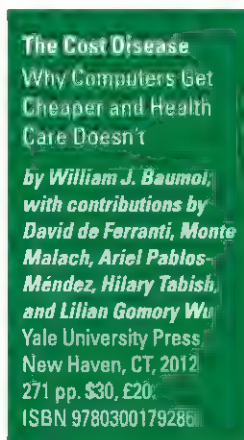
fall but use to increase. In other words, the price of treating cardiovascular disease may be dropping as bypass is replaced with stents, and brand-name statins with generics, but we may be still spending more because we are diagnosing and treating more people.

Furthermore, the distinction between the level of spending and the growth of spending is central for policy debates. There is no denying that growth of health care today will influence its level tomorrow. But if that’s true, the growth of health care yesterday influenced its level today. Baumol is open to waste being an explanation for the level of health care spending—yet as this simple example illustrates, his forthrightness opens up a Pandora’s box of concerns about waste in health care.

Lastly, regardless of the cause of the rise, one thing that everyone agrees on is that health care spending is increasing rapidly. Given government’s role as the largest purchaser of health care, this means that taxes have to go up. The U.S. Congress has shown little appetite for that, and other Organization for Economic Co-operation and Development countries can’t raise their taxes any further. Confronted with this reality, it is difficult to ignore the pressures to reduce waste, increase competition, and adopt high-value technologies. In *The Cost Disease*, Baumol cautions us that in the zeal to reduce health care spending, we should not forget the central role of innovations outside of the sector. As those enrich us, we can surely afford more health care.

#### References

1. D. M. Cutler, M. McClellan, J. P. Newhouse, D. Remer, *Q. J. Econ.* **113**, 991 (1998).



The reviewer is at the Harvard Kennedy School of Government, Harvard University, Cambridge, MA 02138, USA. E-mail: amitabh.chandra@harvard.edu

10.1126/science.1232064



## SCIENCE EDUCATION

# Crowdsourcing and Curating Online Education Resources

Darrell Porcello\* and Sherry Hsi

The Internet is a growing source of open educational resources (OERs) focused on Science, Technology, Engineering, and Math (STEM). These STEM OERs are not only shared openly and free for all to use, but often provide licenses that permit modification and reuse. Educators must have access to tools that pinpoint valuable resources while avoiding substandard ones. We discuss how multiple information sources, user communities, and online platforms might be coordinated to craft effective experiences in digital-rich learning environments.

There is no shortage of STEM OER collections. Public education and government agencies, television stations, state-level after-school organizations, science museums, and other organizations produce high-quality educational content for the Web and form extensive collections of collaborative, project-based, and open-ended STEM educational activities. Individual educators, scientists, and hobbyists use online platforms like Instructables, MakeProjects, and Pinterest to self-publish instructions for creative projects.

But as the number of STEM OERs grows online, how do educators decide what collections to use when searching for digital content? In a large kindergarten-to-high school (K–12) annual U.S. national survey, 41% of principals responded that it was “difficult to evaluate quality of digital content” (1), but >50% of teachers responded that the most important factors in evaluating content were “being referred by a colleague,” “free,” and “created by educators” (2), none of which is necessarily a hallmark of quality.

This highlights a difference within the online world of OERs. On one hand, collections using crowdsourcing allow a wide range of online users to contribute, choosing their own descriptions and keywords to catalog, review, and manage OERs. This can produce large and loose collections.

Lawrence Hall of Science, University of California, Berkeley, Berkeley, CA 94720USA.

\*Author for correspondence: porcello@berkeley.edu



Although dedicated users from the resulting online communities might be more willing to detail their instructional experiences and personal connections to OERs, overall quality may be quite variable. On the other hand, having professional staff with disciplinary expertise populate, catalog, and maintain curated collections usually results in fine-tuned, coherent, and smaller collections. Although these collections grow more slowly, often with less vocal user communities, they can quickly respond to new quality or educational standards.

Over the past decade, online platforms for STEM OERs have vacillated between these two poles. New efforts are combining the best aspects of both strategies to create sustainable online platforms to make it easier for educators to discover and use high-quality STEM OERs, confident in their scientific accuracy and pedagogical approach.

## Four Components Essential to OER Success

*Convergence Toward Common Metadata.* A standard set of terms, or metadata, used by a dedicated community of users to tag digital resources is a necessary characteristic of STEM OER collections. Grade level, subject area, cost per group, and resource type are just a few of the metadata fields relevant to educators. For example, metadata could allow an educator using Howtosmile.org, a free digital library of almost 3500 STEM OERs for out-of-school educators, to identify 82 hands-on activities on evolution for 8- to 11-year-olds.

The diverse wealth of crowdsourced online tools can benefit from professional coordination and quality control.

The National Science Digital Library (NSDL), initially funded by the U.S. National Science Foundation, set out to establish a common set of metadata fields and controlled vocabulary—a well-defined list of words to choose from when populating a metadata field, e.g., “biology” or “physics” for subject area—for online STEM educational resources by knitting together disciplinary and audience-specific communities (3). This provided the foundation for a long-standing consortium of online platforms for STEM OERs [e.g., (4)]. The core infrastructure team of the NSDL recently updated to the Learning

Application Readiness (LAR) metadata format in response to the increasing demand for STEM OERs to be “aligned to educational goals, curriculum, or professional development needs of users” (5).

Synergistic efforts of the Learning Resource Metadata Initiative (LRMI), funded by the Bill and Melinda Gates Foundation, establish a simplified set of standards to tag all educational online content, making it easier to publish, discover, and deliver quality OERs on the Web (6). Careful cataloging through metadata fuels advanced search engines and more effective discovery of STEM OERs by educators. Metadata can also provide information about how a resource aligns to curricular standards for STEM OERs.

*Balancing Expert and Community Definitions of Quality.* Learning resource and metadata quality are required for STEM OER online platforms to be accepted by parents, educators, and administrators, but who decides what is quality information? In the Wikipedia model, the written articles are largely crowdsourced, although core community members monitor and control the quality of information. As one of the most-visited sites on the Internet, with more than 23 million articles, the open digital encyclopedia has almost 80,000 volunteer editors who regularly contribute and edit content (7). Online STEM OER communities do not have this critical mass to use crowdsourcing as the sole source of quality control. It can play a part, but a professional or trained volunteer

staff is required to curate a high-quality collection of STEM OERs.

In addition, as standards alignment and student achievement metrics become more critical parameters for teachers and administrators choosing STEM OERs, professional services are required for increased reliability and accuracy in metadata creation. These points are demonstrated in NASA Wavelength.org, a new STEM OER collection from NASA where resources are reviewed by educators using a defined set of criteria (8), aligned to the AAAS Project 2061 Benchmarks for Science Literacy (9) when appropriate, and offered through a powerful search engine and a visual browse organized by relevant educational concepts. The peer educator and subject-area expert review process for the CPALMS online platform (10), aimed at Florida K–12 teachers, can only accept STEM OERs based on rigorous and standards-driven instructional materials.

As digital libraries evolve to identify effective teaching strategies and just-in-time information for educators, a new specialized profession is emerging for a dedicated cyber-librarian. This person would review incoming resources against a set of quality criteria to ensure only the best materials with strong STEM content, pedagogy, and standards alignments are included in STEM OER collections. The “cybrarian” also can serve as the key decision-maker in weighing administrator goals, adding regional-specific content, and determining use with traditionally under-represented populations in STEM or for students with disabilities.

**Community Input.** User voices can shape the public face and enhance the usability of online platforms for STEM OERs. Although users can author and submit new content to grow a collection, the most practical community input lies within “digital footprints,” e.g., page views, comments, ratings, or newly formed subcollections, left by users’ online interactions and behaviors across an online platform. Users often leave footprints during activities they do regardless of their benefit to the community. For example, users on Howtosmile.org are >10 times more likely to create and save a subcollection (11) of STEM hands-on activities than leave a comment or rating for an individual resource. A user’s subcollection might inform other users exploring a set of STEM OERs. Web sites like Gooru (12) are combining STEM OERs into lesson plans to attract educators.

Another strategy for community input is to have users participate in cataloging duties or earn rewards for ranking content. InBloom (13), formally the Shared Learning Collab-

orative, is introducing an easy to use LRMI-based tagging tool for educators to catalog online resources, whereas a forthcoming student-centered platform called Sparticl from Twin Cities Public Television (14) uses “folksonomies”—tags offered by community folks—and user ranking to better deliver STEM OERs to teens. No matter how it is eventually used, genuine community input for an online platform can only begin after there is first a critical mass of cataloged, high-quality STEM OERs established.

**Interoperability.** When an educator is searching for a resource, like an interactive animation illustrating the steps of mitosis, it would be more efficient if a single query could search across multiple online collections, rather than having the educator visit multiple Web sites. Interoperability enables information flow across multiple online platforms to ensure broad-based access to STEM OERs. Imagine searching for STEM OERs similar to using a single site to search for tickets from multiple airlines.

One necessary step toward interoperability is the adoption of an openly licensed, standardized metadata format for STEM OERs. Pushing beyond a basic set of library record fields from the long-standing Dublin Core metadata standard, this new, expanded metadata standard, with an updated controlled vocabulary, can address specific characteristics of STEM OERs and their users. Additions might include reading level, learning style preferences, assessment data, material costs, standards alignment, or user accessibility. The effort toward common metadata has led to several aggregator Web sites that search over large sets of STEM OERs including NSDL.org, Informalscience.org from the Center for Advancement of Informal Science Education (CAISE) (15), the cross-U.S. federal agency Learning Registry (16), and the EU Open Science Resources Project (17).

Although this work represents progress, an agreement on a STEM OER metadata standard has not been reached within the education community. But interoperability does not stop at metadata. NSDL has begun to promote a standard set of community input called “paradata” (18) as another way to share contextualized usage data about a resource and other relevant information across multiple online platforms. The hope is that STEM OERs listed on multiple platforms will retain usage information to establish a common set of digital footprints to be viewable at all points of access. Interoperability must stretch to the technical back-end systems of online platforms to include standard

metadata harvesting, resource vitality, and analytics protocols. Following good Linked Open Data (19) practices will better interconnect STEM OERs and enable greater flexibility for application development based on data from online platforms.

STEM OERs are becoming important parts of teaching experiences inside and outside the classroom. As search and discovery for STEM OERs become more seamless and natural to the online workflow of the educator and student, the four critical components described above will drive advanced architecture to streamline delivery within browsers, mobile devices, smart boards, and future educational technologies. A distributed, yet fully interconnected, online landscape of STEM OERs will improve quality and the user experience and will help avoid inadvertently recreating resources that already exist during times of dwindling budgets for new materials. When creating or disseminating new STEM OERs, a sensible strategy would be to leverage existing projects to deliver OERs in a responsible and efficient manner online.

#### References and Notes

1. Project Tomorrow, 2011 Speak-Up Report (Project Tomorrow, Irvine, CA, 2012); [www.tomorrow.org/speak-up/zSU11\\_PersonalizedClassroom\\_EducatorsReport.html](http://www.tomorrow.org/speak-up/zSU11_PersonalizedClassroom_EducatorsReport.html).
2. 2010 Speak-Up Report (2011); [www.tomorrow.org/speakup/pdfs/SU10\\_3EofEducation\\_Educators.pdf](http://www.tomorrow.org/speakup/pdfs/SU10_3EofEducation_Educators.pdf).
3. L. L. Zia, *D-Lib* 6, (2000). [www.dlib.org/dlib/october00/zia/10zia.html](http://www.dlib.org/dlib/october00/zia/10zia.html) 10.1045/october2000-zia
4. Including comPADRE (Physics), ChemEd DL (Chemistry), CLEAN (Climate and Energy), AMSER (Technical and Community Colleges), Engineering Pathway, Teachers' Domain (Media), MSP2 (Middle School Teachers), CPALMS (Florida K-12 Teachers), DLESE (Geosciences), and Howtosmile.org.
5. NSDL IAR, <https://wiki.ucar.edu/display/nsdl/docs/LAR+Concepts>.
6. LRMI, [www.lrmi.net/about](http://www.lrmi.net/about).
7. Wikimedia Foundation, 2011–2012 Annual Report; <http://wikimediafoundation.org/wiki/FAQ/en>.
8. NASA Wavelength.org Review Criteria; <http://nasareviews.strategies.org/reviewcriteria.html>.
9. Project 2061, [www.project2061.org/publications/bsl/](http://www.project2061.org/publications/bsl/).
10. CPALMS review process: [www.cpalms.org/cpalms/review.aspx](http://www.cpalms.org/cpalms/review.aspx).
11. Howtosmile.org lists: <http://howtosmile.org/userlists/recent>.
12. Gooru, <http://about.goorulearning.org/>.
13. InBloom, <https://www.inbloom.org/>.
14. Sparticl from Twin Cities Public Television, [www.sparticl.org/about/](http://www.sparticl.org/about/).
15. CAISE's Informalscience.org project, <http://informalscience.org/perspectives/blog/welcome-to-informalscienceorg>.
16. The Learning Registry, <http://learningregistry.org>.
17. Open Science Resources (OSR) Project, [www.openscienceresources.eu](http://www.openscienceresources.eu).
18. NSDL, Paradata; <https://wiki.ucar.edu/display/nsdl/docs/Paradata>.
19. Linked Open Data—What is it? A video from Europeana; <http://vimeo.com/36752317>.

**Acknowledgments:** Authors are affiliated with Howtosmile.org, NASA Wavelength.org, and Informalscience.org.

10.1126/science.1234722



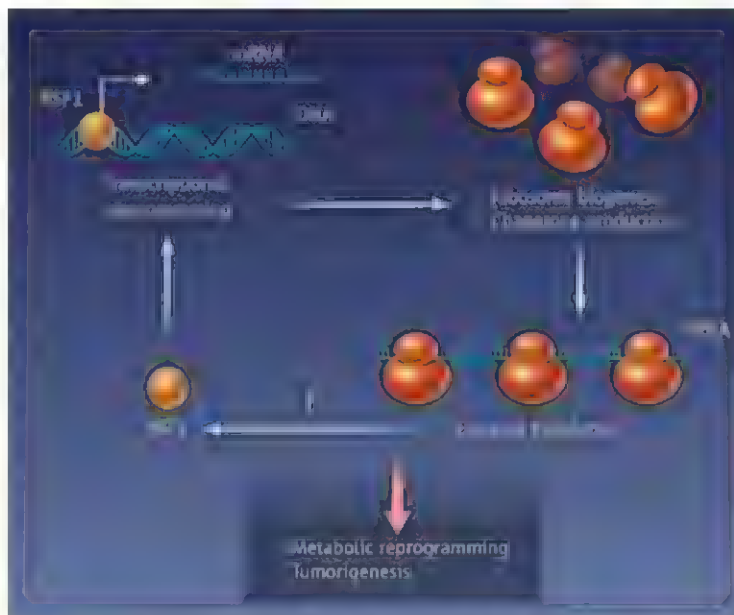
# Trans-HSF1 Express

Valentina Gandin and Ivan Topisirovic

Protein synthesis is elevated in many cancers (1). To cope with increased protein load and protein folding defects caused by genetic abnormalities, malignant cells bolster their chaperone system. Heat-shock transcription factor 1 (HSF1) is a major activator of chaperone-encoding genes. In cancer cells, HSF1 also affects the transcription of genes that are implicated in tumorigenesis (2), thereby shaping the “malignant transcriptome.” On page 250 of this issue, Santagata *et al.* (3) suggest that HSF1 acts as a central node of a regulatory network that “senses” messenger RNA (mRNA) translation rates and enables malignant cells to respond to increased protein loads by reprogramming transcription.

Santagata *et al.* deployed a series of unbiased genome-wide approaches to demonstrate that suppression of global mRNA translation abrogates HSF1 binding to target genes. The authors further determined that a class of compounds (rocaglates) that blocks translation also inhibits the transcriptional activity of HSF1. Rohinitib, a rocaglate with the highest potency of HSF1 inhibition, abolished glucose uptake and glycolysis in cancer cells and blocked proliferation of premalignant and malignant cells, while only marginally affecting proliferation of normal cells.

Cross talk between translational and transcriptional machineries in this HSF1-ribosome pathway bears resemblance to the unfolded protein response (UPR) that is triggered by the accumulation of unfolded and misfolded proteins in the endoplasmic reticulum (4). The UPR shuts down global protein synthesis by inactivating eukaryotic translation initiation factor 2 (eIF2) while stimulating translation of a specific subset of stress-related mRNAs that encode major transcriptional regulators



**Coupled programs.** In cancer cells, mRNA translation is increased, boosting the overall protein load (stress) and generating a repertoire of proteins that promote tumorigenesis. In the model shown, the transcription factor HSF1 “senses” this increase in mRNA translation and modifies transcription to increase chaperone capacity and ribosome biogenesis, thereby bolstering translation. The hyperactivation of this translation-transcription network, centered on HSF1, leads to metabolic reprogramming and drives neoplastic growth.

of UPR genes (such as activating transcription factor 4) (4). Like the HSF1-ribosome pathway, UPR plays a central role in tumorigenesis, wherein it is thought to promote cancer cell survival under various types of stress and therefore to contribute to tumor progression and the development of chemoresistance (5). The findings of Santagata *et al.* point to a partnership between translational and transcriptional programs that plays an important role not only in stress response but also in cancer initiation and progression (see the figure). The precise mechanism that underlies modulation of HSF1 transcription activity in response to changes in mRNA translation remains to be deciphered. Analogous to UPR, it is plausible that changes in translation of a subset of mRNAs affect HSF1 activity. Alternatively, inhibition of translation and subsequent dissociation of chaperones from ribosomes should be expected to increase the binding of chaperones to HSF1 and its inactivation.

Intriguingly, whereas inhibitors of the elongation step (cycloheximide) and the initiation step (rohinitib) of mRNA translation both decreased expression of HSF1 target

Ribosome activity is linked to the activity of a transcription factor in cancer cells.

genes, only rohinitib selectively attenuated proliferation of malignant cells. Rocaglates prevent the initiation of translation by interfering with eIF4A, an RNA helicase component of the eIF4F translation initiation complex (6). The eIF4A helicase unwinds secondary structure present in the 5′ untranslated region (5′UTR) of mRNA so that a ribosome can scan toward the codon that initiates translation. It is thought that eIF4A inhibitors [silvestrol (a rocaglate), pateamine A, and hippuristanol] exhibit robust antineoplastic effects in vitro and in vivo in multiple cancer models by selectively blocking the translation of oncogenic mRNAs that bear long, highly structured 5′UTRs that depend on the unwinding activity of eIF4A (6, 7). Santagata *et al.* show that in addition to restraining production of pro-oncogenic proteins at the

level of translation, rohinitib may also suppress neoplastic growth by inactivating the HSF1 transcription network. It remains to be determined whether rohinitib induces selective changes in the profile of mRNAs that are translated, particularly those encoding proteins that favor tumorigenesis.

Cancer cells increase aerobic glycolysis (the “Warburg effect”) to meet high bioenergetic and biosynthetic demands of neoplastic growth. Translation of mRNA is thought to be the most energy-consuming process in the cell (8). Accordingly, cancer cells adapt to nutrient deprivation by decreasing energy consumption. This is accomplished in part by reducing the rate of translation elongation, a process that is controlled by the adenosine monophosphate-activated protein kinase–eukaryotic elongation factor 2 kinase pathway (9). Santagata *et al.* demonstrate that rohinitib reduces aerobic glycolysis in a panel of cancer cell lines, which correlates with changes in the amounts of mRNAs that encode factors that function in glucose uptake (thioredoxin interacting protein) or glucose metabolism (phosphoglycerate kinase 1). Although it

Lady Davis Institute for Medical Research, Sir Mortimer B. Davis–Jewish General Hospital, and Department of Oncology, McGill University, Montréal, Québec, H3A 1A3, Canada. E-mail: ivan.topisirovic@mcgill.ca

remains to be resolved whether HSF1 directly controls expression of genes implicated in energy metabolism in response to rohitinib, these findings imply that the HSF1 regulatory network that couples translational and transcriptional programs contributes to metabolic reprogramming of malignant cells.

The steady-state compositions of the eukaryotic transcriptomes only loosely correspond to the composition of their proteomes, indicating that posttranscriptional regulatory mechanisms collaborate with the transcriptional networks to modulate cellular activities, including cell proliferation and survival (10). Santagata *et al.* show that in cancer cells, a

decrease in mRNA translation profoundly alters transcriptional programs by altering the activity of HSF1. In turn, HSF1 activates the transcription of ribosomal genes (2), whereas ribosome-associated chaperones stimulate translation elongation by promoting the transition of nascent mRNA chains through the ribosome exit tunnel (11, 12).

The plasticity of malignant proteomes that enables cancer cells to adapt to various types of stress appears to be achieved by feedback loops that coordinate transcription and translation. Networks that orchestrate these responses could potentially be exploited to devise new and better cancer treatments.

## References

1. D. Silvera *et al.*, *Nat. Rev. Cancer* **10**, 254 (2010).
2. M. L. Mendillo *et al.*, *Cell* **150**, 549 (2012).
3. S. Santagata *et al.*, *Science* **341**, 1238303 (2013). DOI: 10.1126/science.1238303
4. G. D. Pavitt, D. Ron, *Cold Spring Harb. Perspect. Biol.* **4**, a012278 (2012).
5. Y. Ma, L. M. Hendershot, *Nat. Rev. Cancer* **4**, 966 (2004).
6. A. Malina *et al.*, *Cold Spring Harb. Perspect. Biol.* **4**, a012377 (2012).
7. Y. V. Svitkin *et al.*, *RNA* **7**, 382 (2001).
8. D. F. Rolfe, G. C. Brown, *Physiol. Rev.* **77**, 731 (1997).
9. G. Leprévier *et al.*, *Cell* **153**, 1064 (2013).
10. J. D. Keene, *Nat. Rev. Genet.* **8**, 533 (2007).
11. R. Shalgi *et al.*, *Mol. Cell* **49**, 439 (2013).
12. B. Liu, Y. Han, S. B. Qian, *Mol. Cell* **49**, 453 (2013).

10.1126/science.1242359

## MATERIALS SCIENCE

# Droplets Out of Equilibrium

Thomas M. Hermans<sup>1</sup>, Holger Frauenrath<sup>2</sup>, Francesco Stellacci<sup>2</sup>

Living systems create structures and functions of remarkable complexity by mastering self-assembly in different equilibrium and nonequilibrium states. Three states can be distinguished: equilibrium, non-dissipative nonequilibrium (or kinetically trapped), and dissipative (or dynamic) non-equilibrium. On page 253 of this issue, Timonen *et al.* (1) report on a model system in which all three states are accessible (see the figure) and show how this leads to a range of well-ordered structures.

Most inorganic structures such as gems and minerals are equilibrium structures, which generally form spontaneously in such a way that the free energy is minimized. Some organic structures also form in this way, such as some folded proteins (2) or structure materials like collagen. Most supramolecular materials, which aim to mimic the hierarchical structures of biomaterials, are equilibrium structures (3, 4).

The next level of complexity is found in structures that reside in kinetically trapped or metastable states. These structures are typically far from

their thermodynamic equilibrium but are kept in a local state by deep potential or kinetic barriers. Examples include martensitic steel, most folded proteins (5), and cell membranes. Biological systems control the formation of these structures with sophisticated processing techniques, such as directed crystallization or the use of chaperones in protein folding (2).

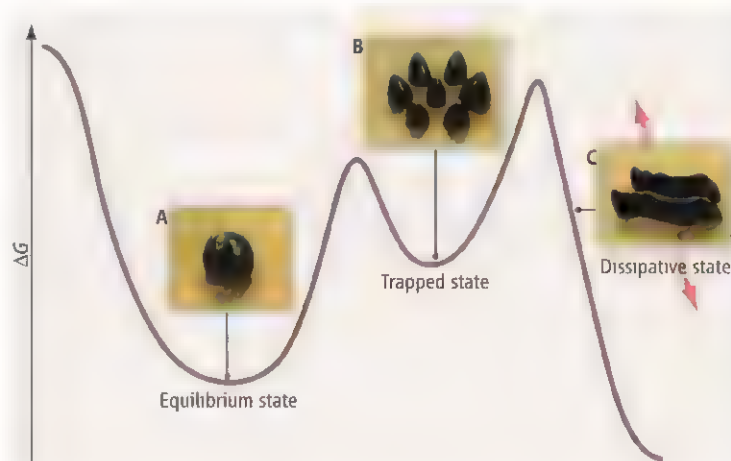
However, life is enabled by dissipative (or dynamic) assemblies that do not fall in either of these two categories. Prigogine's seminal works on complexity showed that there are steady thermodynamic states that, in order to exist, must either consume energy or continuously and quasi-reversibly exchange energy

Magnetic droplets can be switched between static and dynamic structures.

into entropy and vice versa (6, 7). The prime example is the cytoskeleton, where nucleoside triphosphates are hydrolyzed to their diphosphate analogs, providing chemical energy for forming long fibrous assemblies that give structural support to the cell membrane. At first glance, the continuous consumption of energy seems wasteful, but it enables the natural systems to repair or rapidly adjust their shape and functions.

In synthetic systems, a lot of progress has been made in developing equilibrium structures (8–10), but dissipative structures are still very scarce (11). Timonen *et al.* now report that magnetic droplets spontaneously split and assemble into well-defined geometric patterns under equilibrium conditions. These patterns can be altered by supplying them with energy, leading to dissipative nonequilibrium structures, and all equilibrium and dissipative structures can be kinetically trapped.

The authors show that a single droplet of ferrofluid on a superhydrophobic surface divides into multiple droplets in a way that depends on the strength and gradient of the magnetic field of the magnet placed below the surface. Each little droplet can be considered as an individual dipole being attracted to the center of the magnet. In addition, droplets that come



**Three self-assembly states.** Timonen *et al.* started with a single droplet that can be described in terms of equilibrium thermodynamics (A). When a magnetic field is applied, the system forms an ordered arrangement of multiple droplets, an example of a kinetically trapped state (B). When an oscillating field is applied to the kinetically trapped state, putting energy on the system, a dissipative assembly state develops (C). *G*, Gibbs free energy.

<sup>1</sup>Institut de Science et d'Ingénierie Supramoléculaires, Université de Strasbourg, 67083 Strasbourg Cedex, France. <sup>2</sup>Institute of Materials, Ecole Polytechnique Fédérale de Lausanne, 1015 Lausanne, Switzerland. E-mail: francesco.stellacci@epfl.ch



sufficiently close will repel each other. The balance between global attraction and local repulsion leads to the observed, highly symmetric equilibrium droplet patterns. When the magnetic field is removed, the patterns remain constant, showing that the system is in a kinetically trapped state.

The equilibrium droplet patterns can be altered reproducibly by feeding energy into the system. A periodically moving magnetic field gives rise to energy dissipation that leads to much more complex assembly geometries. For slow oscillations, the equilibrium droplet pattern simply translocates as a whole, but less ordered dissipative patterns emerge for fast oscillations, probably once the dissipation energy flux has passed a certain threshold.

In classical dissipative structures, such as reaction-diffusion patterns, Rayleigh-Bénard convection cells, or schools of fish, there is no order in or very close to the thermodynamic equilibrium. Only at a certain distance from the equilibrium state, beyond a critical point, do highly ordered configurations emerge (6). Moreover, order in such systems arises abruptly in a manner resembling a sharp phase transition. By contrast, Timonen *et al.*

(1) start out with an ordered equilibrium structure, which gradually decreases its order with increasing distance from equilibrium. Here, energy dissipation decreases the symmetry of the system.

The main challenge in studying dissipative structures is to identify the exact form and magnitude of dissipation. In Timonen *et al.*'s system, this could be magnetoelastic losses, viscous dissipation, or losses due to eddy-currents. Grzybowski and co-workers (12) have shown that viscous dissipation can be computed numerically for nonequilibrium structures of magnetic spinners assembling via vortex-vortex interactions, but their system does not allow for a simple experimental verification of the theory. For magnetic nonequilibrium structures like those presented by Timonen *et al.*, it could be beneficial to use an electromagnet to drive the system. In analogy to a calorimeter, where current is used to keep the temperature constant, the current in the electromagnet could be measured to keep the magnetic field constant. The current needed to create dissipative structures would provide further insights into the rates of dissipation.

Timonen *et al.*'s report shows that liquid droplets on nonwetting surfaces provide a rich platform for studying dissipative structures. The gradual transition of equilibrium to dissipative structures reported by Timonen *et al.* could potentially be applied to molecular self-assembling structures, which are usually well-ordered in their equilibrium state. Pushing supramolecular structures out of equilibrium might just be the way to create emergent structures with functions as complex as those of living systems.

#### References

1. J. V. I. Timonen *et al.*, *Science* **341**, 253 (2013).
2. D. Baker, D. A. Agard, *Biochem.* **33**, 7505 (1994).
3. M. Muthukumar *et al.*, *Science* **277**, 1225 (1997).
4. L. Brunsfeld *et al.*, *Chem. Rev.* **101**, 4071 (2001).
5. C. M. Dobson, *Nature* **426**, 884 (2003).
6. G. Nicolis, I. Prigogine, *Self-Organization in Nonequilibrium Systems* (Wiley, New York, 1977).
7. G. Nicolis, I. Prigogine, G. Nocolis, *Exploring Complexity* (Freeman, New York, 1989).
8. J.-M. Lehn, *Supramolecular Chemistry: Concepts and Perspectives* (VCH, Weinheim, 1995).
9. G. M. Whitesides, B. Grzybowski, *Science* **295**, 2418 (2002).
10. S. I. Stupp *et al.*, *Science* **276**, 384 (1997).
11. B. A. Grzybowski *et al.*, *Soft Matter* **5**, 1110 (2009).
12. K. V. Tretyakov *et al.*, *Soft Matter* **5**, 1279 (2009).

10.1126/science.1241793

## CHEMISTRY

# 100 Years of Atomic Theory

David C. Clary

In 1913, Niels Bohr published a groundbreaking paper that introduced a new way of understanding atomic phenomena (1). Entitled "On the Constitution of Atoms and Molecules," the article brought together for the first time the model of the atom developed by Rutherford, which consisted of a positively charged nucleus surrounded by negatively charged electrons, with the theory for quantization of radiation developed by Planck. The paper became one of the most influential of the 20th century.

Although the model for the hydrogen atom described in the paper was superseded within 13 years by developments in quantum theory and wave mechanics, the work introduced several new concepts that have stood the test of time. These include the existence of stationary states, in which an atomic or molecular system can have a precise energy and the transition from one state to another can be accompanied by the emission or

absorption of radiation. In addition, Bohr used Planck's constant  $h$  to identify the frequency  $\nu$  of radiation as

$$\nu = (W_2 - W_1)/h \quad (1)$$

for a transition from an initial state of energy  $W_1$  to a final state with energy  $W_2$ . These principles are second nature to scientists in 2013, but were radical a hundred years ago.

At the time of Bohr's paper, it was known through the work of Rydberg, following on from Balmer, that the frequency of a line in the visible spectrum of the hydrogen atom was given by

$$\nu = R(1/n_1^2 - 1/n_2^2) \quad (2)$$

where  $R$  is the empirically determined Rydberg constant and  $n_1$  and  $n_2$  are integers. The special feature of Bohr's theory was that it gave  $R$  purely in terms of fundamental con-

One hundred years ago, Niels Bohr's pioneering paper on the electronic structure of the hydrogen atom revolutionized atomic theory.



stants as  $R = 2\pi^2me^4/h^3$ , where  $m$  and  $e$  are the mass and charge of the electron, respectively. It was this finding in particular that caught the attention of the notables of the day, with Einstein describing it as "very remarkable" and Bertrand Russell stating this was "perhaps the most sensational evidence in favor of Bohr's theory" (2).

To justify the introduction of quantum numbers in his theory, Bohr assumed that the angular momentum of the electron in the hydrogen atom was quantized and that

Department of Physical and Theoretical Chemistry, University of Oxford, Oxford OX1 3QZ, UK. E-mail: david.clary@chem.ox.ac.uk

electrons have orbits of fixed radius depending on their quantum number. This concept gave the famous planetary picture of the atomic age, with electrons moving in orbits with well-defined radii around a nucleus.

This was a period when several new theories of the atom were being developed, and Bohr's ideas were not readily accepted by all. However, a subsequent note (3) in which Bohr showed that his theory also accurately explained the spectrum of the  $\text{He}^+$  ion, with a correction introduced to account for the mass of the nucleus, did much to convert doubters. In addition, his theory explained precisely the lines observed for the hydrogen atom from the infrared to the ultraviolet, including new observations made after 1913.

Bohr's revolutionary paper was part of a trilogy, with the second and third papers dealing with many-electron atoms and molecules, respectively (4, 5). The two subsequent papers extended some ideas of the first paper, but the results did not agree as well with experiments. Furthermore, Bohr's assumptions that  $\text{H}_2\text{O}$  was a linear molecule and that  $\text{H}_2^+$  was unstable did not gain much favor from chemists (6). However, the

papers did discuss several phenomena that proved to be significant later, including the understanding of x-rays, magnetic properties of atoms and molecules, and radioactivity. Bohr also deduced correctly that  $\beta$  particles were electrons emitted by the nucleus.

Some other theoretical concepts introduced in Bohr's trilogy of papers did not hold up. More sophisticated theories gave no angular momentum in the electronic ground state of the hydrogen atom. Furthermore, his theory could not explain the spectra of atoms with more than one electron, the intensities of spectral lines, effects of magnetic fields on atoms, fine structure, and hyperfine structure. However, subsequent extensions of Bohr's theory by himself, Sommerfeld, and others did make some improvements such as the introduction of elliptical orbits for the electrons and the quantization of the radial motion of the electron together with its angular momentum. This modified approach has found useful applications in understanding the dynamics of atoms and molecules to the present day (7).

Bohr's bold idea that a unifying theory of electronic structure must exist that can

explain all properties of atoms and molecules was tantalizing. In 1926, Schrödinger published his equation that essentially achieves this aim (8). Today, 100 years after Bohr's breakthrough, it is not just spectra that can be calculated accurately to explain and predict experiments but also the detailed energetics and dynamics of atoms and molecules (9). Any modern publication concerned with understanding the properties of molecules, not just in physics and chemistry but also in fields from materials science to molecular biology, will use concepts derived from Bohr's pioneering paper.

#### References

1. N. Bohr, *Philos. Mag.* **26**, 1 (1913).
2. H. Kragh, *Niels Bohr and the Quantum Atom 1913-25* (Oxford Univ. Press, Oxford, 2012).
3. N. Bohr, *Nature* **92**, 231 (1913).
4. N. Bohr, *Philos. Mag.* **26**, 476 (1913).
5. N. Bohr, *Philos. Mag.* **26**, 857 (1913).
6. H. Kragh, *Phys. Today* **66**, 36 (2013).
7. E. Bianchi, H. M. Haggard, *Phys. Rev. Lett.* **107**, 011301 (2011).
8. E. Schrödinger, *Ann. Phys.* **79**, 361 (1926).
9. D. C. Clary, *Science* **314**, 265 (2006).

10.1126/science.1240200

## DEVELOPMENTAL BIOLOGY

# Enhancing Pluripotency and Lineage Specification

Wei Xie<sup>1,2</sup> and Bing Ren<sup>1,2</sup>

**E**mbryonic stem cells (ESCs) and induced pluripotent stem cells (iPSCs) hold great promise in regenerative medicine. Realizing this potential requires a thorough understanding of the genetic programs regulating their pluripotency and lineage commitment. Recent studies have generated a wealth of information regarding the transcriptional circuitry underlying self-renewal and lineage commitment of ES cells. Here we review these studies, focusing on a type of cis-regulatory sequences called enhancers and their potential roles in pluripotency and cell fate determination. We also discuss how such information can help ES cell research and regenerative medicine, together

with the challenges to understand the functions and regulation of these elements.

#### Characteristics of Enhancers

Enhancers have been proposed to act as a pivot of lineage identity and developmental potential (1). Hundreds of thousands of putative enhancers have been annotated in the human genome (see the table). In particular, putative enhancers involved in pluripotency and lineage specification have been found by analysis of human embryonic stem cells (hESCs) and several hESC-derived cell types and constitute a sizable portion of regulatory elements in their genomes. During differentiation of ESCs, enhancer activity is highly dynamic, transitioning through several states characterized by distinct patterns of deoxyribonuclease I (DNase I) hypersensitivity, chromatin modifications, and transcription factor binding (1). This transition between different enhancer states is correlated with lineage-specific gene expression

The identification of large numbers of human embryonic stem cell enhancers provides a useful tool to study cell fate and disease.

(2–5). Enhancers frequently harbor binding sites or DNA motifs of transcription factors that are important for lineage identity (4, 6–8). In particular, genes coding for key regulators of cell identities are surrounded and regulated by “super enhancers” (9), which harbor unusually high levels of transcription factor binding. Binding of transcription factors to enhancers appears to precede their binding to promoters during reprogramming of somatic cells to iPSCs, which suggests that enhancer programming is among one of the first cellular events necessary for cell fate transition (10).

#### Exploiting Stem Cell Enhancers

Although the full catalog of enhancers in the human genome is still unknown, the identification of enhancers in hESCs and iPSCs will likely have a large impact on several fronts. For example, it will facilitate studies of molecular mechanisms underlying disease-linked sequence variants. Of noncoding dis-

<sup>1</sup>Ludwig Institute for Cancer Research and <sup>2</sup>Department of Cellular and Molecular Medicine, University of California San Diego School of Medicine, 9500 Gilman Drive, La Jolla, CA 92093-0653, USA. <sup>3</sup>Peking-Tsinghua Center for Life Sciences, MOE Key Laboratory of Bioinformatics, School of Life Sciences, Tsinghua University, Beijing 100084, China. E-mail: biren@ucsd.edu; xiewei121@gmail.com



# RECENT GENOMIC STUDIES FOR ANNOTATING PUTATIVE ENHANCERS IN hESCs AND THEIR DERIVATIVES

Cell type	# Of putative enhancers [or DHSs or transcription factor (TF) binding sites if indicated]	Identification method
<b>Studies focused on hESCs and/or their derivatives</b>		
hESC H1 (16)	~58,000	Histone modifications
hESC H9 and derived neuroectoderm cells (3)	~7,000 (hESCs)	p300, BRG1 and histone modifications
hESC H1 and BMP4 differentiated hESC (2)	~29,000 (hESCs) ~33,000 (hESC-BMP4)	Histone modifications
hESC H9 and derived neural crest cells (NCCs) (11)	~5,000 (NCC)	p300 and histone modifications
hESC H1 and derived mesendoderm, trophoblast-like cells, neural progenitor cells, and mesenchymal stem cells (4)	~13,000 to ~43,000 for each cell type. ~89,000 in all hESCs and hESC derivatives	Histone modifications
hESC HUES64 and derived mesoderm, neuroectoderm, and definitive endoderm (5)	~54,000 to ~78,000 for each cell type	Histone modifications
<b>Other large-scale studies that include hESCs and/or their derivatives</b>		
9 cell types, including hESC H1 (8)	3.8% of the genome sequences (hESC)	Histone modifications
125 cell types, including several hESC and iPSC lines (15)	~1,176,000 (total distal DHSs in all cell types)	DHS mapping
5 cell lines, including hESC H1 (17)	~4,476,000 (total distal TF binding sites)	TF binding
349 cell types, including several hESC and iPSC lines, and hESC derivatives (7)	~90,000 to ~370,000 (distal and proximal DHSs for each cell type)	DHS mapping
29 cell types, including several hESC and iPSC lines, hESC-derived neurons, and neural progenitor cells (6)	~94,000 per cell type	Histone modifications

ease-linked single-nucleotide polymorphisms (SNPs) identified from genome-wide association studies (GWAS), 76.6% either fall into a DNase I-hypersensitive site (DHS), a marker for putative enhancers, or are in complete linkage with SNPs in a nearby DHS (7). One hypothesis is that these SNPs may disrupt transcription factor binding sites at enhancers, which leads to misregulation of their targeted genes. This can now be tested in hESCs or patient-derived iPSCs, in which disease-linked SNPs can be engineered in the genome to create risk variant carrying and isogenic “wild-type” pluripotent cell lines. These lines can be further differentiated into cell types of interest as disease models to study the causal effects of these SNPs on potential disease-related gene expression patterns.

Locations of enhancers could also help pinpoint binding sites of lineage-specific transcription factors, which often occupy hundreds of thousands of loci in the genome. Transcription factors falling within active enhancers are more likely to be conserved and functional (11). Furthermore, motif analysis of enhancer sequences can help identify regu-

lators of specific cell lineages. For example, such analysis has led to the identification of novel regulators (nuclear receptors NR2F1/F2) of human neural crest cells (11). In addition, cell type-specific enhancers can facilitate the development of lineage-specific biomarkers to specify appropriate cell types. Such markers may help further optimize hESC and iPSC differentiation protocols, or identify subsets of cells within a differentiated population that more closely resemble their in vivo counterparts. Another potential benefit of using enhancer-based biomarkers is that enhancers can be primed or poised before activation, which allows preselection of hESCs and iPSCs before induction of differentiation. For example, different iPSC lines demonstrate distinct lineage differentiation efficiencies (12). It would be interesting to examine whether enhancer activity can be used to distinguish iPSCs for their differentiation potentials. Further, global enhancer activity can be monitored for benchmarking hESC- and hiPSC (human iPSC)-derived cell types against tissues derived in vivo. As ES cells are raised and maintained in cell culture, it is

critical to determine how well these hESC- and hiPSC-based differentiation processes recapitulate in vivo development. For instance, aberrant gene expression and promoter regulation were found when comparing hESC-derived pancreatic endoderm cells differentiated in vivo and in vitro (13). Cell culture can also induce expansion of large histone H3 lysine 9 trimethylated (H3K9me3) domains (6), which are associated with constitutive heterochromatin. Given that enhancer activity is highly dynamic, it is conceivable that they may be more sensitive to environmental changes and culture conditions.

## Remaining Challenges

Despite the identification of large numbers of hESC enhancers, it remains challenging to elucidate the gene-regulatory programs underlying pluripotency and cell differentiation. One reason is that the targets of these enhancers are not easy to define, as an enhancer often controls more than one gene, and the target gene is not necessarily the nearest one (1, 14). Current approaches to

address this problem are still imperfect. In one approach, chromatin state at enhancers is used to identify promoters sharing similar chromatin profiles in nearby regions across multiple cell types (8, 15). Although correlated activity may reflect coordinated regulation between enhancers and promoters, it can also be indirect or even irrelevant. In another approach, chromosome conformation capture techniques (3C) and derivatives (such as HiC) were used to directly assess the interaction between enhancers and promoters (14). However, such interaction-based analyses are not yet satisfactory owing to the low resolution of identified long-range interactions. It is also unclear if interaction alone can accurately predict functional regulation.

The extent to which each enhancer contributes to target gene expression is generally undefined except for a handful of enhancers such as those at the  $\beta$ -globin gene (14). To examine the effect of enhancers on transcription, one would need to mutate the element in its endogenous locus and characterize the target gene expression. Given the rapid progress in genome editing technol-

ogy, it is tempting to predict that large numbers of putative enhancers will eventually be genetically engineered in a high-throughput manner. Further, how enhancers are regulated needs to be more precisely elucidated. Molecular mechanisms governing enhancers are much less clear compared with those for promoters. For example, more needs to be learned about the factors that initiate, establish, and maintain the active, poised, and silenced states of enhancers, as well as the extent to which DNA looping participates in gene activation. This will enable a fuller understanding of the role of enhancers in the genetic programs of pluripotency and lineage specification (16, 17).

Recent “omics” studies have uncovered a large number of putative enhancers that can program the transcriptional networks in pluripotent cells. However, these rich data sets have revealed more questions than answers. This is only the first step toward understanding the molecular mechanisms of pluripotency, and eventually realizing the potentials of hESCs and iPSCs.

#### References and Notes

1. C. Buecker, J. Wysocka, *Trends Genet.* **28**, 276 (2012).
2. R. D. Hawkins *et al.*, *Cell Res.* **21**, 1393 (2011).
3. A. Rada-Iglesias *et al.*, *Nature* **470**, 279 (2011).
4. W. Xie *et al.*, *Cell* **153**, 1134 (2013).
5. C. A. Gifford *et al.*, *Cell* **153**, 1149 (2013).
6. J. Zhu *et al.*, *Cell* **152**, 642 (2013).

7. M. T. Maurano *et al.*, *Science* **337**, 1190 (2012).
8. J. Ernst *et al.*, *Nature* **473**, 43 (2011).
9. W. A. Whyte *et al.*, *Cell* **153**, 307 (2013).
10. A. Soufi, G. Donahue, K. S. Zaret, *Cell* **151**, 994 (2012).
11. A. Rada-Iglesias *et al.*, *Cell Stem Cell* **11**, 633 (2012).
12. C. Bock *et al.*, *Cell* **144**, 439 (2011).
13. R. Xie *et al.*, *Cell Stem Cell* **12**, 224 (2013).
14. J. H. Gibcus, J. Dekker, *Cell* **49**, 773 (2013).
15. R. E. Thurman *et al.*, *Nature* **489**, 75 (2012).
16. R. D. Hawkins *et al.*, *Cell Stem Cell* **6**, 479 (2010).
17. M. B. Gerstein *et al.*, *Nature* **489**, 91 (2012).

**Acknowledgments:** We apologize to those authors whose works are not covered here owing to space limitations. This work is supported by funds from the Ludwig Institute for Cancer Research, NIH (grants U01ES017166 and 5U01HL107442), and the California Institute for Regenerative Medicine (RN2-00905) to B.R.

10.1126/science.1236254

## ENGINEERING

# Multiscale Design and Integration of Sustainable Building Functions

Maria Paz Gutierrez<sup>1</sup> and Luke P. Lee<sup>2</sup>

**B**uildings and cities must move toward balancing resources and advancing risk preparedness in support of robust sustainability and climate change action (1–5). To date, the design of sustainable buildings has optimized the generation of energy separately from the regeneration of water and the processing of waste. However, the integration of macro-, micro-, and nanoscale engineering principles has enabled examples of synergistic optimization of energy generation with water and the processing of waste. Innovative multiscale design can allow buildings to wholly contain utilities, rather than merely providing routes for their delivery.

As early as the fourth century BCE, Greek philosophers and builders harnessed the Sun for energy in houses, communities, and even cities, such as Priene and Olynthus. To prevent further destruction of the forests around their city, Romans adopted solar-oriented architecture from classic Greece, advancing it to a much wider range of climate applications. Roman builders invented solar-oriented openings with glass (i.e., south-facing windows) to heat rooms (6). With the spirit of more than two millen-

nia of solar-oriented architecture, an MIT team in 1947 demonstrated the Solar House II, which used sunlight to heat water tanks on a facade to heat interior space (7). More recently built examples of net-zero design at the residential scale demonstrated integration of water-based radiation through ceiling panels that absorb sunlight. These panels transfer the heat into thermal storage facilities that heat the residence in winter by a heat exchange process (8).

In skyscrapers, architects and engineers have piloted multiple built and research models to advance an integrated optimization of energy, water, and waste (9). The Pearl River Tower in China demonstrates the integration of reduction, reclamation, passive absorption, and generation of energy. This project features multiple integrated technologies, such as a reclamation scheme accomplished through water harvested from chilled surfaces to control interior humidity. Once filtered, this water is reused for interior plant irrigation and toilet flushing. Here, a single integrated technology serves both functions for energy reduction (dehumidification) and water recovery. The implementation of the triple net-zero concept (zero energy, zero emissions, zero waste) has been demonstrated at the residential level, and many other buildings have shown the feasibility of nearly net-zero energy (7, 8).

Currently, through the Emerging Frontiers in Research and Innovation (EFRI)

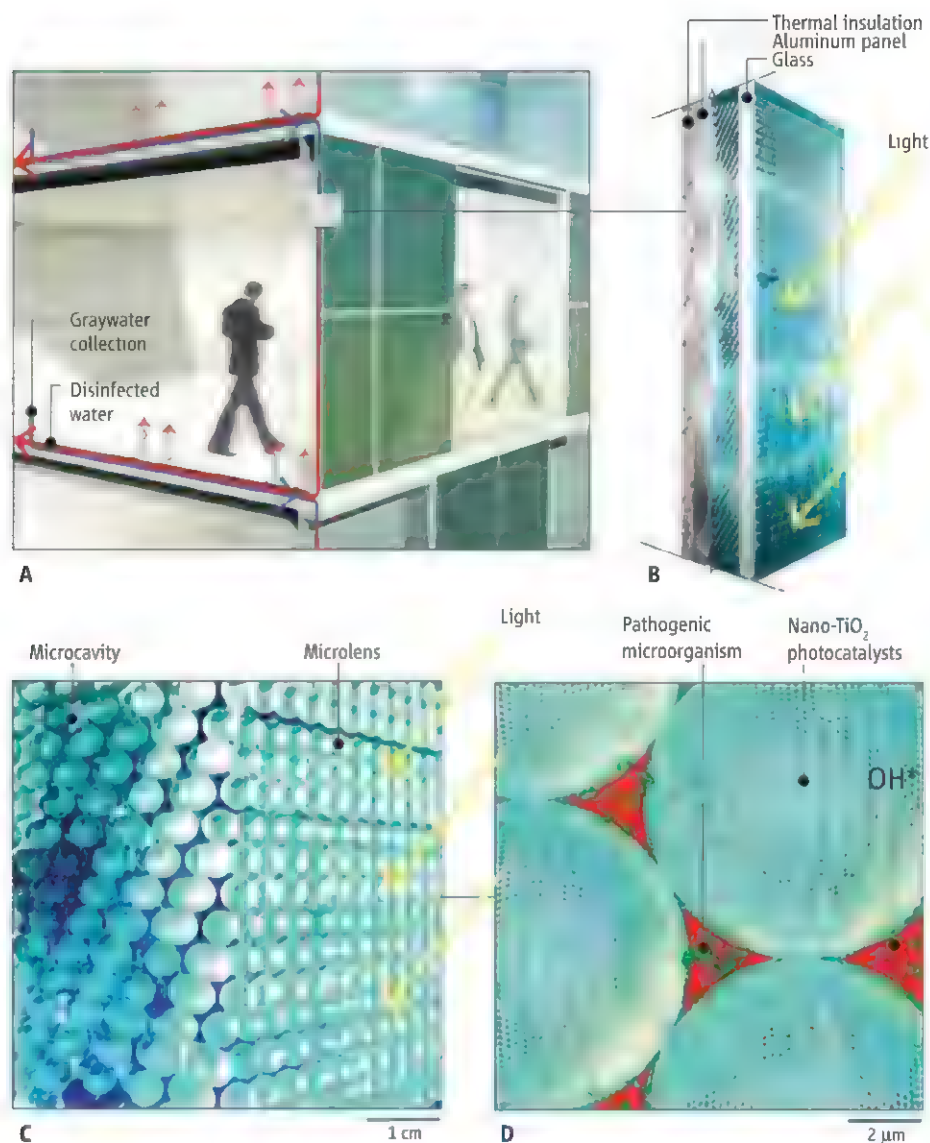
Designing systems from nano- to macroscale can optimize the synergistic integration of sustainable energy and waste treatment in buildings.

office of the National Science Foundation, 10 teams are participating in the Science in Energy and Environmental Design (SEED) group. Among these interdisciplinary teams, a few are researching new building technologies that integrate nano- and microengineering principles for building-scale applications (10). The focus is on developing self-regulated and multifunctional building enclosures that act as “living walls, materials and systems.” A University of Colorado team is researching a living wall for automatic thermal regulation, with a goal of net-zero energy and water conservation. The living wall comprises two optimized microvascular networks and a distributed phase-change medium (PCM) that absorbs or releases heat. The research develops a new polymer and microvascular fluid channels to establish a wall system with autonomous movement of air and water to charge or discharge the PCM for optimized thermal regulation (10).

A University of Pennsylvania team is developing eSkin, which is inspired by human smooth muscle cells that alter their extracellular matrices and their surrounding environments. The facade is composed of engineered microstructure patterns in passively responsive materials to generate three-dimensional surface and optical effects for light transmission calibration. With embedded sensors and imagers, eSkin modulates passive solar energy, light,

<sup>1</sup>Department of Architecture, University of California, Berkeley, CA 94270, USA. <sup>2</sup>Departments of Bioengineering, Electrical Engineering, and Computer Science, Berkeley Sensor and Actuator Center, University of California, Berkeley, CA 94270, USA. E-mail: mpazgut@berkeley.edu; lplee@berkeley.edu





**Integrative sustainable building technologies.** Multiscale design is illustrated from macro- to nanoscales. (A) A schematic axonometric drawing of the SOAP decentralization system: graywater collection, solar-activated disinfection (facade), and recirculation (radiant floor heating). (B) A single SOAP panel containing (C) a photocatalytic optofluidic network is created by multiple layers of integrated photocatalytic reactors. (D) Pathogenic microorganisms are disinfected via photocatalytic  $\text{TiO}_2$  nanoparticles. The larger support particles act as microlenses to concentrate solar energy and to generate an efficient photocatalytic effect.

and moisture by using microstructured patterns to respond to local performance criteria (10).

Another example is solar optics-based active panels (SOAP) technology for graywater reuse and integrated solar energy harvesting (11). In this project, graywater is recovered from washing (sinks, bathtubs, and laundry) by disinfection, in buildings that require extreme water conservation, cooling through the day and heating during the night because of major diurnal temperature swings (as found in arid climates). Once collected, graywater is exposed to a solar-based optofluidic platform in the

facade, where an efficient photocatalytic disinfection process is activated by sunlight throughout the day. Effective disinfection of pathogenic microorganisms can be achieved via integrated photocatalytic titanium dioxide ( $\text{TiO}_2$ ) nanoparticles on microlens arrays.

By integrating nanophotocatalytic elements on microlenses, the panel system improves light capture, transmission, and the efficiency of water disinfection in a broad range of geometries and facade orientations. Expanded nanophotonic architectures can increase the density of catalytic sites if the panels must deliver more capac-

ity. The disinfected water is recirculated at night for radiant floor heating as a by-product of the process, providing synergistic water and waste regeneration and energy generation. Once the water is used as a thermal source, it is brought into the building for reuse in toilet flushing and/or laundry.

Integrated optimization of resources in buildings can decentralize the delivery of utilities in cities. Potential benefits include substantial cost savings in energy inputs and fewer disruptions from power outages or infrastructure failures. Further advances in sustainable building technology will demand research collaborations among architects, engineers, and scientists. Building control functions must monitor and forecast interior and exterior conditions and occupancy in order to optimize energy use (12). New active materials may self-generate, regenerate, or undergo phases from the nanoscale to the architectural scale (13). To streamline this innovation, architects, scientists, and engineers will have to make substantial advances in building materials, as well as multiscale building analysis (14, 15). Multiscale designs in which water, energy, and waste are synergistically integrated can mark a new era for "resourcing" resources in buildings.

#### References and Notes

1. J. P. Holdren, *Science* **319**, 424 (2008).
2. I. Sartori et al., *Energy Build.* **48**, 220 (2012).
3. C. Rosenzweig et al., *Nature* **467**, 909 (2010).
4. P. Hernandez, P. Kenny, *Energy Build.* **42**, 815 (2010).
5. U.S. Department of Energy, Zero Energy Buildings; <http://zeb.buildinggreen.com>.
6. K. Butti, J. Perlin, *A Golden Thread: 2500 Years of Solar Architecture and Technology* (Van Nostrand, New York, 1980).
7. M. Davies, *Int. J. Energy Res.* **10**, 305 (1986).
8. W. Sobek, K. Sedlbauer, H. Schuster, in *Technology Guide: Principles, Applications and Trends*, H.-J. Bullinger, Ed. (Springer, New York, 2009), pp. 432–435.
9. R. R. Frechette, R. Gilchrist, in *CTBUH: Proceedings of the Council on Tall Buildings and Urban Habitat's 8th World Congress*, Dubai, United Arab Emirates, 3 to 5 March 2008, pp. 7–16.
10. Science in Energy and Environmental Design (SEED) Awards; [www.nsf.gov/eng/efri/fy10awards\\_SEED.jsp](http://www.nsf.gov/eng/efri/fy10awards_SEED.jsp)
11. Solar Optics-based Active Pasteurization (SOAP) for Greywater Reuse and Integrated Thermal (GRIT) Building Control; [www.nsf.gov/awardsearch/showAward?AWD\\_ID=1038279](http://www.nsf.gov/awardsearch/showAward?AWD_ID=1038279).
12. N. Gershenfeld et al., *Science* **327**, 1086 (2010).
13. M. Ashby et al., *Nanomaterials, Nanotechnologies and Design: An Introduction for Engineers and Architects* (Butterworth-Heinemann, Amsterdam, 2009).
14. A. Malkawi, G. Augenbroe, *Advanced Building Simulation* (Spon, New York, ed. 1, 2004), pp. 1–5.
15. J. E. Fernández, *Science* **315**, 1807 (2007).

**Acknowledgments:** Supported by the NSF EFRI SEED award.

10.1126/science.1237278

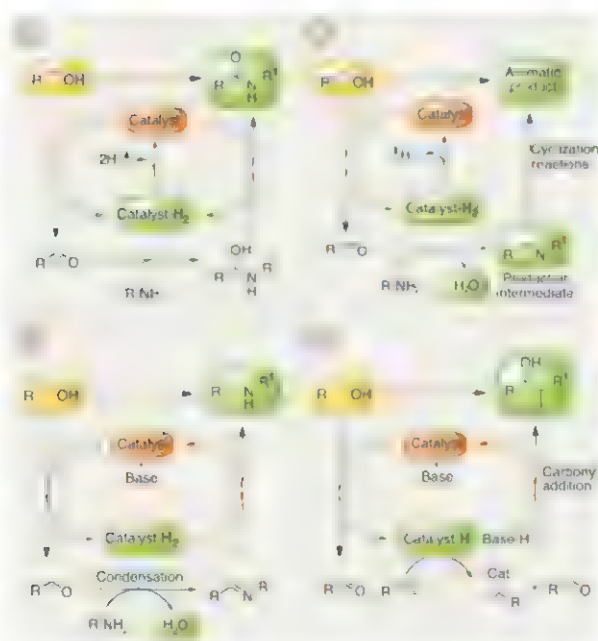
# Applications of Acceptorless Dehydrogenation and Related Transformations in Chemical Synthesis

Chidambaram Gunanathan and David Milstein\*

**Background:** Acceptorless dehydrogenation (AD) reactions can result not only in simple removal of hydrogen gas from various substrates but also, importantly, in surprisingly efficient and environmentally benign ("green") synthetic methodologies when intermediates resulting from the initial dehydrogenation process undergo further reactions.

**Advances:** Traditionally, dehydrogenation/oxidation reactions of organic compounds have been performed using stoichiometric amounts of inorganic oxidants, in addition to employing various additives, cocatalysts, and catalytic systems that result in generation of copious stoichiometric, often toxic, waste. Catalytic transfer hydrogenation methods, in which stoichiometric amounts of sacrificial organic acceptor compounds are used, also generate stoichiometric amounts of organic waste. Recent developments in catalysis by metal complexes have resulted in AD reactions that release hydrogen gas and in related reactions in which dehydrogenation is followed by in situ consumption of the generated hydrogen equivalents and no net hydrogen gas is liberated. These reactions circumvent the need for conventional oxidants or sacrificial acceptors and provide an assortment of applications in organic synthesis, including several methods based on further reactivity of the dehydrogenated intermediate compounds. Moreover, the evolved hydrogen gas is valuable in itself.

**Outlook:** Further development of new ADs for green, efficient chemical synthesis is expected to be greatly influenced by fundamental organometallic chemistry as a basis for catalyst design. Such processes are highly desirable and are expected to gradually displace elaborate conventional laboratory and industrial synthetic methods. They may also provide opportunities for hydrogen storage cycles, because the dehydrogenation reactions can be reversed under hydrogen pressure using the same catalyst. In general, AD and related dehydrogenative coupling reactions have the potential for redirecting synthetic strategies to the use of sustainable resources, devoid of toxic reagents and deleterious side reactions, with no waste generation.



**Dehydrogenation strategies in organic synthesis.** (A) Successive AD with release of hydrogen gas. The catalyst liberates H<sub>2</sub> from both starting compound and intermediate, exemplified by dehydrogenative coupling of primary alcohols with amines to form amides. (B) AD with H<sub>2</sub> and water release. A dehydrogenated intermediate couples with nucleophiles, exemplified by dehydrogenative coupling of alcohols with amines (liberating water) to form imines that can be isolated or carried on to products such as pyrazines. (C) Borrowing hydrogen. The catalyst dehydrogenates the substrate and formally transfers the H atoms to an unsaturated intermediate, exemplified by coupling of ammonia or amines with alcohols to form new amines, liberating water, but not H<sub>2</sub>. (D) Coupling of redox pairs. Dehydrogenation generates an electrophile and a nucleophile that react to form C-C bonds. Neither H<sub>2</sub> nor water is evolved.

READ THE FULL ARTICLE ONLINE

<http://dx.doi.org/10.1126/science.1229712>



Cite this article as C. Gunanathan, D. Milstein, *Science* **341**, 1229712 (2013). DOI: 10.1126/science.1229712

## ARTICLE OUTLINE

### Precursors to Modern AD

#### Alkane Dehydrogenation

#### Alcohol Dehydrogenation

#### Dehydrogenative Coupling of Alcohols to Form Esters

#### Dehydrogenative Coupling of Alcohols with Amines to Form Amides

#### Dehydrogenative Coupling with Concomitant Condensation Reactions

#### Alkane Metathesis

#### Alkylation of Amines by Borrowing Hydrogen Methodology

#### Alcohols as a Source of Electrophiles and Nucleophiles

#### Outlook

## ADDITIONAL RESOURCES

J. Choi *et al.*, Dehydrogenation and related reactions catalyzed by iridium pincer complexes. *Chem. Rev.* **111**, 1761–1779 (2011). doi: 10.1021/cr1003503

C. Gunanathan, D. Milstein, Metal-ligand cooperation by aromatization-dearomatization. *Acc. Chem. Res.* **44**, 588–602 (2011). doi: 10.1021/ar2000265

J. F. Bower, M. J. Krische, Formation of C-C Bonds via iridium-catalyzed hydrogenation and transfer hydrogenation. *Top. Organomet. Chem.* **34**, 107–138 (2011). doi: 10.1007/978-3-642-15334-1\_5

## RELATED ITEMS IN SCIENCE

J. R. Zbieg *et al.*, Enantioselective C-H crotylation of primary alcohols via hydrohydroxyalkylation of butadiene. *Science* **336**, 324–327 (2012). doi: 10.1126/science.1219274

A. J. A. Watson, J. M. J. Williams, The give and take of alcohol activation. *Science* **329**, 635–636 (2010). doi: 10.1126/science.1191843

C. Gunanathan *et al.*, Direct synthesis of amides from alcohols and amines with liberation of H<sub>2</sub>. *Science* **317**, 790–792 (2007). doi: 10.1126/science.1145295

A. S. Goldman *et al.*, Catalytic alkane metathesis by tandem alkane dehydrogenation-olefin metathesis. *Science* **312**, 257–261 (2006). doi: 10.1126/science.1123787

The list of author affiliations is available in the full article online.

\*Corresponding author. E-mail: david.milstein@weizmann.ac.il





## **AAAS is here – bringing scientific expertise to policy making.**

Good science policy is the result of politicians understanding science and scientists understanding policy. Toward this end, AAAS manages the Science & Technology Policy Fellowships program, which embeds scientists and engineers in the federal government for up to two years. From Congress to the State Department, each class of Fellows contributes to the policy-making process while getting hands-on experience at the intersection of science and policy. As a AAAS member your dues support these efforts. If you're not yet a AAAS member, join us. Together we can make a difference.

To learn more, visit [aaas.org/plusyou/fellows](https://aaas.org/plusyou/fellows)



# Applications of Acceptorless Dehydrogenation and Related Transformations in Chemical Synthesis

Chidambaram Gunanathan<sup>1</sup> and David Milstein<sup>2\*</sup>

Conventional oxidations of organic compounds formally transfer hydrogen atoms from the substrate to an acceptor molecule such as oxygen, a metal oxide, or a sacrificial olefin. In acceptorless dehydrogenation (AD) reactions, catalytic scission of C–H, N–H, and/or O–H bonds liberates hydrogen gas with no need for a stoichiometric oxidant, thereby providing efficient, nonpolluting activation of substrates. In addition, the hydrogen gas is valuable in itself as a high-energy, clean fuel. Here, we review AD reactions selectively catalyzed by transition metal complexes, as well as related transformations that rely on intermediates derived from reversible dehydrogenation. We delineate the methodologies evolving from this recent concept and highlight the effect of these reactions on chemical synthesis.

Anticipation of fossil fuel depletion and growing environmental concerns urge chemists and chemical industries to search for alternative raw materials and for atom-economical, environmentally benign synthetic methods. In this context, acceptorless dehydrogenation (AD) reactions, in which hydrogen is liberated and new bonds prospectively generated by further reactions of the dehydrogenated products, are emerging as a powerful approach, circumventing the need for stoichiometric oxidants or prefunctionalization of substrates.

Removal of hydrogen atoms from adjacent atomic centers of a hydrogen-rich organic molecule is in most cases a thermodynamically unfavorable process. Thus, dehydrogenation of organic compounds often requires stoichiometric or excess molar amounts of oxidants such as oxygen, peroxides, iodates, and metal oxides (Fig. 1A) or sacrificial hydrogen acceptors (Fig. 1B), leading to wasteful by-product generation. In the more atom-economical AD reaction, molecular hydrogen must be effectively removed from the reaction mixture to drive the equilibrium toward the products (Fig. 1C). Alternatively, the liberated hydrogen can also be used in situ to hydrogenate unsaturated intermediates generated from a condensation reaction.

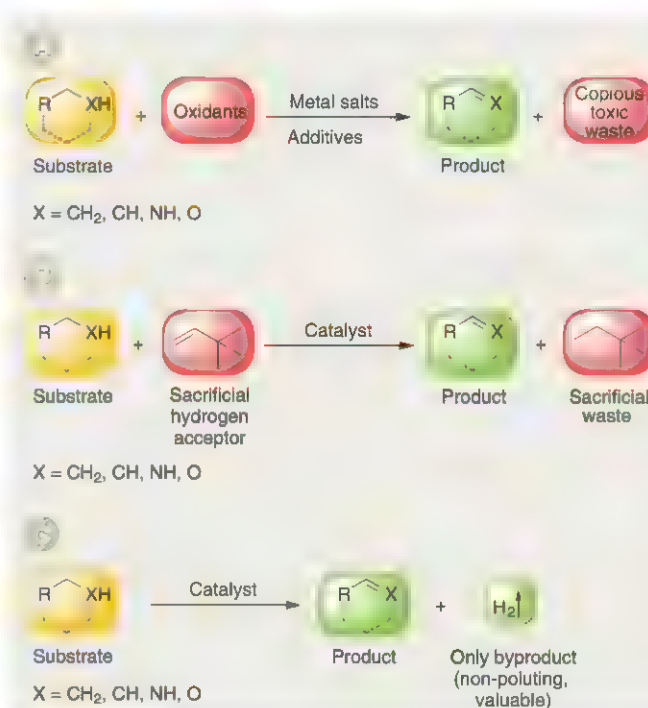


**Fig. 1. Classes of dehydrogenation reaction. (A)** Dehydrogenation/oxidation by conventional oxidants. **(B)** Hydrogen-transfer reactions. Liberated hydrogen binds to a sacrificial acceptor molecule. **(C)** AD. Dehydrogenation leads to liberation of hydrogen gas, which is removed from the reaction mixture under reflux conditions or by vacuum.

Our group has developed a class of AD reactions in which the catalyst dehydrogenates both the starting compound and an intermediate compound, leading to the net-oxidized product with liberation of two equivalents of hydrogen (Fig. 2A). Reactions have also been developed in which both liberation of hydrogen and elimination of water take place (Fig. 2B). In a related class of reactions, termed the “borrowing hydrogen” approach, the catalyst hydrogenates an

intermediate using the hydrogen removed from the starting compound. This method is also called “hydrogen autotransfer” (Fig. 2C); it does not involve net hydrogen evolution, and the overall process is redox neutral. Dehydrogenation reactions can also couple a redox pair such as an alcohol and an alkene, to provide products of formal alcohol C–H functionalization; upon alcohol dehydrogenation (in the presence of catalytic base), the generated metal hydride intermediate adds to the alkene to give a nucleophilic metal alkyl, followed by reaction of the latter with the intermediate keto compound to form a C–C bond (Fig. 2D). AD reactions provide environmentally benign synthetic methodologies for the preparation of an assortment of useful products, in addition to the generation of valuable hydrogen gas. For example, amines and amides, which are traditionally prepared by multistep processes using stoichiometric amounts of activating reagents, can be obtained in a single synthetic step from alcohols with minimal waste by means of AD.

Because X–H bonds (X = C, O, or N) are ubiquitous among organic molecules, selective AD followed by further tandem functionalization can provide a diverse stream of products. This strategy has been achieved mostly as a result of advancement in the field of catalysis by transition metal complexes. Dehydrogenation reactions classified by the substrates and catalysts have been reviewed (1–3). Here, we highlight AD reactions catalyzed by soluble transition metal complexes from the perspective of the strategies outlined in Fig. 2, with particular emphasis on selective coupling reactions leading to useful products efficiently and atom-economically.

## Precursors to Modern AD

In organic synthesis, the oxidation/dehydrogenation is carried out using conventional methods, which use stoichiometric amounts or excess of inorganic oxidants such as chromium(IV) reagents (4), pressurized oxygen (5), or peroxides, in addition to employing various additives, cocatalysts, and catalytic systems combined with metal complexes and TEMPO (2,2,6,6-tetramethylpiperidyl-1-oxo) that result in stoichiometric waste generation, which is undesirable environmentally and economically (6). In addition, pressurized oxygen and peroxides pose explosion hazards. To circumvent these problems, dehydrogenation methods without use of conventional oxidants were developed. Early investigations of AD emanated from heterogeneous catalysis. Dehydrogenation of linear primary alcohols resulted in  $\beta$ -branched primary alcohols as a result

<sup>1</sup>School of Chemical Sciences, National Institute of Science Education and Research (NISER), Bhubaneswar 751005, India. <sup>2</sup>Department of Organic Chemistry, The Weizmann Institute of Science, Rehovot 76100, Israel.

\*Corresponding author. E-mail: david.milstein@weizmann.ac.il



of condensation of the intermediate aldehydes followed by dehydration and hydrogenation, as reported in the late 1800s by Guerbet, much before hydrogen-transfer reactions were reported (7). The simple hydrogen-transfer reaction has its origin in the Oppenauer oxidation of secondary alcohols to ketones in the presence of acetone, mediated by aluminum *tert*-butoxide (8) and later catalyzed by transition metal complexes. Hydrogen transfer using alkanes as the hydrogen source is much more difficult due to the generally unreactive C–H bonds. In 1979, Crabtree achieved stoichiometric dehydrogenation of alkanes using a cationic iridium(III) metal complex (9) in the presence of a hydrogen acceptor. Pioneering examples of catalytic alkane hydrogen-transfer reactions by soluble complexes were independently reported by Felkin and colleagues (10) and Crabtree and colleagues (11).

### Alkane Dehydrogenation

In pioneering work, Aoki and Crabtree reported AD of cyclooctane using  $[\text{IrH}_2(\text{O}_2\text{CCF}_2\text{CF}_3)(\text{PCy}_3)]$  as catalyst, which gave 36 turnovers to cyclooctene under reflux conditions (12). Stability of the applied homogeneous catalysts at higher temperatures, which is essential for these reactions, severely limited scope and efficiency. However, an efficient AD reaction was achieved by Xu *et al.* (13) using the Ir(PCP) pincer complex **1a** (Fig. 3A). Later, the sterically less-crowded complex **1b** developed by Liu and Goldman provided close to 1000 turnovers in AD of cyclooctane; linear alkanes were also dehydrogenated (14). The high thermal stability of pincer complexes, coupled with the effectiveness of iridium complexes in C–H activation, resulted in catalysts **1a** and **1b** being the most effective complexes for AD of alkanes.

### Alcohol Dehydrogenation

Traditionally, alcohol oxidations are primarily performed using toxic strong oxidants such as periodates or chromium oxides, which generate toxic stoichiometric waste (4, 6). Greener alternatives have also been developed (15). For example, a method of TEMPO-catalyzed dehydrogenation of alcohols with sodium hypochlorite has been developed and commonly used in both small- and large-scale applications (Fig. 3B). However, the method suffers from the need for a stoichiometric amount of sodium hypochlorite, the need for a cocatalyst [e.g., 10 mole percent (mol %) NaBr] in addition to the use of chlorinated solvents, and the equivalent amount of sodium chloride produced for every molecule of alcohol dehydrogenated (16). In contrast, several examples of oxidant-free catalytic AD of secondary alcohols to the corresponding ketones were reported (Fig. 3C) in which hydrogen gas is the only by-product. Early examples required the presence of an acid as a hydride ion acceptor (17–20). The ruthenium PNP [2,6-bis-(di-*tert*-butylphosphinomethyl)pyridine] pincer complex **2**, reported by our group, catalyzes the dehydrogenation of secondary alcohols using low catalyst loading, demonstrating the potential

of pincer complexes in the dehydrogenation of alcohols (21). However, complex **2** required activation by a base. The modified catalysts **3a** and **3b** can catalyze the reaction under neutral conditions using low loading of 0.1 mol % (22). The iridium complexes **4** (23) and **5** (24) also catalyze this reaction. The catalytic activity of **5** is comparable to that of ruthenium complex **3b**, whereas complex **4** shows higher efficiency. In addition to the synthetic potential, the dehydrogenation of secondary alcohols to ketones is also of interest from the point of view of hydrogen production from simple and biorenewable alcohols. Combining the ruthenium precursor  $[\text{RuH}_2(\text{CO})(\text{PPh}_3)_3]$  [used earlier for this reaction (20)] with PNP-type pincer ligands was shown to be highly effective in hydrogen production from *iso*-propanol (25).

AD of primary alcohols to yield the corresponding aldehydes (Fig. 3, D and E) is less common, as often ruthenium complexes are deactivated by decarbonylation of the aldehydes. Synthesis of aldehydes from alcohols was reported recently by Fujita and Yamaguchi (26) using the iridium catalyst **6a**. The modified water-soluble catalyst **6b** catalyzes the dehydrogenation of both secondary and primary alcohols in water. This catalyst family operates by a mechanism involving metal-ligand cooperation (27, 28).

### Dehydrogenative Coupling of Alcohols to Form Esters

Esterification is one of the most important fundamental reactions in synthetic organic chemistry, with applications in the production of an

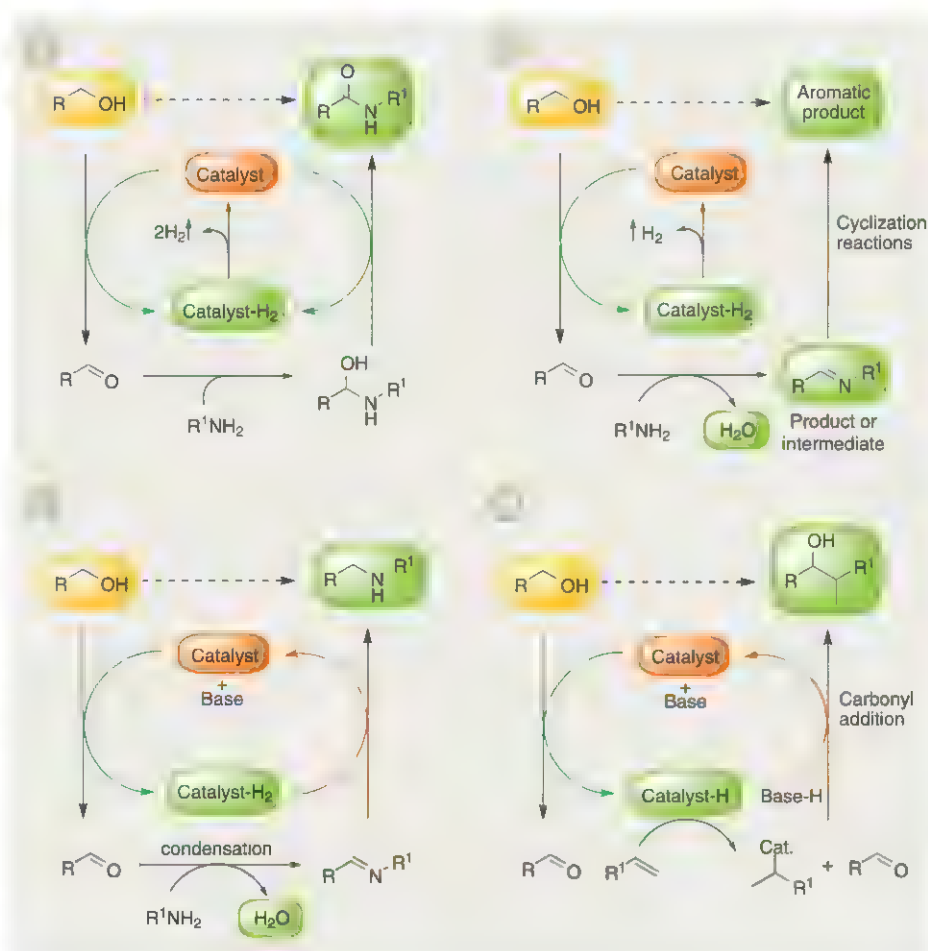


**Fig. 2. Dehydrogenation strategies in organic synthesis, exemplified by reactions of alcohols.** (A) Successive AD with release of hydrogen gas. The catalyst liberates  $\text{H}_2$  (the sole by-product) from both starting compound and intermediate generated by reaction with a nucleophilic substrate. "Catalyst- $\text{H}_2$ " indicates formal abstraction of two hydrogen atoms by the catalyst. (B) AD with hydrogen and water release. An intermediate formed by dehydrogenation of the starting compound can couple with nucleophiles; the resulting products can be isolated or can undergo further addition or cyclization reactions with or without further  $\text{H}_2$  liberation. (C) Borrowing hydrogen. The catalyst dehydrogenates the substrate at the outset and formally transfers the H atoms to an unsaturated intermediate. Hydrogen gas is not evolved, and the reaction often involves elimination of water as a by-product. (D) Coupling of redox pairs. The catalyst dehydrogenates the substrate to generate an electrophile and metal-hydride; addition of the latter to an unsaturated substrate forms a nucleophilic metal alkyl that reacts with the electrophile to form a C–C bond. Neither hydrogen gas nor water are produced.

assortment of fine chemicals ranging from fragrances to pharmaceuticals. Elaborating on the dehydrogenation of secondary alcohols catalyzed by complex **2**, rational design of the pincer complexes **7-9**, based on metal-ligand cooperation involving aromatization-dearomatization sequences of the pyridine-based ligand (see Fig. 5G), resulted in the direct catalytic dehydrogenative coupling of primary alcohols to esters with high

efficiency (Fig. 4A) (29). The aromatic, coordinatively saturated complexes **7** and **8** require the presence of a catalytic amount of a base, for in situ generation of the corresponding dearomatized complexes by deprotonation, which are the actual catalysts. Installing a hemilabile amine arm, which can play an important role in the catalytic cycle by opening a coordination site, resulted in precatalyst **8**. Treatment with a base

affords unsaturated, dearomatized complex **9**, an excellent catalyst for dehydrogenative coupling of alcohols to form esters with liberation of H<sub>2</sub> under neutral conditions. Only traces of aldehydes are formed.

This catalytic reaction provides an efficient, atom-economical, environmentally friendly pathway for the synthesis of esters. It can be carried out in a solvent or with neat liquid reagents. Previous examples of dehydrogenative coupling of alcohols to esters were considerably less efficient (30–32). Shvo's catalyst provided benzyl benzoate and pentyl pentanoate from the corresponding neat alcohols at 137° to 145°C, although yields and reaction times were not reported (31). Murahashi demonstrated dehydrogenative coupling of various alcohols to esters using RuH<sub>2</sub>(PPh<sub>3</sub>)<sub>3</sub> (2 mol %) in refluxing mesitylene (180°C) for 24 hours (32). The acridine catalyst **10** prepared by our group also catalyzes this transformation in the presence of a catalytic amount of base in refluxing solvent or under neat conditions (33). Complexes **3a** and **3b** (22), as well as the PNS [2-((tert-butylthio)methyl)-6-((di-tert-butylphosphino)methyl)pyridine] pincer ruthenium complex [(PNS)RuHCl(CO)] (34), analogous to complex **8**, and the iridium complex **5** (24) also catalyze the dehydrogenative esterification of alcohols. Catalytic conversion of ethanol, a bio-renewable alcohol, to ethyl acetate and molecular hydrogen is of particular interest because ethyl acetate is a widely used industrial bulk chemical. In this context, further fine-tuning of steric and electronic factors of the pincer backbone (35, 36) and screening of known pincer complexes (37) provided efficient catalysts.

Dehydrogenative cross-coupling of primary with secondary alcohols to form mixed esters was achieved for an assortment of primary and secondary alcohols, in a molar ratio of 1/2.5, using the bipyridine-based, dearomatized catalyst **12** (Fig. 4B) (38). In general, transesterification (ester to ester transformation) is not an atom-economical process, because it produces, in addition to the desired ester, an equivalent amount of alcohol. Our group has developed a distinct mode of transesterification, in which hydrogen gas is formed as a by-product, rather than alcohols, upon reaction of esters with secondary alcohols catalyzed by complex **9** (Fig. 4C). When symmetrical esters (i.e., having the same R groups) are used, both the acyl and alkoxy fragments of the substrate ester are incorporated into the product ester with liberation of hydrogen (39). This cross-selectivity is a result of slower dehydrogenation of the secondary alcohol to the corresponding ketone as compared with the dehydrogenative coupling of the primary alcohol to ester. Diols can undergo an intramolecular reaction to provide the corresponding lactones with hydrogen liberation (22) with complex **3b** as catalyst (Fig. 4D).

Currently practiced methods for the synthesis of polyesters are generally not atom-economical and not environmentally benign. They are normally

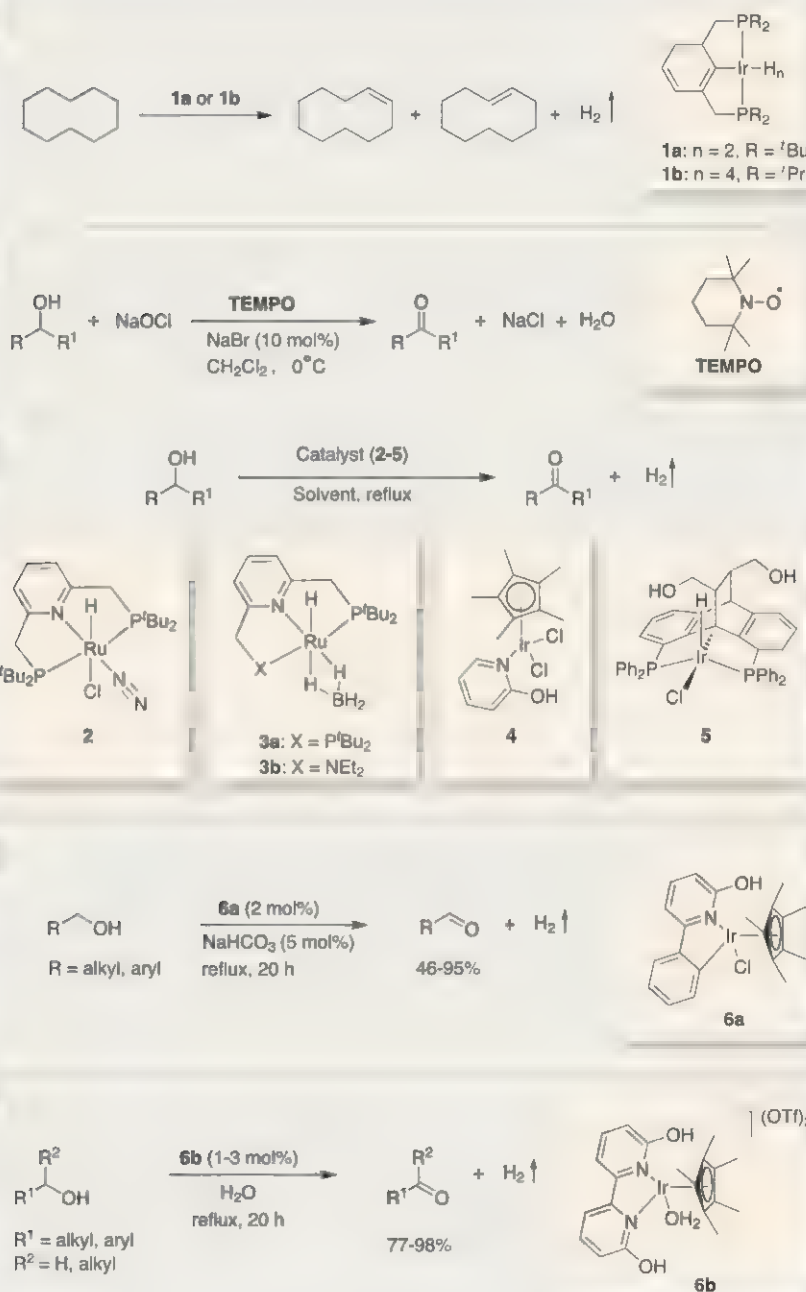


**Fig. 3. Examples of dehydrogenation.** (A) Dehydrogenation of an alkane catalyzed by iridium pincer complexes. (B) Dehydrogenation of primary and secondary alcohols by conventional oxidants. (C) Dehydrogenation of secondary alcohols by well-defined ruthenium and iridium complexes. (D and E) Dehydrogenation of primary alcohols. (D) Synthesis of aldehydes. (E) Synthesis of aldehydes and ketones in water solution.



based on carboxylic acid derivatives, prepared using toxic reagents and generating toxic by-products and salts; subsequent polycondensation with diols also generates salt waste, which can be challenging to remove from viscous polymer solutions, often resulting in low conversion and poor polymer properties. By using the in situ-generated complex **9** (from commercially available complex **8**) as a catalyst, Robertson and colleagues have demonstrated a remarkable process (40) for the synthesis of polyesters from diols (Fig. 4E). Efficient removal of the generated hydrogen was achieved by performing the polymerization reaction under reduced pressure, resulting in formation of high-molecular-weight polyesters.

Very recently, primary alcohols were oxidized by our group to the corresponding carboxylic acid salts using water as the terminal oxidant, with liberation of hydrogen (41). The precatalyst **11** was used for the in situ generation of catalyst **12** (Fig. 4F), which catalyzes this transformation under acceptorless conditions. Interestingly, water plays the role of both oxygen donor and reaction medium. Complex **9** is also known to stoichiometrically split water, by consecutive thermal H<sub>2</sub> and light-induced O<sub>2</sub> generation (42).

#### Dehydrogenative Coupling of Alcohols with Amines to Form Amides

Intermolecular dehydrogenative coupling of alcohols with amines is the most atom-economical method for amide synthesis (43). However, this catalytic reaction was difficult to envision, since hemiaminal formation was expected to follow alcohol dehydrogenation. Subsequent spontaneous water elimination would then form an imine that could undergo hydrogenation with the liberated H<sub>2</sub> to yield a secondary amine (from primary amine reagents). We discovered that this transformation (44) could indeed be catalyzed by the dearomatized pincer complex **9** (Fig. 5A). A range of alcohols reacted with alkyl and aryl amines and diamines to produce amides with liberation of hydrogen under low catalyst loading (0.1 mol %). Moreover, the reactions are selective toward the primary amine functionality under these conditions. Following this discovery, a number of catalytic systems were reported for this transformation with various ruthenium precursors in combination with carbene and/or phosphine ligands, although these systems required higher loading of metal complex and ligands in addition to the need for substoichiometric amounts of base; selected examples (45–47) are given in Fig. 5B.

Synthesis of amides from esters and amines is also a potentially attractive method. Complex **9** efficiently catalyzes this transformation (Fig. 5C) with liberation of H<sub>2</sub> under neutral conditions (48). Similar to the alcohol acylation process (Fig. 4C), both the acyl and alkoxo fragments of the symmetrical esters are incorporated in the amide product. One outcome of this reaction is

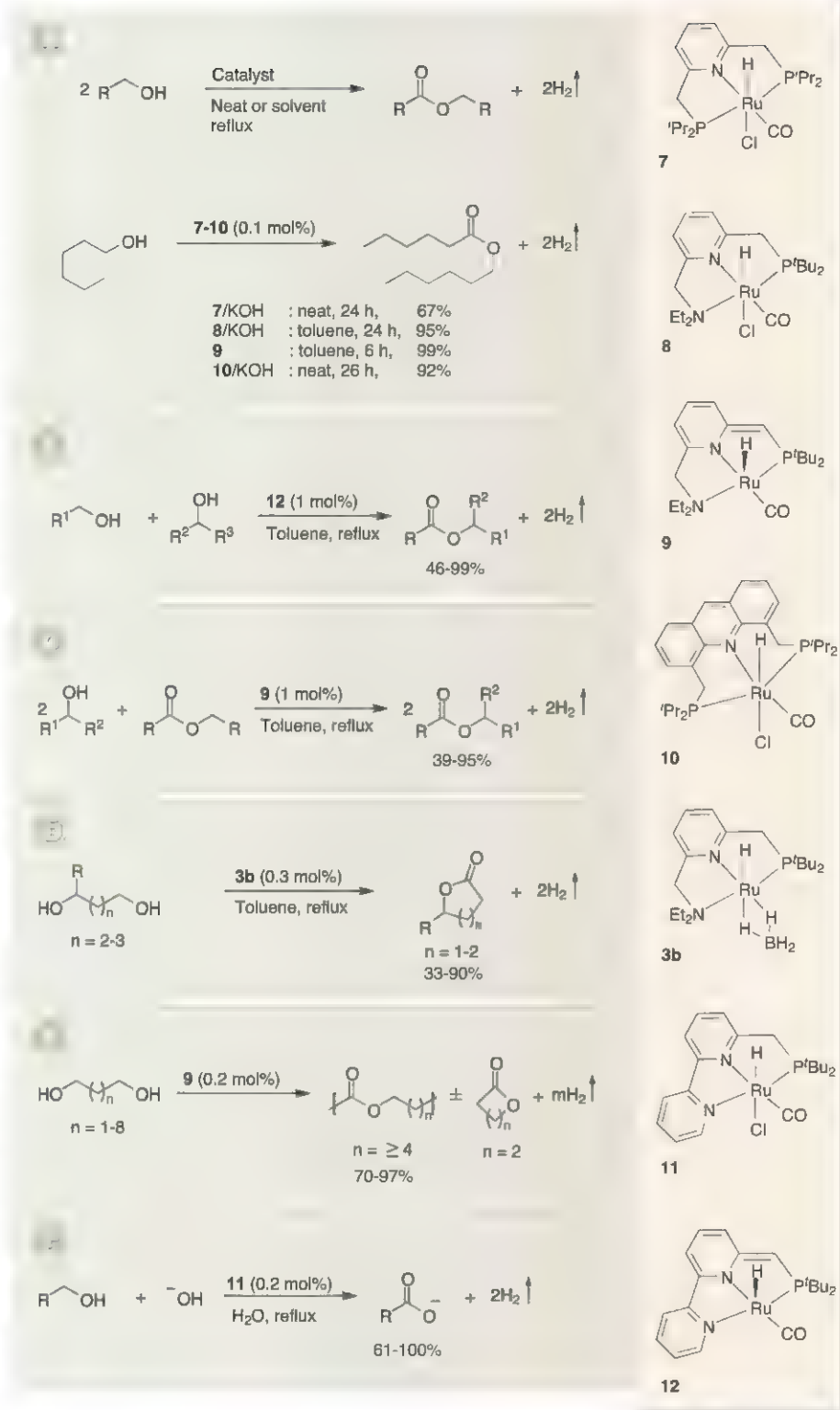


**Fig. 4. Direct synthesis of esters from alcohols.** (A) Synthesis of esters by dehydrogenative coupling of primary alcohols. These reactions are catalyzed by the rationally designed dearomatized, unsaturated PNN pincer complex **9**, and its precursor **8**, as well as the less reactive PNP complex **7**. (B to F) Application of alcohol dehydrogenative coupling reactions under acceptorless conditions. (B) Synthesis of esters from cross-coupled primary and secondary alcohols. (C) Synthesis of mixed esters by transesterification of esters using secondary alcohols. (D) Synthesis of lactones from diols. (E) Synthesis of polyesters from diols. (F) Synthesis of carboxylic acid salts from alcohols using water.

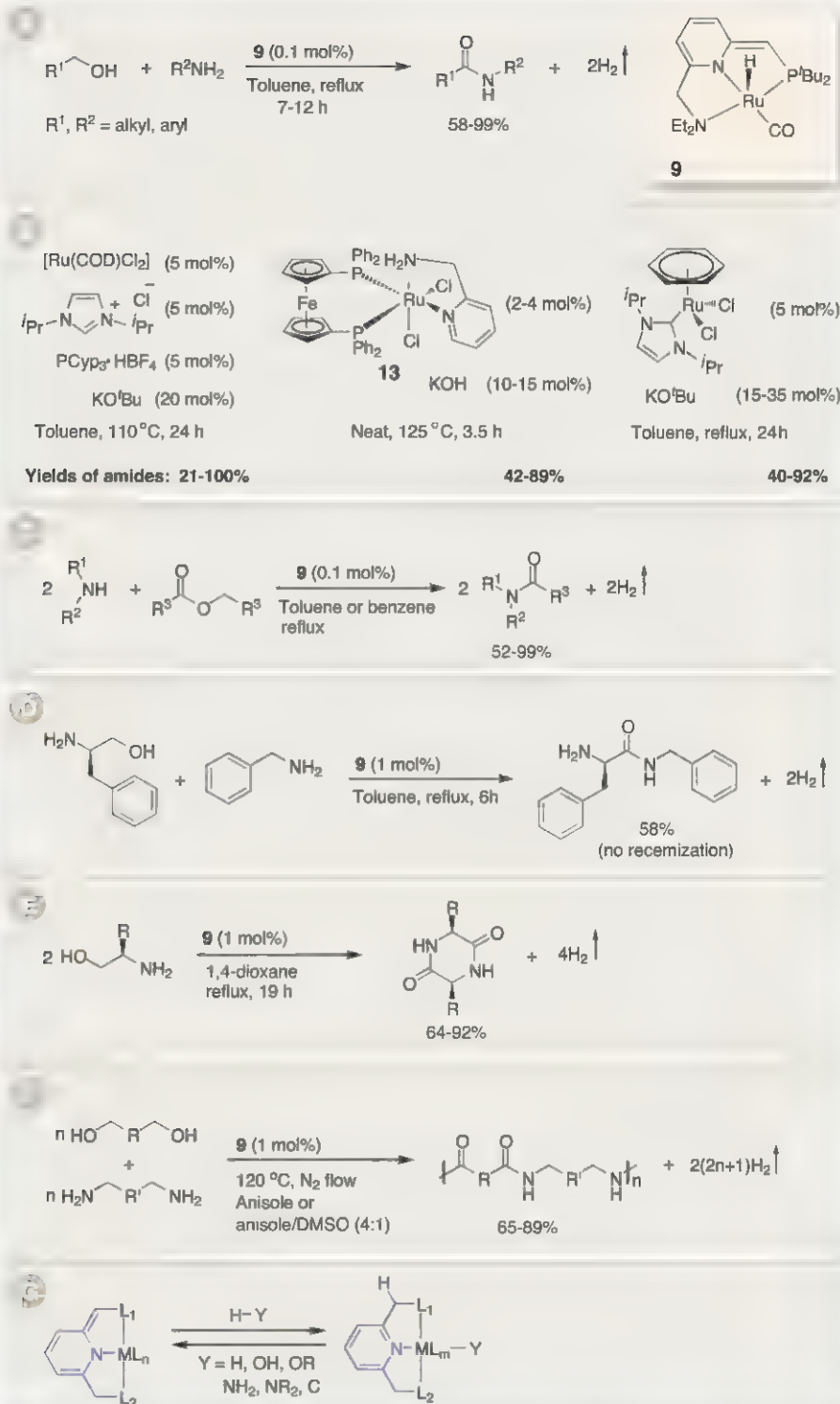


**Fig. 5. Direct synthesis of amides from alcohols and amines.** (A) Discovery of dehydrogenative coupling of alcohols with amines to form amides with liberation of hydrogen, catalyzed by the pincer complex **9**. (B) Selected examples of other catalytic systems developed later for the same transformation. (C to F) Applications of catalyst **9** in acceptorless dehydrogenative coupling processes involving amines. (C) Synthesis of amides from esters and amines. (D) Synthesis of a chiral amide from (S)-2-amino-3-phenylpropan-1-ol and benzylamine. (E) Synthesis of cyclic dipeptides from β-amino-alcohols. (F) Synthesis of polyamides from diols and diamines. (G) Metal-ligand cooperation by facile aromatization and dearomatization sequences (highlighted in blue). The dearomatized ligand participates in various bond activation and reversible bond-formation reactions and plays a key role in catalysis.

that ethyl acetate, a cheap and abundant ester, can be used as a convenient, atom-economical acetylation agent of amines, producing hydrogen as the only by-product; this is clearly advantageous over the commonly employed acetylation agents. Amino alcohols also participate in the acylation of amines. Gratifyingly, chiral amino-alcohols react with retention of configuration (Fig. 5D), a likely attribute of the neutral reaction conditions (49). As complex **9** catalyzes the amidation of amines using amino-alcohols, we reasoned that use of amino-alcohols alone might result in formation of linear or cyclic peptides. Indeed, complex **9** catalyzes the conversion of various amino-alcohols (bearing substituents larger than methyl α to the amine group) to the corresponding cyclic dipeptides (diketopiperazines) as the only products in very good yields with liberation of H<sub>2</sub> (Fig. 5E). In the case of alaninol, oligopeptides were formed. Using catalyst **9**, we have also developed the catalytic synthesis of polyamides (50) from diols and diamines. Before we published this work, Zeng and Guan reported (51) the direct polyamidation reaction using the now commercially available catalyst **9**. Optimization studies by them revealed the need for polar solvents for successful polymerization of diols and diamines, anisole being a suitable polar solvent, resulting in high number-average molecular weights (*M<sub>n</sub>*) of the polyamides (3.2 kD in toluene versus 13.8 kD in anisole). *M<sub>n</sub>* of the polyamides were further improved (22.6 kD) by the addition of small amounts of dimethyl sulfide. Polymers bearing secondary amine groups in the backbone, potentially useful for gene delivery, were obtained by Zeng and Guan (51), with no need for a wasteful protection-deprotection sequence, due to the selectivity of **9** toward the amidation of primary amine groups (Fig. 5F).

Ru-pincer complexes (**7** to **12**) developed by our group are believed to operate by a mode of metal-ligand cooperation (Fig. 5G) involving aromatization-dearomatization of the pincer ligand (52, 53). Dearomatized pincer complexes can activate primary alcohols, yielding the corresponding saturated hydrido alkoxo complexes, with aromatization. The mechanism of further dehydrogenation of the alkoxy ligand, which could follow β-hydride elimination, remains unclear at this stage (54). However, esterification and amidation reactions likely proceed through hemiacetal and hemiaminal intermediates, respectively, formed by nucleophilic attack by the alcohol or amine on an intermediate aldehyde that is either coordinated to the metal or free in solution (55, 56). Catalyst **9**, and its bipyridine analog **12**, also effectively catalyze under mild conditions the hydrogenolysis reactions of esters to alcohols (57), amides to alcohols and amines (58), and the hydrogenation of the CO<sub>2</sub>-derived organic carbonates and formates as mild, green, two-step routes to methanol (when dimethyl carbonate or methyl formate are used) (59). Methyl carbamates and urea derivatives were also hydrogenated to alcohols and amines under mild conditions (60). Density functional theory (DFT) calculations carried out by other groups on our



amidation reaction (55, 56) and on the microscopic reverse, hydrogenation of amides (61), further support the involvement of suggested intermediates.

### Dehydrogenative Coupling with Concomitant Condensation Reactions

The acridine pincer ruthenium catalyst **10** catalyzes the conversion of alcohols to acetals in very good yields, liberating hydrogen and water (Fig. 6A) (33, 62). The reaction proceeds via enol-ether intermediates, which upon further alcohol addition yield acetals. The recently developed ruthenium complex **14** also catalyzes this transformation (63).

The RuPNP pincer complex **15** catalyzes the dehydrogenative coupling of alcohols with amines, unexpectedly leading to imine products (Fig. 6B) rather than to amides, as catalyzed by the analogous RuPNN complex **9** [PNN is 2-(di-tert-butylphosphinomethyl)-6-diethylaminomethylpyridine] (64). It is possible that in the case of complex **15**, intermediate aldehyde dissociates from the metal complex, forming free hemiaminal in solution, whereas in the case of **9**, a coordinated aldehyde is attacked by the amine and no free hemiaminal is involved. The reason for the discrepancy might be a lack of the hemilabile amine "arm" and higher steric hindrance in **15**. The free hemiaminal eliminates water, providing a method for the synthesis of imines, with no subsequent hydrogenation to the corresponding amines. DFT calculations on imine formation catalyzed by **15** are in line with the observed selectivity (65). An analogous RuPNP catalyst with amine-based pincer "arms" (66), a Ru-carbene complex (67), and an OsPOP [POP is 4,6-bis(diisopropylphosphino)dibenzofuran] complex (68) were also later reported to catalyze this transformation. Using amino alcohols, complex **15** catalyzes formation of pyrazines (Fig. 6C). Apparently, the reaction proceeds through a cyclic diimine intermediate, which undergoes further dehydrogenation to provide the aromatic pyrazines (49). Dehydrogenative coupling of diols and amines can lead to pyrroles. Thus, reaction of 2,5-hexandiol and alkylamines catalyzed by complex **13** in the presence of sodium formate resulted in formation of *N*-alkyl-2,5-dimethylpyrroles in a dehydrogenative Paal-Knorr pyrrole synthesis (Fig. 6D) (46). Very recently, synthetic approaches to pyrroles were reported, based on alcohol dehydrogenation, imine formation, and base-promoted condensation. Thus,  $\text{Ru}_3(\text{CO})_{12}$  with an added diphosphine and a base catalyzes the reaction of 1,2 diols with amines and ketones, resulting in a variety of functionalized pyrroles (Fig. 6E) (69). The IrPNP complex **16**, developed by Michlik and Kempe, in the presence of base catalyzes the dehydrogenative coupling of  $\beta$ -amino-alcohols with secondary alcohols to form pyrroles; the proposed mechanism involves ketimine formation from the ketone and amino-alcohol, followed by Ir-catalyzed dehydrogenation and base-promoted condensation to result in elegant synthesis of pyrroles in very good yields with diverse substituents (Fig. 6F) (70). This reaction is also efficiently cat-

alyzed by the bipyridine-based RuPNN complex **11**, following a similar mechanism, as reported by our group very recently (71).

### Alkane Metathesis

Combining alkane dehydrogenation and the borrowing approach, Goldman, Brookhart and co-workers achieved alkane metathesis in a three-step tandem sequence using two different catalysts (72). The iridium complex (**17**) dehydrogenates alkanes in the first step to produce the respective alkenes, which are converted into either longer or shorter alkenes by the Mo-based Schrock metathesis

catalyst (**18**) in the second step. The hydrogen obtained in the first step hydrogenates the alkenes, thus providing a near thermodynamically neutral process (Fig. 7). Although the terminal alkene is the kinetic dehydrogenation product, isomerization of the double bond along the chain and then cross metathesis of the isomerized products lead to a broad distribution of hydrocarbons.

### Alkylation of Amines by Borrowing Hydrogen Methodology

The limited reactivity of alcohols toward nucleophiles can be readily overcome upon de-

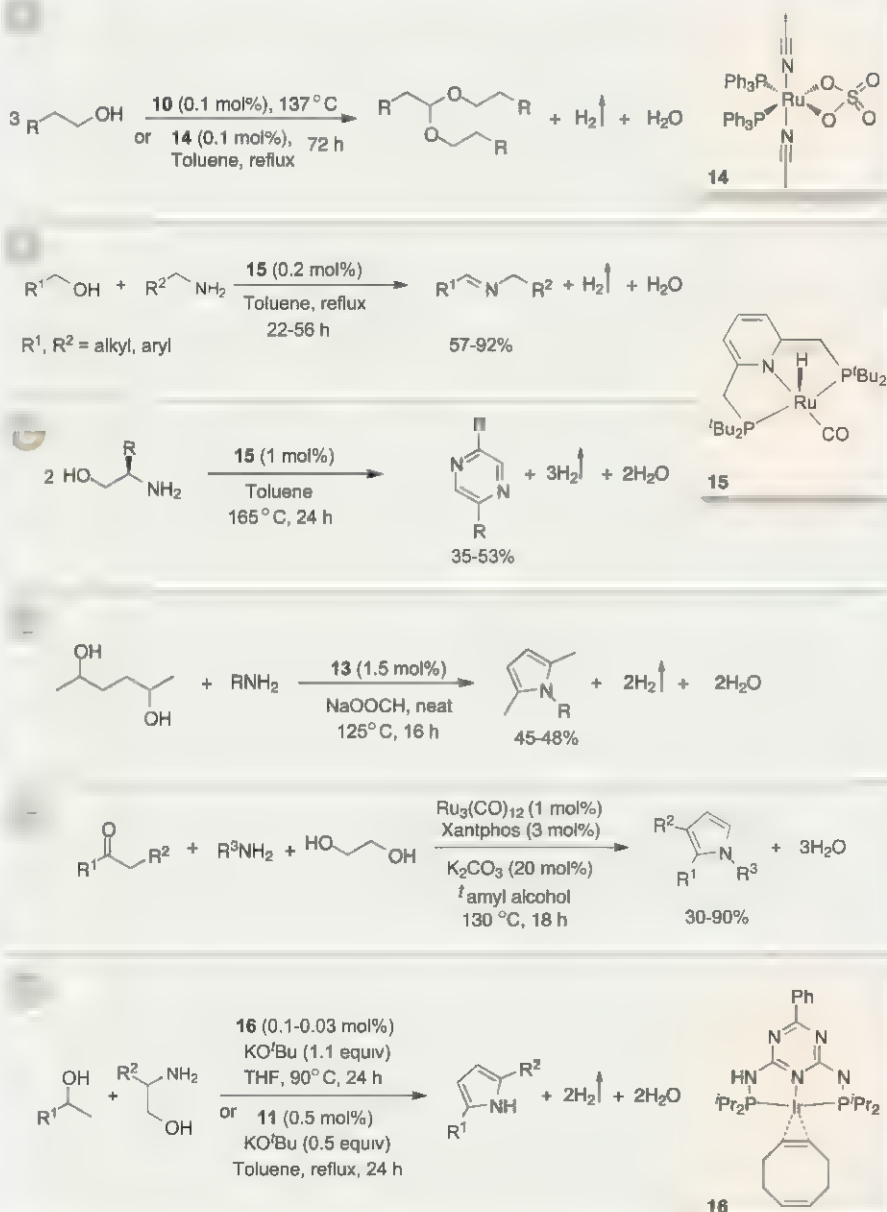


**Fig. 6. Acceptorless dehydrogenative coupling reactions that proceed with loss of water. (A)** Direct synthesis of acetals from alcohols. **(B)** Synthesis of imines from alcohols and amines. **(C)** Synthesis of pyrazines from amino-alcohols. **(D)** Synthesis of pyrroles from diols and amines. **(E)** Three-component synthesis of pyrroles. **(F)** Synthesis of pyrroles from alcohols and amino-alcohols.

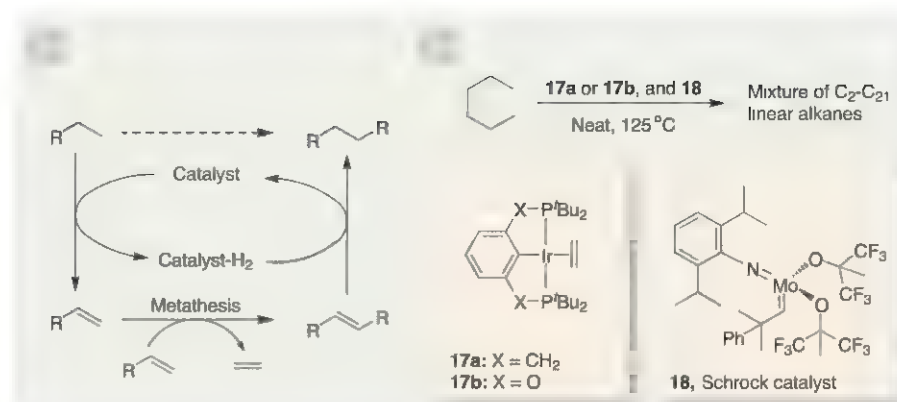


**Fig. 7. Alkane metathesis via borrowing methodology.** (A) General strategy. Catalytic C–H activation is coupled with catalytic olefin metathesis for net alkane metathesis. (B) Metathesis of *n*-hexane by **17a** or **17b** and **18**.

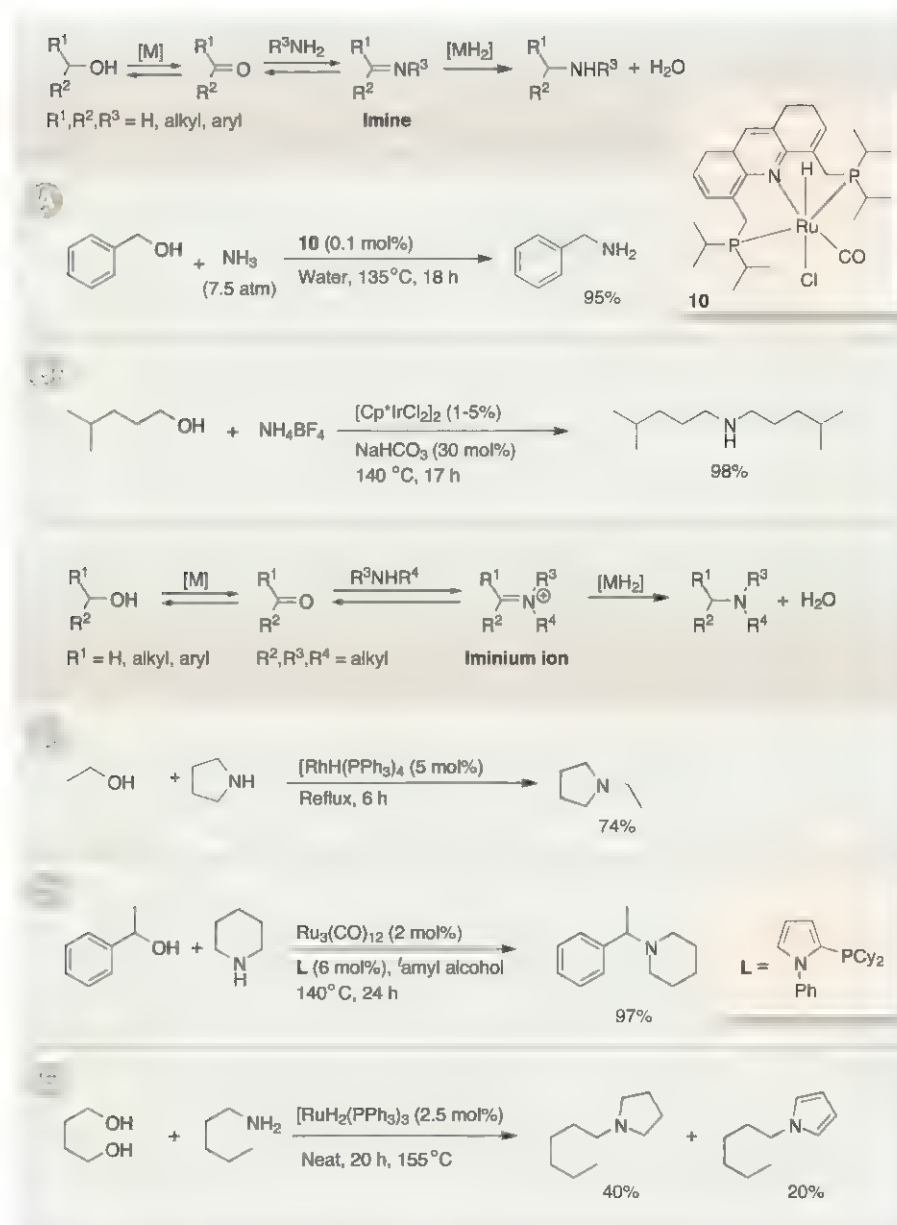


**Fig. 8. Alkylation of amines using alcohols.** Products targeted include (A) primary amines, (B) secondary amines, (C and D) tertiary amines, and (E) heterocycles, all with very good selectivities.

hydrogenation to the corresponding carbonyl compounds, which are amenable to nucleophilic addition reactions (Fig. 2) (73). Nitrogen-containing compounds, ranging from primary amines to heterocycles, were obtained using the metal-catalyzed, alcohol-borrowing hydrogen pathway (Fig. 8) (74). In pioneering work, Gnngg *et al.* reported that [RhH(PPh<sub>3</sub>)<sub>4</sub>] catalyzed N-alkylation of amines by alcohols (Fig. 8C) (75). Murahashi *et al.* and Tsuji *et al.* reported catalysis by ruthenium complexes for the preparation of a range of secondary and tertiary amines (76), including indoles (Fig. 8E) (77). Selective synthesis of primary amines from ammonia and electrophiles is a challenging task, because the primary amine intermediate is more nucleophilic than ammonia, and it undergoes competing alkylation reactions when conventional alkylating reagents such as alkyl halides are used, resulting in a mixture of products. Alkylation of amines by the borrowing hydrogen pathway can circumvent this problem, and selectivity could be reached by a suitable choice of ligands and catalyst design. For example, primary amines were selectively synthesized by our group from primary alcohols and ammonia, using the acridine-derived ruthenium pincer complex **10** under mild conditions and low catalyst loading (Fig. 8A); selectivity in this case is enhanced by the steric bulk around the metal center, lending preference to ammonia coordination. Reactions can also be performed using water as reaction medium, resulting in enhanced selectivity (78). Recently, **10** was also used as a catalyst for the preparation of diamines from the diols derived from vegetable oils (79). Secondary alcohols could also be employed using different ligands and metal precursors (80, 81). Secondary and tertiary amines were selectively obtained from ammonium salts (Fig. 8B) and primary alcohols using an iridium complex by Fujita and colleagues (82, 83) and Eary and Clausen (84). Beller and co-workers developed phosphine ligands that, in combination with Ru(0), were effective catalysts for the synthesis of tertiary amines (Fig. 8D) (85). In general, ruthenium and iridium complexes were found to be good catalysts for alkylation of amines as well as amides (86). Whereas reaction of ammonia and primary amines with carbonyl compounds proceeds by imine intermediates, use of secondary amines leads to the formation of iminium ion intermediate. Both imine and iminium ion intermediates are hydrogenated by the catalyst using the hydrogen obtained from starting alcohols to deliver the primary or secondary and tertiary amines, respectively.

Williams and co-workers have demonstrated that borrowing hydrogen tactics can be applied in alkylation processes often used in the synthesis of drugs (Fig. 9A); on the laboratory scale, they obtained various pharmaceuticals employing alcohols in place of conventional alkyl halides (87). Berliner reported the synthesis of PF 03463275, a GlyT1 inhibitor developed for the treatment of schizophrenia, by applying the borrowing-



hydrogen methodology on a multikilogram scale (88), with  $(\text{Cp}^*\text{IrCl}_2)_2$  as catalyst (Fig. 9B). The strategic advantage of the borrowing hydrogen methodology was also applied in the synthesis of natural products such as noranabasamine (89), isolated from the dart frog (Fig. 9C). A combination of  $\text{RuH}_2(\text{CO})(\text{PPh}_3)_3$  and xantphos ligand was used by Beller and co-workers for the selective diamination of isosorbide, which is obtained from D-glucose (81). The versatility of the alkylation of amines by borrowing-hydrogen methodology allowed the preparation of primary, secondary, and tertiary amines from alcohols, including biomass-derived alcohols (3, 85). Because the methodology is already being adopted in large-scale synthesis and tolerates various functional groups, it is well on its way to displacing the conventional alkylation reactions in organic synthesis that rely on alkyl halides.

### Alcohols as a Source of Electrophiles and Nucleophiles

Construction of C–C bonds through the borrowing-hydrogen concept has been achieved using two different approaches, in which the alcohols are modified to manifest either electrophilic or nucleophilic reactivity. Upon alcohol dehydrogenation, the generated carbonyl compounds can act as electrophiles and undergo coupling reactions with nucleophiles to generate unsaturated intermediates; further hydrogenation by using hydrogen borrowed from the alcohols in the first step provides the product of the net redox-neutral tandem process (Fig. 10A). In contrast, dehydrogenation of secondary alcohols in the presence of a base can turn the resulting electrophilic carbonyl compounds into nucleophilic enolates, which can react with electrophiles through the  $\beta$ -carbon center (Fig. 10B). Like amine alkylation by borrowing-hydrogen methods (C–N bond formation), several different types of carbon nucleophiles can be used for C–C bond formation by this strategy. Grigg reported early examples of C–C bond formation through borrowing hydrogen in which aryl acetonitriles were alkylated by primary alcohols using ruthenium and rhodium catalysts and a stoichiometric base (90); other metal catalysts and nucleophiles were employed later (91). Williams and co-workers devised efficient alkylation methods of carbon nucleophiles catalyzed by ruthenium and iridium complexes using low catalyst loading. For example, an active methylene compound was alkylated (92) by benzyl alcohol using  $\text{RuH}_2(\text{CO})(\text{PPh}_3)_3$  and xantphos ligand in very good yield (Fig. 10C). Recently, oxindole was also alkylated by the borrowing-hydrogen method (93). Use of  $[\text{Ir}(\text{cod})\text{Cl}]_2 + \text{PPh}_3$  allowed Obora and Ishii to perform such reactions without an additional base at elevated temperature (94). The borrowing-hydrogen approach can also be applied to the Wittig reaction in which the alcohol functions as a surrogate to aldehydes (Fig. 10D) (95). Amine products can also be obtained from the aza-Wittig reaction (96).

$\beta$ -alkylation of alcohols was achieved using iridium and ruthenium catalysts (Fig. 10, E and F) (97, 98). In addition, upon dehydrogenation, amines can also give rise to electrophilic reactivity and can undergo self-coupling or coupling reactions with other amines (74).

Unlike the borrowing-hydrogen strategies described in Fig. 10, A and B, C–C coupling can also be achieved without using preformed nucleophiles. Bower and Krische developed reactions that involve alcohols and partially unsaturated substrates such as alkenes, dienes, alkynes, and allenes (99), which result in products of formal alcohol  $\alpha$ -C–H functionalization (Fig. 2D). This strategy involves alcohol dehydrogenation to generate a metal-hydride intermediate that adds to the unsaturated substrate, generating a nucleophilic intermediate capable of aldehyde addition

reactions. Very recently, Krische and co-workers also uncovered an alternative mechanism for such C–C bond formation (100). Excellent stereoselectivities were achieved in several transformations; for example, a catalyst generated in situ from  $\text{RuH}_2(\text{CO})(\text{PPh}_3)_3$ , a diphosphine and a chiral acid catalyzes *anti*-diastereoselective and enantioselective C–H crotylation of primary alcohols (Fig. 10G) (101).

### Outlook

AD is a rapidly growing area, propelled by the profound influence of fundamental organometallic chemistry, in part based on metal-ligand cooperation. This has led to reactions such as the dehydrogenative coupling of amines with alcohols to form amides, peptides, and polyamides under neutral conditions with liberation of hy-

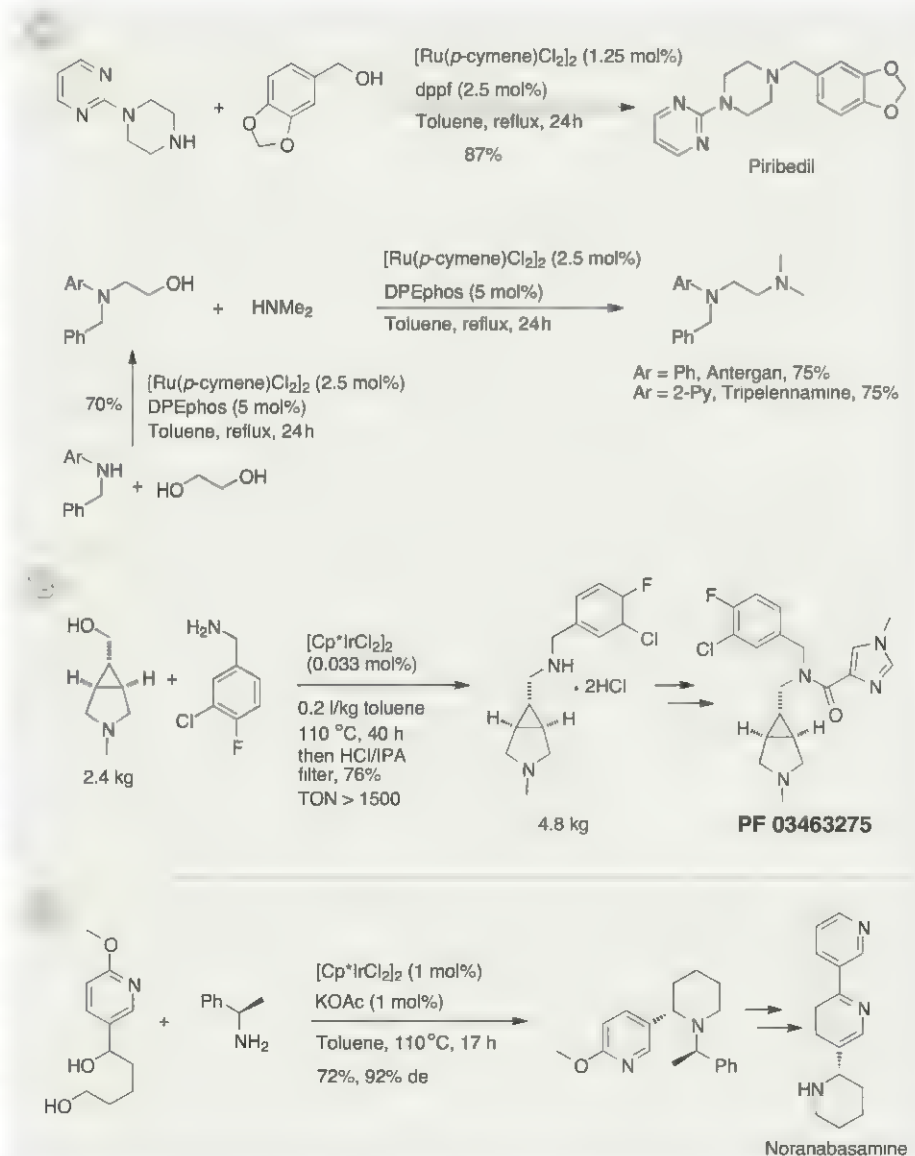


**Fig. 9. Application of the borrowing hydrogen methodology. (A)** Laboratory synthesis of various pharmaceuticals. **(B)** Demonstration on multi-Kg scale. **(C)** Application in total synthesis of a natural product.

drogen gas and no waste generation. The related dehydrogenation reactions that do not evolve hydrogen gas—namely the borrowing-hydrogen methodology and the coupling of redox pairs via intermediate generation of nucleophiles and electrophiles—allow construction of both C–N and C–C bonds from alcohols and provide efficient, atom-economical access to an assortment of

useful products. The strides made thus far exemplify the power of dehydrogenation as an activation tactic by generation of more reactive unsaturated intermediate compounds, which can then couple in situ with other substrates and provide effective catalytic processes under mild, environmentally benign conditions. As AD is increasingly applied in transformations of complex and bio-

renewable molecules, we feel that many additional useful applications are bound to unfold.

## References and Notes

- G. E. Döbereiner, R. H. Crabtree, Dehydrogenation as a substrate-activating strategy in homogeneous transition-metal catalysis. *Chem. Rev.* **110**, 681–703 (2010). doi: 10.1021/cr900202j
- J. Choi, A. H. MacArthur, M. Brookhart, A. S. Goldman, Dehydrogenation and related reactions catalyzed by iridium pincer complexes. *Chem. Rev.* **111**, 1761–1779 (2011). doi: 10.1021/cr1003503
- A. C. Marr, Organometallic hydrogen transfer and dehydrogenation catalysts for the conversion of bio-renewable alcohols. *Catal. Sci. Technol.* **2**, 279 (2012). doi: 10.1039/c1cy00338k
- J. Muzart, Chromium-catalyzed oxidations in organic synthesis. *Chem. Rev.* **92**, 113–140 (1992). doi: 10.1021/cr0009a005
- T. Punniyamurthy, S. Velusamy, J. Iqbal, Recent advances in transition metal catalyzed oxidation of organic substrates with molecular oxygen. *Chem. Rev.* **105**, 2329–2364 (2005). doi: 10.1021/cr050523v
- G. Tojo, M. Fernández, *Oxidation of Alcohols to Aldehydes and Ketones: A Guide to Current Common Practice* (Springer Science, New York, 2007).
- M. C. R. Guerbet, *Acad. Sci. Paris* **128**, 1002 (1899).
- R. V. Oppenauer, Eine methode der dehydrierung von sekundären alkoholen zu ketonen. I. Zur herstellung von sterinketonen und sexualhormonen. *Recl. Trav. Chim. Pays Bas* **56**, 137–144 (1937). doi: 10.1002/recl.19370560206
- R. H. Crabtree, J. M. Mihelcic, J. M. Quirk, Iridium complexes in alkane dehydrogenation. *J. Am. Chem. Soc.* **101**, 7738–7740 (1979). doi: 10.1021/ja00520a030
- D. Baudry, M. Ephritikhine, H. Felkin, R. Holmes-Smith, The selective catalytic conversion of cycloalkanes into cycloalkenes using a soluble rhenium polyhydride system. *J. Chem. Soc. Chem. Commun.* **1983**, 788 (1983). doi: 10.1039/c39830000788
- M. J. Burk, R. H. Crabtree, C. P. Parnell, R. J. Uriarte, Selective stoichiometric and catalytic carbon-hydrogen bond cleavage reactions in hydrocarbons by iridium complexes. *Organometallics* **3**, 816–817 (1984). doi: 10.1021/om00083a034
- T. Aoki, R. H. Crabtree, Homogeneous tungsten, rhenium, and iridium catalysts in alkane dehydrogenation driven by reflux of substrate or of cosolvent or by inert-gas flow. *Organometallics* **12**, 294–298 (1993). doi: 10.1021/om00026a013
- W. Xu *et al.*, Thermochemical alkane dehydrogenation catalyzed in solution without the use of a hydrogen acceptor. *Chem. Commun. (Camb.)* **1997**, 2273–2274 (1997). doi: 10.1039/a705105k
- F. Liu, A. S. Goldman, Efficient thermochemical alkane dehydrogenation and isomerization catalyzed by an iridium pincer complex. *Chem. Commun. (Camb.)* **1999**, 655–656 (1999). doi: 10.1039/a900631a
- L. Que Jr., W. B. Tolman, Biologically inspired oxidation catalysis. *Nature* **455**, 333–340 (2008). doi: 10.1038/nature07371
- R. A. Sheldon, I. W. C. E. Arends, G. J. Ten Brink, A. Dijkman, Green, catalytic oxidations of alcohols. *Acc. Chem. Res.* **35**, 774–781 (2002). doi: 10.1021/ar010075n
- H. B. Charman, Hydride transfer reactions catalysed by rhodium-tin complexes. *J. Chem. Soc. B* **1970**, 584 (1970). doi: 10.1039/j2970000584
- A. Dobson, S. D. Robinson, Catalytic dehydrogenation of primary and secondary alcohols by Ru(OCCF<sub>3</sub>)<sub>2</sub>(CO)(PPh<sub>3</sub>)<sub>2</sub>. *J. Organomet. Chem.* **87**, C52 (1975). doi: 10.1016/S0022-328X(00)88159-0

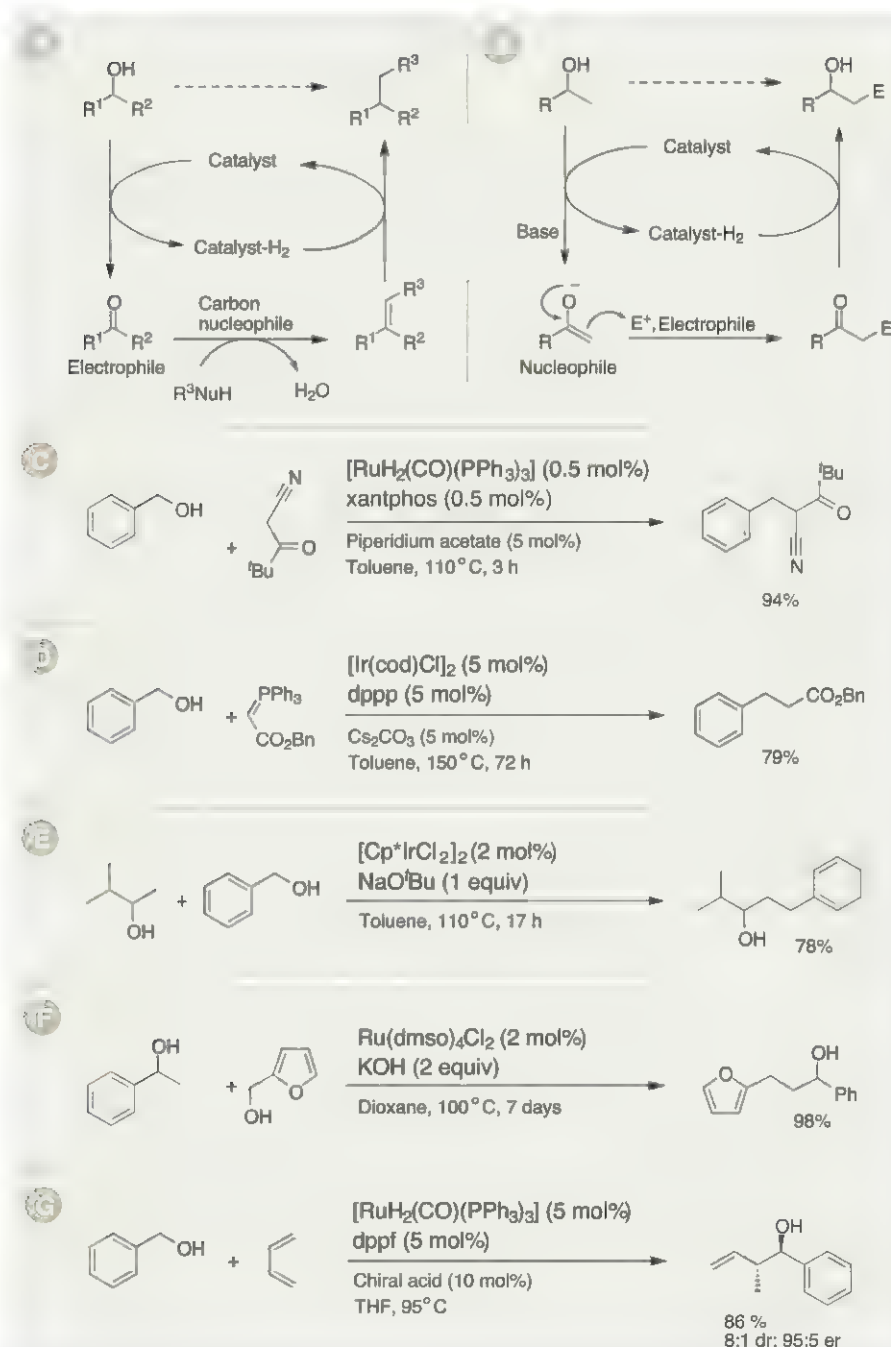


**Fig. 10. C–C bond formation using alcohols as sources of electrophiles and nucleophiles. (A)** Borrowing hydrogen strategy for C–C bond formation, in which the alcohol transformed into an electrophilic intermediate. **(B)** Borrowing hydrogen strategy for β-alkylation, in which the alcohol is transformed into a nucleophilic intermediate. **(C and D)** Typical examples of the strategy shown in (A). **(E and F)** Typical examples of the strategy shown in (B). **(G)** A nucleophilic intermediate is generated from the alkene: enantioselective C–H functionalization of primary alcohols.



19. D. Morton, D. J. Cole-Hamilton, Rapid thermal hydrogen production from alcohols catalysed by [Rh(2,2'-bipyridyl)<sub>2</sub>]Cl. *J. Chem. Soc. Chem. Commun.* **1987**, 248 (1987). doi: 10.1039/c39870000248
20. G. B. W. L. Ligthart *et al.*, Highly sustainable catalytic dehydrogenation of alcohols with evolution of hydrogen gas. *Tetrahedron Lett.* **44**, 1507–1509 (2003). doi: 10.1016/S0040-4039(02)02842-3
21. J. Zhang, M. Gandelman, L. J. W. Shimon, H. Rozenberg, D. Milstein, Electron rich, bulky ruthenium PNP-type complexes: Acceptorless catalytic alcohol dehydrogenation. *Organometallics* **23**, 4026–4033 (2004). doi: 10.1021/om049716j
22. J. Zhang, E. Balaraman, G. Leituss, D. Milstein, Electron-rich PNP- and PNN-type ruthenium(II) hydride borohydride pincer complexes: Synthesis, structure, and catalytic dehydrogenation of alcohols and hydrogenation of esters. *Organometallics* **30**, 5716–5724 (2011). doi: 10.1021/om200595m
23. K. Fujita, N. Tanino, R. Yamaguchi, Ligand-promoted dehydrogenation of alcohols catalyzed by Cp\*Ir complexes: A new catalytic system for oxidant-free oxidation of alcohols. *Org. Lett.* **9**, 109–111 www.ncbi.nlm.nih.gov/entrez/query.fcgi?cmd=Retrieve&db=PubMed&list\_uids=17192097&dopt=Abstract (2007). doi: 10.1021/ol062806v
24. S. Musa, I. Shaposhnikov, S. Cohen, D. Gelman, Ligand-metal cooperation in PCP pincer complexes: rational design and catalytic activity in acceptorless dehydrogenation of alcohols. *Angew. Chem. Int. Ed.* **50**, 3533–3537 www.ncbi.nlm.nih.gov/entrez/query.fcgi?cmd=Retrieve&db=PubMed&list\_uids=21412960&dopt=Abstract (2011). doi: 10.1002/anie.2011007367
25. M. Nielsen *et al.*, Efficient hydrogen production from alcohols under mild reaction conditions. *Angew. Chem. Int. Ed.* **50**, 9593–9597 www.ncbi.nlm.nih.gov/entrez/query.fcgi?cmd=Retrieve&db=PubMed&list\_uids=21948701&dopt=Abstract (2011). doi: 10.1002/anie.201104722
26. K. Fujita, T. Yoshida, Y. Imori, R. Yamaguchi, Dehydrogenative oxidation of primary and secondary alcohols catalyzed by a Cp\*Ir complex having a functional C,N-chelate ligand. *Org. Lett.* **13**, 2278–2281 www.ncbi.nlm.nih.gov/entrez/query.fcgi?cmd=Retrieve&db=PubMed&list\_uids=21473566&dopt=Abstract (2011). doi: 10.1021/ol2005424
27. R. Kawahara, K. Fujita, R. Yamaguchi, Dehydrogenative oxidation of alcohols in aqueous media using water-soluble and reusable Cp\*Ir catalysts bearing a functional bipyridine ligand. *J. Am. Chem. Soc.* **134**, 3643–3646 www.ncbi.nlm.nih.gov/entrez/query.fcgi?cmd=Retrieve&db=PubMed&list\_uids=22339738&dopt=Abstract (2012). doi: 10.1021/ja210857z
28. Y. Maenaka, T. Suenobu, S. Fukuzumi, Hydrogen evolution from aliphatic alcohols and 1,4-selective hydrogenation of NAD<sup>+</sup> catalyzed by a [C,N] and a [C,C] cyclometalated organoiridium complex at room temperature in water. *J. Am. Chem. Soc.* **134**, 9417–9427 www.ncbi.nlm.nih.gov/entrez/query.fcgi?cmd=Retrieve&db=PubMed&list\_uids=22577897&dopt=Abstract (2012). doi: 10.1021/ja302788c
29. J. Zhang, G. Leituss, Y. Ben-David, D. Milstein, Facile conversion of alcohols into esters and dihydrogen catalyzed by new ruthenium complexes. *J. Am. Chem. Soc.* **127**, 10840–10841 www.ncbi.nlm.nih.gov/entrez/query.fcgi?cmd=Retrieve&db=PubMed&list\_uids=16076184&dopt=Abstract (2005). doi: 10.1021/ja052862b
30. S.-I. Murahashi, K. Ito, T. Naota, Y. Maeda, Ruthenium catalyzed transformation of alcohols to esters and lactones. *Tetrahedron Lett.* **22**, 5327–5330 (1981). doi: 10.1016/S0040-4039(01)92493-1
31. Y. Blum, Y. Shvo, Catalytically reactive ( $\eta^4$ -tetracyclone) (CO)<sub>2</sub>(H)<sub>2</sub>Ru and related complexes in dehydrogenation of alcohols to esters. *J. Organomet. Chem.* **282**, C7–C10 (1985). doi: 10.1016/0022-328X(85)87154-0
32. S.-I. Murahashi, T. Naota, K. Ito, Y. Maeda, H. Taki, Ruthenium-catalyzed oxidative transformation of alcohols and aldehydes to esters and lactones. *J. Org. Chem.* **52**, 4319–4327 (1987). doi: 10.1021/jo00228a032
33. C. Gunanathan, L. J. W. Shimon, D. Milstein, Direct conversion of alcohols to acetals and H<sub>2</sub> catalyzed by an acridine-based ruthenium pincer complex. *J. Am. Chem. Soc.* **131**, 3146–3147 www.ncbi.nlm.nih.gov/entrez/query.fcgi?cmd=Retrieve&db=PubMed&list\_uids=19216551&dopt=Abstract (2009). doi: 10.1021/ja808893g
34. M. Gargir *et al.*, PNN-type ruthenium pincer complexes. *Organometallics* **31**, 6207–6214 (2012). doi: 10.1021/om300516j
35. D. Spasyuk, S. Smith, D. G. Gusev, From esters to alcohols and back with ruthenium and osmium catalysts. *Angew. Chem. Int. Ed.* **51**, 2772–2775 www.ncbi.nlm.nih.gov/entrez/query.fcgi?cmd=Retrieve&db=PubMed&list\_uids=22319022&dopt=Abstract (2012). doi: 10.1002/anie.201108956
36. D. Spasyuk, D. G. Gusev, Acceptorless dehydrogenative coupling of ethanol and hydrogenation of esters and imines. *Organometallics* **31**, 5239–5242 (2012). doi: 10.1021/om300670r
37. M. Nielsen, L. Junge, A. Kammer, M. Beller, Towards a green process for bulk-scale synthesis of ethyl acetate: Efficient acceptorless dehydrogenation of ethanol. *Angew. Chem. Int. Ed.* **51**, 5711–5713 www.ncbi.nlm.nih.gov/entrez/query.fcgi?cmd=Retrieve&db=PubMed&list\_uids=22517628&dopt=Abstract (2012). doi: 10.1002/anie.201200625
38. D. Srinani, E. Balaraman, B. Gnanaprakasam, Y. Ben-David, D. Milstein, Ruthenium pincer-catalyzed cross-dehydrogenative coupling of primary alcohols with secondary alcohols under neutral conditions. *Adv. Synth. Catal.* **354**, 2403–2406 (2012). doi: 10.1002/adsc.201200438
39. B. Gnanaprakasam, Y. Ben-David, D. Milstein, Ruthenium pincer-catalyzed acylation of alcohols using esters with liberation of hydrogen under neutral conditions. *Adv. Synth. Catal.* **352**, 3169–3173 (2010). doi: 10.1002/adsc.201000663
40. D. M. Hunsicker, B. C. Dauphinais, S. P. Mc Ilraith, N. J. Robertson, Synthesis of high molecular weight polyesters via in vacuo dehydrogenative polymerization of diols. *Macromol. Rapid Commun.* **33**, 232–236 www.ncbi.nlm.nih.gov/entrez/query.fcgi?cmd=Retrieve&db=PubMed&list\_uids=22173989&dopt=Abstract (2012). doi: 10.1002/marc.201100653
41. E. Balaraman, E. Khaskin, G. Leituss, D. Milstein, Catalytic transformation of alcohols to carboxylic acid salts and H<sub>2</sub> using water as the oxygen atom source. *Nat. Chem.* **5**, 122–125 www.ncbi.nlm.nih.gov/entrez/query.fcgi?cmd=Retrieve&db=PubMed&list\_uids=23344447&dopt=Abstract (2013). doi: 10.1038/nchem.1536
42. S. W. Kohl *et al.*, Consecutive thermal H<sub>2</sub> and light-induced O<sub>2</sub> evolution from water promoted by a metal complex. *Science* **324**, 74–77 www.ncbi.nlm.nih.gov/entrez/query.fcgi?cmd=Retrieve&db=PubMed&list\_uids=19342584&dopt=Abstract (2009). doi: 10.1126/science.1168600
43. V. R. Pattabiraman, J. W. Bode, Rethinking amide bond synthesis. *Nature* **480**, 471–479 www.ncbi.nlm.nih.gov/entrez/query.fcgi?cmd=Retrieve&db=PubMed&list\_uids=22193101&dopt=Abstract (2011). doi: 10.1038/nature10702
44. C. Gunanathan, Y. Ben-David, D. Milstein, Direct synthesis of amides from alcohols and amines with liberation of H<sub>2</sub>. *Science* **317**, 790–792 www.ncbi.nlm.nih.gov/entrez/query.fcgi?cmd=Retrieve&db=PubMed&list\_uids=17690291&dopt=Abstract (2007). doi: 10.1126/science.1145295
45. L. U. Nordström, H. Vogt, R. Madsen, Amide synthesis from alcohols and amines by the extrusion of dihydrogen. *J. Am. Chem. Soc.* **130**, 17672–17673 www.ncbi.nlm.nih.gov/entrez/query.fcgi?cmd=Retrieve&db=PubMed&list\_uids=19061316&dopt=Abstract (2008). doi: 10.1021/ja808129p
46. N. D. Schley, G. E. Döbereiner, R. H. Crabtree, Oxidative synthesis of amides and pyrroles via dehydrogenative alcohol oxidation by ruthenium diphosphine diamine complexes. *Organometallics* **30**, 4174–4179 (2011). doi: 10.1021/om2004755
47. C. Chen, Y. Zhang, S. H. Hong, N-heterocyclic carbene based ruthenium-catalyzed direct amide synthesis from alcohols and secondary amines: Involvement of esters. *J. Org. Chem.* **76**, 10005–10010 www.ncbi.nlm.nih.gov/entrez/query.fcgi?cmd=Retrieve&db=PubMed&list\_uids=22084902&dopt=Abstract (2011). doi: 10.1021/jo201756z
48. B. Gnanaprakasam, D. Milstein, Synthesis of amides from esters and amines with liberation of H<sub>2</sub> under neutral conditions. *J. Am. Chem. Soc.* **133**, 1682–1685 www.ncbi.nlm.nih.gov/entrez/query.fcgi?cmd=Retrieve&db=PubMed&list\_uids=21247162&dopt=Abstract (2011). doi: 10.1021/ja109944n
49. B. Gnanaprakasam, E. Balaraman, Y. Ben-David, D. Milstein, Synthesis of peptides and pyrazines from  $\beta$ -amino alcohols through extrusion of H<sub>2</sub> catalyzed by ruthenium pincer complexes: Ligand-controlled selectivity. *Angew. Chem. Int. Ed.* **50**, 12240–12244 www.ncbi.nlm.nih.gov/entrez/query.fcgi?cmd=Retrieve&db=PubMed&list\_uids=22031234&dopt=Abstract (2011). doi: 10.1002/anie.201105876
50. B. Gnanaprakasam, E. Balaraman, C. Gunanathan, D. Milstein, Synthesis of polyamides from diols and diamines with liberation of H<sub>2</sub>. *J. Polym. Sci. A Polym. Chem.* **50**, 1755–1765 (2012). doi: 10.1002/pola.25943
51. H. Zeng, Z. Guan, Direct synthesis of polyamides via catalytic dehydrogenation of diols and diamines. *J. Am. Chem. Soc.* **133**, 1159–1161 www.ncbi.nlm.nih.gov/entrez/query.fcgi?cmd=Retrieve&db=PubMed&list\_uids=21204554&dopt=Abstract (2011). doi: 10.1021/ja106958s
52. C. Gunanathan, D. Milstein, Metal-ligand cooperation by aromatization-dearomatization: A new paradigm in bond activation and “green” catalysis. *Acc. Chem. Res.* **44**, 588–602 www.ncbi.nlm.nih.gov/entrez/query.fcgi?cmd=Retrieve&db=PubMed&list\_uids=21739968&dopt=Abstract (2011). doi: 10.1021/ar2000265
53. C. Gunanathan, D. Milstein, Bond activation by metal-ligand cooperation: Design of “green” catalytic reactions based on aromatization-dearomatization of pincer complexes. *Top. Organomet. Chem.* **37**, 55–84 (2011). doi: 10.1007/3418\_2011\_6
54. M. Montag, J. Zhang, D. Milstein, Aldehyde binding through reversible C–C coupling with the pincer ligand upon alcohol dehydrogenation by a PNP-ruthenium catalyst. *J. Am. Chem. Soc.* **134**, 10325–10328 www.ncbi.nlm.nih.gov/entrez/query.fcgi?cmd=Retrieve&db=PubMed&list\_uids=22703115&dopt=Abstract (2012). doi: 10.1021/ja303121v
55. G. Zeng, S. Li, Insights into dehydrogenative coupling of alcohols and amines catalyzed by a (PNN)-Ru(II) hydride complex: Unusual metal-ligand cooperation. *Inorg. Chem.* **50**, 10572–10580 www.ncbi.nlm.nih.gov/entrez/query.fcgi?cmd=Retrieve&db=PubMed&list\_uids=21942421&dopt=Abstract (2011). doi: 10.1021/ic200205e
56. H. Li *et al.*, Computational study on the catalytic role of pincer ruthenium(II)-PNN Complex in directly synthesizing amide from alcohol and amine: The origin of selectivity of amide over ester and imine. *Organometallics* **30**, 5233–5247 (2011). doi: 10.1021/om200620n
57. J. Zhang, G. Leituss, Y. Ben-David, D. Milstein, Efficient homogeneous catalytic hydrogenation of esters to alcohols. *Angew. Chem. Int. Ed.* **45**, 1113–1115 www.ncbi.nlm.nih.gov/entrez/query.fcgi?cmd=Retrieve&db=PubMed&list\_uids=16389607&dopt=Abstract (2006). doi: 10.1002/anie.200503771
58. E. Balaraman, B. Gnanaprakasam, L. J. W. Shimon, D. Milstein, Direct hydrogenation of amides to alcohols and amines under mild conditions. *J. Am. Chem. Soc.* **132**, 16756–16758 www.ncbi.nlm.nih.gov/entrez/query.fcgi?cmd=Retrieve&db=PubMed&list\_uids=21049928&dopt=Abstract (2010). doi: 10.1021/ja1080019
59. E. Balaraman, C. Gunanathan, J. Zhang, L. J. W. Shimon, D. Milstein, Efficient hydrogenation of organic carbonates, carbamates and formates indicates alternative routes to methanol based on CO<sub>2</sub> and CO. *Nat. Chem.* **3**, 609–614 www.ncbi.nlm.nih.gov/entrez/query.fcgi?cmd=Retrieve&db=PubMed&list\_uids=21778980&dopt=Abstract (2011). doi: 10.1038/nchem.1089
60. E. Balaraman, Y. Ben-David, D. Milstein, Unprecedented catalytic hydrogenation of urea derivatives to amines and methanol. *Angew. Chem. Int. Ed.* **50**, 11702–11705

- www.ncbi.nlm.nih.gov/entrez/query.fcgi?cmd=Retrieve&db=PubMed&list\_uids=22052711&dopt=Abstract (2011). doi: 10.1002/anie.201106612
61. D. Cantillo, Mechanistic insights on the ruthenium-catalyzed hydrogenation of amides: C–N vs. C–O cleavage. *Eur. J. Inorg. Chem.* **2011**, 3008–3013 (2011). doi: 10.1002/ejic.201100443
  62. C. Gunanathan, B. Gnanaprakasam, M. A. Iron, L. J. W. Shimon, D. Milstein, “Long-range” metal ligand cooperation in H<sub>2</sub> activation and ammonia-promoted hydride transfer with a ruthenium-acridine pincer complex. *J. Am. Chem. Soc.* **132**, 14763–14765 (2010). doi: 10.1021/ja107770y
  63. E. Kossov, Y. Diskin-Posner, G. Leitav, D. Milstein, Selective acceptorless conversion of primary alcohols to acetals and dihydrogen catalyzed by the ruthenium(II) complex Ru(PPh<sub>3</sub>)<sub>2</sub>(NCCCH<sub>3</sub>)<sub>2</sub>(SO<sub>4</sub>). *Adv. Synth. Catal.* **354**, 497–504 (2012). doi: 10.1002/adsc.201100672
  64. B. Gnanaprakasam, J. Zhang, D. Milstein, Direct synthesis of imines from alcohols and amines with liberation of H<sub>2</sub>. *Angew. Chem. Int. Ed.* **49**, 1468–1471 (2010). doi: 10.1002/anie.200907018
  65. H. Li, X. Wang, M. Wen, Z. Wang, Computational insight into the mechanism of selective imine formation from alcohol and amine catalyzed by the ruthenium(II)-PNP pincer complex. *Eur. J. Inorg. Chem.* **2012**, 5011–5020 (2012). doi: 10.1002/ejic.201200473
  66. L. He, T. Chen, D. Gong, Z. Lai, K. Huang, Enhanced reactivities toward amines by introducing an imine arm to the pincer ligand: Direct coupling of two amines to form an imine without oxidant. *Organometallics* **31**, 5208–5211 (2012). doi: 10.1021/om300422v
  67. A. Maggi, R. Madsen, Dehydrogenative synthesis of imines from alcohols and amines catalyzed by a ruthenium N-heterocyclic carbene complex. *Organometallics* **31**, 451–455 (2012). doi: 10.1021/om201095m
  68. M. A. Esteruelas, N. Honeczek, M. Oliván, E. Oñate, M. Valencia, Direct access to PDP-type osmium(II) and osmium(IV) complexes: Osmium a promising alternative to ruthenium for the synthesis of imines from alcohols and amines. *Organometallics* **30**, 2468–2471 (2011). doi: 10.1021/om200290u
  69. M. Zhang, H. Neumann, M. Beller, Selective ruthenium-catalyzed three-component synthesis of pyrroles. *Angew. Chem. Int. Ed.* **52**, 597–601 (2013). doi: 10.1002/anie.201206082
  70. S. Michlik, R. Kempe, A sustainable catalytic pyrrole synthesis. *Nat. Chem.* **5**, 140–144 (2013). doi: 10.1038/nchem.1547; pmid: 23344449
  71. D. Srimani, Y. Ben-David, D. Milstein, Direct synthesis of pyrroles by dehydrogenative coupling of β-aminoalcohols with secondary alcohols catalyzed by ruthenium pincer complexes. *Angew. Chem. Int. Ed.* **52**, 4012–4015 (2013). doi: 10.1002/anie.201300574
  72. A. S. Goldman et al., Catalytic alkane metathesis by tandem alkane dehydrogenation-olefin metathesis. *Science* **312**, 257–261 (2011). doi: 10.1126/science.1123787
  73. A. J. A. Watson, J. M. J. Williams, The give and take of alcohol activation. *Science* **329**, 635–636 (2010). doi: 10.1126/science.1191843
  74. G. Guillena, D. J. Ramón, M. Yus, Hydrogen autotransfer in the N-alkylation of amines and related compounds using alcohols and amines as electrophiles. *Chem. Rev.* **110**, 1611 (2010). doi: 10.1021/cr900228
  - Retrieved from: PubMed&list\_uids=19928825&dopt=Abstract (2010). doi: 10.1021/cr900228
  75. R. Grigg, T. R. B. Mitchell, S. Suththavaiyakit, N. Tongpenyai, Transition metal-catalyzed N-alkylation of amines by alcohols. *J. Chem. Soc. Chem. Commun.* **1981**, 611 (1981). doi: 10.1039/c3981000061
  76. S.-I. Murahashi, K. Kondo, T. Hakata, Ruthenium catalyzed synthesis of secondary or tertiary amines from amines and alcohols. *Tetrahedron Lett.* **23**, 229–232 (1982). doi: 10.1016/S0040-4039(00)86792-1
  77. T. Tsuji, K.-T. Huh, Y. Ohsugi, Y. Watanabe, Ruthenium complex catalyzed N-heterocyclization: Syntheses of N-substituted piperidines, morpholines, and piperazines from amines and 1,5-diols. *J. Org. Chem.* **50**, 1365–1370 (1985). doi: 10.1021/jo00209a004
  78. C. Gunanathan, D. Milstein, Selective synthesis of primary amines directly from alcohols and ammonia. *Angew. Chem. Int. Ed.* **47**, 8661–8664 (2008). doi: 10.1002/anie.200803229
  79. G. Wäther et al., α,ω-Functionalized C19 monomers. *ChemSusChem* **4**, 1052–1054 (2011). doi: 10.1002/cssc.201100187
  80. D. Pingin, C. Müller, D. Vogt, Direct amination of secondary alcohols using ammonia. *Angew. Chem. Int. Ed.* **49**, 8130–8133 (2010). doi: 10.1002/anie.201002583
  81. S. Imm et al., Improved ruthenium-catalyzed amination of alcohols with ammonia: Synthesis of diamines and amino esters. *Angew. Chem. Int. Ed.* **50**, 7599–7603 (2011). doi: 10.1002/anie.201103199
  82. R. Yamaguchi, S. Kawagoe, C. Asai, K. Fujita, Selective synthesis of secondary and tertiary amines by Cp\*indium-catalyzed multialkylation of ammonium salts with alcohols. *Org. Lett.* **10**, 181–184 (2008). doi: 10.1021/ol702522x
  83. K. Fujita, Z. Li, N. Ozeki, R. Yamaguchi, N-alkylation of amines with alcohols catalyzed by a Cp\*Ir complex. *Tetrahedron Lett.* **44**, 2687–2690 (2003). doi: 10.1016/S0040-4039(03)00371-X
  84. C. T. Eary, D. Clausen, Preparation of substituted 1,2,3,4-tetrahydroquinolines and 2,3,4,5-tetrahydro-1H-benzol[1,4]diazepines from catalytic Cp\*Ir hydrogen transfer N-heterocyclization of anilino alcohols. *Tetrahedron Lett.* **47**, 6899–6902 (2006). doi: 10.1016/j.tetlet.2006.07.033
  85. S. Bähn et al., The catalytic amination of alcohols. *Chem. Cat. Chem.* **3**, 1853–1864 (2011). doi: 10.1002/cctc.201100255
  86. M. H. S. A. Hamid, P. A. Slatford, J. M. J. Williams, Borrowing hydrogen in the activation of alcohols. *Adv. Synth. Catal.* **349**, 1555–1575 (2007). doi: 10.1002/adsc.200600638
  87. M. H. S. A. Hamid et al., Ruthenium-catalyzed N-alkylation of amines and sulfonamides using borrowing hydrogen methodology. *J. Am. Chem. Soc.* **131**, 1766–1774 (2009). doi: 10.1021/ja807323a
  88. M. A. Berliner et al., Use of an indium-catalyzed redox neutral alcohol-amine coupling on kilogram scale for the synthesis of a GlyT1 inhibitor. *Org. Process Res. Dev.* **15**, 1052–1062 (2011). doi: 10.1021/op200174k
  89. L. Miao, S. C. DiMaggio, H. Shu, M. L. Trudell, Enantioselective syntheses of both enantiomers of noranabasamine. *Org. Lett.* **11**, 1579–1582 (2009). doi: 10.1021/ol900228
  90. R. Grigg, T. R. B. Mitchell, S. Suththavaiyakit, N. Tongpenyai, Oxidation of alcohols by transition metal complexes part V. Selective catalytic monoalkylation of arylacetoneitriles by alcohols. *Tetrahedron Lett.* **22**, 4107–4110 (1981). doi: 10.1016/S0040-4039(01)82078-5
  91. S. Whitney, R. Grigg, A. Derrick, A. Keep, [Cp\*IrCl<sub>2</sub>]<sub>2</sub>-catalyzed indirect functionalization of alcohols: Novel strategies for the synthesis of substituted indoles. *Org. Lett.* **9**, 3299–3302 (2007). doi: 10.1021/ol71274v
  92. P. A. Slatford, M. K. Whittlesey, J. M. J. Williams, C–C bond formation from alcohols using a Xantphos ruthenium complex. *Tetrahedron Lett.* **47**, 6787–6789 (2006). doi: 10.1016/j.tetlet.2006.07.069
  93. T. Jensen, R. Madsen, Ruthenium-catalyzed alkylation of oxindole with alcohols. *J. Org. Chem.* **74**, 3990–3992 (2009). doi: 10.1021/jo900341w
  94. Y. Obara, Y. Ishii, Iridium-catalyzed reactions involving transfer hydrogenation, addition, N-heterocyclization, and alkylation using alcohols and diols as key substrates. *Synlett* **2011**, 30–51 (2011). doi: 10.1055/s-0030-1259094
  95. M. G. Edwards, J. M. J. Williams, Catalytic electronic activation: indirect “Wittig” reaction of alcohols. *Angew. Chem. Int. Ed.* **41**, 4740–4743 (2002). doi: 10.1002/anie.200290034
  96. G. Cami-Kobeci, J. M. J. Williams, Conversion of alcohols into N-alkyl anilines via an indirect aza-Wittig reaction. *Chem. Commun. (Camb.)* **2004**, 1072 (2004). doi: 10.1039/b402020k
  97. K. Fujita, C. Asai, T. Yamaguchi, F. Hanasaka, R. Yamaguchi, Direct β-alkylation of secondary alcohols with primary alcohols catalyzed by a CpIr complex. *Org. Lett.* **7**, 4017–4019 (2005). doi: 10.1021/ol051517o
  98. R. Martínez, D. J. Ramón, M. Yus, RuCl<sub>2</sub>(DMSO)<sub>4</sub> catalyzes the β-alkylation of secondary alcohols with primary alcohols through a hydrogen autotransfer process. *Tetrahedron* **62**, 8982–8987 (2006). doi: 10.1016/j.tet.2006.07.012
  99. J. F. Bower, M. J. Krische, Formation of C–C bonds via iridium-catalyzed hydrogenation and transfer hydrogenation. *Top. Organomet. Chem.* **34**, 107 (2011). doi: 10.1002/top.200600000
  100. J. C. Leung, L. M. Geary, T. Y. Chen, J. R. Zbieg, M. J. Krische, Direct, redox-neutral prenylation and geranylation of secondary carbinol C–H bonds. C4-regioselectivity in ruthenium-catalyzed C–C couplings of dienes to α-hydroxy esters. *J. Am. Chem. Soc.* **134**, 15700–15703 (2012). doi: 10.1021/ja3075049
  101. J. R. Zbieg, E. Yamaguchi, E. L. McInturf, M. J. Krische, Enantioselective C–H crotylation of primary alcohols via hydrohydroxyalkylation of butadiene. *Science* **336**, 324–327 (2012). doi: 10.1126/science.1219274

**Acknowledgments:** Supported by the European Research Council (ERC) under the FP7 framework (no. 246837) and by the Kimmel Center for Molecular Design. C.G. thanks the Department of Science and Technology and NISER, and he is a Ramanujan Fellow. D.M. is the Israel Matz Professorial Chair of Organic Chemistry.

10.1126/science.1229712



# Tight Coordination of Protein Translation and HSF1 Activation Supports the Anabolic Malignant State

Sandro Santagata, Marc L. Mendillo, Yun-chi Tang, Aravind Subramanian, Casey C. Perley, Stéphane P. Roche, Bang Wong, Rajiv Narayan, Hyoungtae Kwon, Martina Koeva, Angelika Amon, Todd R. Golub, John A. Porco Jr., Luke Whitesell,\* Susan Lindquist\*

**Introduction:** Ribosome biogenesis is commonly up-regulated to satisfy the increased anabolic demands associated with malignant transformation and tumor growth. Many different oncogenic signaling pathways converge on the ribosome to increase translational flux. Despite the detailed understanding of ribosome regulation in cancer, it is not clear whether the net translational activity of the ribosome can itself regulate transcriptional programs that support and promote the malignant state.

**Methods:** To investigate the transcriptional effects of modulating translational activity in malignant cells, we used integrated chemical and genetic approaches, including a gene signature-based genetic and chemical screen of more than 600,000 gene expression profiles (LINCS database) and an independent, reporter-based chemical screen of more than 300,000 compounds. A lead compound was tested in several cell lines unified by their increased dependence on HSF1 activation for growth and survival, and in an in vivo cancer model.

**Results:** Inhibiting translation led to large changes in the transcriptome. The single most enriched category consisted of genes regulated by the heat-shock transcription factor, HSF1. The most down-regulated mRNA was *HSPA8*, which encodes the constitutive HSP70 chaperone that helps to fold nascent polypeptides. The expression of many other genes that HSF1 coordinates to support cancer was also strongly affected. HSF1 protein levels were unchanged, but HSF1 DNA occupancy was nearly eliminated. Inhibition of the HSF1-regulated gene expression program is thus a dominant transcriptional effect elicited by inhibiting protein translation.

Using a gene signature of HSF1 inactivation to query the LINCS database revealed a strong connection between HSF1 inactivation and perturbations that inhibit protein translation, including a broad spectrum of chemical and genetic interventions that target the ribosome, eukaryotic initiation factors (eIFs), aminoacyl tRNA synthetases, and upstream signaling/regulatory pathways that control translation.

Our high-throughput small-molecule screen identified rocaglamide A, an inhibitor of translation initiation, as the strongest inhibitor of HSF1 activation. An analog of this compound, RHT, increased thioredoxin-interacting protein (TXNIP) mRNA and protein levels and decreased glucose uptake and lactate production. Cell-based cancer models characterized by high dependence on HSF1 activation for growth and survival were highly sensitive to RHT, as were cells derived from diverse hematopoietic malignancies. RHT had a strong antitumor effect—with marked inhibition of HSF1 activity and glucose uptake—against xenografted acute myeloid leukemia cells.

**Discussion:** The ribosome functions as a central information hub in malignant cells: Translational flux conveys information about the cell's metabolic status to regulate the transcriptional programs that support it. Multiple unbiased chemical and genetic approaches establish HSF1 as a prime transducer of this information, centrally poised to regulate the transcription of genes that support protein folding, biomass expansion, anabolic metabolism, cellular proliferation, and survival. Targeting translation initiation may offer a strategy for reversing HSF1 activation, disabling metabolic and cytoprotective pathways in malignant cells.

**HSF1 at the crossroads of protein translation and metabolism.** (Left) Cancers activate an HSF1-regulated transcriptional program to adapt to the anabolic demands of relentless biomass expansion. Glucose uptake increases, and expression of TXNIP, an inhibitor of glucose uptake, drops. (Right) Down-regulating translation with rocaglate scaffold initiation inhibitors reverses cancer-associated HSF1 activation. Glucose uptake drops as TXNIP levels rise.

READ THE FULL ARTICLE ONLINE

<http://dx.doi.org/10.1126/science.1238303>



Cite this article as S. Santagata *et al.*, *Science* **341**, 1238303 (2013). DOI: 10.1126/science.1238303

## FIGURES IN THE FULL ARTICLE

Fig. 1. Inhibiting protein translation inactivates HSF1.

Fig. 2. LINCS analysis reveals that targeting protein translation inactivates HSF1.

Fig. 3. Chemical screens reveal that targeting translation control inactivates HSF1.

Fig. 4. Inhibiting translation initiation with rocaglates ablates HSF1 DNA binding.

Fig. 5. Rocaglates modulate tumor energy metabolism.

Fig. 6. Rocaglates selectively target aneuploid cancer cells and nontransformed cells with cancer-associated genetic aberrations.

Fig. 7. Rocaglates suppress tumor growth, *HSPA8* mRNA levels, and glucose uptake in vivo.

## SUPPLEMENTARY MATERIALS

Materials and Methods

Figs. S1 to S9

Tables S1 to S5

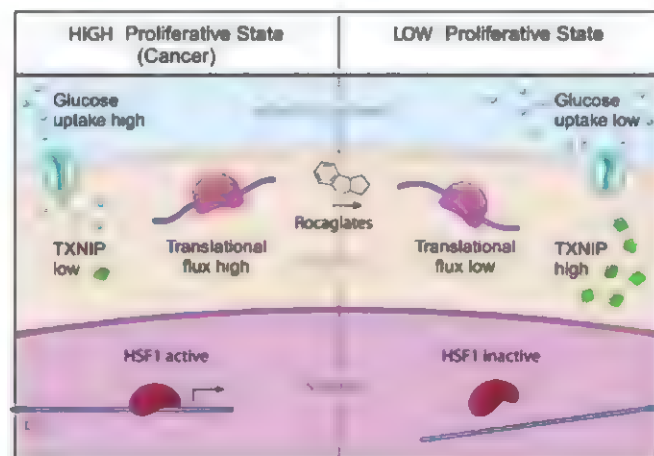
References and Notes

## RELATED ITEMS IN SCIENCE

V. Gandin, I. Topisirovic, Trans-HSF1 express.

*Science* **341**, 242-243 (2013).

DOI: 10.1126/science.1242359



The list of author affiliations is available in the full article online.

\*Corresponding author. E-mail: whitesell@wi.mit.edu (L.W.); lindquist\_admin@wi.mit.edu (S.L.)

# Tight Coordination of Protein Translation and HSF1 Activation Supports the Anabolic Malignant State

Sandro Santagata,<sup>1,2,3\*</sup> Marc L. Mendillo,<sup>3,4\*</sup> Yun-chi Tang,<sup>4,5†</sup> Aravind Subramanian,<sup>6</sup> Casey C. Perley,<sup>3,4</sup> Stéphane P. Roche,<sup>7</sup> Bang Wong,<sup>6</sup> Rajiv Narayan,<sup>6</sup> Hyoungtae Kwon,<sup>3,4</sup> Martina Koeva,<sup>3,4</sup> Angelika Amon,<sup>4,5</sup> Todd R. Golub,<sup>6</sup> John A. Porco Jr.,<sup>7</sup> Luke Whitesell,<sup>3†</sup> Susan Lindquist<sup>3,4†</sup>

The ribosome is centrally situated to sense metabolic states, but whether its activity, in turn, coherently rewires transcriptional responses is unknown. Here, through integrated chemical-genetic analyses, we found that a dominant transcriptional effect of blocking protein translation in cancer cells was inactivation of heat shock factor 1 (HSF1), a multifaceted transcriptional regulator of the heat-shock response and many other cellular processes essential for anabolic metabolism, cellular proliferation, and tumorigenesis. These analyses linked translational flux to the regulation of HSF1 transcriptional activity and to the modulation of energy metabolism. Targeting this link with translation initiation inhibitors such as rocaglates deprived cancer cells of their energy and chaperone armamentarium and selectively impaired the proliferation of both malignant and premalignant cells with early-stage oncogenic lesions.

**R**egulation of ribosome activity is critical for supporting cellular proliferation. In cancer, ribosome biogenesis is commonly increased to satisfy the increased anabolic demands associated with malignant transformation and tumor growth (1–4). In addition, many different oncogenic signaling pathways converge on the ribosome to modulate its function (5, 6). These inputs are integrated, and the net ribosomal translational activity is tuned to reflect the metabolic and proliferative state of the cell. Despite the detailed understanding of ribosome regulation in cancer, it is not well understood whether the net translational activity of the ribosome can itself be conveyed to regulate transcriptional programs that support and promote the malignant state. Is a coherent and coordinated transcriptional response triggered by modulating translation activity?

## Results

### Inhibiting Translational Flux Inactivates HSF1

To investigate the transcriptional effects of reducing translational flux through the ribosome in malignant cells, we analyzed the mRNA expression profiles of breast cancer cells after treatment with various inhibitors of translation elongation (anisomycin, emetine, cephaeline, and cycloheximide). Large changes in the transcriptome were highly correlated across all four inhibitors [Pearson correlation coefficient ( $r$ ) between 0.85 to 0.97 for all pairwise correlations]. The most strongly enriched category consisted of genes regulated by promoters that contain DNA binding motifs for the heat-shock transcription factor known as heat shock factor 1 (HSF1) ( $P = 9.87 \times 10^{-7}$ ) (Fig. 1A and table S1). Of the 13,258 genes measured, the single most down-regulated mRNA was *HSPA8*, which encodes a constitutive HSP70 chaperone that folds nascent polypeptides as they emerge from the ribosome (Fig. 1B and table S2) (7). *HSPA1A*, a cancer-induced *HSP70* gene, was also among the 10 most down-regulated mRNAs. This transcriptional response suggested that reduced translational flux causes a profound shift in the activity of HSF1.

In a wide range of cancers, HSF1 regulates a transcriptional network that is distinct from the conventional network activated by thermal stress (8). This cancer network includes many classic “heat-shock” genes. But, it also includes a broad cadre of other genes that play critical roles in malignancy, some of which are positively regulated by HSF1 and some negatively regulated. All four inhibitors of translation elongation affected genes in the HSF1 cancer network ( $P = 0.016$ ) (Fig. 1C and fig. S1). Genes that are positively regulated

by HSF1 were down-regulated when translational flux through the ribosome was reduced. These genes included drivers of cell proliferation and mitogenic signaling (such as *CENPA*, *CKS1B*, and *PRKCA*), transcription and mRNA processing (such as *LSM2* and *LSM4*), protein synthesis (such as *FXR1* and *MRPL18*), energy metabolism (such as *MAT2A*, *SLC5A3*, *PGK1*, *MBOAT7*, and *SPR*), and invasion/metastasis (such as *EMP2* and *LTBP1*). In a complementary fashion, genes that are negatively regulated by HSF1 were up-regulated when translational flux through the ribosome was reduced. These included genes that promote differentiation (such as *NOTCH2NL*), cellular adhesion (such as *EFEMP1* and *LAMA5*), and apoptosis (such as *BCL10*, *CFLAR*, and *SPTAN1*).

This effect of translation inhibition on HSF1-regulated transcription led us to examine the genome-wide pattern of DNA occupancy by HSF1 in breast cancer cells. After a 6-hour exposure to cycloheximide, we performed chromatin immunoprecipitation coupled with massively parallel DNA sequencing (ChIP-Seq) using a previously validated antibody against HSF1 (8). Despite cycloheximide treatment, HSF1 protein levels themselves remained unchanged (Fig. 1D). In contrast to DNA occupancy by RNA-polymerase II (which was not globally reduced), HSF1 occupancy was nearly eliminated (Fig. 1, E to G, fig. S2, and table S3). This held true for genes that were either positively or negatively regulated by HSF1, as well as for genes shared with the classic heat-shock response and genes specific to the HSF1 cancer program (table S3). Together, these data pointed to a link between the activity of the ribosome and the activity of HSF1.

### LINCS Establishes Translation as a Potent Regulator of HSF1 in Cancer Cells

To further investigate the link between the HSF1 activity and translational program, we turned to an expression-profiling resource created by the Library of Integrated Network-based Cellular Signatures (LINCS) program (Fig. 2 and supplementary materials, materials and methods). The LINCS database is a large catalog of gene-expression profiles collected from human cells treated with chemical (small-molecule) and genetic [short hairpin RNA (shRNA)] perturbations.

We generated a query signature for HSF1 inactivation from expression profiles of breast cancer cells that had been treated with HSF1 shRNAs (supplementary materials, materials and methods) (8). This signature included both genes that were up-regulated by HSF1 inactivation and down-regulated by HSF1 inactivation. We compared our HSF1 query signature with LINCS expression profiles from nine cell lines that are currently the most extensively characterized in this database (Fig. 2A). Eight of these are cancer lines of diverse histopathologic origin. These lines have been treated individually with 3866 small-molecule compounds or 16,665 shRNAs targeting 4219 genes. The compounds used for these gene expression

<sup>1</sup>Department of Pathology, Brigham and Women's Hospital (BWH), and Harvard Medical School, Boston, MA 02215, USA. <sup>2</sup>Dana Farber Cancer Institute, Boston, MA 02215, USA. <sup>3</sup>Whitehead Institute for Biomedical Research (WIBR), Cambridge, MA 02142, USA. <sup>4</sup>Howard Hughes Medical Institute, Department of Biology, Massachusetts Institute of Technology (MIT), Cambridge, MA 02142, USA. <sup>5</sup>David H. Koch Institute for Integrative Cancer Research and Howard Hughes Medical Institute, MIT, Cambridge, MA 02142, USA. <sup>6</sup>Broad Institute of MIT and Harvard, Cambridge, MA 02142, USA. <sup>7</sup>Department of Chemistry, Center for Chemical Methodology and Library Development (CMLD-BU), Boston University, Boston, MA 02215, USA.

\*These authors contributed equally to this work.

†Present address: Institute of Health Sciences, Shanghai Institutes for Biological Sciences, Chinese Academy of Sciences & Shanghai Jiao Tong University School of Medicine, 20025 Shanghai, China.

‡Corresponding author. E-mail: whitesell@wi.mit.edu (L.W.); lindquist\_admin@wi.mit.edu (S.L.)



profiles encompassed U.S. Food and Drug Administration (FDA)-approved drugs and known bioactives. The shRNAs used were directed against the known targets of these compounds, against genes in related pathways, or against other genes that have been implicated in a variety of human diseases. In all, we compared our HSF1 signature with 161,636 LINC signatures, each generated from at least three replicates (for a total of 614,216 profiles.)

As expected, the LINC perturbations that negatively correlated with our HSF1 inactivation signature were enriched for known activators of HSF1. They included shRNAs that target components of the proteasome. They also included compounds that inhibit the proteasome and that inhibit HSP90 (Fig. 2, B and C and table S4).

The LINC perturbations that positively correlated with our HSF1 inactivation signature were most highly enriched for translation inhibitors (cephalexin, cycloheximide, and emetine) (Fig. 2, B and C, and table S4). These perturbations were also highly enriched for compounds that target

signaling pathways that regulate protein translation: phosphatidylinositol 3-kinase (PI3K)/mammalian target of rapamycin (mTOR) inhibitors (Fig. 2B and table S4). Of the nearly 200 gene ontology classes analyzed, the ribosome subunit family was the single most enriched (Fig. 2, B and C, and table S4). In addition, eukaryotic initiation factors (eIFs) and aminoacyl tRNA synthetases were also highly enriched. This unbiased analysis using the LINC database demonstrates the connection between translational flux and the function of HSF1 in cancer.

### An Unbiased High-Throughput Chemical Screen for HSF1 Inhibitors

To find alternate ways to inhibit HSF1, we performed a large high-throughput chemical screen. We screened 301,024 compounds through the U.S. National Institutes of Health (NIH) Molecular Libraries Probe Center Network (MLPCN; Pubchem AID, 2118) (Fig. 3A) using an HSF1-regulated reporter driven by consensus heat-shock elements (HSEs). To accommodate constraints of

the high-throughput 384-well format (supplementary materials, materials and methods), we used a reporter cell line stably transduced with a luminescence-based reporter and induced HSF1 activation with a simple proteotoxic stressor (the proteasome inhibitor MG132).

Approximately 2500 hit compounds from the primary screen, which blocked induction of the reporter, were then counter-screened with an independent dual reporter cell line (Fig. 3B) so as to eliminate nonselective inhibitors. This second line had been stably transduced with two constructs, one encoding a green fluorescent protein (GFP) driven by HSEs and the other encoding a red fluorescent protein (RFP) driven by a doxycycline-regulated control promoter. Compounds that selectively inhibit HSF1 activity should suppress GFP expression in this cell line but should not suppress doxycycline-mediated induction of RFP. Notably, compounds that are thought to selectively inhibit HSF1—such as triptolide, quercetin, KNK423, and KNK437 (9)—all suppressed both reporters (fig. S3). Thus, these compounds

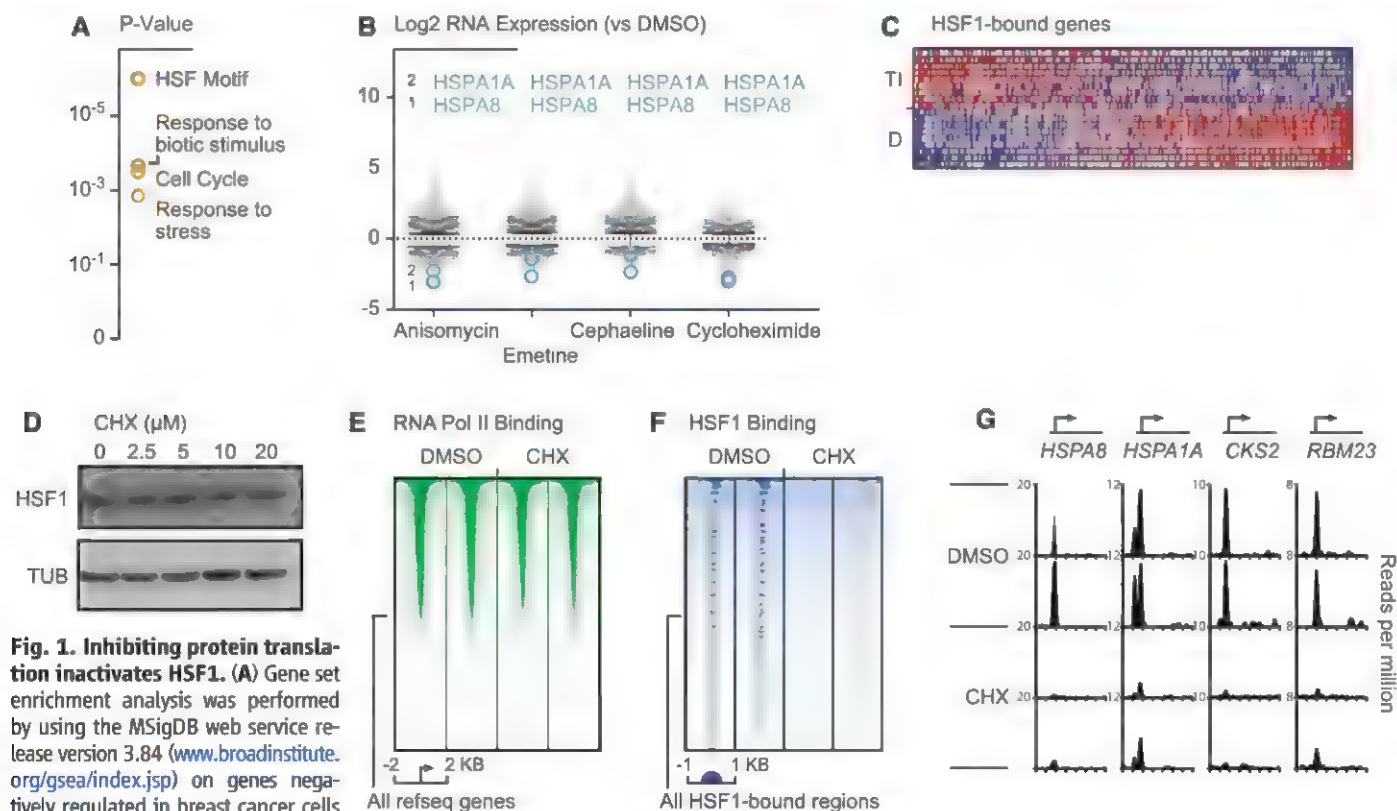


**Fig. 1. Inhibiting protein translation inactivates HSF1.** (A) Gene set enrichment analysis was performed by using the MSigDB web service release version 3.84 ([www.broadinstitute.org/gsea/index.jsp](http://www.broadinstitute.org/gsea/index.jsp)) on genes negatively regulated in breast cancer cells following a 6-hour incubation with inhibitors of protein translation elongation. Selected results are displayed; complete GSEA results are provided in table S1. (B) Scatter plot of levels of mRNA transcripts (log2) after a 6-hour incubation with the indicated inhibitors of protein translation elongation versus control dimethyl sulfoxide (DMSO). The levels of HSPA1A and HSPA8 are indicated for each elongation inhibitor. (C) Translation elongation inhibitors alter the basal transcriptional program of HSF1 in breast cancer cells. Genes bound by HSF1 in MCF7 were ranked by their differential expression between cells treated with translation elongation inhibitors (TI) and control DMSO (D). Each column represents a gene and is normalized across the column, with high expression in red and low expression in blue. (D) An immunoblot shows the levels of HSF1 protein and the loading

control tubulin after a 6-hour exposure to the indicated concentrations of cycloheximide (CHX). (E) Heat map of RNA polymerase II ChIP-Seq read density in MCF7 cells that were treated with DMSO or 10 μM CHX for 6 hours. Genomic regions from -2 kb to +2 kb relative to the transcription start site for all RefSeq genes are shown. (F) Heat map of HSF1 ChIP-Seq read density in MCF7 cells that were treated with DMSO or 10 μM CHX for 6 hours. Genomic regions from -1 kb to +1 kb relative to the peak of HSF1 binding for all HSF1-enriched regions (union of all HSF1-enriched regions in the four data sets depicted here) are shown. (G) Representative genes bound by HSF1 in MCF7 cells (HSPA8, HSPA1A, CKS2, and RBM23). The x axis depicts from -2kb from the transcription start site (TSS) to 5 kb from the TSS for each gene.

are far less specific for HSF1 than commonly assumed.

More to the point, the chemical screen results also suggested a link between HSF1 activation and the translation machinery. By far the most potent and selective hit to emerge from the 301,024 compounds we tested was the rocaglate known as rocaglamide A [median inhibitory concentration ( $IC_{50}$ ) of ~50 nM for the heat shock reporter versus  $IC_{50}$  >1000 nM for the control reporter] (Fig. 3C). This natural product inhibits the function of the translation initiation factor eIF4A, a DEAD box RNA helicase (10, 11). Presumably, it passed counterscreening in our secondary assay with the dual reporter system because translation of the doxycycline-regulated RFP control does not require the classical cap-dependent initiation complex.

To define structure-activity relationships for inhibition of the HSE reporter by rocaglamide A, we used our dual reporter system to test 38

additional rocaglates (fig. S4). These included both natural products and totally synthetic analogs prepared with photocycloaddition methods (12, 13). Five hydroxamate analogs were more potent than rocaglamide A at inhibiting the HSE reporter while retaining similar selectivity (table S5). The most potent inhibitor had an  $IC_{50}$  of ~20 nM (table S5). We named this compound [previously reported as “8e” (13)] Rohinitib (or RHT), for Rocaglate Heat Shock, Initiation of Translation Inhibitor.

### Characterizing the Effects of RHT on Cancer Cells

To validate findings from our engineered reporter system, we measured the effects of RHT on the basal expression of several endogenous HSF1-regulated transcripts (Fig. 3D and figs. S5 and S6). RHT did not reduce the transcript levels of the control housekeeping genes *B2M* and *GAPDH*. Nor did it reduce the transcript levels of *HSF1*

itself (Fig. 3D and fig. S6A). However, mRNA levels of *Hsp40* (*DNAJ1*) and *Hsp70* genes (*HSPA1B* and *HSPA8*) dropped substantially. The most dramatically affected was the constitutively expressed *HSPA8* gene (>90% reduction) (Fig. 3D). This was also the gene that we had found to be the most strongly repressed by translation elongation inhibitors (Fig. 1B).

The effects of RHT were not due to reductions in HSF1 protein levels, which remained constant (Fig. 3E and fig. S6B). The sharp decrease in *HSP70* mRNA levels in response to RHT held true across a histologically diverse panel of human cancer cell lines (MCF7, breast adenocarcinoma; MO91, myeloid leukemia; CHP100, sarcoma; and HeLa, cervical carcinoma) as well as in artificially transformed 293T kidney cells (Fig. 3D and fig. S6, A and C). RHT had a much smaller effect on *HSP70* mRNA levels in proliferating but nontumorigenic diploid cells (WI38 and IMR90) (fig. S6C).

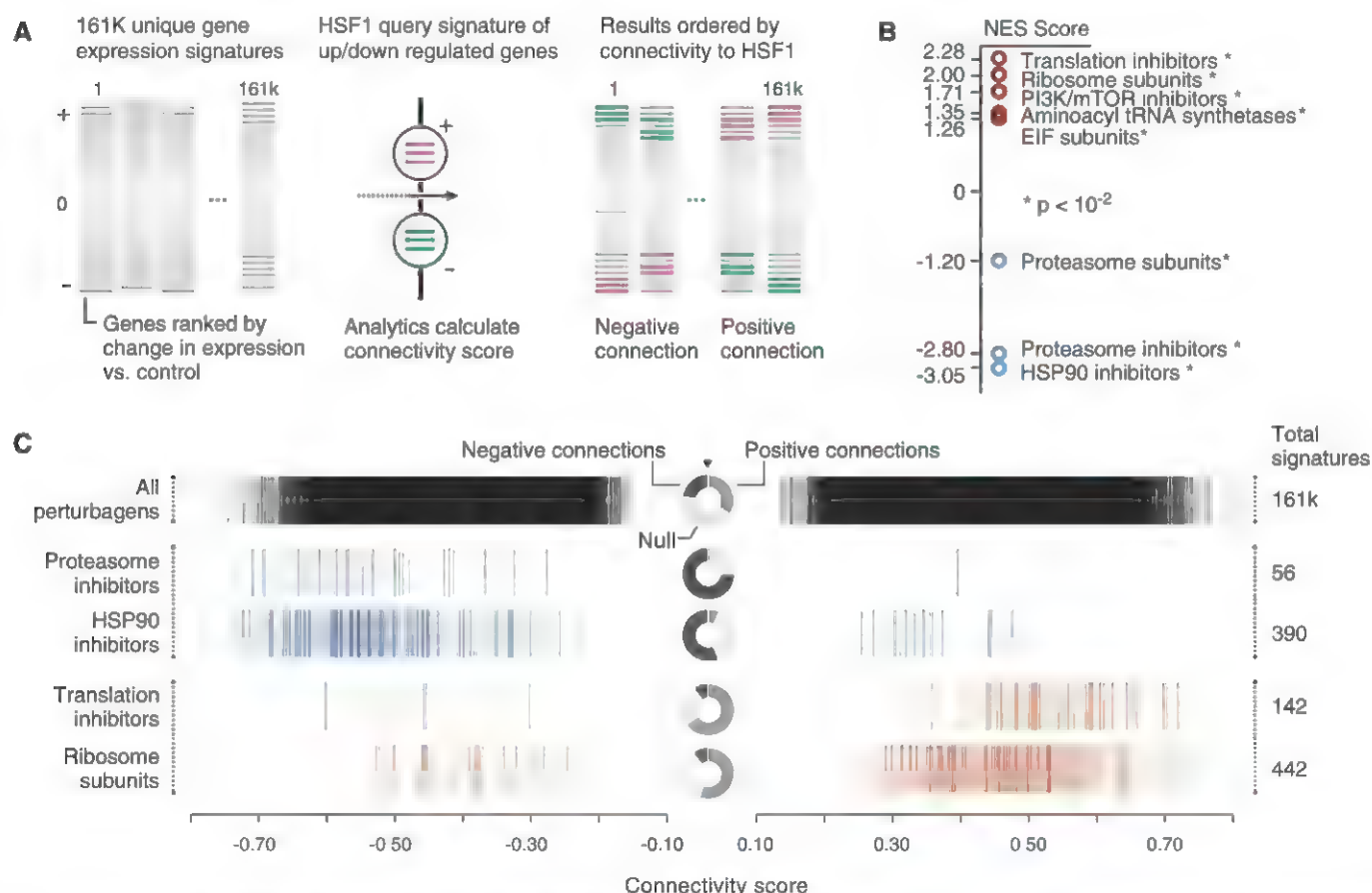


**Fig. 2. LINCS analysis reveals that targeting protein translation inactivates HSF1.** (A) Schematic representation of the LINCS analysis used to identify chemical and genetic modulators that are correlated with HSF1 inactivation (supplementary materials, materials and methods). Pink represents genes whose levels increase, and green represents genes whose levels decrease, after shRNA-mediated knockdown of HSF1. (B) GSEA results of our HSF1 inactivation signature LINCS analysis. Perturbation signatures were rank-ordered by connectivity with the HSF1 inactivation signature, and enrichment was determined for KEGG pathway gene sets and ATC chemical classes (details are available in the supplementary materials, materials and methods).

Normalized enrichment score (NES) of selected results are plotted (complete GSEA results are provided in table S4). (C) Barcode plot of the connectivity score of all of the individual perturbations comprising the indicated enriched chemical or gene sets. The bagel plot in the center of the barcode plot summarizes the positive, negative, and null (not connected) fractions for the indicated enriched class. All perturbations that are positively or negatively connected for the indicated enriched classes are shown. Total perturbations in each class are indicated on the right of the plot. Blue represents negatively connected, and red represents positively connected, classes of enriched perturbations.



To obtain a more direct and global view of RHT's effects on HSF1 activity, we examined genome-wide promoter occupancy by means of ChIP-Seq analysis. RHT virtually abolished HSF1 binding throughout the genome (Fig. 4, A and B; fig. S6D; and table S3). As had occurred with cycloheximide, RHT affected both genes that are positively regulated by HSF1 and genes that are negatively regulated by HSF1 (Fig. 4A). Furthermore, it affected both classic heat-shock genes and genes specific to the HSF1 cancer program (table S3). The effects on HSF1 DNA occupancy occurred at concentrations of cycloheximide and RHT that inhibit the ribosome activity to a similar extent (Fig. 4C).

### Rocaglates Modulate Tumor Energy Metabolism

While characterizing the effects of RHT on the transcriptome, we noted that treated cells failed to acidify the culture medium (detected incidentally by the color of the pH indicator phenol red included in standard media). This suggested a reversal of the "Warburg effect," a metabolic shift responsible for increased lactic acid production by many cancers. Genetic compromise of HSF1 drives a shift in metabolism in both cell culture and animal models (14, 15). Hence, this effect of RHT is consistent with inactivation of HSF1.

Our mRNA expression profiling of rocaglate-treated breast cancer cells also revealed that mRNA levels for thioredoxin-interacting protein

(TXNIP) were up-regulated. TXNIP is a powerful negative regulator of glucose uptake and is a well-established regulator of cellular energy status (16, 17). Its expression is dramatically reduced in malignant cells, leading to increased glucose uptake (18). Conversely, increasing TXNIP levels leads to reduced glucose uptake (16). The induction of TXNIP mRNA by RHT was observed across a diverse panel of tumor cell lines (Fig. 5A). TXNIP protein levels also increased sharply despite a marked reduction in the levels of other short-lived proteins, such as p53 (Fig. 5B). Although we did not detect HSF1 bound to the TXNIP locus, HSF1 null cells showed higher levels of TXNIP (fig. S7). In addition, HSF1 did directly regulate a group of other genes involved in energy metabolism (including *MAT2A*, *SLC5A3*, and *PGK1*). At a functional level, the effects of RHT were associated with concentration-dependent reductions in both glucose uptake and lactate production (Fig. 5C). Thus, the effects of RHT on protein translation, HSF1 activation, and energy metabolism—processes lying at the core of the anabolic state of cancer—appear to be coordinated.

### Rocaglates Selectively Target Pre-Malignant Cells with Early-Stage Oncogenic Lesions

Does this tight coordination create vulnerabilities for the malignant phenotype that could be exploited as a therapeutic strategy? We looked at a range of cell-based cancer models unified by their

increased dependence on HSF1 activation for growth and survival. Although it occurs very early during oncogenesis, simple loss of the tumor suppressor *Nf1* leads to an increase in HSF1 protein levels, nuclear localization, and transcriptional activation (19). We treated mouse embryonic fibroblasts (MEFs) in which *Nf1* was knocked out and wild-type littermate control MEFs in which HSF1 was not activated, with either RHT or with cycloheximide. The two cell types were similarly sensitive to cycloheximide. However, *Nf1*-null MEFs were more sensitive than were wild-type MEFs to RHT (Fig. 6A). In this model for an early event in tumorigenesis, targeting translation initiation rather than translation elongation seems to provide a more selective, better tolerated approach for disrupting the link between translation and HSF1 activation.

A second engineered system allowed us to ask whether rocaglates would selectively inhibit the growth of cells carrying a simple chromosomal aberration that models another common early event in the development of cancer: aneuploidy. Chromosomal imbalances lead to both increased energy and proteotoxic stress. This is reflected by the elevation of the HSF1-regulated chaperone protein HSP72, encoded by *HSPA1A* (20). We isolated MEFs from mice carrying Robertsonian fusions for chromosome 13 (21). These MEFs (TS13) carry a single extra copy of 120 Mb of chromosome 13, introducing an additional copy of 843 genes.

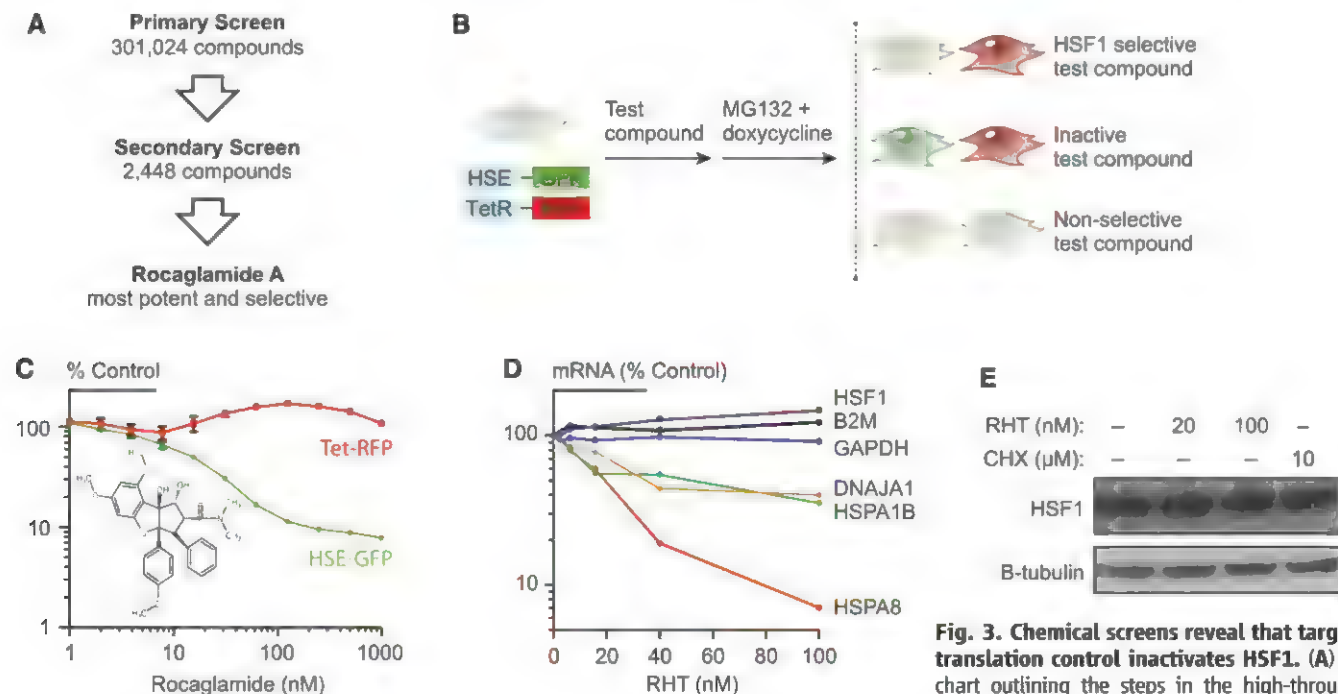


**Fig. 3. Chemical screens reveal that targeting translation control inactivates HSF1.** (A) Flowchart outlining the steps in the high-throughput MLPCN screen for inhibitors of HSF1 activation. (B)

Schematic of dual-reporter cell line used to counter-screen primary screen hits. GFP expression is regulated by a heat shock-inducible promoter. RFP expression is regulated by a doxycycline response element (TetR). (C) Effect of rocaglamide A on the HSE-driven GFP and doxycycline-driven RFP signals after incubation with 2.5 mM MG132 and 2 μg/ml doxycycline. Chemical structure of rocaglamide A is displayed in the inset. Error bars indicate mean ± SEM of quadruplicates. (D) Effect of RHT on HSF1-regulated and control endogenous mRNA transcript levels in MO-91 leukemia cells measured by means of nanosting nCounter after a 6-hour incubation with indicated concentrations of RHT. Levels of endogenous transcript are shown as percent of DMSO-treated control. Mean of duplicates are reported. (E) HSF1 protein levels are not affected in MO-91 leukemia cells treated with RHT. Immunoblot shows the levels of HSF1 protein and the loading control (Tubulin) after a 6-hour exposure to the indicated concentrations of RHT.

Cycloheximide, as well as conventional cytotoxic chemotherapeutics (taxol and hydroxyurea), inhibited the growth of both trisomic and littermate control MEFs to an equal extent (Fig. 6B and fig. S8). But, trisomic MEFs ( $P < 0.0001$ ) were more sensitive than wild-type MEFs to RHT (Fig. 6B). Thus, again in this model for an early neoplastic change that activates HSF1, targeting translation initiation seems to provide a better tolerated, more selective approach for targeting the malignant state.

HSF1 activation is even more prominent in advanced malignancies (8, 22, 23). For example, colon cancers frequently show immunohistochemical evidence of strong HSF1 activation (Fig. 6C) and this correlates with poor clinical outcome (8). We mined publicly available expression profiling from colon cancer lines with highly aneuploid karyotypes [chromosomal instability (CIN)] and from colon cancer lines with near-euploid karyotypes but microsatellite instability (MIN). The CIN lines expressed markedly higher levels of *HSPA1A*, which is consistent with greater levels of proteotoxic stress and greater activation of the HSF1-regulated cancer program (Fig. 6, D and E). Next, we tested several patient-derived colon cancer lines with CIN and several patient-derived colon cancer lines with MIN for sensitivity to inhibition by RHT. The CIN lines were much more sensitive than were the MIN lines. Non-

transformed colon epithelial cell lines with euploid chromosome content were the least sensitive of all the lines we tested (Fig. 6F).

### Rocaglates Suppress the Growth of Cancer Cells and Tumors

Some rocaglates have previously been shown to exert profound anticancer activity (10, 24–26). We tested RHT against a collection of cell lines including nontransformed diploid lines and cancer cell lines with diverse histopathological origins and oncogenic lesions (Fig. 7A). The nontransformed cell lines were relatively resistant to RHT ( $IC_{50}$  from 100 to 300 nM). All cancer cell lines were sensitive to RHT ( $IC_{50} < 30$  nM); the hematopoietic tumor cell lines were especially sensitive ( $IC_{50} \leq 6$  nM). We used one of these hematopoietic tumor lines, the M0-91 cell line originally derived from a patient with acute myeloid leukemia (27), to further characterize the effects of RHT. RHT strongly suppressed *HSPA8* mRNA levels in M0-91 cells and induced *TXNIP* mRNA (Fig. 7B). In addition, RHT sharply decreased glucose uptake by these cells (Fig. 7C).

Are the effects of RHT in cell culture achievable at drug exposures that are systemically tolerable in animals? To directly address this critical issue of therapeutic index, we first used standard in vitro assays to test whether RHT had sufficiently drug-like properties to justify testing in

mice (fig. S9). We assessed aqueous solubility, plasma stability, plasma protein binding, hepatic microsome stability, and cellular permeability (fig. S9A). No severe liabilities were found. We next established minimally toxic parameters for dosing mice with RHT and performed a plasma pharmacokinetic study after administration of 1 mg/kg subcutaneously (fig. S9, B and C). Peak plasma levels were far in excess of those required for the key biological activities we had demonstrated in cell culture. Moreover, levels required for anticancer activity in vitro were maintained in excess of 2 hours in vivo.

We next established subcutaneous tumor xenografts of the human myeloid leukemia cell line M091 in nonobese diabetic (NOD)–severe combined immunodeficient (SCID) immunocompromised mice. When the mean tumor volume reached 100 mm<sup>3</sup>, we administered RHT at 1 mg/kg for 4 consecutive days each week for 3 weeks (Fig. 7D). Over the treatment period, there was no evidence of gross systemic toxicity (fig. S9D). RHT mediated marked, sustained inhibition of the growth of this very aggressive myeloid malignancy (Fig. 7D).

We then pursued pharmacodynamics studies. Mice bearing xenografts were given a single dose of RHT. Tumors were explanted 4 hours later, and *HSPA8* and *TXNIP* mRNA levels were determined by means of reverse transcription polymerase chain reaction (RT-PCR) (Fig. 7E). Similar to

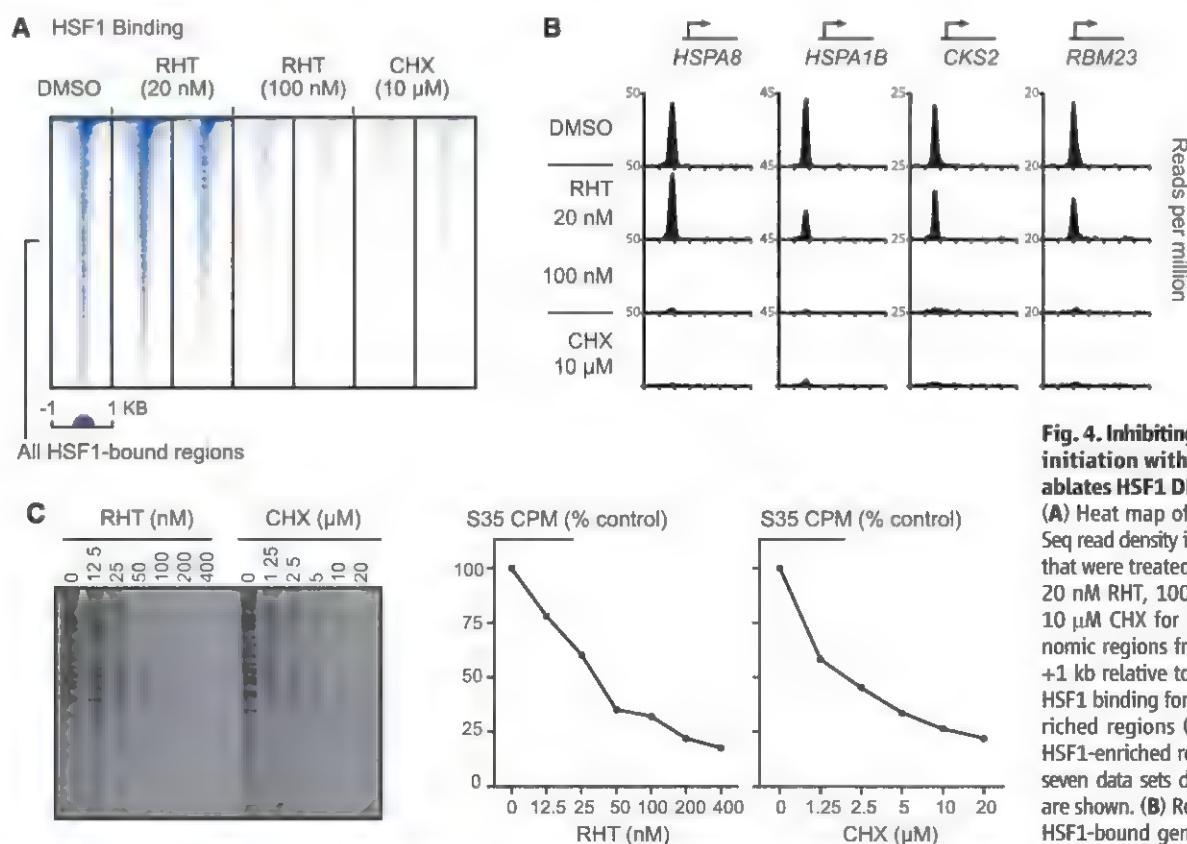


**Fig. 4. Inhibiting translation initiation with rocaglates ablates HSF1 DNA binding.** (A) Heat map of HSF1 ChIP-Seq read density in M0-91 cells that were treated with DMSO, 20 nM RHT, 100 nM RHT, or 10 μM CHX for 6 hours. Genomic regions from -1 kb to +1 kb relative to the peak of HSF1 binding for all HSF1-enriched regions (union of all HSF1-enriched regions in the seven data sets depicted here) are shown. (B) Representative HSF1-bound genes in M0-91 cells (*HSPA8*, *HSPA1B*, *CKS2*, and *RBM23*).

The x axis depicts from -2 kb from the transcription start site (TSS) to 5 kb from the TSS for each gene. (C) Autoradiograph of 535-labeled protein lysates from MCF7 cells treated for 6 hours with the indicated concentrations of RHT or CHX. Graphs show the counts per minute from acetone precipitation of proteins in each sample, quantitated by using a scintillation counter.



the effects we observed in cell culture, RHT caused a strong decrease in *HSP48* transcript levels and a strong increase in *TXNIP* transcript levels. In a separate experiment, we monitored the uptake of fluorescently labeled 2-deoxyglucose 48 hours after RHT dosing. RHT strongly suppressed uptake of this glucose analog by these tumors (Fig. 7F). Clearly, the effects of RHT achieved in cell culture could also be achieved in whole animals.

## Discussion

HSF1 provides essential support for the malignant state by blocking apoptotic responses and promoting protein synthesis, anabolic energy metabolism, mitogenic signaling pathways, and pathways that facilitate invasion and metastasis (8, 14, 15, 19, 23, 28–30). Here, we show that the ability of HSF1 to maintain this cancer program is exquisitely sensitive to translational activity.

Our work establishes that the ribosome could function as a central information hub: Translational flux conveys information about the cell's metabolic status to regulate the transcriptional programs that support it. The specific molecular mechanisms are likely to be multifaceted, but HSF1 is clearly a linchpin in this process. One plausible mechanism for the effects of translation inhibitors on HSF1 activity could involve the translation of mRNA for a modifier of HSF1 transcriptional activity that is sensitive to subtle changes in translation activity, involving eIF4A and/or other initiation factors. Because HSF1 regulates the expression of genes encoding for ribosomal subunits and other regulators of translation (8, 15, 31), the existence of a feedforward regulatory circuit involving the protein translation machinery and HSF1 is also possible.

HSF1 is centrally poised to support protein folding and biomass expansion as well as many other functions to which malignant cells are addicted (8, 14, 15, 32). We postulate that the translation/HSF1 link we have uncovered in cancer may derive from ancient systems geared to align and synchronize essential cellular functions for growth and survival. In comparison, in the nematode HSF1 is a longevity factor, and in yeast it is an essential gene that participates in cotranslational quality control (33–35).

In man, the translation/HSF1 link is particularly important in supporting the malignant phenotype because it can respond to varied metabolic inputs that are commonly dysregulated in cancer (5, 6, 36–38). This translation/HSF1 link allows these metabolic inputs to bolster the cytoprotective milieu, helping tumor cells to accommodate the drastic internal imbalances arising during oncogenesis as well as the severe external stresses arising from therapeutic interventions (39). The tight coordination of protein translation and HSF1 activation, together with the many ways that cells integrate the derangements of malignancy with translational activity, suggests that unifying principles drive HSF1 activation across the extraordinarily wide range of human cancers in which that activation occurs (8, 22).

Although cancer cells often co-opt powerful, adaptive nononcogene systems for their benefit (40), it now appears that by co-opting the link between the ribosome and HSF1, cancers become especially vulnerable to agents that target translation and its upstream regulatory pathways. In this regard, our animal experiments suggest that targeting translation initiation may offer a strategy for reversing HSF1 activation and disabling the metabolic and cytoprotective addictions of malignant cells.

## Materials and Methods

### Cell Lines

WI38, CHP100, HeLa, 293T, PC3, MCF7, and NIH3T3 cells were purchased from American Type Culture Collection (ATCC). Immortalized *Nf1* knockout MEFs and littermate wild-type control MEFs were kind gifts from K. Cichowski. Littermate-derived euploid and trisomic primary MEFs were described previously (20). RHT treatments experiments were performed by using chromosome 13 trisomic cell lines and littermate control euploid cell lines that carried a single Robertsonian translocation. Early-passage MEFs

were used to ensure that additional karyotypic changes had not yet occurred. Two primary human cell lines (CCD112 CoN and CCD841 CoN), five MIN lines (HCT-116, HCT-15, DLD-1, SW48, and LoVo), and five CIN lines (Caco2, HT-29, SW403, SW480, and SW620) were obtained from ATCC. Chromosome number and karyotype information were obtained from the National Cancer Institute database and the COSMIC data set at the Sanger Institute. M0-91 cells were previously described (27). The M0-91 cell line used in this study were established from explanted M0-91 tumors that had been xenografted once in mice. All cell cultures were maintained under 5% CO<sub>2</sub> in media according to their specifications.

### mRNA Expression Profiling and Analysis

Expression profiles for MCF7 cells treated for 6 hours with anisomycin (15  $\mu$ M), emetine (7  $\mu$ M), cephaeline (6  $\mu$ M), and cycloheximide (14  $\mu$ M) were previously deposited in the Connectivity Map (41). MCF7 cells were treated with 200 nM rocaglamide A or 50 nM RHT for 6 hours, and RNA was then purified after extraction with TRIzol reagent [Invitrogen (Carlsbad, CA), catalog no. 15596-026]. Gene expression analysis was

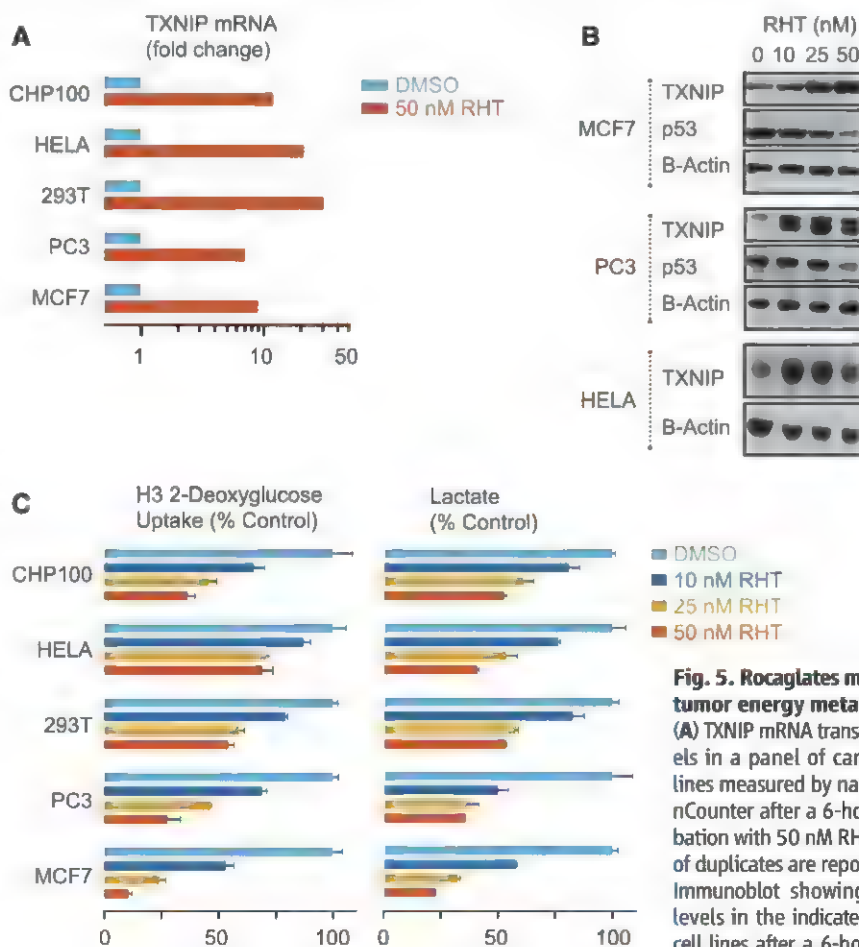


**Fig. 5. Rocaglates modulate tumor energy metabolism.** (A) TXNIP mRNA transcript levels in a panel of cancer cell lines measured by nanostring nCounter after a 6-hour incubation with 50 nM RHT. Mean of duplicates are reported. (B) Immunoblot showing TXNIP levels in the indicated cancer cell lines after a 6-hour incubation with the indicated concentration of RHT.  $\beta$ -actin is the loading control. The effect on p53, a short half-life protein, is shown. (C) Effects of the indicated amount of RHT on [H3]-2-deoxyglucose uptake (left) and lactate production (right) in a panel of cancer cell lines after 8 hours of incubation. Error bars indicate mean  $\pm$  SEM of triplicates.

performed by using Affymetrix (Santa Clara, CA) GeneChip HT Human Genome U133A 96-Array Plates, and data was analyzed as previously described (8). All microarray raw data were de-

posited in a public database [National Center for Biotechnology Information Gene Expression Omnibus (GEO) pending]. Gene set enrichment analysis of the differentially expressed genes

after treatment of MCF7 cells with translation elongation inhibitors was performed by using the gene set enrichment analysis (GSEA) Web site release version 3.84 (42). Enrichment for

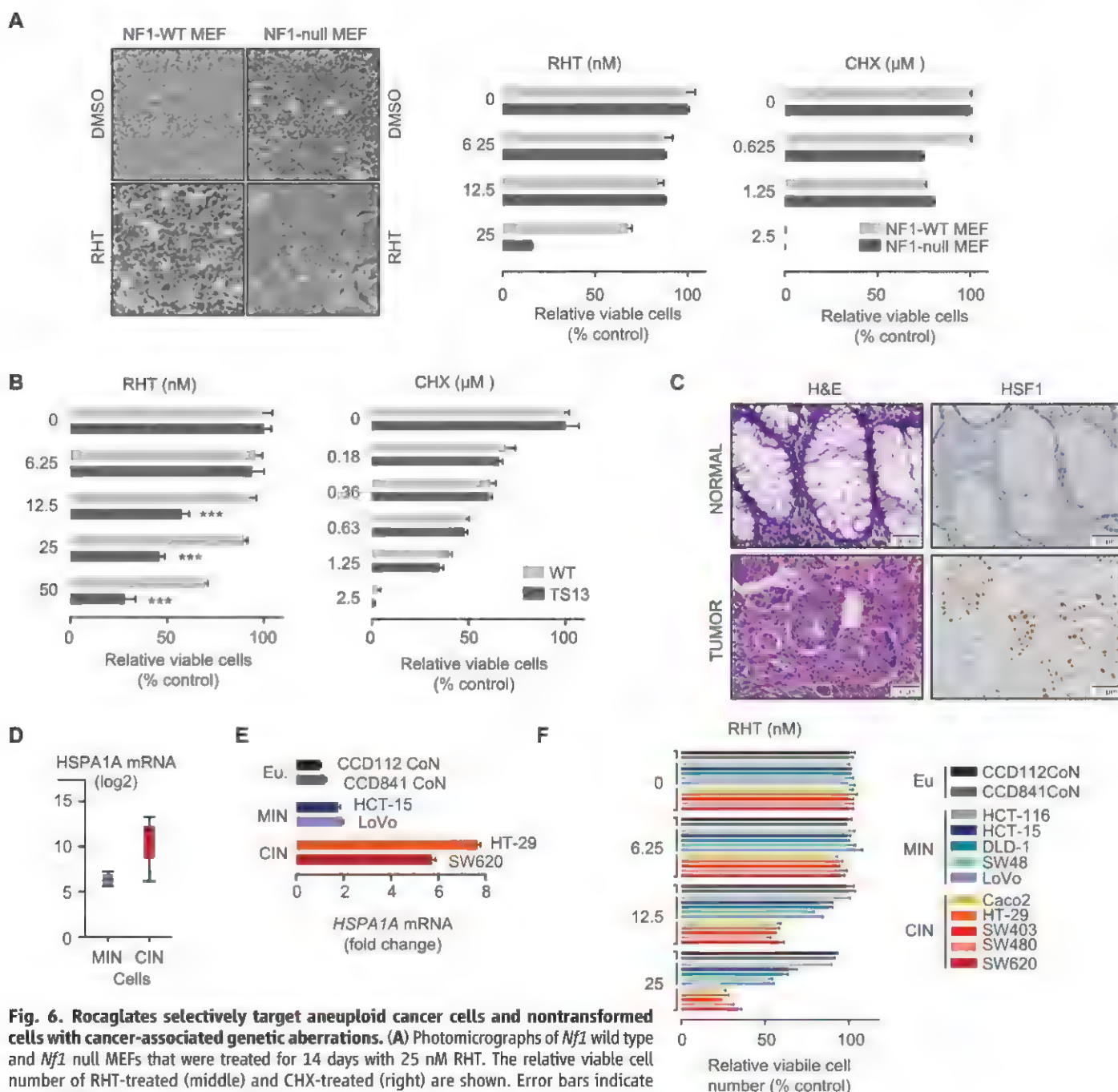


**Fig. 6. Rocaglates selectively target aneuploid cancer cells and nontransformed cells with cancer-associated genetic aberrations.** (A) Photomicrographs of *Nf1* wild type and *Nf1* null MEFs that were treated for 14 days with 25 nM RHT. The relative viable cell number of RHT-treated (middle) and CHX-treated (right) are shown. Error bars indicate mean  $\pm$  SEM of  $n = 6$  replicates. (B) Effect of 72 hours treatment with either RHT (left) or cycloheximide (right) on the proliferation of MEFs carrying a single extra copy of 120 Mb of chromosome 13 (TS13) compared with MEFs derived from littermate controls (WT), [mean  $\pm$  SD,  $n = 3$  replicates,  $***P < 0.001$ , two-way analysis of variance (ANOVA)]. (C) Photomicrographs of normal colon epithelial cells and invasive colon adenocarcinoma (hematoxylin and eosin stains and HSF1 immunohistochemistry) from the same section of a human tumor resection (immunostained simultaneously). HSF1-expressing cells stain brown, and HSF1-negative cells stain blue from the toluidine blue counterstain. Scale bar, 50  $\mu$ m. (D) *HSPA1A* mRNA transcript levels are elevated in colorectal adenocarcinomas with high-grade aneuploid karyotypes. Data from three MIN and nine CIN colon cancer cell lines from the GSK Cancer Cell Line Genomic Profiling Data as described in the methods. Box plot, bar is median, and whiskers are min and max (three cell lines in MIN category in triplicate 9 cell lines in CIN category in triplicate). (E) RT-PCR analysis of *HSPA1A* mRNA levels in the indicated euploid nontransformed cell lines, and MIN and CIN cancer cell lines. Error bars indicate mean  $\pm$  SD of triplicates. (F) Effect of RHT on the proliferation of a panel of cell lines with high-grade aneuploid karyotypes (CIN lines: Caco2, HT29, SW403, SW480, and SW620); near-euploid karyotypes with microsatellite instability (MIN lines: HCT-116, HCT-15, DLD-1, SW48, and LoVo); or nontransformed colon epithelial cell lines with a euploid chromosomal number (CCD112CoN and CCD841CoN), (mean  $\pm$  SD,  $n = 3$  replicates,  $***P < 0.001$ , two-way ANOVA) treated for 72 hours.



HSF1-bound genes among the genes differentially expressed after treatment of MCF7 cells with translation elongation inhibitors was conducted by using GSEA v2.08 software (42). HSF1-bound genes in MCF7 cells were defined as those genes bound in at least two of the four data sets [two data sets from this study and two from (8)].

Evaluation of *HSPA1A* mRNA levels was performed by using data from the GlaxoSmithKline (GSK) Cancer Cell Line Genomic Profiling Data (<https://cabig.nci.nih.gov/community/caArray>) GSK-data. MIN lines used were HCT15, LS174T, SW48. CIN lines used were NCIH508, NCIH747, SW1116, SW1417, SW403, SW480, SW620, T84, and SW948.

### ChIP-Seq and ChIP-PCR

Described in supplementary materials, materials and methods.

### Immunoblot

Described in supplementary materials, materials and methods.

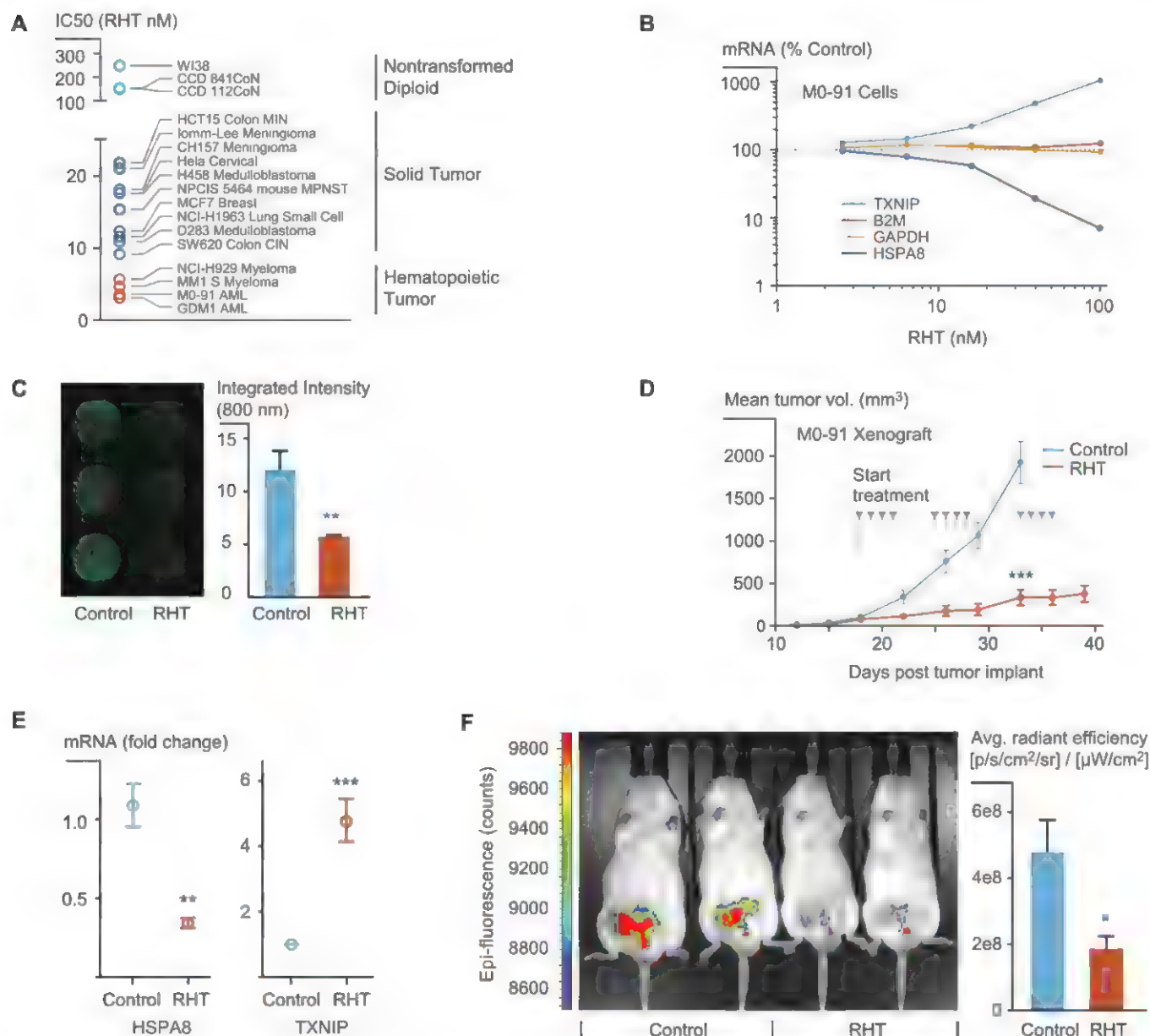


**Fig. 7. Rocaglates suppress tumor growth, *HSPA8* mRNA levels and glucose uptake in vivo.** (A) Scatter plot of IC<sub>50</sub> values of the growth of a diverse panel of cell lines treated with RHT. Cells were treated for 5 days. Red indicates hematopoietic cancer lines, dark blue indicates solid tumor cell lines, and light blue indicates euploid nontransformed cells. (B) mRNA levels of *HSPA8*, *TXNIP*, and control housekeeping genes in M0-91 cells treated with RHT. Mean of duplicates are reported. (C) Glucose uptake of IR Dye 800CW 2-deoxyglucose (2-DG) in M0-91 cell lines treated with RHT. Imaging was performed by using LICOR. (Right) Quantitation of measured intensity (error bars indicate mean + SEM;  $P < 0.005$ , two-tailed  $t$  test,  $n = 4$  replicates). (D) Plot of the tumor volume of M0-91 acute myeloid leukemia xenografts treated with vehicle or RHT. The mean tumor volume (in cubic millimeters) is plotted over time. Mice were treated with subcutaneous injections starting on day 18 after implantation [either vehicle alone or

RHT (1 mg/kg), on days marked by downward pointing arrows]. Eight mice were in each treatment group (error bars indicate mean + SEM;  $P < 0.0001$ ). (E) RT-PCR analysis of *HSPA8* and *TXNIP* mRNA levels from tumor xenografts after a single treatment of either vehicle or RHT (1 mg/kg, subcutaneous; five mice in each group). Tumors were harvested 4 hours after treatment (error bars indicate mean + SEM; *HSPA8*,  $P < 0.005$ ; *TXNIP*,  $P < 0.0005$ , two-tailed  $t$  test,  $n = 5$  replicates). (F) Representative image of epifluorescence of IRDye 800CW 2-deoxyglucose (2-DG) uptake in M0-91 xenografts. Mice bearing tumors were treated with vehicle or RHT (1 mg/kg) as described in the supplementary materials, materials and methods; four mice in each group. Images were acquired 48 hours after the last treatment. (Right) Quantitation of measured radiant efficiency from epifluorescence of IRDye 800CW 2-DG from images of M0-91 xenografts (error bars indicate mean + SEM;  $P = 0.031$ , two-tailed  $t$  test,  $n = 4$  replicates).

### LINCS Analysis

To identify chemical and genetic modulators that are correlated with HSF1 inactivation, we queried LINCS supported by the NIH Common Fund. This resource at the Broad Institute is a massive expression-profiling initiative to catalog the cellular consequences of both small-molecule and genetic perturbations. The expression data were generated by using a high-throughput Luminex-based assay (Luminex, Austin, TX) as described previously (43). Whole-genome expression profiles are inferred from changes in the expression of 1000 landmark genes. The changes in gene expression resulting from each of the genetic and chemical perturbations are rank-ordered from highest to lowest according to their differential expression relative to control treatments. Changes in gene expression caused by a novel perturbation (the “query” signature) can then be compared with the cataloged expression profiles. Profiles that are positively correlated with the query signature are given a positive score, whereas profiles that are negatively correlated to the query signature are given a negative score.

For the analysis, we generated an HSF1 inactivation signature (table S4) of the 50 genes most positively regulated (reduced expression upon HSF1 depletion with shRNA) and 10 genes most negatively regulated (increased expression upon HSF1 depletion with shRNA) in the breast cancer cell lines, MCF7 and BPLER (44) [average of the difference between the ha6 shRNA and scrambled shRNA control values between the two cell lines (8)], that were also bound by HSF1 in our ChIP-seq experiments. This signature was used to query all 161,636 shRNA and compound signatures (collapsed from a total of 614,216 individual profiles from at least three biological replicates) in the LINCS data set produced in nine cell lines (MCF7, breast cancer; HT29, colon cancer; HEPG2, hepatoblastoma; A549, lung cancer; HCC515, lung cancer; A375, melanoma; PC3, prostate cancer; VCAP, prostate cancer; HA1E, immortalized but nontransformed kidney epithelium). A connectivity score was assigned to each of the expression profiles from the 161,636 perturbations on the basis of a weighted Kolmogorov-Smirnov statistic as previously described (42, 43). GSEA (42) was performed on this rank-ordered list in order to determine gene or chemical classes that were most enriched among the positively and negatively connected signatures. The sets analyzed by means of GSEA encompassed the shRNAs corresponding to the genes comprising all 186 KEGG pathway gene sets. The sets also included 110 chemical classes grouped according to the Anatomical Therapeutic Chemical (ATC) Classification System. In addition, we added a set composed of elongation initiation factors. Statistical significance was tested by using 100 random sets size-matched to the set being tested.

### Reporter cell lines

Y9 reporter NIH3T3 cells (45) were infected with lentivirus for the doxycycline regulatable

pTRIPZ-nonsilencing construct (RHS4743). These cells were heat shocked and incubated with doxycycline and then sorted by use of flow cytometry to isolate strong enhanced GFP (eGFP) and Turbo RFP (tRFP) expressors. Sorting was repeated twice for enrichment. Noninduced cells were sorted to remove cells expressing eGFP and tRFP at baseline to make R4.1 B4 cells.

To make the high-throughput screening cell line NIH3T3HGL, the parent vector LV-eGFP $\Delta$ LUC was modified by removing the cytomegalovirus promoter and introducing a 470-bp fragment of the human HSP70B' construct upstream of the eGFP promoter. NIH3T3 cells were infected with lentivirus generated from this construct, and the high eGFP expressors were isolated by means of flow cytometry after heat shock.

### High-Throughput Small-Molecule Screen

Described in supplementary materials, materials and methods.

### Dual Reporter Cell Assay

Described in supplementary materials, materials and methods.

### Rocaglamide/Rocaglate Derivatives

Rocaglamide/rocaglate derivatives were prepared with total synthesis methods as previously described (12, 13).

### Nanostring/nCounter Analysis

The cells were lysed at a concentration of 10,000 cells/ $\mu$ L with RTL buffer [Qiagen (Valencia, CA) catalog no. 79216] and dissociated using a cell shredder (Qiagen catalog no. 79656). The total RNA in 5  $\mu$ L of lysate was hybridized with the capture and reporter probes overnight at 65°C and processed according to the nCounter recommended protocol. Target/probe complexes were immobilized in nCounter Cartridges for data collection using an nCounter Digital. The data was analyzed according to the manufacturer's guidelines. All data were normalized to the expression levels of house keeping genes (*ACTB*, *B2M*, *GAPDH*, *GUSB*, *HPRT1*, and *RPL10*).

### S35 Labeling

MCF7 cells were grown to confluence in six-well dishes in standard Dulbecco's minimum essential medium (DMEM) (+10% fetal bovine serum). The cells were rinsed twice in 1 $\times$  phosphate-buffered saline (PBS) and then placed in DMEM without methionine or cysteine [Life Technologies (Guilford, CT) no. 21013024] for 30 min. EasyTag S35 protein labeling mix (NEG772002MC) was added for 15 min. The cells were rinsed twice in 1 $\times$  PBS and then lysed in TNEK buffer. Cell lysates were prepared in TNEK buffer {50 mM Tris, pH 7.4; NP-40 1%; EDTA 2 mM; KCl 200 mM and protease inhibitor cocktail [Roche Diagnostics (Indianapolis, IN) catalog no. 11836153001]}. Samples (15  $\mu$ g total protein/lane) were analyzed by means of SDS-polyacrylamide gel electrophoresis. The gel was incubated for 10 min in 0.7 M

sodium salicylate and 10% glycerol. The dried gel was used to expose film. Counts per minute were assessed by using a scintillation counter.

### Glucose Uptake

500,000 cells plated in 24-well tissue culture plates were treated for 8 hours with RHT. The cells were then washed in 1 $\times$  PBS ( $\times$ 2) and placed in glucose-free and serum-free DMEM for 20 min. Glucose uptake was measured by using <sup>3</sup>H-2-Deoxyglucose (<sup>3</sup>H-2DG), incubation for 15 min (final 1  $\mu$ Ci/ml, 50  $\mu$ M 2DG). The cells were washed with 1 ml of cold 1 $\times$  PBS ( $\times$ 2), lysed with 0.2 M sodium hydroxide, and then counted by use of scintillation. Experiments were performed in triplicate. Parallel treated cultures cells were stained with Sytox-green (Invitrogen, catalog no. S7020) for normalization. Each analysis was performed three times. The SEM is displayed.

Glucose uptake was also measured by using IRD800 2-deoxyglucose (Fig. 7C). M0-91 cells were washed and resuspended in glucose-free medium (10<sup>6</sup> cells/ml). Cells were dispensed (100  $\mu$ L/well) in triplicate wells and incubated for 20 min with 5  $\mu$ M of the IRDye 800CW 2-DG Optical Probe [LI-COR Biosciences (Lincoln, NB) catalog no. 926-08946]. The cells were then washed  $\times$ 4 with cold PBS, and the signal was acquired by using an infrared Odyssey imaging system (LI-COR Biosciences).

### Lactate Production

500,000 cells were plated in 24-well tissue culture plates and were treated for 8 hours with RHT. After two washes with 1 $\times$  PBS, the cells were incubated for 30 min at 37°C in 500  $\mu$ L of filter sterilized 1 $\times$  Krebs buffer (126 mM NaCl, 2.5 mM KCl, 1.2 mM NaH<sub>2</sub>PO<sub>4</sub>, 1.2 mM MgCl<sub>2</sub>, 2.5 mM CaCl<sub>2</sub>, 10 mM Glucose, 25 mM NaHCO<sub>3</sub>, 10 mM HEPES-KOH pH 7.4). The supernatant was collected, and the lactate was measured with a Lactate Assay Kit [BioVision (Milpitas, CA) catalog no. K-607] according to the manufacturer's guidelines. Parallel treated cultures cells were stained with Sytox Green (Invitrogen, catalog no. S7020) for normalization. Each analysis was performed three times. The SEM is displayed.

### Cell Viability Assay

Relative cell growth and survival were measured in 96-well microplate format by using the fluorescent detection of resazurin dye reduction as an endpoint (544 nm excitation and 590 nm emission). Two thousand adherent cells and 10,000 suspension cells were plated 24 hours before compound exposure (for 72 hours). Each analysis was performed three times. For all bar graphs, the SEM is displayed, unless indicated otherwise.

### Immunohistochemistry

Paraffin blocks of human colon adenocarcinoma tissue were obtained from the archives of BWH in accordance with the regulations for excess tissue use stipulated by the BWH institutional review



board. Immunohistochemistry for HSF1 was performed as previously described (8).

### Drug Metabolism and Pharmacokinetic Studies

Described in supplementary materials, materials and methods.

### Xenograft Experiment

5e7 M0-91 cells were implanted with Matrigel (BD Biosciences, San Jose, CA) subcutaneously in the right inguinal region of NOD-SCID mice. When the mean tumor volume reached 100 mm<sup>3</sup>, RHT formulated in hydroxypropyl beta-cyclodextrin was administered by means of subcutaneous par-enteral administration (1 mg/kg) according to the treatment schedule shown in Fig. 7D. Tumor size was measured twice each week by a lab member (M.D.) who was blinded to the treatment groups. There were eight mice in each treatment group (RHT-treated or vehicle-treated). Body weight was measured twice each week. Body condition score (BCS) as monitored by facility vets did not go below 2+ in either treatment group throughout the experiment.

### In Vivo Glucose Uptake Experiment

M0-91 cells were inoculated into the inguinal region of NOD-SCID mice. Seventeen days later, the mice were treated with a dose of RHT (1 mg/kg; 4 mice) or vehicle control (4 mice). Four hours later, the mice were given retro-orbital injections of 100  $\mu$ l IRDye 800CW 2-DG Optical Probe (10 nmol; LI-COR Biosciences, no. 926-08946), and then an additional 4 hours later, these mice were again treated with RHT (1 mg/kg) or vehicle control. Thirty-six hours after the last RHT dose, mice were imaged (IVIS; excitation 745 nm, emission 800 nm). Data were analyzed by using Living Image software (PerkinElmer, Waltham, MA).

### Real-Time PCR

RNA was purified with RNEasy columns (Qiagen, catalog no. 74104). Quantitative PCR to evaluate mRNA levels was performed by using RT2 SYBR Green qPCR Mastermix (SABiosciences) and primer assay pairs (SABiosciences, Valencia, CA) on a 7900HT ABI Detection System.

### References and Notes

- D. Ruggero, P. P. Pandolfi, *Nat. Rev. Cancer* **3**, 179–192 (2003). doi: 10.1038/nrc1015; pmid: 12612653
- J. C. Chan et al., *Sci. Signal.* **4**, ra56 (2011). doi: 10.1126/scisignal.2001754; pmid: 21878679
- R. J. White, *Nat. Rev. Mol. Cell Biol.* **6**, 69–78 (2005). doi: 10.1038/nrm1551; pmid: 15688068
- K. M. Hannan et al., *Mol. Cell. Biol.* **23**, 8862–8877 (2003). doi: 10.1128/MCB.23.23.8862-8877.2003; pmid: 14612424
- D. Silvera, S. C. Formenti, R. J. Schneider, *Nat. Rev. Cancer* **10**, 254–266 (2010). doi: 10.1038/nrc2824; pmid: 20332778
- P. P. Roux, I. Topisirovic, *Cold Spring Harb. Perspect. Biol.* **4**, a012252 (2012). doi: 10.1101/cshperspect.a012252; pmid: 22888049
- F. U. Hartl, M. Hayer-Hartl, *Science* **295**, 1852–1858 (2002). doi: 10.1126/science.1068408; pmid: 11884745
- M. L. Mendillo et al., *Cell* **150**, 549–562 (2012). doi: 10.1016/j.cell.2012.06.031; pmid: 22863008
- L. Whitesell, S. Lindquist, *Expert Opin. Ther. Targets* **13**, 469–478 (2009). doi: 10.1517/1472220902832697; pmid: 19335068
- M. E. Bordeleau et al., *J. Clin. Invest.* **118**, 2651–2660 (2008). pmid: 18551192
- J. M. Chambers et al., *Org. Lett.* **15**, 1406–1409 (2013). doi: 10.1021/ol400401d; pmid: 23461621
- C. M. Rodrigo, R. Cencic, S. P. Roche, J. Pelletier, J. A. Porco Jr., *J. Med. Chem.* **55**, 558–562 (2012). doi: 10.1021/jm201263k; pmid: 22128783
- S. P. Roche, R. Cencic, J. Pelletier, J. A. Porco Jr., *Angew. Chem. Int. Ed. Engl.* **49**, 6533–6538 (2010). doi: 10.1002/anie.201003212; pmid: 20687060
- X. Jin, D. Moskopidis, N. F. Mivechi, *Cell Metab.* **14**, 91–103 (2011). doi: 10.1016/j.cmet.2011.03.025; pmid: 21723507
- C. Dai, L. Whitesell, A. B. Rogers, S. Lindquist, *Cell* **130**, 1005–1018 (2007). doi: 10.1016/j.cell.2007.07.020; pmid: 17889646
- H. Parikh et al., *PLoS Med.* **4**, e158 (2007). doi: 10.1371/journal.pmed.0040158; pmid: 17472435
- C. A. Stoltzman et al., *Proc. Natl. Acad. Sci. U.S.A.* **105**, 6912–6917 (2008). doi: 10.1073/pnas.0712199105; pmid: 18458340
- S. Y. Kim, H. W. Suh, J. W. Chung, S. R. Yoon, I. Choi, *Cell. Mol. Immunol.* **4**, 345–351 (2007). pmid: 17976314
- C. Dai et al., *J. Clin. Invest.* **122**, 3742–3754 (2012). doi: 10.1172/JCI62727; pmid: 22945628
- Y. C. Tang, B. R. Williams, J. J. Siegel, A. Amon, *Cell* **144**, 499–512 (2011). doi: 10.1016/j.cell.2011.01.017; pmid: 21315436
- B. R. Williams et al., *Science* **322**, 703–709 (2008). doi: 10.1126/science.1160058; pmid: 18974345
- S. Santagata et al., *Proc. Natl. Acad. Sci. U.S.A.* **108**, 18378–18383 (2011). doi: 10.1073/pnas.1115031108; pmid: 22042860
- F. Fang, R. Chang, L. Yang, *Cancer* **118**, 1782–1794 (2012). doi: 10.1002/cncr.26482; pmid: 22009757
- L. Alinari et al., *Clin. Cancer Res.* **18**, 4600–4611 (2012). doi: 10.1158/1078-0432.CCR-12-0839; pmid: 22791882
- R. Cencic et al., *PLoS ONE* **4**, e5223 (2009). doi: 10.1371/journal.pone.0005223; pmid: 19401772
- D. M. Lucas et al., *Blood* **113**, 4656–4666 (2009). doi: 10.1182/blood-2008-09-175430; pmid: 19190247
- M. Okabe et al., *Leuk. Res.* **19**, 933–943 (1995). doi: 10.1016/0145-2126(95)00039-9; pmid: 8632663
- L. Meng, V. L. Gabai, M. Y. Sherman, *Oncogene* **29**, 5204–5213 (2010). doi: 10.1038/onc.2010.277; pmid: 20622894
- S. Santagata et al., *ACS Chem. Biol.* **7**, 340–349 (2012). doi: 10.1021/cb200353m; pmid: 22050377
- K. L. Scott et al., *Cancer Cell* **20**, 92–103 (2011). doi: 10.1016/j.ccr.2011.05.025; pmid: 21741599
- V. L. Gabai et al., *Mol. Cell. Biol.* **32**, 929–940 (2012). doi: 10.1128/MCB.05921-11; pmid: 22215620
- S. D. Westerheide, J. Anckar, S. M. Stevens Jr., L. Sistonen, R. I. Morimoto, *Science* **323**, 1063–1066 (2009). doi: 10.1126/science.1165946; pmid: 19229036
- O. Brandman et al., *Cell* **151**, 1042–1054 (2012). doi: 10.1016/j.cell.2012.10.044; pmid: 23178123
- J. S. Hahn, Z. Hu, D. J. Thiele, V. R. Iyer, *Mol. Cell. Biol.* **24**, 5249–5256 (2004). doi: 10.1128/MCB.24.12.5249-5256.2004; pmid: 15169889
- A. L. Hsu, C. T. Murphy, C. Kenyon, *Science* **300**, 1142–1145 (2003). doi: 10.1126/science.1083701; pmid: 12750521
- S. D. Chou, T. Prince, J. Gong, S. K. Calderwood, *PLoS ONE* **7**, e39679 (2012). doi: 10.1371/journal.pone.0039679; pmid: 22768106
- S. M. Hensen et al., *Cell Stress Chaperones* **17**, 743–755 (2012). doi: 10.1007/s12192-012-0347-1; pmid: 22797943
- T. Peng, T. R. Golub, D. M. Sabatini, *Mol. Cell. Biol.* **22**, 5575–5584 (2002). doi: 10.1128/MCB.22.15.5575-5584.2002; pmid: 12101249
- L. Whitesell, S. Santagata, N. U. Lin, *Curr. Mol. Med.* **12**, 1108–1124 (2012). doi: 10.2174/156652412803306657; pmid: 22804235
- N. L. Solimini, J. Luo, S. J. Elledge, *Cell* **130**, 986–988 (2007). doi: 10.1016/j.cell.2007.09.007; pmid: 17889643
- J. Lamb et al., *Science* **313**, 1929–1935 (2006). doi: 10.1126/science.1132939; pmid: 17008526
- A. Subramanian et al., *Proc. Natl. Acad. Sci. U.S.A.* **102**, 15545–15550 (2005). doi: 10.1073/pnas.0506580102; pmid: 16199517
- D. Peck et al., *Genome Biol.* **7**, R61 (2006). doi: 10.1186/gb-2006-7-7-r61; pmid: 16859521
- T. A. Ince et al., *Cancer Cell* **12**, 160–170 (2007). doi: 10.1016/j.ccr.2007.06.013; pmid: 17692807
- T. J. Turbyville et al., *J. Nat. Prod.* **69**, 178–184 (2006). doi: 10.1021/jp058095b; pmid: 16499313

**Acknowledgements:** We thank T. Volkert, J. Love, S. Gupta, and the WIRB–Genome Technology Core for sequencing support; S. Malstrom (Koch Institute for Integrative Cancer Research) for assistance with in vivo imaging; G. Bell, P. Thiru, and A. Lancaster for assistance with informatics analysis; the Connectivity Map team at the Broad Institute for generation of the LINC data set and query tools; Joe Negri and the MLPCN team at the Broad Institute for chemical screening; and M. Duquette for assistance with animal experiments. We also thank C. Rodrigo (Boston University) for compound synthesis. We thank the Lindquist laboratory for helpful discussions and suggestions. The work was supported by the Johnson & Johnson's Corporate Office of Science and Technology focused funding program (L.W.), the Marble Fund (S.L.), and NIH R01 CA175744-01 (L.W.). The MLPCN screen was supported by R03 MH086465-01 and R03 DA027713-01 to L.W. This work was supported by the NIH Common Fund's LINC program (SU54HG006093, "Large scale gene expression analysis of cellular states") to T.R.G. J.A.P. Jr. is supported by R01 GM073855. S.L. is an Investigator of the Howard Hughes Medical Institute. M.L.M. was supported by American Cancer Society New England Division–SpinOdyssey (PF-09-253-01-DMC). S.S. is supported by NIH (K08NS064168), the Brain Science Foundation, the American Brain Tumor Association, the Beez Foundation, the V Foundation, and the Jared Brantman Sunflowers for Life Fund. The expression profiling and ChIP-Seq data are deposited in GEO (GSE45853). The MLPCN chemical screening data are deposited in Pubchem (AID: 2118).

### Supplementary Materials

[www.sciencemag.org/content/full/341/6143/1238303/suppl/DC1](http://www.sciencemag.org/content/full/341/6143/1238303/suppl/DC1)

Materials and Methods

Figs. S1 to S9

Reference (46)

Tables S1 to S5

25 March 2013; accepted 24 May 2013

10.1126/science.1238303

# Bright Hot Impacts by Erupted Fragments Falling Back on the Sun: A Template for Stellar Accretion

Fabio Reale,<sup>1,2\*</sup> Salvatore Orlando,<sup>2</sup> Paola Testa,<sup>3</sup> Giovanni Peres,<sup>1,2</sup> Enrico Landi,<sup>4</sup> Carolus J. Schrijver<sup>5</sup>

Impacts of falling fragments observed after the eruption of a filament in a solar flare on 7 June 2011 are similar to those inferred for accretion flows on young stellar objects. As imaged in the ultraviolet (UV)—extreme UV range by the Atmospheric Imaging Assembly onboard the Solar Dynamics Observatory, many impacts of dark, dense matter display uncommonly intense, compact brightenings. High-resolution hydrodynamic simulations show that such bright spots, with plasma temperatures increasing from  $\sim 10^4$  to  $\sim 10^6$  kelvin, occur when high-density plasma ( $> 10^{10}$  particles per cubic centimeter) hits the solar surface at several hundred kilometers per second, producing high-energy emission as in stellar accretion. The high-energy emission comes from the original fragment material and is heavily absorbed by optically thick plasma, possibly explaining the lower mass accretion rates inferred from x-rays relative to UV–optical–near infrared observations of young stars.

Mass accretion from the circumstellar disk onto the stellar surface plays an important role in the late phases of star formation (1, 2). Young low-mass stars are presumably connected to and interact with circumstellar disks through magnetic funnels (3). The plasma accretes along the funnels at nearly free-fall velocity (hundreds of kilometers/second) onto the central young star. Most evidence for accretion originates from the region of impact of the disk material onto the stellar chromosphere and includes infrared and optical excess emission in lines and continuum (4–6) and a soft (energy  $< 0.7$  keV) x-ray excess above the coronal emission from dense ( $10^{11}$  to  $10^{13}$  cm<sup>-3</sup>) and hot (2 to 4 MK) plasma (7–9). Hot impact spots are observed in photospheric emission (10).

Current models suggest that the impact region is rather complex because of the interplay between radiation and hydrodynamics (11–14): The streams might be highly structured in both density and velocity, leading to inhomogeneous impact spots; the impacting material is heated to millions of degrees by kinetic energy dissipation and might partially sink into the chromosphere, its emission being substantially absorbed by the thick chromosphere and by the dense falling material itself. The impact can also drive strong motions and feed material into surrounding coronal

structures (14), as recently suggested for the classical T Tauri star TW Hydrae (accretion-fed corona) (15, 16). The density and velocity of the accreting material determine the temperature of the hot plasma and the sinking depth (13). This complexity hampers a deep understanding of the dynamical and radiative properties of the plasma in the impact region and, ultimately, of the accretion processes in young stars.

Here, we study plasma impacts observed after the solar flare on 7 June 2011 at 6 UT that show interesting analogies with inferred stellar accretion impacts. The flare was categorized as “M class” on the Global Online Enrollment System scale of the National Oceanic and Atmospheric Administration. It was observed by the ultraviolet (UV) and extreme UV (XUV) narrowband channels of the Atmospheric Imaging Assembly (AIA) (17) on board the Solar Dynamics Observatory (SDO) (18), with high spatial resolution ( $\sim 0.6$  arc sec per pixel) and high cadence (12 s) (19) (see supplementary materials, section S1). During the flare, we clearly see, in all SDO/AIA XUV channels, that a dense, dark filament is broken and violently ejected (movie S1). The cloud propagates outward at a speed of several hundred kilometers per second and fragments in all directions. The fastest fragments escape in the form of a typical coronal mass ejection (20), observed by the Solar and Heliospheric Observatory/Large Angle and Spectrometric Coronagraph (21) white light telescope. Slower fragments fall back onto the solar surface. They are visible in all AIA XUV channels as dark, irregular, and moving strips on the brighter background corona. During their fall, the fragments change their morphology, stretching and dividing further (19), but they generally maintain a coherent structure and remain dark throughout their trajectory. When the fragments

hit the solar surface, they drive intense brightenings in the impact region, visible in all AIA XUV and UV channels. Here, we focus our attention on these impacts (movies S2 and S3).

Before hitting the surface, many downfalling fragments follow similar parabolic trajectories (movie S2); one trajectory was traced to be close to a free fall from combining AIA and STEREO-SECCHI EUVI (22) images. We have measured several impact speeds to be in the range of 300 to 450 km/s (see supplementary materials, section S1.2), similar to typical stellar accretion flow speeds (23). We know that the fragments are dense and cool, because we see them in absorption in the XUV channels. From the amount of absorption, we constrain their density in the range of  $2$  to  $10 \times 10^{10}$  cm<sup>-3</sup> with a temperature of  $\sim 3 \times 10^4$  K (see supplementary materials, section S1.1). The impacts are dispersed over a large fraction of the solar surface (Fig. 1). The typical cross section of impacting fragments is around 2000 to 4000 km, whereas the long side of elongated fragments can extend to  $> 10^4$  km. The duration of the brightenings ranges between 1 and  $\geq 6$  min in the XUV and UV spectra. During each brightening, the XUV emission typically increases by factors of 2 to 5 over the unperturbed conditions.

According to magnetograms measured with the SDO/Heliioseismic and Magnetic Imager (HMI) (fig. S4), the trajectories of the falling fragments and most impacts occur in regions where the magnetic field is rather weak. Most fragments do not decelerate while falling, and the ram and thermal pressures of the fragments at the impacts are estimated to be substantially larger than the local magnetic pressure (supplementary materials, section S1.3). Thus, we can assume that the magnetic field does not play an important role in the impacts, and we can describe the plasma evolution with a purely hydrodynamic model of plasma blobs, falling in a low-density corona with an impact speed of 400 km/s and a density of  $5 \times 10^{10}$  cm<sup>-3</sup> (both in the measured ranges). We ran several two-dimensional simulations (cylindrical geometry) to match the observed variety of cases: a spherical droplet (with a radius of 2000 km), a train of droplets, and an elongated fragment (stream). An accurate description of the evolution required a very high spatial resolution (down to  $\sim 5$  km; see supplementary materials, section S2.1).

In our simulations, the very dense model fragments fell freely in the tenuous ambient atmosphere with a faint bow shock preceding them. As they hit the chromosphere, they penetrated and smashed against the layers whose pressure was equal to the ram pressure of the infalling fragment (movie S4). The single spherical droplet was soon squashed to a thin, dense, and hot layer and then bounced back, forming an outward surge that expanded at a speed of  $\sim 200$  km/s. The surge reached temperatures above  $10^5$  K, but it cooled down in a few seconds, due to the rapid expansion and radiative losses.

<sup>1</sup>Dipartimento di Fisica e Chimica, Università di Palermo, Piazza del Parlamento 1, 90134 Palermo, Italy. <sup>2</sup>Istituto Nazionale di Astrofisica (INAF)/Osservatorio Astronomico di Palermo, Piazza del Parlamento 1, 90134 Palermo, Italy. <sup>3</sup>Harvard-Smithsonian Center for Astrophysics, 60 Garden Street, MS 58, Cambridge, MA 02138, USA. <sup>4</sup>Department of Atmospheric, Oceanic and Space Sciences, University of Michigan, Ann Arbor, MI 48109, USA. <sup>5</sup>Lockheed Martin Advanced Technology Center, Palo Alto, CA 94304, USA.

\*Corresponding author. E-mail: reale@astropa.unipa.it



For comparison with observations, we computed the emission that would be detected with the AIA XUV channels where we expected the plasma to be mostly optically thin; that is, 94, 131, 171, 193, 211, and 335 Å. In agreement with the observation, the emission evolution was similar in all the channels (Fig. 1 and movie S5). The plasma became visible in this channel when it rose above the transition region while it bounced back. Although the surge expanded over several tens of seconds, the plasma remained bright for a much shorter time ( $\sim 20$  s) (Fig. 1) and then faded out rapidly, due to the cooling and rarefaction. The brightening region also remained small, not much larger than the initial size of the droplet; it was the internal part of the outward surge and

was almost featureless and hemispherical. The plasma did not rise substantially above the surface. We traced that most of the emission came from the original impacting droplet, with very little contribution from the ambient material.

The simulations with the train of droplets and the stream showed longer-living (to more than 100 s) and larger-scale (up to  $\sim 10,000$  km) bouncing structures (movies S6 to S9). Although the emitting plasma was in a shell, integration along the line of sight kept the emission concentrated along the central axis. The longer-lasting stream emission was structured in sequences of evolving blobs and fringes (Fig. 1).

The morphology of the emission in the simulations matches the observations, up to the later

phases when coupling to the surrounding magnetic field becomes important. The size of the emitting region and the temporal evolution of the emission in the simulations are in quantitative agreement with the observations. The observed light curves (fig. S5) have shapes, flux, and time scales similar to those derived from the simulations (fig. S9). The observed brightenings generally last longer than the simulated ones, as can be expected because the impacting fragments may be much more extended than the modeled ones or can be made by showers of smaller-scale blobs, slightly displaced from one another.

Simulations either with a much smaller density of the falling droplet ( $5 \times 10^9 \text{ cm}^{-3}$ ) (movie S10) or a much smaller impact speed (250 km/s)

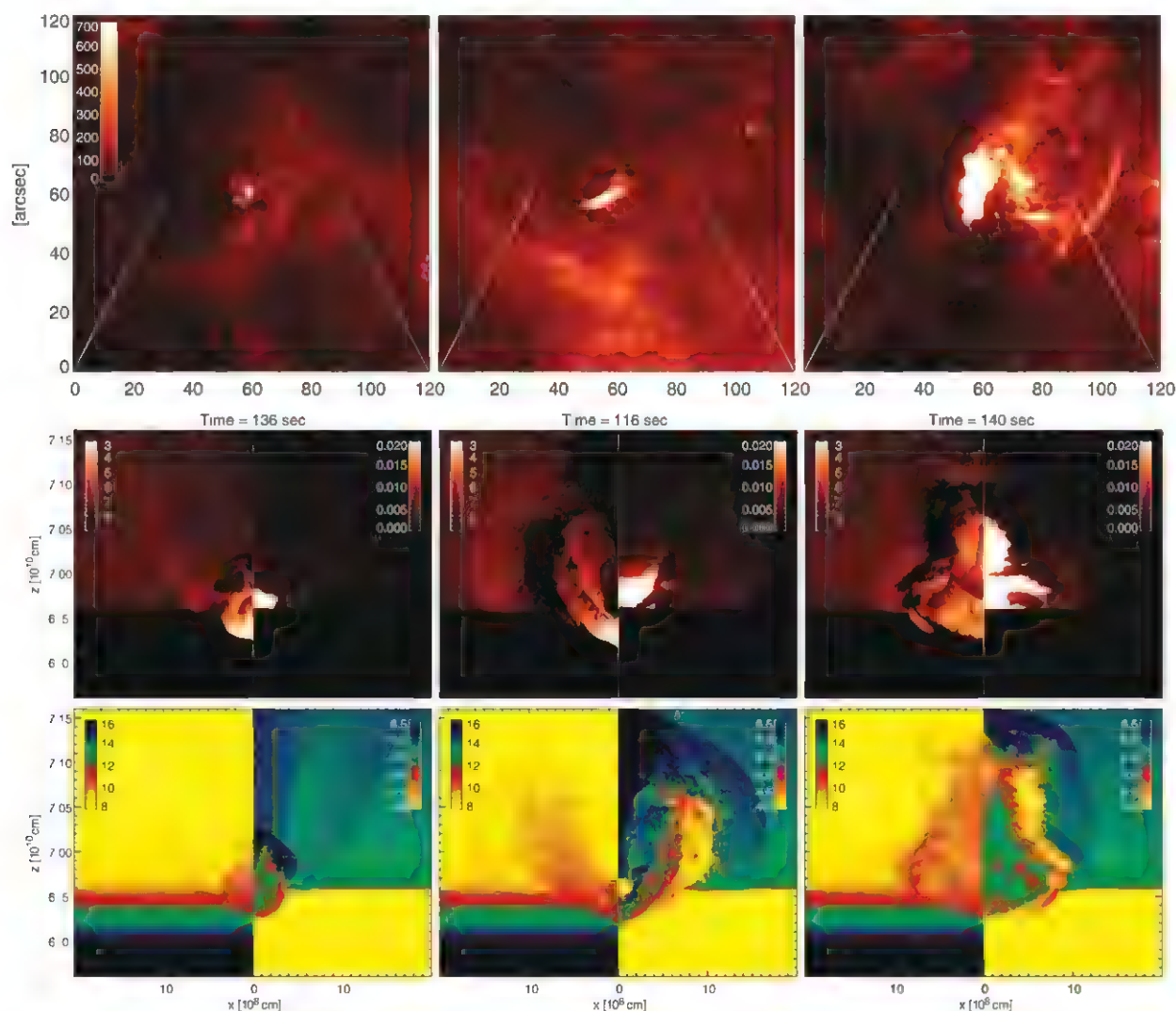


**Fig. 1. Observed and modeled impact brightenings.** (Top) Observed impacts of dense fragments erupted after an M-class solar flare on 7 June 2011 in the SDO/AIA 171 Å channel. Three cases are shown, representative of small- to large-scale impact brightenings (from left to right, taken at 7:26:25, 7:29:02, and 08:09:49 UT, with the plot origin at  $[x, y] = [357'', -132'']$ ,  $[468'', -137'']$ ,  $[335'', -130'']$  from the disk center). The color palette is data number (DN) per second per pixel. The white lines indicate how the width of the lower rows scales to the first row. (Middle) Simulated impacts of fragments that drive the respective brightenings (from left to right: droplet, train of droplets,

and stream) with a hydrodynamic model (at the labeled times since the beginning of the simulation). The left side of each map is a cross section of the emission in the 171 Å channel (logarithmic scale,  $\text{DN cm}^{-3} \text{ s}^{-1}$ ), and the right side is the emission integrated along the horizontal line of sight; i.e., tangential to the solar surface ( $4223 \text{ DN per pixel per second}$ ). When integrating, we exclude the heavily absorbed emission; i.e., by plasma at high density ( $> 10^{10} \text{ cm}^{-3}$ ) or below the transition region (see supplementary materials, section S2.2). (Bottom) Cross sections of the logarithm of the density (left, per cubic centimeter) and temperature (right, kelvin).

(movie S11) were unable to produce substantial emission (fig. S9A), indicating that the scenario is coherent. Thus, our hydrodynamic simulations show that the hot and bright impacts after the eruption are caused by the high density ( $>10^{10} \text{ cm}^{-3}$ ) and speed (free-fall speed, 300 to 450 km/s) of the downfalling debris. These values are close to those of the plasma involved in stellar accretion flows.

For most stellar accretion flows [see (15) for an exception], the mass accretion rates derived from x-rays are consistently lower (by one or more orders of magnitude) than the corresponding rates derived from UV optical near infrared observations (24–26). According to our analysis of a solar event, the impact of the dense fragments leads to detectable high-energy emission. From the model, we find that the mass of plasma responsible for the brightenings in the 171 Å channel (see supplementary materials, section S3) ranges between 5 and 30% of the original mass of the fragments. This is mainly because of the absorption by the optically thick chromosphere and/or by the dense part of the material outflowing after the impact (depending on the orientation of the impact region with respect to the line of sight). In addition, the simulations tell us that droplets with low density or low velocity are unable to produce substantial emission; the observations tell us that some of the falling fragments produce no detectable brightening. Therefore, both the absorption of x-ray emission from dense plasma and the wide range of velocity and density values of the infalling fragments contribute to underestimating the mass accretion rate from the XUV band.

Our simulations also show that the XUV emission arises from the original impacting material. Although our fragmented solar downflows differ from the conceptual stellar accretion flows (which are hypothesized to be continuous streams, chan-

neled by the magnetic field), the structure of the impact region (presenting hot plasma partially rooted in the chromosphere) is similar in the two cases. Moreover, as suggested recently (19), the accretion flows are likely to be frayed, even when they are magnetically confined and stream along straight tubes. Therefore, the dynamics and energetics spatially resolved in the solar observations are a template and laboratory to study accretion processes in astrophysics.

## References and Notes

1. D. Lynden-Bell, J. E. Pringle, *Mon. Not. R. Astron. Soc.* **168**, 603–637 (1974).
2. L. Hartmann, *Accretion Processes in Star Formation*, Cambridge Astrophysics Series (Cambridge Univ. Press, New York, 1998).
3. A. Koenigl, *Astrophys. J.* **370**, L39–L43 (1991).
4. C. Bertout, G. Basri, J. Bouvier, *Astrophys. J.* **330**, 350–373 (1988).
5. A. Natta, L. Testi, S. Randich, *Astron. Astrophys.* **452**, 245–252 (2006).
6. G. J. Herczeg, L. A. Hillenbrand, *Astrophys. J.* **681**, 594–625 (2008).
7. J. H. Kastner, D. P. Huenemoerder, N. S. Schulz, C. R. Canizares, D. A. Weintraub, *Astrophys. J.* **567**, 434–440 (2002).
8. A. Telleschi, M. Güdel, K. R. Briggs, M. Audard, L. Scelsi, *Astron. Astrophys.* **468**, 443–462 (2007).
9. C. Argiroffo, A. Maggio, G. Peres, *Astron. Astrophys.* **465**, L5–L8 (2007).
10. J.-F. Donati et al., *Mon. Not. R. Astron. Soc.* **386**, 1234–1251 (2008).
11. J. J. Drake, *13th Cambridge Workshop on Cool Stars, Stellar Systems and the Sun*, vol. 560 of *ESA Special Publication*, F. Favata, G. A. J. Hussain, B. Battrick, Eds. (European Space Agency, Noordwijk, 2005), p. 519.
12. H. M. Günther, J. H. M. M. Schmitt, J. Robrade, C. Liefke, *Astron. Astrophys.* **466**, 1111–1121 (2007).
13. G. G. Sacco et al., *Astron. Astrophys.* **522**, A55 (2010).
14. S. Orlando et al., *Astron. Astrophys.* **510**, A71 (2010).
15. N. S. Brckhouse, S. R. Cranmer, A. K. Dupree, G. J. M. Luna, S. Woik, *Astrophys. J.* **710**, 1835–1847 (2010).
16. A. K. Dupree et al., *Astrophys. J.* **750**, 73 (2012).
17. J. R. Lemen et al., *Sol. Phys.* **275**, 17–40 (2012).
18. W. D. Pesnell, B. J. Thompson, P. C. Chamberlin, *Sol. Phys.* **275**, 3–15 (2012).

19. D. E. Innes, R. H. Cameron, L. Fletcher, B. Inhester, S. K. Solanki, *Astron. Astrophys.* **540**, L10 (2012).
20. X. Cheng et al., *Astrophys. J.* **745**, L5 (2012).
21. G. E. Brueckner et al., *Sol. Phys.* **162**, 357–402 (1995).
22. J.-P. Wuelser et al., *Society of Photo-Optical Instrumentation Engineers (SPIE) Conference Series*, S. Fineschi, M. A. Gummin, Eds. (SPIE, San Diego, 2004), vol. 5171, pp. 111–122.
23. N. Calvet, E. Guilbrink, *Astrophys. J.* **509**, 802–818 (1998).
24. E. Guilbrink, L. Hartmann, C. Briceño, N. Calvet, *Astrophys. J.* **492**, 323–341 (1998).
25. J. Muzerolle, N. Calvet, C. Briceño, L. Hartmann, L. Hillenbrand, *Astrophys. J.* **535**, L47–L50 (2000).
26. R. L. Curran et al., *Astron. Astrophys.* **526**, A104 (2011).

**Acknowledgments:** We thank B. De Pontieu for help and suggestions. F.R., G.P., and S.O. acknowledge support from Italian Ministero dell'Università e Ricerca and Agenzia Spaziale Italiana, contract I/023/09/0. P.T. was supported by contract SP02H1701R from Lockheed-Martin to the Smithsonian Astrophysical Observatory. P.T. and C.J.S. are supported by NASA contract NNG04EA00C for the SDO AIA. E.L. is supported by NASA grants NNX11AC20G and NNX10AQ58G and NSF grant AGS-1154443. S.O. acknowledges partial support from the INAF. The software used in this work was, in part, developed by the U.S. Department of Energy-supported Advanced Simulation and Computing/Alliance Center for Astrophysical Thermonuclear Flashes at the University of Chicago. We acknowledge the CINECA Award HP10CEG9MW and INAF/Osservatorio Astronomico di Palermo for high-performance computing resources and support. SDO data were supplied courtesy of the SDO/HMI and SDO/AIA consortia. SDO is the first mission to be launched for NASA's Living With a Star Program. See the supplementary materials for details on the data, data analysis, and modeling.

## Supplementary Materials

www.sciencemag.org/cgi/content/full/science.1235692/DC1  
Materials and Methods  
Supplementary Text  
Figs. S1 to S9  
Table S1  
References (27–40)  
Movies S1 to S18

28 January 2013; accepted 5 June 2013

Published online 20 June 2013;

10.1126/science.1235692

# Switchable Static and Dynamic Self-Assembly of Magnetic Droplets on Superhydrophobic Surfaces

Jaakko V. I. Timonen,<sup>1,\*†</sup> Mika Latikka,<sup>1</sup> Ludwik Leibler,<sup>2</sup> Robin H. A. Ras,<sup>1,\*</sup> Olli Ikkala<sup>1,\*</sup>

Self-assembly is a process in which interacting bodies are autonomously driven into ordered structures. Static structures such as crystals often form through simple energy minimization, whereas dynamic ones require continuous energy input to grow and sustain. Dynamic systems are ubiquitous in nature and biology but have proven challenging to understand and engineer. Here, we bridge the gap from static to dynamic self-assembly by introducing a model system based on ferrofluid droplets on superhydrophobic surfaces. The droplets self-assemble under a static external magnetic field into simple patterns that can be switched to complicated dynamic dissipative structures by applying a time-varying magnetic field. The transition between the static and dynamic patterns involves kinetic trapping and shows complexity that can be directly visualized.

Functional patterns and structures are essential in a wide variety of natural and engineered systems (1). They often form of small

subunits by autonomous self-assembly, which is driven by free-energy gradients (2). Static self-assembly denotes a process in which the system

reaches an energy minimum (equilibrium) wherein the ordered structure appears. Archetypical examples are structured block copolymers (3, 4), nanoparticles (5, 6), nanorods (7), liquid crystals (8), and hierarchical supramolecular systems (9). They find applications in data storage (10) and structural colors (11), for instance. On the other hand, dynamic self-assembly denotes a process in which the structure forms when the system is forcefully kept away from an energy minimum (out of equilibrium) by continuous energy supply and dissipation (12, 13). Dynamic self-assembly is most notably encountered in biological systems (14–16),

<sup>1</sup>Department of Applied Physics, Aalto University (formerly Helsinki University of Technology), P.O. Box 15100, FI-02150 Espoo, Finland. <sup>2</sup>Matière Molle et Chimie, UMR 7167 CNRS-ESPCI, Ecole Supérieure de Physique et Chimie Industrielles, 10 rue Vauquelin, 75005 Paris, France.

\*Corresponding author. E-mail: jaakko.timonen@aalto.fi (J.V.I.T.); robin.ras@aalto.fi (R.H.A.R.); olli.ikkala@aalto.fi (O.I.)

†Present address: Non-Equilibrium Energy Research Center, Northwestern University, 2145 Sheridan Road, Evanston, IL 60208, USA



but seminal works have shown that it can also be created artificially (12, 13, 17).

Dynamic self-assembly has been suggested as a route to adaptive systems beyond what static self-assembly can offer (2, 13, 18). However, dynamic assembly is challenging to realize and understand because it cannot be predicted through energy minimization. It is also sensitive to small,

local changes in the interactions between the elementary units and the external energy supply (13). We approach this problem by introducing a model system that functions in the interface of static and dynamic self-assembly and can be switched between them. The system relies on manipulation of mobile magnetic ferrofluid droplets (19–21) on a low-friction lotus-leaf-like (22)

superhydrophobic surface (23–27) with an external magnetic field. In the following text, we first show how an external magnetic trigger can be used for creating self-assembled ferrofluid droplet populations from a single parent droplet. Then, we demonstrate that the static equilibrium patterns can be transformed reversibly to dynamic dissipative patterns by feeding them energy through

**Fig. 1. Magnetically triggered ferrofluid droplet division on a superhydrophobic surface.**

(A) Schematic side-view of the magnetic field geometry of a cylindrical permanent magnet (white lines, magnetic field; black lines, constant field contours). State of the droplet is indicated as follows: 1, near-zero field (nearly spherical droplet); 2, weak field (slightly deformed droplet); 3, strong field (conical spiked droplet); and 4, above critical field (two daughter droplets). (B) Photographs of a 20- $\mu$ l ferrofluid droplet (movie S1) upon increasing the field from 80 Oe ( $dH/dz$  3.5 Oe/mm) to 680 Oe ( $dH/dz$  66 Oe/mm). Notice the small asymmetry in daughter-droplet sizes and the small satellite droplet between the two (fig. S3). (C) Frames of a high-speed video of the division (movie S2) and (D) the corresponding distance between the daughter droplets as a function of time, approaching the distance determined by static self-assembly.

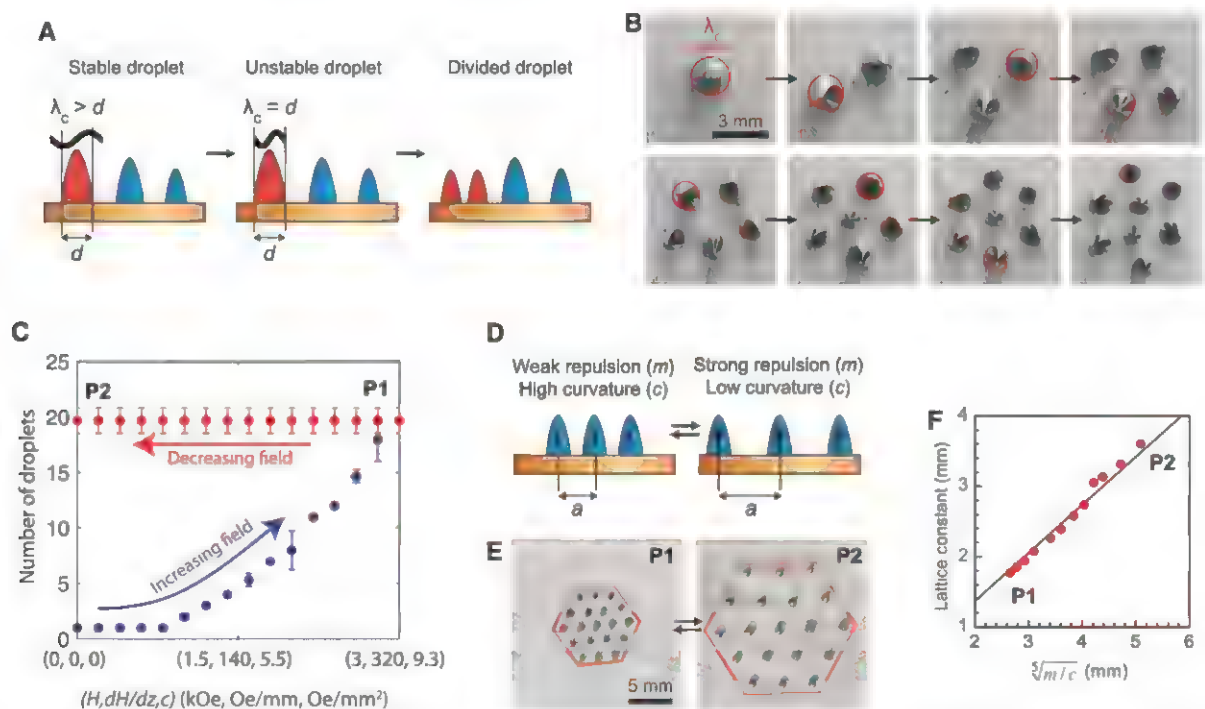
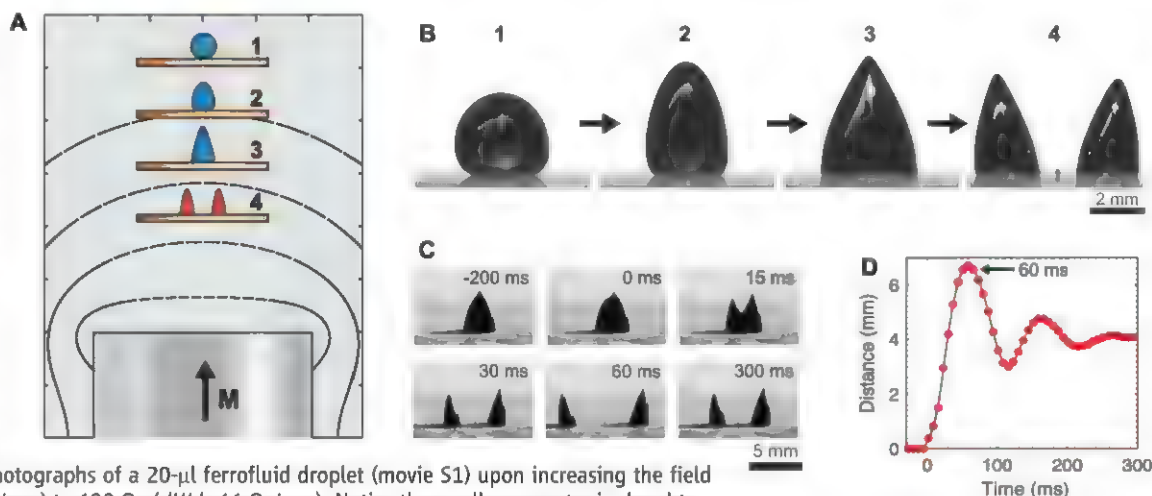


**Fig. 2. Self-assembled droplet patterns in axisymmetric magnetic field.**

(A) Scheme of the division instability.  $\lambda_c$ , critical wavelength;  $d$ , diameter. (B) Photographs of the stepwise division and self-assembly of a 10- $\mu$ l droplet. The largest droplet marked with a red circle (the diameter corresponds to  $\lambda_c$ ; see Eq. 1) divides in each step (movie S3). Magnetic field strength was increased from 1.0 kOe ( $dH/dz$  82 Oe/mm) for one droplet to 1.9 kOe ( $dH/dz$  193 Oe/mm) for eight droplets. (C) Number of droplets as a function of increasing and decreasing magnetic field, showing hysteresis due to the

kinetic trapping. P1; high magnetic field; P2, low magnetic field. Error bars indicate SD of three data sets. (D) Scheme of controlling the lattice constant in the kinetically trapped patterns by adjusting the magnetic field curvature ( $c$ ) and the magnetic moment of the droplets ( $m$ ).  $a$ , nearest-neighbor distance. (E) Snapshots of a 19-droplet pattern with two extreme periodicities at high and low magnetic fields. (F) The corresponding nearest-neighbor distance as a function of  $\sqrt{m/c}$ . Red dots denote experimental measurements; the black line indicates the best linear fit.

an oscillating magnetic field. We highlight the important role of kinetic trapping as a stabilizer on both static and dynamic patterns and directly visualize the complexity of the transition.

In an elementary experiment, one droplet of aqueous ferrofluid (fig. S1) (28) is placed on a superhydrophobic surface and subjected to a confining field of a cylindrical permanent magnet below the substrate (Fig. 1A and fig. S2). Gradually increasing the field strength  $H$  and the vertical gradient  $dH/dz$  acting on the droplet (by decreasing the gap between the magnet and the surface) leads to a deformation of the droplet into a spiked cone and cleavage into two smaller droplets at the critical field strength (Fig. 1B and movie S1). The division takes a few tens of milliseconds (Fig. 1C and movie S2), after which the daughter droplets briefly oscillate before settling at their equilibrium separation (Fig. 1D).

The division of the droplet is due to a combination of high magnetic field and high vertical magnetic field gradient and, therefore, does not take place in a homogeneous magnetic field (fig. S4). The division is related to the normal-field instability of ferrofluids (Rosensweig instability) (19), but differs from it in several ways. The classic Rosensweig pattern [see (29) for a demonstration] appears in a homogeneous perpendicular magnetic field on a horizontal flat surface of ferrofluid. It has the critical periodicity of  $\lambda_c^{\text{Rosenweig}} = 2\pi\sqrt{\sigma/\rho g}$ , where  $\sigma$  and  $\rho$  are sur-

face tension and density of the fluid, respectively, and  $g$  is the gravitational acceleration (30). In contrast, the gravitational force in our system is negligible compared with the magnetic force due to the vertical field gradient; that is,  $\frac{d}{dz}(\mu_0 H M V)$ , where  $\mu_0$  is permeability of vacuum,  $M$  is magnetization, and  $V$  is volume of the droplet. This magnetic force can be up to two orders of magnitude larger than the gravitational force (fig. S5). Thus, we can approximate the critical wavelength in our system as

$$\lambda_c \approx 2\pi\sqrt{\frac{\sigma}{\frac{d}{dz}(\mu_0 H M)}} \quad (1)$$

Importantly, Eq. 1 has a different interpretation compared with the Rosensweig pattern. In this case, Eq. 1 does not determine the periodicity of the pattern but instead gives the criterion for the splitting: a droplet divides when the critical wavelength becomes smaller than the droplet diameter. This implies that the largest droplet is always the most susceptible to dividing (Fig. 2A), which was experimentally confirmed when the magnetic field was increased to generate larger droplet populations (Fig. 2B and movie S3), up to 75 droplets (fig. S6). In further contrast, the Rosensweig pattern is reversible (the pattern decays when the field is removed), but our patterns are not: the droplets do not coalesce back to a single

droplet when the static magnetic field is switched off (Fig. 2C and movie S3). This irreversibility is due to the daughter droplets being kinetically trapped to remain separate; that is, there is a potential energy barrier between the global one-droplet energy minimum and any multidroplet pattern. The kinetic trapping is caused by the magnetic repulsion of the droplets and the nonwetting nature of the substrate (which ensures that the droplets are not physically connected). Later, we show a route back to the original one-droplet state through dynamic self-assembly.

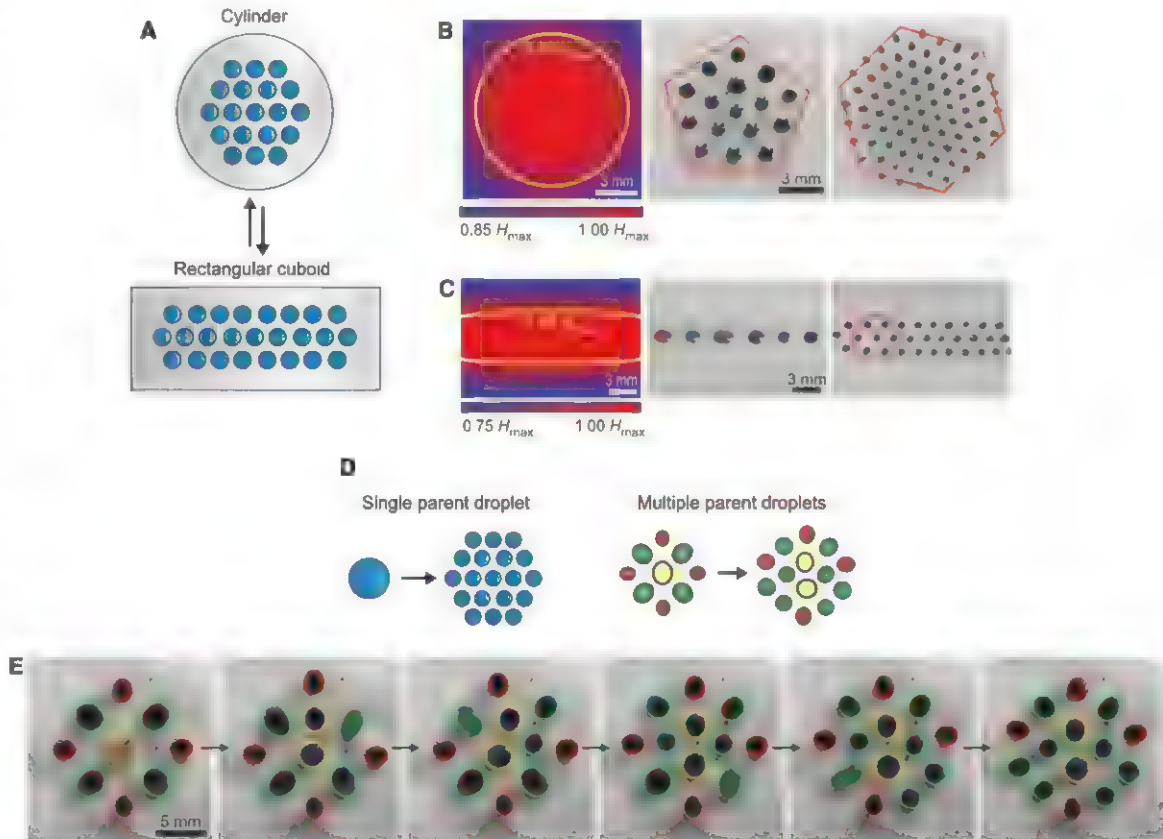
The droplet pattern quickly rearranges to accommodate the newly formed droplet after each division (Fig. 2B and movie S3). The rearrangement is driven by the minimization of energy, which is a sum of the dipolar repulsion between the magnetized droplets and their attraction toward the increasing gradient of the external magnetic field

$$U = \frac{\mu_0}{4\pi} \sum_{i=1}^N \sum_{j=i+1}^N \frac{m_i m_j}{|\mathbf{r}_i - \mathbf{r}_j|^3} - \mu_0 \sum_{i=1}^N m_i \left( H - \frac{1}{2} c |\mathbf{r}_i|^2 \right) \quad (2)$$

where  $m_i$  and  $m_j$  are magnetic moments of the droplets;  $\mathbf{r}_i$  and  $\mathbf{r}_j$  are positions of the droplets; and  $c = -\frac{d^2 H}{dz^2}$  is the confining curvature of the

### Fig. 3. More complicated patterns.

(A) Scheme of changing the geometry of the magnetic field (top view). (B) Axisymmetric magnetic field (cylindrical magnet) and the corresponding patterns with five- and six-fold symmetries and (C) nonaxisymmetric magnetic field (rectangular cuboid magnet) and the corresponding close-packed ribbon patterns with an overall twofold symmetry (movie S5). All four patterns in (B) and (C) were created from a single 20- $\mu\text{l}$  parent droplet.  $H_{\text{max}}$ , maximum magnetic field strength. (D) Scheme for changing the number of parent droplets. (E) An example of switching a hierarchical pattern of 9 droplets with fourfold symmetry to another hierarchical pattern of 14 droplets with twofold symmetry (movie S6). The dividing droplet is marked with a solid color. The magnetic field strength was increased from 1060 Oe ( $dH/dz$  61 Oe/mm) to 1240 Oe ( $dH/dz$  72 Oe/mm).





magnetic field (fig. S2). The rearrangement after each division is nearly perfect due to the low friction that originates from the surface's high contact angles and low contact angle hysteresis. In contrast, other surfaces with higher contact angle hysteresis did not allow the minimum energy patterns to be reached (movie S4).

The lattice constant of the patterns could be adjusted by changing the ratio between the repulsion and attraction by changing the distance between the surface and the magnet (Fig. 2, D to F), in good agreement with the scaling relation for the nearest-neighbor distance  $a \propto \sqrt[3]{m/c}$  predicted from Eq. 2. Importantly, the periodicity changes are completely reversible (provided that the field is not increased above the next division threshold). Thus, the droplets are free to move, despite the number of droplets being kinetically trapped (Fig. 2C).

More complicated patterns are readily achieved by using other magnetic field geometries, such as that of a nonaxisymmetric rectangular cuboid magnet (Fig. 3A). The lacking axial symmetry changes the typical five- and sixfold patterns observed with cylindrical magnets (Fig. 3B) to

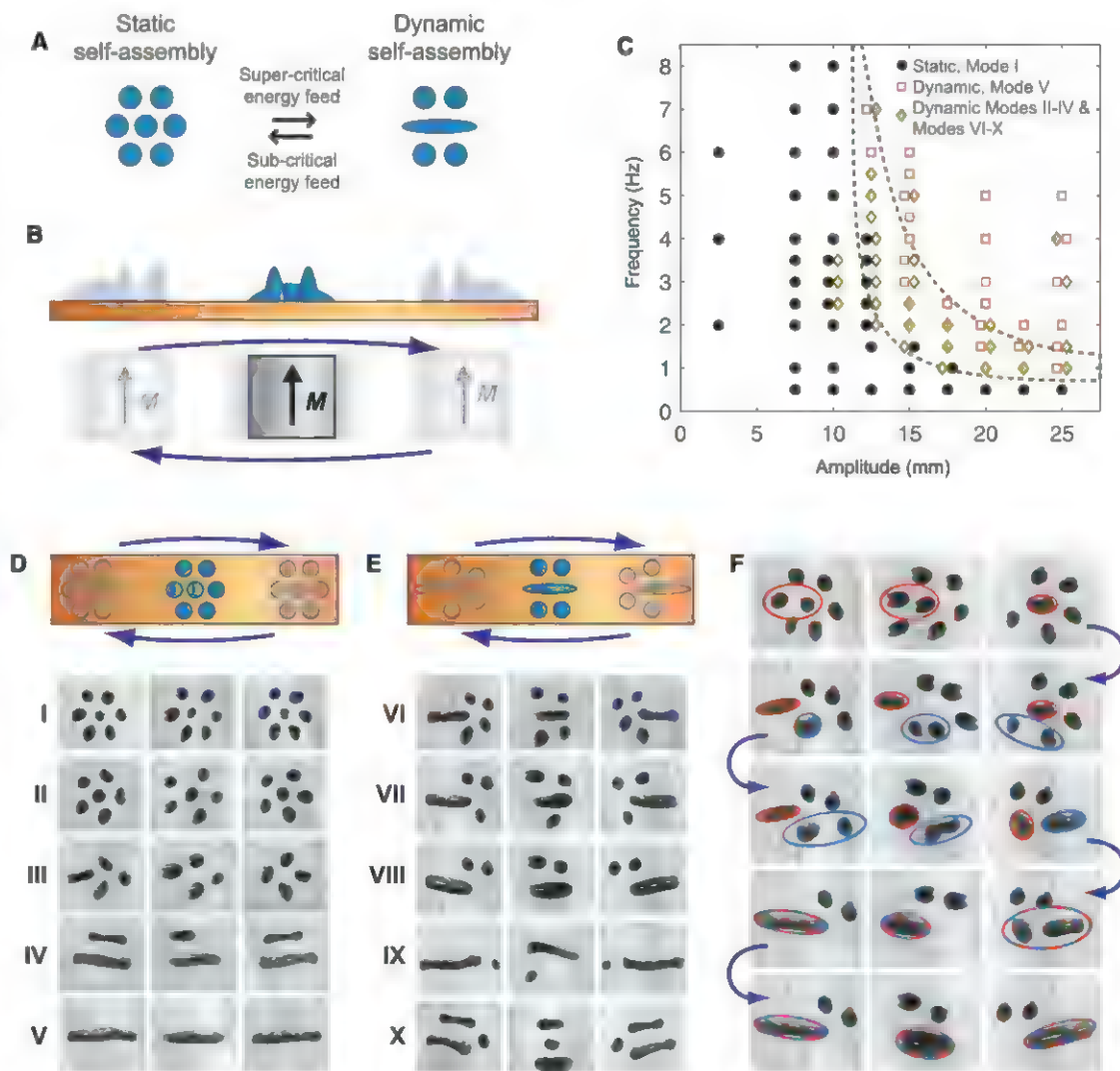
close-packed ribbons with an overall twofold symmetry (Fig. 3C and movie S5). On the other hand, starting with multiple differently sized parent droplets (Fig. 3D) makes switching between hierarchical patterns possible (Fig. 3E, fig. S7, and movie S6).

The static patterns transform to dynamic ones when they are provided with a sufficient continuous energy feed to keep them away from the energy minimum (Fig. 4A). We realized the energy feed by oscillating the permanent magnet horizontally below the substrate with amplitude  $A$  and frequency  $f$  (Fig. 4B). At low energy feed rates (small amplitude and frequency), a typical static seven-droplet pattern simply moves with the oscillating magnet as a whole and, thus, remains close to the energy minimum (Fig. 4, C and D, mode I, and movie S7). However, the droplets start to coalesce above a threshold amplitude and frequency, leading to the emergence of numerous dynamic patterns consisting of elongated droplets and/or regular circular droplets (Fig. 4, D and E, modes II to X, and movies S7 and S8). The transition threshold is determined by the time-dependent dissipative magnetic forces,

which cause shortening in the distances between the droplets (fig. S8). Thus, the dynamic magnetic force is an external trigger that can free the static pattern from its kinetic trap (Fig. 2C). It allows the number and sizes of the droplets to be changed, leading to the rearrangement of the pattern.

Simulations showed that the coalescence and rearrangement starts from droplet pairs whose distance is affected the most by the energy feed (Fig. 4F and fig. S8). However, immediately after the first coalescence, the behavior of the pattern becomes difficult to predict, as seen from the complex and seemingly chaotic coalescence and division of droplets (movie S8, mode IX). This complexity originates mostly from small differences in initial positions and sizes of the droplets (fig. S6). However, complexity can arise, even in individually pipetted droplet patterns (movie S10), and is actually seen also in switching of some static patterns (fig. S9 and movie S11). Yet, even the most chaotic transient droplet motions eventually stabilize into kinetically trapped patterns that are permanent until the oscillating field is switched off, after which the

**Fig. 4. Reversible switching between static and dynamic self-assembly.** (A) Scheme of the switching. (B) Practical realization of the energy feed by horizontally oscillating the permanent magnet below the superhydrophobic surface. (C) Phase diagram of the seven-droplet pattern in the field of 1130 Oe ( $dH/dz$  132 Oe/mm), showing the transition boundary (dashed lines). (D) Scheme of mode I and photographs of dynamic patterns that do not change their appearance during the cycle of the driving field (movie S7). (E) Scheme of mode VI and photographs of dynamic patterns that change their shape (but not the number of droplets) periodically with the external magnetic field (movie S8). (F) Photographs of the intermediate steps in the formation of mode VIII during 2.5 oscillations of the driving field ( $f = 3$  Hz,  $A = 12.5$  mm) (movie S9).



patterns decay back to the static seven-droplet pattern within a fraction of a second.

Dynamic patterns rely critically on low friction and energy dissipation (movie S12). The geometry of the dynamic patterns cannot be described in terms of energy minimization (Eq. 2), because they are far from the energy minimum. Instead, the patterns are better described and rationalized as dynamic states wherein the droplet number is kinetically trapped [as in the static patterns (Fig. 2C)]. Patterns can be classified into those that alternate (Fig. 4E) or do not alternate (Fig. 4D) during the cycled energy feed. Alternation is caused by different mobilities of the droplets: Elongated ones are more mobile because of the higher ratio between the driving and dissipative forces.

Dynamic self-assembly can be used as a switch between droplet patterns with different numbers of droplets. In contrast to the division instability, dynamic self-assembly decreases the number of droplets. This allows the irreversibility of the droplet formation in static self-assembly (Fig. 2C) to be overcome. For example, driving any static pattern to the mode V dynamic pattern (single elongated droplet) and decreasing the magnetic field while oscillating the magnet allows recovery of the original one-droplet state (movie S13). This is the final unit operation required to realize a complete cycle from a single liquid droplet to complicated static and dynamic patterns and, finally, back to the starting state (fig. S10).

Externally driven magnetic droplets on superhydrophobic surfaces form a versatile model system for studying and visualizing complicated phenomena in self-assembly. We used this model

to demonstrate switching between static and dynamic self-assembly and to show the usefulness of kinetic trapping that most often is viewed only as a hindrance for assembly. The most diverse patterns were found to occur near the boundary where static patterns switch to dynamic ones. The transition is complex, and its detailed investigations will pave the way toward a better understanding of the onset of dynamic dissipative self-assembly.

#### References and Notes

1. P. Bali, *Nature's Patterns: A Tapestry in Three Parts* (Oxford Univ. Press, Oxford, 2011).
2. G. M. Whitesides, B. Grzybowski, *Science* **295**, 2418–2421 (2002).
3. F. S. Bates *et al.*, *Science* **336**, 434–440 (2012).
4. A.-V. Ruzette, L. Leibler, *Nat. Mater.* **4**, 19–31 (2005).
5. Y. Xia *et al.*, *Nat. Nanotechnol.* **6**, 580–587 (2011).
6. E. V. Shevchenko, D. V. Talapin, N. A. Kotov, S. O'Brien, C. B. Murray, *Nature* **439**, 55–59 (2006).
7. K. Liu, N. Zhao, E. Kumacheva, *Chem. Soc. Rev.* **40**, 656–671 (2011).
8. T. Kato, N. Mizoshita, K. Kishimoto, *Angew. Chem. Int. Ed.* **45**, 38–68 (2006).
9. O. Ikkala, G. ten Brinke, *Science* **295**, 2407–2409 (2002).
10. S. Park *et al.*, *Science* **323**, 1030–1033 (2009).
11. J. Yoon, W. Lee, E. L. Thomas, *MRS Bull.* **30**, 721–726 (2005).
12. B. A. Grzybowski, C. J. Campbell, *Chem. Eng. Sci.* **59**, 1667–1676 (2004).
13. B. A. Grzybowski, C. E. Wilmer, J. Kim, K. P. Browne, K. J. M. Bishop, *Soft Matter* **5**, 1110–1128 (2009).
14. S. Kauffman, *At Home in the Universe: The Search for Laws of Self-Organization and Complexity* (Oxford Univ. Press, Oxford, 1995).
15. E. Karsenti, *Nat. Rev. Mol. Cell Biol.* **9**, 255–262 (2008).
16. A. M. Mateus, N. Gorfinkel, A. M. Arias, *Semin. Cell Dev. Biol.* **20**, 877–884 (2009).
17. B. A. Grzybowski, H. A. Stone, G. M. Whitesides, *Nature* **405**, 1033–1036 (2000).

18. K. V. Tretyakov, K. J. M. Bishop, B. A. Grzybowski, *Soft Matter* **5**, 1279–1284 (2009).
19. R. E. Rosensweig, *Ferrohydrodynamics* (Dover Publications, New York, 1997).
20. J.-C. Bacri, F. Elias, in *Morphogenesis: Origins of Patterns and Shapes*, P. Bourguin, A. Lesne, Eds. (Springer, Heidelberg, 2011), pp. 15–19.
21. R. Massart, *IEEE Trans. Magn.* **17**, 1247–1248 (1981).
22. W. Barthlott, C. Neinhuis, *Planta* **202**, 1–8 (1997).
23. I. A. Larmour, S. E. J. Bell, G. C. Saunders, *Angew. Chem. Int. Ed.* **46**, 1710–1712 (2007).
24. X. F. Gao *et al.*, *Adv. Mater.* **19**, 2213–2217 (2007).
25. H. Mertaniemi *et al.*, *Adv. Mater.* **23**, 2911–2914 (2011).
26. H. Mertaniemi, R. Forchheimer, O. Ikkala, R. H. A. Ras, *Adv. Mater.* **24**, 5738–5743 (2012).
27. T. Verho *et al.*, *Proc. Natl. Acad. Sci. U.S.A.* **109**, 10210–10213 (2012).
28. R. Massart, E. Dubois, V. Cabun, E. Hasmonay, *J. Magn. Mater.* **149**, 1–5 (1995).
29. D. Castelvécchi, *Phys. Rev. Focus* **15**, 18 (2005).
30. B. Berkovsky, V. Bashitovoi, *IEEE Trans. Magn.* **16**, 288–297 (1980).

**Acknowledgments:** We acknowledge financial support from the National Doctoral Programme in Materials Physics, Nokia Research Center, the Academy of Finland, a European Research Council Advanced Grant, and the Finnish Agency of Technology and Innovation (TEKES). Electron microscopy was performed using the devices of the Nanomicroscopy Center of Aalto University. We thank A. Walther (RWTH Aachen University), A. Kuzyk, and M. Kostianen for comments on the manuscript and T. Huhtamäki and J. Korhonen for preparing the silicone nanoflament surfaces.

#### Supplementary Materials

www.sciencemag.org/cgi/content/full/341/6143/253/DC1  
Materials and Methods  
Supplementary Text  
Figs. S1 to S10  
References (31–35)  
Movies S1 to S14

7 December 2012; accepted 10 June 2013  
10.1126/science.1233775

## Ultrahigh Magnetoresistance at Room Temperature in Molecular Wires

R. N. Mahato,<sup>1</sup> H. Lülfi,<sup>2</sup> M. H. Siekman,<sup>1,3</sup> S. P. Kersten,<sup>4</sup> P. A. Bobbert,<sup>4</sup> M. P. de Jong,<sup>1</sup> L. De Cola,<sup>2,5</sup> W. G. van der Wiel<sup>1\*</sup>

Systems featuring large magnetoresistance (MR) at room temperature and in small magnetic fields are attractive owing to their potential for applications in magnetic field sensing and data storage. Usually, the magnetic properties of materials are exploited to achieve large MR effects. Here, we report on an exceptionally large (>2000%), room-temperature, small-field (a few millitesla) MR effect in one-dimensional, nonmagnetic systems formed by molecular wires embedded in a zeolite host crystal. This ultrahigh MR effect is ascribed to spin blockade in one-dimensional electron transport. Its generic nature offers very good perspectives to exploit the effect in a wide range of low-dimensional systems.

In spintronic devices, the electron's spin is exploited for information processing. Typically, these devices contain layered structures with an electrical resistance that is dependent on the relative orientation of the magnetization of their magnetic layers; thus, the resistance can be altered by an external magnetic field, a phenomenon called magnetoresistance (MR). Examples include giant magnetoresistance (GMR) devices (1, 2), which are multilayer stacks of ferromagnetic

materials separated by a nonmagnetic metal spacer layer, and tunnel magnetoresistance (TMR) devices (3, 4), which have a tunnel barrier as the spacer. Here, we explore entirely different physics in a nonmagnetic system, relying on a mechanism akin to spin blockade in quantum devices.

The Pauli principle precludes that an electron can tunnel into a state already occupied by another electron with the same spin. This spin blockade for two electrons starting from a spin-

triplet configuration was first observed in quantum dots (QDs) at cryogenic temperatures (5). Spin blockade can be lifted by spin relaxation, mixing in singlet character. It has been shown that hyperfine interaction can lift spin blockade in QDs (6). The importance of hyperfine interaction on spin dynamics has also been recognized in the context of an intrinsic, room-temperature MR effect in organic semiconductors (7, 8). Carrier transport is influenced by spin-dependent reactions, which are subject to the competition between an external magnetic field  $B$  and the random hyperfine fields  $B_{\text{hf}}$  (~1 mT) of the nuclei. At small  $B$  (Fig. 1A), hyperfine interactions

<sup>1</sup>NanoElectronics Group, MESA+ Institute for Nanotechnology, University of Twente, P.O. Box 217, 7500 AE, Enschede, Netherlands. <sup>2</sup>Institut de Science et d'Ingénierie Supramoléculaires (ISIS), Université de Strasbourg, 8 Allée Gaspard Monge, 67000 Strasbourg, France. <sup>3</sup>Transducers Science and Technology Group, MESA+ Institute for Nanotechnology, University of Twente, P.O. Box 217, 7500AE Enschede, Netherlands. <sup>4</sup>Theory of Polymers and Soft Matter, Department of Applied Physics, Eindhoven University of Technology, P.O. Box 513, 5600 MB, Eindhoven, Netherlands. <sup>5</sup>Karlsruher Institut für Technologie (KIT), Institut für Nanotechnologie Hermann-von-Helmholtz-Platz 1, D-76344 Eggenstein-Leopoldshafen, Germany.

\*Corresponding author. E-mail: w.g.vanderwiel@utwente.nl



mix in singlet character, hence lifting the blockade. However, at larger  $B$ ,  $B_{\text{hf}}$  is overshadowed, so that spin blockade cannot be lifted (Fig. 1B). Unlike in QDs, spin blockade in organic molecules can occur at room temperature because of the much stronger wave function confinement, leading to a much larger energy spacing between the lowest singlet and triplet states.

In organic semiconductors exhibiting three-dimensional (3D) hopping conduction, the MR is rather small. It has been predicted, however, that confinement of the current path in molecular systems could lead to a strong increase of the MR (9). Here, we realize such a system experimentally. Our system (Fig. 2) consists of strictly 1D wires, formed by subliming organic dye molecules, DXP (N,N'-bis(2,6-dimethylphenyl)-perylene-3,4,9,10-tetracarboxylic diimide), into the channels of zeolite L crystals in the presence of potassium as counterion of its alumina sites (10). Zeolite L is a well-known, electrically insulating aluminosilicate crystalline system (11), which consists of many thousands of separated channels with a maximum diameter of 1.26 nm, running through the whole crystal and oriented perfectly parallel to the cylinder  $c$  axis. The geometrical constraints of the zeolite host structure allow for the formation of 1D chains of highly uniaxially oriented, closely spaced molecules. The 2.2-nm-long DXP molecules only fit into a channel in their length direction. Although DXP's rigid van der Waals width is  $\sim 0.76$  nm, DXP can be inserted into the 0.71-nm channel opening above  $\sim 175^\circ\text{C}$  (12). We used relatively small size zeolites (30- to 100-nm height; 200- to 500-nm diameter), enabling an 86% DXP loading degree (10). At these high filling ratios, (hopping) electron transport along molecular wires can be readily observed in our conducting-probe atomic force microscopy (CP-AFM) experiments, making this system suitable for 1D transport measurements. DXP-loaded zeolites have been applied before as artificial photonic antenna systems (11), where energy transfer occurs due to near-field interaction. A number of studies report on the electrical conductivity of zeolites loaded with metal atoms (13, 14) or conductive polymers (15, 16), as well as on the effect of inserting different charge-balancing cations (17–19). However, most of this work focuses on bulk systems of a large number of randomly oriented zeolites, with the exception of (20).

Magnetotransport measurements were carried out on DXP-loaded zeolites on top of an ITO/PEDOT:PSS [indium tin oxide/poly(3,4-ethylenedioxythiophene):poly(styrenesulfonate)] substrate at room temperature in an ultrahigh vacuum CP-AFM with a PtSi tip. We estimate that  $\sim 10^2$  channels contribute in parallel to electron transport (10). The measurements were obtained from zeolites with heights of 30, 45, 60, 80, and 90 nm. For every height, the results were reproduced for at least two different zeolites. The current ( $I$ )–voltage ( $V$ ) characteristics in Fig. 3 are almost symmetric in voltage, in accordance

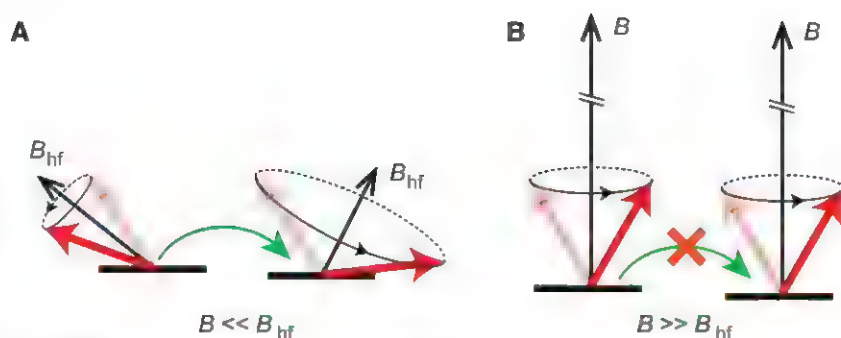


**Fig. 1. Magnetic field dependence of spin blockade.** Shaded (unshaded) arrows indicate an initial (final) spin configuration at neighboring sites before (after) spin precession. (A) For  $B \ll B_{\text{hf}}$ , spin blockade can be lifted due to spin mixing induced by hyperfine interaction. (B) If  $B \gg B_{\text{hf}}$ , spin mixing is suppressed and spin blockade can occur.

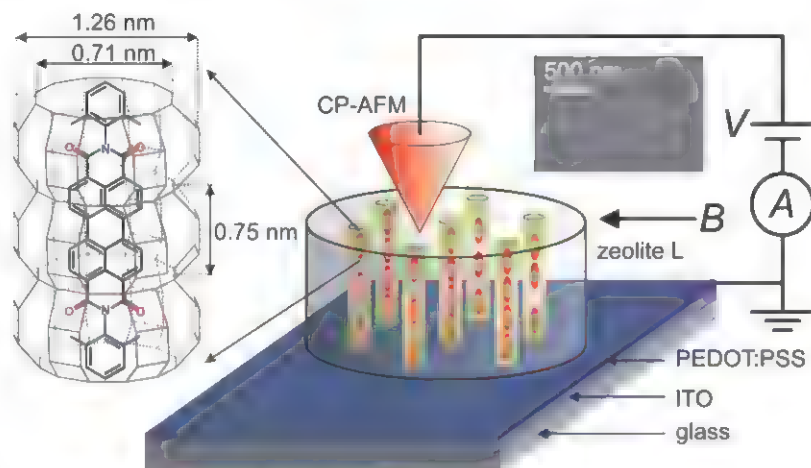


**Fig. 2. Measurement setup and sample structure.** The CP-AFM measures the conduction of the molecules (red ellipsoids) aligned in zeolites on ITO/PEDOT:PSS. (Left) Zeolite channel with a DXP molecule inside. (Upper right) Scanning electron micrograph of zeolites.

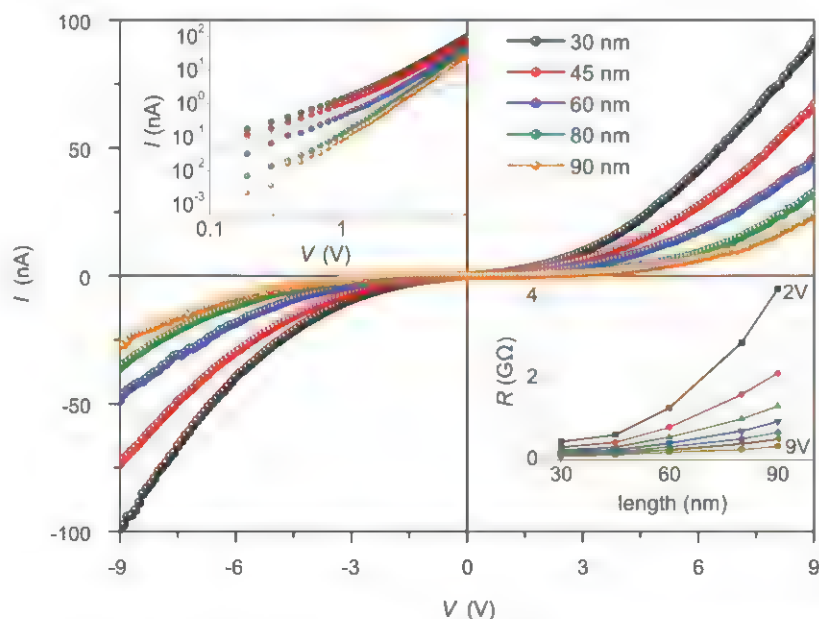


**Fig. 3. Electrical characterization of DXP-loaded zeolites.** Room-temperature  $I$ - $V$  characteristics for different channel length. (Upper left inset) Same data on log-log scale. The straight dashed line indicates a linear dependence. (Lower right inset) Resistance  $R = V/I$  versus channel length.

with the similarity of the work functions of the two contacts. The  $I$ - $V$  characteristics are typical for energetically disordered systems with hopping transport. The upper left inset displays the same data on a logarithmic  $I$  scale, showing a transition from a linear behavior (indicated by the dashed line) at low voltage to a superlinear power-law behavior at high voltage. The resistance,  $R = V/I$ , as a function of channel length for different voltages, is given in the lower right inset. The increase of the resistance with length changes from exponential at low voltage to linear at higher voltages. As the resistance is dependent on channel length, the conductivity is limited by the molecular wires rather than by the contacts. The symmetric  $I$ - $V$  curves and absence of an injection barrier indicate unipolar transport. Both PEDOT:PSS and PtSi have work functions around  $-5$  eV (21, 22), roughly in the middle between the energies of the highest occupied and lowest unoccupied molecular orbital (HOMO and LUMO) of DXP ( $-6.0$  and  $-3.9$  eV, respectively) (23). This seems to be at odds with the absence of an injection barrier. However, the mobile potassium ions in the channels could substantially change the injection barrier by creating dipole layers at the zeolite surface, lowering the barrier for electron injection. This would be consistent with electron

transport (see below), but our considerations would be equally valid for hole transport. The linear regime in the  $I$ - $V$  curves points at the presence of free charges, and hence free spins, in the channels already at low voltage. These should result from diffusion from the contacts (PEDOT:PSS layer and PtSi tip) into the interior of the zeolite, yielding an exponentially decaying charge concentration profile compatible with the observed exponential dependence of the resistance on channel length at low voltage. We confirmed that empty zeolites do not show any detectable current up to 9 V. Likewise, CP-AFM measurements on ITO PEDOT:PSS substrates give linear  $I$ - $V$ s with negligible resistance (10).

Figure 4A shows the current-voltage characteristic for a 60-nm channel length at zero magnetic field and at 14 mT perpendicular to the wires, plotting  $|I|$  on a logarithmic scale. Despite the small magnetic field, a very strong current suppression is observed at 14 mT, especially at lower voltage. To study the magnetic field dependence of the current through the molecular wires in more detail, we define the magnetoconductance (MC) as

$$MC(B) \equiv \frac{I(B) - I(0)}{I(0)} \quad (1)$$

where  $I(B)$  is the current at magnetic field  $B$ , and  $I(0)$  the current at zero magnetic field, yielding a maximum possible negative MC of  $-100\%$ . Figure 4B shows  $MC(B)$  at different bias voltages for a 60-nm wire length. We observe a very large, negative MC, monotonically increasing with decreasing voltage. Similar behavior was observed for other wire lengths (10).

The  $MC(B)$  curves can be fitted well with the empirical line shape

$$MC(B) \propto \frac{B^2}{(B_0 + |B|)^2} \quad (2)$$

applied before in the context of organic magnetoresistance (OMAR) (7). It has a characteristic width  $B_0$ , related to the magnitude of the hyperfine fields. The fitted  $B_0$  values (fig. S2) vary between 2 and 6 mT, comparable to values obtained for OMAR (7), and show almost no voltage dependence. The mT field scale agrees well with the typical hyperfine coupling in  $\pi$ -conjugated molecules, clearly pointing at a molecular origin. The very large room-temperature MC approaching the maximum possible value of  $-100\%$  is notable.

The voltage dependence is more clearly represented if we convert MC to the more common MR, defined by

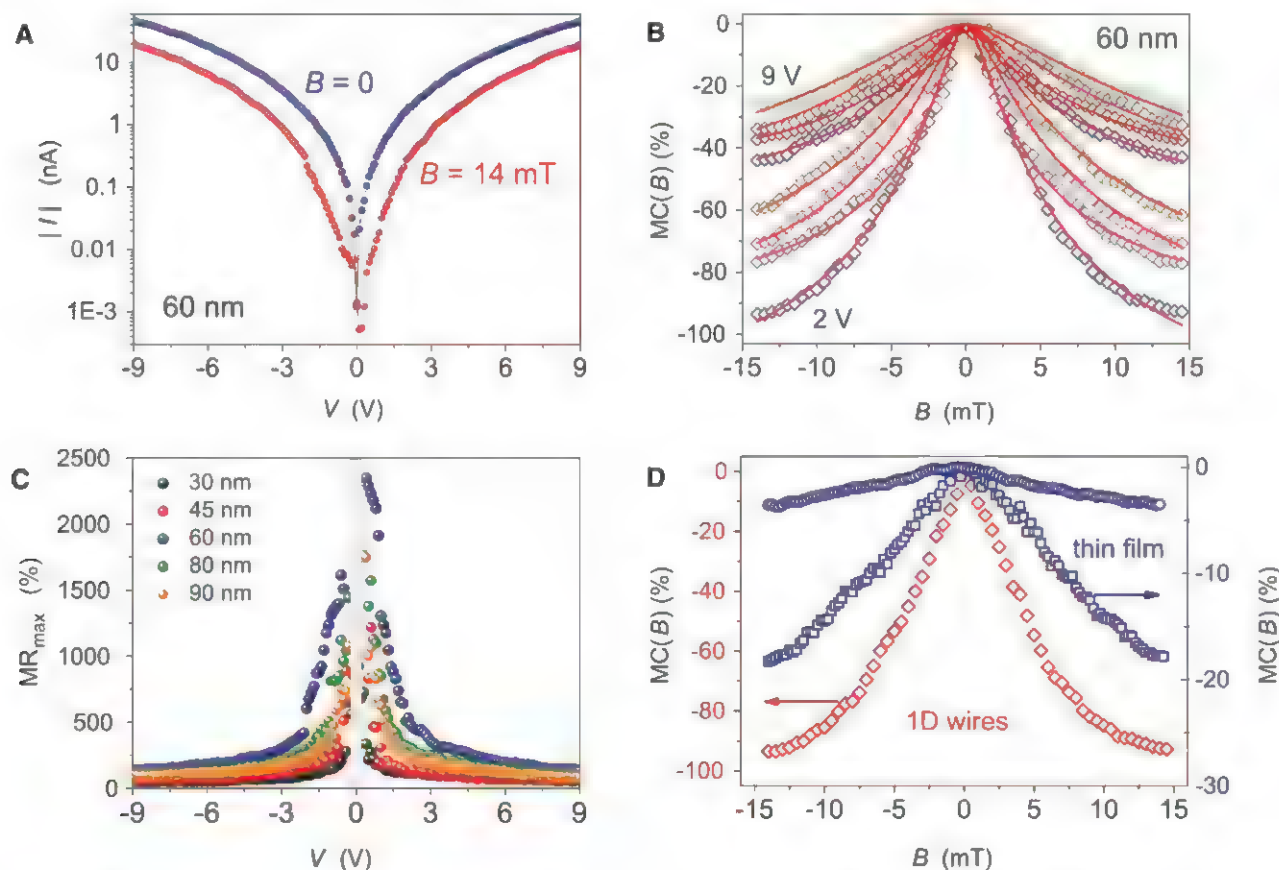


**Fig. 4. Room-temperature MR.** (A)  $I$ - $V$  characteristics of DXP-loaded zeolite with 60-nm channel length at  $B = 0$  and 14 mT. (B) Magnetoconductance  $MC(B)$  at different bias voltages for 60-nm channel length. The red curves are fits to Eq. 2. (C) Maximum magnetoresistance  $MR_{\text{max}} = [R(B_{\text{max}}) - R(0)]/R(0)$ , as a function of  $V$  for

different channel lengths. (D) Comparison between MC in a  $\sim 40$ -nm DXP film measured by a 250- $\mu\text{m}$ -diameter Pt wire (blue circles), the same film measured by a CP-AFM PtSi tip (blue squares), and 60-nm-long 1D DXP wires measured by a PtSi CP-AFM tip (red diamonds).



$$\text{MR}(B) \equiv \frac{R(B) - R(0)}{R(0)} = \frac{I(0) - I(B)}{I(B)} \quad (3)$$

where  $R(B)$  is the resistance at magnetic field  $B$  and  $R(0)$  the resistance at zero field. We have derived  $\text{MR}_{\text{max}}(V)$  from the  $I$ - $V$ s for different channel lengths at zero magnetic field and maximum magnetic field,  $B_{\text{max}}$ , according to  $\text{MR}_{\text{max}}(V) = [I(V,0) - I(V,B_{\text{max}})]/I(V,B_{\text{max}})$ , (Fig. 4C). The MR increases rapidly with decreasing voltage, reaching a maximum value of more than 2000% for 60-nm wire length when approaching 0 V. Because the current levels are below the noise limit close to 0 V, we have not been able to determine  $\text{MR}_{\text{max}}$  here.

The MR values in our molecular wires compare favorably with values reported for other systems under similar conditions. The highest room-temperature TMR value reported to date is 600% for an epitaxial CoFeB/MgO/CoFeB magnetic tunnel junction (24). Colossal magnetoresistance (CMR) manganites exhibit very large low-temperature MR at several tesla (25); however, room-temperature, low-field MR values are a few tens of percents (26, 27). For nanocomposites containing magnetic nanoparticles, MR values similar to those in CMR experiments have been demonstrated under comparable experimental conditions (28). A large room-temperature MR effect of a few tens of percents was also reported for a graphene nanoribbon field-effect transistor (29).

We ascribe our very large MR values to the unique 1D character of our system. Indeed, nonstructured DXP thin films show much lower MR values (Fig. 4D). When a ~40-nm DXP film is contacted with a PtSi CP-AFM tip in the same setup, we measure a maximum MC of around -20%. With a Pt wire of 250- $\mu\text{m}$  diameter instead of the PtSi tip, the maximum MC is reduced to about -5%. These results strongly suggest that confinement of the current path is crucial for explaining our results, in line with recent numerical studies (9). Explanations based on spin-dependent interactions involving excited states (30, 31) can be ruled out, because the MR is also present—and even more pronounced—below the DXP HOMO-LUMO gap (~2 eV). The fact that for DXP the energy required to form doubly negatively charged states is remarkably small [~0.2 eV from cyclic voltammetry measurements (23)] suggests that such states are involved in transport. We therefore propose that the current is carried by electrons and that spin blockade is caused by two electrons residing on neighboring molecules attempting to form a doubly negatively charged molecule in a spin-singlet configuration by hopping of one of the electrons. The energetic disorder generally present in organic systems facilitates formation of doubly charged molecules at favorable locations. Moreover, the presence of a positively charged potassium ion close to a DXP molecule strongly reduces its LUMO level, also facilitating double charging. Simula-

tions show that with these ingredients, MC values close to -100% indeed can be obtained with MC ( $B$ ) curves having the line shape of Eq. 2 (10). Further analysis should provide more insight into the details of the mechanism behind the effect, but the present experimental results clearly point at spin blockade tuned by a competition between the external magnetic field and the random internal hyperfine field.

#### References and Notes

1. M. N. Baibich *et al.*, *Phys. Rev. Lett.* **61**, 2472–2475 (1988).
2. G. Binasch, P. Grünberg, F. Saurenbach, W. Zinn, *Phys. Rev. B* **39**, 4828–4830 (1989).
3. M. Jullière, *Phys. Lett.* **54**, 225–226 (1975).
4. J. S. Moodera, L. R. Kinder, T. M. Wong, R. Meservey, *Phys. Rev. Lett.* **74**, 3273–3276 (1995).
5. K. Ono, D. G. Austing, Y. Tokura, S. Tarucha, *Science* **297**, 1313–1317 (2002).
6. R. Hanson, L. P. Kouwenhoven, J. R. Petta, S. Tarucha, L. M. K. Vandersypen, *Rev. Mod. Phys.* **79**, 1455–1455 (2007).
7. T. Francis, Ö. Mermer, G. Veeraraghavan, M. Wohlgenannt, *New J. Phys.* **6**, 185 (2004).
8. W. Wagemans *et al.*, *Spin* **1**, 93–108 (2011).
9. S. P. Kersten, S. Meskers, P. A. Bobbert, *Phys. Rev. B* **86**, 045210 (2012).
10. Materials and methods are available as supplementary materials on Science OnLine.
11. G. Calzaferri, S. Huber, H. Maas, C. Mirkowski, *Angew. Chem. Int. Ed.* **42**, 3732–3758 (2003).
12. P. Bornhauser, G. Calzaferri, *J. Phys. Chem.* **100**, 2035–2044 (1996).
13. P. A. Anderson *et al.*, *Dalton Trans.* **19**, 3122–3128 (2004) and references therein.
14. M. J. Kelly, *J. Phys. Condens. Matter* **7**, 5507–5519 (1995).
15. T. Bein, in *Recent Advances and New Horizons in Zeolite Science and Technology*, H. Chan, S. I. Woo, S. E. Park, Eds. (Elsevier, Amsterdam, 1996), pp. 295–322.
16. D. J. Cardin, *Adv. Mater.* **14**, 553 (2002).
17. U. Simon, M. E. Franke, in *Host-Guest-Systems Based on Nanoporous Crystals*, F. Laeri, F. Schüth, U. Simon, M. Wark, Eds. (Wiley, Weinheim, 2003), pp. 364–378.
18. M. Alvaro *et al.*, *Chem. Mater.* **18**, 26–33 (2006).
19. F. J. Jansen, R. A. Schoonheydt, *J. Chem. Soc., Faraday Trans.* **69**, 1338 (1973).
20. Z. K. Tang *et al.*, *Science* **292**, 2462 (2001).
21. A. M. Nardes *et al.*, *Org. Electron.* **9**, 727–734 (2008).
22. H. Bentmann, A. A. Demkov, R. Gregory, S. Zoeller, *Phys. Rev. B* **78**, 205302 (2008).
23. S. K. Lee *et al.*, *J. Am. Chem. Soc.* **121**, 3513–3520 (1999).
24. S. Ikeda *et al.*, *Appl. Phys. Lett.* **93**, 082508 (2008).
25. G. Q. Gong *et al.*, *Appl. Phys. Lett.* **67**, 1783 (1995).
26. P. K. Siwach, H. K. Singh, O. N. Srivastava, *J. Phys. Condens. Matter* **20**, 273201 (2008).
27. Y.-T. Zhang, Z.-Y. Chen, C.-C. Wang, Q. Jie, H.-B. Lü, *J. Magn. Magn. Mater.* **321**, 1199–1201 (2009).
28. F. J. Yue *et al.*, *J. Phys. D Appl. Phys.* **44**, 025001 (2011).
29. J. Bai *et al.*, *Nat. Nanotechnol.* **5**, 655–659 (2010).
30. V. N. Prigodin, J. D. Bergeson, D. M. Lincoln, A. J. Epstein, *Synth. Met.* **156**, 757–761 (2006).
31. P. Desai, P. Shukla, T. Kreouzis, W. P. Gillin, *Phys. Rev. B* **76**, 235202 (2007).

**Acknowledgments:** We thank B. Koopmans, L. Abelnann, L. P. Kouwenhoven, Y. Tokura, and S. Tarucha for fruitful discussions. We acknowledge financial support from the Netherlands Technology Foundation STW, the European Research Council, ERC Starting Grant nos. 240433 and 280020, ERC Advanced Grant no. 247365, NanoScience Europe program (NanoSci-ERA), grant no. 11003, and the Foundation for Fundamental Research on Matter (FOM), part of the Netherlands Organisation for Scientific Research (NWO). A link to the data reported here is included in the supplementary materials. R.N.M. and M.H.S. carried out the magnetoresistance experiments and performed the data analysis. H.L. performed the zeolite L crystal synthesis and molecular loading. W.G.v.d.W. conceived the experiments and planned and supervised the project. L.D.C. conceived the project together with W.G.v.d.W. and supervised the zeolite synthesis and loading. S.P.K. and P.A.B. performed the theoretical analysis and numerical simulations. M.P.d.J. contributed to planning and supervision. All authors discussed the results, provided important insights, and helped write the manuscript.

#### Supplementary Materials

www.sciencemag.org/cgi/content/full/science.1237242/DC1  
Materials and Methods  
Figs. S1 to S4  
Data Files  
References (32–37)

1 March 2013; accepted 14 June 2013  
Published online 4 July 2013;  
10.1126/science.1237242

## Isotope Ratios of H, C, and O in CO<sub>2</sub> and H<sub>2</sub>O of the Martian Atmosphere

Chris R. Webster,<sup>1\*</sup> Paul R. Mahaffy,<sup>2</sup> Gregory J. Flesch,<sup>1</sup> Paul B. Niles,<sup>6</sup> John H. Jones,<sup>7</sup> Laurie A. Leshin,<sup>3</sup> Sushil K. Atreya,<sup>4</sup> Jennifer C. Stern,<sup>2</sup> Lance E. Christensen,<sup>1</sup> Tobias Owen,<sup>5</sup> Heather Franz,<sup>2</sup> Robert O. Pepin,<sup>8</sup> Andrew Steele,<sup>9</sup> the MSL Science Team†

Stable isotope ratios of H, C, and O are powerful indicators of a wide variety of planetary geophysical processes, and for Mars they reveal the record of loss of its atmosphere and subsequent interactions with its surface such as carbonate formation. We report *in situ* measurements of the isotopic ratios of D/H and <sup>18</sup>O/<sup>16</sup>O in water and <sup>13</sup>C/<sup>12</sup>C, <sup>18</sup>O/<sup>16</sup>O, <sup>17</sup>O/<sup>16</sup>O, and <sup>13</sup>C/<sup>18</sup>O/<sup>12</sup>C/<sup>16</sup>O in carbon dioxide, made in the martian atmosphere at Gale Crater from the Curiosity rover using the Sample Analysis at Mars (SAM)'s tunable laser spectrometer (TLS). Comparison between our measurements in the modern atmosphere and those of martian meteorites such as ALH 84001 implies that the martian reservoirs of CO<sub>2</sub> and H<sub>2</sub>O were largely established ~4 billion years ago, but that atmospheric loss or surface interaction may be still ongoing.

The Sample Analysis at Mars (SAM) suite (*1*) on the Curiosity rover that landed in August 2012 is conducting a search for

organic compounds and volatiles in rocks and soils and characterizing the chemical and isotopic composition of the modern atmosphere. Atmo-

spheric characterization is one of the exploration goals of the Mars Science Laboratory (MSL) mission (2), and it is accomplished using SAM's tunable laser spectrometer (TLS) and its quadrupole mass spectrometer (QMS). Here we focus on TLS measurements; a companion paper (3) focuses on those from the QMS. Results for non-detection by TLS of atmospheric methane are reported elsewhere (4).

Previous measurements of isotopes of H, N, and noble gases in the martian atmosphere to date (5) have indicated enrichment in the heavier isotopes, consistent with the idea of atmospheric loss to space of the lighter isotopes (6, 7). Although meteoritic analyses of  $\delta^{13}\text{C}$  and  $\delta^{18}\text{O}$  (8) in shergottite, nakhlite, and chassigny (SNC)-class meteorites are made at higher precision than the atmospheric measurements to date, they are challenged to correctly account for possible terrestrial contamination (9). Measurements of  $\text{CO}_2$  isotopes at Mars and in particular  $\delta^{13}\text{C}$  values have not been consistent with atmospheric loss (10). Viking (11) measured  $\delta^{13}\text{C}$  and  $\delta^{18}\text{O}$  values of  $23 \pm 43$  per mil (‰) and  $7 \pm 44\%$ . Earth-based spectroscopy has suggested depleted values for  $\delta^{13}\text{C}$  of  $-22 \pm 20\%$  and  $\delta^{18}\text{O}$  of  $18 \pm 18\%$  (9). The recent Phoenix lander measured  $\delta^{13}\text{C}$  and  $\delta^{18}\text{O}$  values for  $\text{CO}_2$  in the martian atmosphere of  $-2.5 \pm 4.3\%$  and  $31 \pm 5.7\%$ , respectively (12). Although uncertainties in these earlier atmospheric measurements of  $\delta^{13}\text{C}$  and  $\delta^{18}\text{O}$  overlap (Table 1), their  $\delta^{13}\text{C}$  values are in marked contrast to measurements of trapped  $\text{CO}_2$  in martian meteorite EETA 79001, generally considered to be closest to the true martian atmosphere and which yielded a  $\delta^{13}\text{C}$  of  $36 \pm 10\%$  (8).

For D/H in water, the difference in ground-state energies of HDO and its parent  $\text{H}_2\text{O}$  are large enough to cause large changes in  $\delta\text{D}$  in equilibrium and nonequilibrium (kinetic) processes (13, 14), especially where condensation or freezing occurs. For this reason, D/H has become a universally important ratio to identify planetary origin and history (7, 15). The 1988 telescopic observation of D/H values in the martian atmosphere that were  $\sim 6$  times that of Earth (7) were pivotal in the idea of atmospheric loss to space from a dense, warm, ancient atmosphere. Initial measurements in meteorites (16) gave a wide range of D/H values that may have included terrestrial contributions. A more recent analysis (17) of the ancient meteorite ALH84001 ( $\sim 4$  billion years old) and young meteorite Shergotty (0.17 billion years old) produced  $\delta\text{D}$  values of 3000

and 4600, respectively. These results have been interpreted (17) as evidence for a two-stage evolution for Martian water—a significant early loss of water to space [before 3.9 billion years ago (Ga)], followed by only modest loss to space during the past 4 billion years. Until Curiosity landed, there had been no in situ measurements of the water isotopic species HDO and  $\text{H}_2^{18}\text{O}$ .

Oxygen isotopes in carbonates and sulfates from martian meteorites do not show any enrichment in  $\delta^{18}\text{O}$  and therefore have not been used as indicators of atmospheric escape (18, 19).

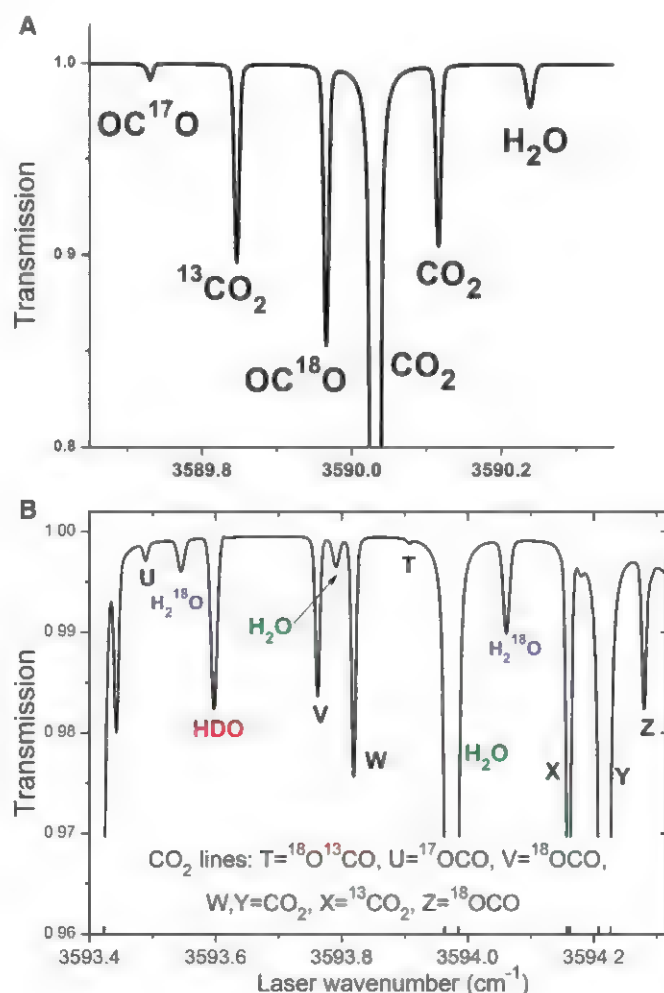
It has been suggested that they are buffered by interaction with a larger O reservoir such as the silicates in the crust, or crustal ice deposits (20), although this is complicated by evidence for disequilibrium between the crust and the atmosphere (21). Oxygen isotopes in  $\text{CO}_2$  and  $\text{H}_2\text{O}$  are therefore likely indicators of more complex interactions between the large reservoir of O in the hydrosphere, lithosphere, and atmosphere of Mars.

TLS is a two-channel tunable laser spectrometer that uses direct and second harmonic detection of infrared (IR) laser light absorbed after

**Table 1. Carbon dioxide isotope ratios  $\%$   $\pm$  2 SEM (standard error of the mean). \*, not measured.**

Measurement	$\delta^{13}\text{C}$	$\delta^{18}\text{O}$	$\delta^{17}\text{O}$	$\delta^{13}\text{C}-^{18}\text{O}$
SAM-TLS	$46 \pm 4$	$48 \pm 5$	$24 \pm 5$	$109 \pm 31$
SAM-QMS (3)	$45 \pm 12$	*	*	*
Phoenix lander (12)	$-2.5 \pm 4.3$	$31.0 \pm 5.7$	*	*
Viking Neutral Mass Spectrometer (11)	$23 \pm 43$	$7 \pm 44$	*	*
SNC meteorites (8, 12, 32)	$36 \pm 10$	$3.9-5.4 \pm 0.1$	$-0.53^* \delta^{18}\text{O} \sim \delta^{13}\text{C} + \delta^{18}\text{O}$	
ALH84001 meteoritic carbonate range (30, 31)	27 to 64	$-9$ to $26$	$-0.53^* \delta^{18}\text{O} \sim \delta^{13}\text{C} + \delta^{18}\text{O}$	
ALH84001 meteoritic carbonate mean value (31)	$46 \pm 8$	$4.6 \pm 1.2$	*	*
Earth telescopes (9)	$-22 \pm 21$	$18 \pm 18$	*	*

**Fig. 1. Spectral scan regions used by the TLS instrument.** Calculated spectra from the HITRAN database (36) for measuring  $\text{CO}_2$  (A and B) and  $\text{H}_2\text{O}$  isotope ratios (B). The HDO line intensity has been increased by a factor of 6 to better represent the martian environment.



<sup>1</sup>Jet Propulsion Laboratory, California Institute of Technology, Pasadena, CA 91109, USA. <sup>2</sup>NASA Goddard Space Flight Center, Greenbelt, MD 20771, USA. <sup>3</sup>Rensselaer Polytechnic Institute, Troy, NY 12180, USA. <sup>4</sup>University of Michigan, Ann Arbor, MI 48105, USA. <sup>5</sup>University of Hawaii, Honolulu, HI 96822, USA. <sup>6</sup>NASA Johnson Space Center, Houston, TX 77058, USA. <sup>7</sup>University of Arizona, Tucson, AZ 85721, USA. <sup>8</sup>University of Minnesota, Minneapolis, MN 55455, USA. <sup>9</sup>Carnegie Institution of Washington, Washington, DC 20015, USA.

\*Corresponding author. E-mail: chris.r.webster@jpl.nasa.gov  
†Mars Science Laboratory (MSL) Science Team authors and affiliations are listed in the supplementary materials.



multipassing a sample cell (1). One laser source is a near-IR tunable diode laser at 2.78  $\mu\text{m}$  that can scan two spectral regions containing  $\text{CO}_2$  and  $\text{H}_2\text{O}$  isotopic lines; the second laser source is an interband cascade laser at 3.27  $\mu\text{m}$  used for methane detection alone (4). The near-IR laser makes 43 passes of a 20-cm-long sample (Herriott) cell that is evacuated with a turbomolecular pump for background scans, then filled to 0.7 mbar using volume expansion of Mars air originally at  $\sim 7$  mbar. TLS scans over individual rovibrational lines in two spectral regions near 2.78  $\mu\text{m}$ ; one centered at 3590  $\text{cm}^{-1}$  for  $\text{CO}_2$  isotopes and a second centered at 3594  $\text{cm}^{-1}$  for both  $\text{CO}_2$  and  $\text{H}_2\text{O}$  isotopes (Figs. 1 and 2). The lines used in both regions have no significant interferences. In the 3594  $\text{cm}^{-1}$  region, the  $\text{CO}_2$  and  $\text{H}_2\text{O}$  lines we used interleave across the spectrum without interference, allowing the determination of accurate isotope ratios across widely varying  $\text{CO}_2$  and  $\text{H}_2\text{O}$  abundances in both atmospheric and evolved gas experiments. The laser scans every second through the target spectral regions. Each 1-s spectrum is then co-added on board in 2-min periods, and the averaged spectra are then down-linked as raw data during a given run, typically of  $\sim 30$  min duration. Data reported here were collected from 6 days (martian sols 28, 53, 73, 79, 81, and 106). During data collection, the Herriott cell and other optics are kept at  $47^\circ \pm 3^\circ\text{C}$  using a ramped heater that also serves to increase the signal-to-noise ratio in spectra by reducing the effect of interference fringes occurring during the 2-min sample period. The measured background amounts (empty cell) of both  $\text{CO}_2$  and  $\text{H}_2\text{O}$  are negligible and also reflect an insignificant contribution to the signal from the instrument foreoptics. TLS is calibrated using certified isotopic standards (22) that improve the accuracy of isotope ratios over using the more uncertain HITRAN (high-resolution transmission molecular absorption) database spectral parameters.

Our  $\text{CO}_2$  isotope ratios (Table 1, table S1, and Fig. 3) are given relative to Vienna Pee Dee belemnite (VPDB) for  $\delta^{13}\text{C}$  and relative to Vienna standard mean ocean water (VSMOW) for all oxygen isotopes (13). The measured value of  $\delta^{13}\text{C}^{18}\text{O}$  agrees within uncertainty to the sum of the individual  $\delta^{13}\text{C}$  and  $\delta^{18}\text{O}$  measurements, providing a valuable check-sum on our results. Also, our measured value for  $\delta^{17}\text{O}$  is half that of  $\delta^{18}\text{O}$ , as predicted from mass-dependent fractionation ( $\delta^{17}\text{O} = 0.528 \times \delta^{18}\text{O}$ ) and consistent with previous SNC meteorite analysis. The independent SAM QMS result for  $\delta^{13}\text{C}$  of  $45 \pm 12\text{‰}$  (3) agrees well with that from TLS at  $46 \pm 4\text{‰}$ , both values notably disagreeing with the much lower Phoenix lander result (12) of  $2.5 \pm 4.3\text{‰}$ . The sol-by-sol data plotted in Fig. 3 is not over a sufficiently long period to assess possible seasonal variation in  $\delta^{13}\text{C}$  or  $\delta^{18}\text{O}$ .

Our measured water abundances of up to 1% by volume in our Herriott cell after atmospheric intake exceed those expected ( $\sim 150$  parts per

**Fig. 2. Observed versus calculated spectra.** A single spectrum (middle section) downloaded from Curiosity (black), showing observed enrichment in  $^{13}\text{CO}_2$  and  $^{18}\text{OCO}$  compared to the calculated HITRAN spectrum (red) based on terrestrial (VPDB and VSMOW) isotope ratios (36). Both spectra are normalized in depth to the  $^{16}\text{O}^{12}\text{C}^{16}\text{O}$  line near 3590.1  $\text{cm}^{-1}$  (Fig. 1). Ringing to the left side of the lines is explained in (22).

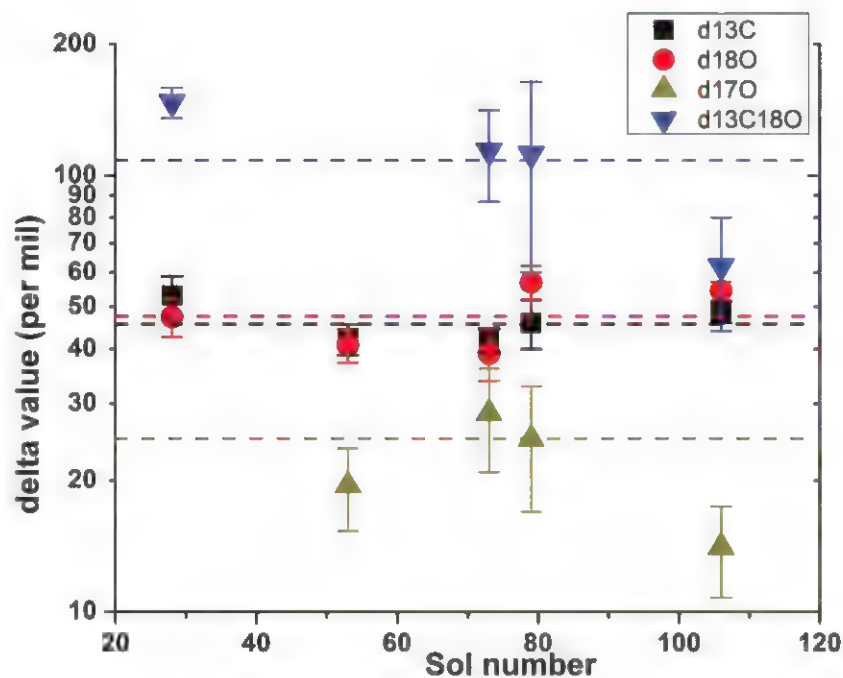
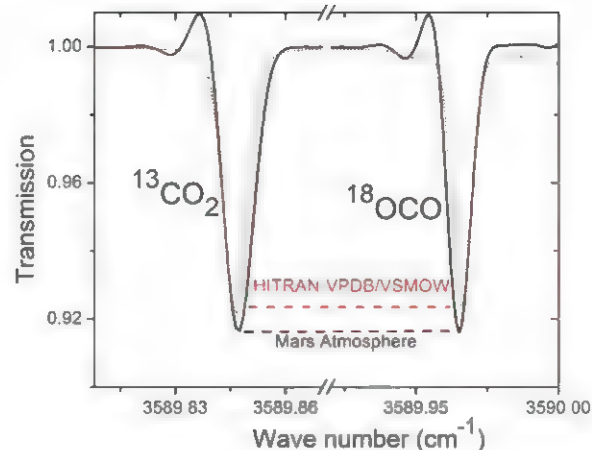


**Fig. 3. Sol-by-sol mean values for  $\text{CO}_2$  isotope ratios.** The mean values for all sols combined (dashed lines) are given in Table 1. See (22) for values and uncertainties of the individual sol data plotted.

million by volume) in martian air, and allowed us to retrieve a value for atmospheric  $\delta\text{D}$ , although with high uncertainty. Because our measured highly enriched  $\delta\text{D}$  values (Table 2 and table S2) are clearly martian and not terrestrial, we attribute the high water mixing ratios to either high near-surface humidity (natural or from enhanced temperatures in the vicinity of the rover) or to water entrained from frozen or liquid sources on or near the heated inlet valve. Also, in evolved gas experiments from pyrolysis of Rocknest fines (23), water was seen coming off at relatively low temperatures that we here identify as representative of the  $\delta\text{D}$  and  $\delta^{18}\text{O}$  values of the martian atmosphere. The TLS measurement of  $\delta\text{D}$  agrees well with observations from ground-based telescopes (24), but the contribution from expected

seasonal cycling (25) is unknown. The enriched atmospheric values contrast with the low primordial D/H values postulated for the martian mantle (26) and are higher than those from our Rocknest higher-temperature studies (23).

Modeling estimates of escape processes and atmospheric stability during Mars' initial history point to catastrophic loss of atmospheric mass, and suggest that many atmospheric species carrying records of early isotopic evolution did not survive beyond approximately 3.7 to 4 Ga (27, 28). Carbonates in the ALH 84001 meteorite derived from an alteration event that occurred at  $\sim 3.9$  Ga (29) preserve our best record of these events. Measurements of ALH 84001 carbonates show enriched isotopic values of  $\delta^{13}\text{C}$   $+27$  to  $+64\text{‰}$  (30, 31),  $\delta\text{D}$  values of  $\sim 3000\text{‰}$  (16, 17), and low

**Table 2. Water isotope ratios ‰ ± 2 SEM. \*, not measured.**

Measurement	$\delta D$	$\delta^{18}O$
SAM-TLS atmosphere	4950 ± 1,080	*
SAM-TLS evolved water: Rocknest fines 230° to 430°C (23)	5880 ± 60	84 ± 10
Meteoritic crustal reservoirs (26)	~5000	*
Earth telescopes (24)	1700–8900	*
ALH 84001 (17)	3000	*
Shergotty USNM 321-1 (17)	4600	*

$\delta^{18}O$  values (32). These values are similar to the composition of the modern martian atmosphere, suggesting that the  $\delta^{13}C$ ,  $\delta D$ , and  $\delta^{18}O$  of the martian atmosphere were enriched early and have not changed much over ~4 billion years. Our higher values of  $\delta D$  and  $\delta^{18}O$  measured in the atmosphere suggest that escape processes may have also continued since 4.0 Ga, in accordance with a two-stage evolutionary process (17) described above.

We observe large enrichments of  $\delta^{18}O$  in atmospheric water vapor and  $CO_2$ . The  $\delta^{18}O$  values of the water vapor are much larger than the  $\delta^{18}O$  observed in carbonates and sulfates in martian meteorites and suggest that the oxygen in water vapor in the martian atmosphere is not in equilibrium with the crust (33, 34) and could have been enriched in heavy isotopes through atmospheric loss. Another possibility is that the elevated oxygen isotope values in the more abundant martian  $CO_2$  are being transferred to the water vapor through photochemical reactions in the atmosphere. However,  $\delta^{18}O$  values of  $CO_2$  in Earth's atmosphere are similarly elevated because of low-temperature equilibration between  $CO_2$  and  $H_2O$ , and this process could also be operative on Mars (12).

In addition to atmospheric loss, other processes such as volcanic degassing and weathering might act to change the isotopic composition of the atmosphere through time. Estimates for the magnitude of these two contributions over the ~4-billion-year history of Mars vary widely (30, 34, 35), yet could have a strong impact on the isotopic composition of the atmosphere and challenge the status quo model described above.

#### References and Notes

- P. R. Mahaffy et al., *Space Sci. Rev.* **170**, 401–478 (2012).
- J. P. Grotzinger et al., *Space Sci. Rev.* **170**, 5–56 (2012).
- P. R. Mahaffy et al., *Science* **341**, 263–266 (2013).
- C. R. Webster, P. R. Mahaffy, S. K. Atreya, G. J. Flesch, K. A. Farley, *Lunar Planet. Sci. Conf.*, abstract 1366 (2013).
- B. M. Jakosky, R. J. Phillips, *Nature* **412**, 237–244 (2001).
- M. B. McElroy, Y. L. Yung, A. O. Nier, *Science* **194**, 70–72 (1976).
- T. Owen, J.-P. Maillard, C. de Bergh, B. L. Lutz, *Science* **240**, 1767–1770 (1988).
- R. H. Carr, M. M. Grady, I. P. Wright, C. T. Pillinger, *Nature* **314**, 248–250 (1985).
- V. A. Krasnopolsky, J. P. Maillard, T. C. Owen, R. A. Toth, M. D. Smith, *Icarus* **192**, 396–403 (2007).

- P. B. Niles et al., *Space Sci. Rev.* **174**, 301–328 (2013).
- A. O. Nier, M. B. McElroy, *Science* **194**, 1298–1300 (1976).
- P. B. Niles, W. V. Boynton, J. H. Hoffman, D. W. Ming, D. Hamara, *Science* **329**, 1334–1337 (2010).
- R. E. Criss, *Principles of Stable Isotope Composition* (Oxford Univ. Press, Oxford, 1999).
- C. R. Webster, A. J. Heymsfield, *Science* **302**, 1742–1745 (2003).
- P. Hartogh et al., *Nature* **478**, 218–220 (2011).
- L. A. Leshin, S. Epstein, E. M. Stolper, *Geochim. Cosmochim. Acta* **60**, 2635–2650 (1996).
- J. P. Greenwood, S. Itoh, N. Sakamoto, E. P. Vicenzi, H. Yurimoto, *Geophys. Res. Lett.* **35**, L05203 (2008).
- J. Farquhar, M. H. Thiemens, *J. Geophys. Res.* **105**, (2000).
- C. S. Romanek et al., *Nature* **372**, 655–657 (1994).
- B. Jakosky, A. Zent, R. Zurek, *Icarus* **130**, 87–95 (1997).
- H. R. Karlsson, R. N. Clayton, E. K. Gibson Jr., T. K. Mayeda, *Science* **255**, 1409–1411 (1992).
- See the supplementary materials on Science Online.
- L. A. Leshin et al., *Lunar Planet. Sci. Conf.*, abstract 2220 (2013).

- D. A. Fisher, *Icarus* **187**, 430–441 (2007) and references therein.
- R. E. Novak et al., *Bull. Am. Astron. Soc.* **35**, 660 (2005).
- T. Usui, C. Alexander, J. Wang, J. Simon, J. Jones, *Earth Planet. Sci. Lett.* **357–358**, 119–129 (2012).
- H. Lammer et al., *Space Sci. Rev.* **174**, 113–154 (2013).
- R. O. Pepin, *Icarus* **111**, 289–304 (1994).
- L. Borg, M. J. Drake, *J. Geophys. Res.* **110**, E12503 (2005).
- P. B. Niles, L. A. Leshin, Y. Guan, *Geochim. Cosmochim. Acta* **69**, 2931–2944 (2005).
- J. W. Valley et al., *Science* **275**, 1633–1638 (1997).
- J. Farquhar, D. T. Johnston, *Rev. Mineral. Geochem.* **68**, 463–492 (2008).
- B. M. Jakosky, J. H. Jones, *Nature* **370**, 328–329 (1994).
- M. Grott, A. Morschhauser, D. Breuer, E. Hauber, *EPSL* **308**, 391–400 (2011).
- J. P. Bibring et al., *Science* **312**, 400–404 (2006).
- L. S. Rothman et al., *J. Quant. Spectrosc. Radiat. Transf.* **110**, 533–572 (2009).

**Acknowledgments:** The research described here was carried out at the Jet Propulsion Laboratory, California Institute of Technology, under a contract with NASA.

#### Supplementary Materials

www.sciencemag.org/cgi/content/full/341/6143/260/DC1  
Materials and Methods  
Supplementary Text  
Figs. S1 to S3  
Tables S1 to S4  
Reference (37)  
MSL Science Team Authors and Affiliations  
18 March 2013; accepted 17 June 2013  
10.1126/science.1237961

## Abundance and Isotopic Composition of Gases in the Martian Atmosphere from the Curiosity Rover

Paul R. Mahaffy,<sup>1\*</sup> Christopher R. Webster,<sup>2</sup> Sushil K. Atreya,<sup>3</sup> Heather Franz,<sup>1</sup> Michael Wong,<sup>3</sup> Pamela G. Conrad,<sup>1</sup> Dan Harpold,<sup>1</sup> John J. Jones,<sup>4</sup> Laurie A. Leshin,<sup>5</sup> Heidi Manning,<sup>6</sup> Tobias Owen,<sup>7</sup> Robert O. Pepin,<sup>8</sup> Steven Squyres,<sup>9</sup> Melissa Trainer,<sup>1</sup> MSL Science Team†

Volume mixing and isotope ratios secured with repeated atmospheric measurements taken with the Sample Analysis at Mars instrument suite on the Curiosity rover are: carbon dioxide ( $CO_2$ ),  $0.960(\pm 0.007)$ ; argon-40 ( $^{40}Ar$ ),  $0.0193(\pm 0.0001)$ ; nitrogen ( $N_2$ ),  $0.0189(\pm 0.0003)$ ; oxygen,  $1.45(\pm 0.09) \times 10^{-3}$ ; carbon monoxide,  $< 1.0 \times 10^{-3}$ ; and  $^{40}Ar/^{36}Ar$ ,  $1.9(\pm 0.3) \times 10^3$ . The  $^{40}Ar/N_2$  ratio is 1.7 times greater and the  $^{40}Ar/^{36}Ar$  ratio 1.6 times lower than values reported by the Viking Lander mass spectrometer in 1976, whereas other values are generally consistent with Viking and remote sensing observations. The  $^{40}Ar/^{36}Ar$  ratio is consistent with martian meteoritic values, which provides additional strong support for a martian origin of these rocks. The isotopic signature  $\delta^{13}C$  from  $CO_2$  of ~45 per mil is independently measured with two instruments. This heavy isotope enrichment in carbon supports the hypothesis of substantial atmospheric loss.

The science and exploration goal of the Mars Science Laboratory (MSL) (1) is to advance our understanding of the potential of the present or past martian environments to support life. An understanding of how the present environment in Gale crater differs from the environment at the time of its forma-

tion requires comprehensive chemical characterization. The first set of experiments of the Sample Analysis at Mars (SAM) investigation (2) (Fig. 1) of the Curiosity rover included measurements of the chemical and isotopic composition of the atmosphere with sequences that employed two of SAM's three instruments. When



combined with composition and isotope data from atmospheric gases trapped in martian meteorites, measurements of the rate of atmospheric escape from orbiting spacecraft, and studies of atmosphere-surface exchange, SAM atmosphere measurements are intended to constrain models of atmospheric loss and climate evolution over geological time.

We report here on results from samples of the martian atmosphere analyzed by SAM's quadrupole mass spectrometer (QMS) and tunable laser spectrometer (TLS) during the first 105 sols (1 sol is a martian day) of the landed mission. These experiments were among the first carried out by SAM (Fig. 1) after several health checks of the instrument. The experiments took place over a period of several weeks from Mars solar longitude (3) of 163.7 to 211.2 (31 August to 21 November 2012) in Gale crater south of the equator (4.5°S, 137°E). All measurements were taken at night (table S1), and weighted means (table S2) are reported.

The mixing ratios of CO<sub>2</sub>, N<sub>2</sub>, Ar, O<sub>2</sub>, CO, Ne, Kr, and Xe at the martian surface were determined by the mass spectrometers on the 1976 Viking Landers (4) more than 3 decades ago. Mass spectrometers on the Viking aeroshells also detected CO<sub>2</sub>, N<sub>2</sub>, Ar, CO, O<sub>2</sub>, O, and NO (5) over an altitude range from 200 to 120 km, approaching or reaching the homopause or the altitude below which the atmosphere is well mixed. Spectroscopic measurements of CO have also been obtained from the Mars Reconnaissance Orbiter [e.g., (6)], the Mars Express Spacecraft (7, 8), and a number of ground-based observations [e.g., (9)], revealing long-term variations correlated with solar activity (9). Recent Herschel submillimeter observations (10) have provided an additional measurement of the mixing ratios for CO (10) of  $9.8(\pm 1.5) \times 10^{-4}$  and for O<sub>2</sub> (11) of  $1.40(\pm 0.12) \times 10^{-3}$ . The CO mixing ratio is found to vary by more than a factor of 4 (from  $\sim 3 \times 10^{-4}$  to  $1.2 \times 10^{-3}$ ) seasonally at polar latitudes, with smaller changes in the equatorial region (6). The relative change in CO reflects enrichment and depletion of noncondensable volatiles during the condensation and sublimation of CO<sub>2</sub>, the principal component of the martian atmosphere.

Argon (<sup>40</sup>Ar) has also been monitored globally from orbit by the gamma-ray spectrometer (GRS) on the Mars Odyssey spacecraft and from the martian surface by the alpha particle x-ray spectrometers (APXS) on the Mars Exploration

rovers at latitudes of -2° and -15°. The GRS-derived Ar mixing ratio exhibits a large seasonal change by as much as a factor of 6 over the southern pole in winter (12) as the atmospheric CO<sub>2</sub> undergoes an annual cycle of condensation and sublimation, producing a 25% change in the surface pressure. Although the GRS data exhibit no seasonal change in Ar in the equatorial region (12), APXS finds that Ar nearly tracks the seasonal changes in surface pressure with a 2- to 3-month phase lag (13).

The mixing ratio of nitrogen can best be determined by in situ measurements because meteorite measurements do not give definitive answers for this atmospheric gas. Variations in isotopic composition of nitrogen in impact glasses of the martian shergottite meteorites EET79001 (14, 15), Zagami (16), and Tissint [e.g., (16, 17)] suggest that, in these samples, atmospheric nitrogen is mixed with an interior component with a lower <sup>15</sup>N/<sup>14</sup>N ratio.

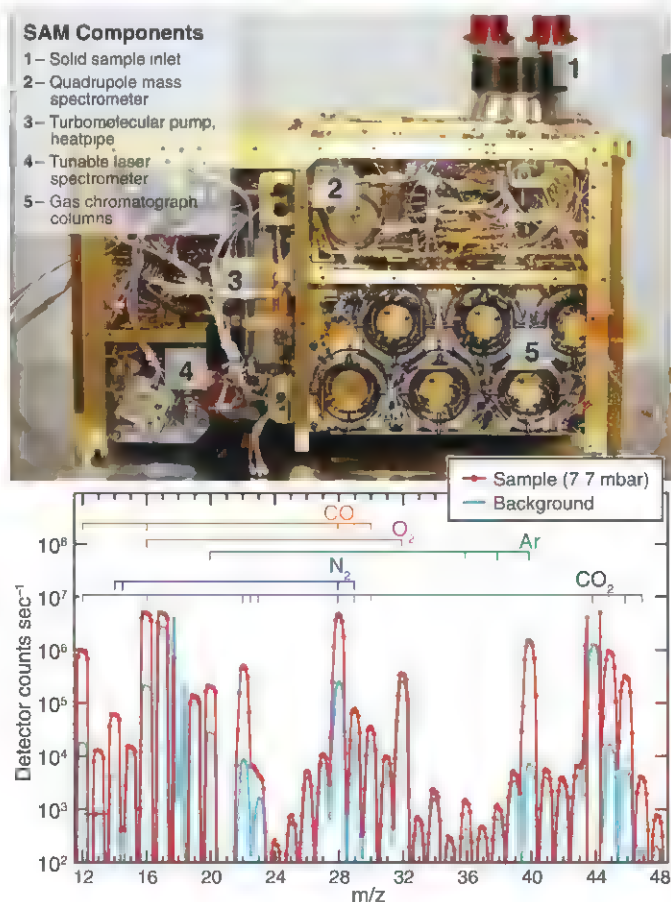
The atmospheric CO<sub>2</sub> isotope  $\delta^{13}\text{C}_{\text{VPDB}}$  (VPDB, Vienna Pee Dee belemnite) (18) has been reported as  $-2.5 \pm 4.3$  per mil (‰) from the Thermal and Evolved Gas Analyzer (TEGA) mass spectrometer on the Phoenix lander (19) and as  $-22 \pm 20$  ‰ from Fourier transform Earth-based spectroscopy (20). The higher-uncertainty measurements of the Viking lander found CO<sub>2</sub> isotopes to be within 50‰ of terrestrial isotopes (4). The aeroshell measurements had similarly

large error bars with reported carbon isotopic composition equivalent to  $\delta^{13}\text{C}_{\text{VPDB}}$  of  $23 \pm 50$ ‰ (5).

Detailed characterization of the SNC (Shergotty, Nakhla, and Chassigny) meteorites (14, 16, 21–24) has revealed a combination of volatile abundances and isotope systematics (14, 15, 21, 25–27) for noble gases, N<sub>2</sub>, and CO<sub>2</sub> that is possible only with origin on Mars or a very Mars-like parent body (28). Although the Viking abundance and isotope measurements provided evidence supporting the hypothesis that the SNCs are from Mars, the meteorites contain volatiles from other sources [for example, magmatic or possible cometary delivery (29)], in addition to trapped atmospheric gases that cause some variations among the meteorite values and differences between meteorite and Viking measurements. In addition to the uncertainties introduced by multiple sources of volatiles in the SNC meteorites, the solubility of the volatiles and their partitioning in glass and in the constituent mineral phases affects both the abundance value and the isotopic signature, including those of the noble gases (30, 31). The SAM data are therefore key to constraining the atmospheric component of data obtainable from meteorites with in situ observations.

Many previous composition measurements analyzed only a single or a small number of species. The SAM instrument suite, with the use of

**Fig. 1. The SAM suite located in the interior of the Curiosity rover uses three instruments to test either atmospheric gas or solid samples. (Top)** An image of SAM with the side panels removed. **(Bottom)** Mass spectrum of the martian atmosphere from sol 45, with mass peaks labeled for the main atmospheric species. Isotopes of argon appear above the background level (blue traces) at mass/charge ratio (*m/z*) 36, 38, and 40 (green ticks at top of plot). Primary ions from isotopologues of CO<sub>2</sub> containing <sup>13</sup>C, <sup>17</sup>C, and/or <sup>18</sup>O, appear at *m/z* 45, 46, and 47 (black ticks at top of plot).



<sup>1</sup>NASA Goddard Space Flight Center, Greenbelt, MD 20771, USA. <sup>2</sup>Jet Propulsion Laboratory, California Institute of Technology, 4800 Oak Grove Drive, Pasadena, CA 91109, USA. <sup>3</sup>University of Michigan, Ann Arbor, MI 48109, USA. <sup>4</sup>NASA Johnson Space Center, Houston, TX 77058, USA. <sup>5</sup>Rensselaer Polytechnic Institute, Troy, NY 12180, USA. <sup>6</sup>Concordia College, Moorhead, MN 56562, USA. <sup>7</sup>University of Hawaii, Honolulu, HI 96822, USA. <sup>8</sup>University of Minnesota, Minneapolis, MN 55455, USA. <sup>9</sup>Cornell University, Ithaca, NY 14853, USA.

\*Corresponding author. E-mail: paul.r.mahaffy@nasa.gov  
†MSL Science Team authors and affiliations are listed in the supplementary materials.

**Table 1. Volume mixing ratio measurements from Curiosity during the first 105 sols of the landed mission.**

Gas	Volume mixing ratio (QMS)
CO <sub>2</sub>	0.960(±0.007)
Ar	0.0193(±0.0003)
N <sub>2</sub>	0.0189(±0.0003)
O <sub>2</sub>	1.45(±0.09) × 10 <sup>-3</sup>
CO	<1.0 × 10 <sup>-3</sup>

both the TLS and QMS, is able to make multiple, high-precision composition measurements over the course of the mission. In addition, SAM's QMS and TLS provide fully independent analyses of carbon isotopes. Repeat runs reported here were carried out at nearly the same time in the early evening on Mars to validate results. Each measurement set of the type implemented to date (32) represents a comprehensive analysis of the main constituents of the martian atmosphere.

SAM confirms the identity of the four most abundant gases in the martian atmosphere, with CO<sub>2</sub> being by far the major constituent. The SAM results for O<sub>2</sub> (Tables 1 and 2) are consistent with the recent Herschel (11) observations. SAM secures an upper limit for the CO mixing ratio (Tables 1 and 2) that is consistent with the Herschel data and the mean of all remote sensing spectroscopic measurements (~9 × 10<sup>-4</sup>). Differences in CO mixing ratios are expected and are related to the abovementioned seasonal effects, as dynamics and mixing rather than chemistry are expected to dominate the behavior of CO in the homosphere due to the 3-year photochemical lifetime of CO. In addition to seasonal effects, localized, heterogeneous surface effects may also affect SAM measurements of CO because of possible adsorption of CO onto the surface during cold martian nights—when SAM data were collected—and reevaporation during warmer daytime. The Herschel observations, on the other hand, are weighted to higher in the atmosphere. Unlike CO, seasonal variation in O<sub>2</sub> has not yet been observed.

The most notable differences between the SAM measurements and previous data are in the relative abundances of Ar and N<sub>2</sub> and in the isotopic compositions of Ar and CO<sub>2</sub>. The Ar/N<sub>2</sub> ratio and the N isotopes provide important constraints to models for assessing the relative contributions of internal and atmospheric sources to gas inclusions in shock-produced glassy martian meteorites. The isotope data are important for constraining models of atmospheric evolution. Whereas Viking found nitrogen and argon to be the second and third most abundant atmospheric gases at 2.7 and 1.6% by volume, respectively, SAM determines nearly equal volume mixing ratios for these constituents. Ar is found to be 21% greater, whereas N<sub>2</sub> is 30% lower than the Viking values. The resulting Ar/N<sub>2</sub> ratio of 1.02

**Table 2. Isotopic composition measurements from Curiosity during the first 105 sols of the landed mission. N/A, not applicable.**

Isotopes	Isotopic composition (QMS)	Isotopic composition (TLS)
<sup>40</sup> Ar/ <sup>36</sup> Ar	1.9(±0.3) × 10 <sup>-3</sup>	N/A
δ <sup>13</sup> C <sub>V-PDB</sub>	45(±12) ‰*	46(±4) ‰†
δ <sup>18</sup> O <sub>V-PDB</sub>	N/A	48(±5) ‰

\*δ<sup>13</sup>C<sub>V-PDB</sub> is derived from *m/z* 12 and 13.

†δ<sup>13</sup>C<sub>V-PDB</sub>, as derived from *m/z* 45 and 46, is described in the supplementary materials.

measured by SAM is ~1.7 times greater than the value reported from Viking measurement (4). Both Ar and N<sub>2</sub> are noncondensable and practically inert gases on Mars, so their relative abundances are not expected to change considerably with time. We suspect that the difference from Viking results is due to different instrumental characteristics rather than some unknown atmospheric process, although seasonal variation in N<sub>2</sub> is yet to be tracked. The use on Mars of a turbomolecular pumping system (33), as well as repeated SAM analyses are expected to produce a more accurate determination of the ratio of these gases than the previous Viking in situ measurements whose mass spectrometers employed small ion pumps.

The SAM QMS offers independent validation of the δ<sup>13</sup>C<sub>V-PDB</sub> value in CO<sub>2</sub> measured by the TLS (34). The average of three SAM QMS atmosphere measurements gives δ<sup>13</sup>C<sub>V-PDB</sub> value of 45 ± 12 ‰, which is fully consistent with the independently measured TLS value of 46 ± 4 ‰ (34). This observed ~5% enrichment in the heavier carbon isotope in the martian atmosphere compares well with previous measurements of <sup>13</sup>C-enriched carbon of atmospheric origin in martian meteorite EETA79001 (22, 35). The data support the hypothesis that significant carbon has been lost from the martian atmosphere over time by sputtering (36).

The <sup>40</sup>Ar/<sup>36</sup>Ar ratio of 1900 ± 300 measured by SAM is within error of the trapped atmosphere measured (15) to be 2050 ± 170 in quenched shock-produced melts in martian meteorite EETA79001 (27, 37, 38) but is considerably smaller than the value of 3000 ± 500 reported by Viking (4). Laboratory studies of shock implantation into silicate liquid have demonstrated that this process is a nearly quantitative recorder of atmospheric composition (39, 40), and the implanted gases in meteorite shock-produced melts compared with the Viking in situ measurements of the atmosphere have been used as the best evidence to tie these meteorites to Mars (14, 15, 21, 41). However, noble gases released from shock-produced glasses in EETA79001 contained at least three components (27): (i) martian air, (ii) terrestrial contamination, and (iii) a martian interior component with low <sup>40</sup>Ar/<sup>36</sup>Ar.

Even with the somewhat lower value measured by SAM, the <sup>40</sup>Ar/<sup>36</sup>Ar of the martian atmosphere is highly elevated relative to the terrestrial ratio of 296. The enrichment in the

radiogenic <sup>40</sup>Ar over nonradiogenic <sup>36</sup>Ar has been interpreted as evidence for significant loss of the primordial martian atmosphere early in the planet's history, followed by partial degassing of Ar. Subsequent loss to space is expected to lead to enrichment of the <sup>40</sup>Ar over <sup>36</sup>Ar (42, 43) by the same processes that have reduced the <sup>36</sup>Ar/<sup>38</sup>Ar ratio in the martian atmosphere. The latter ratio as inferred from EETA79001 glasses (15, 38) was found to be ~4, much different from the terrestrial, chondritic, solar, and jovian (44) values which range in order from 5.3 to ~5.5. It is notable that the <sup>40</sup>Ar/<sup>36</sup>Ar ratio has not changed appreciably since the ejection of EETA79001 from the planet ~700,000 years ago. This provides a constraint on the extent of very recent inputs of gas to the atmosphere from volcanic or cometary sources. The carbon dioxide isotope data support the hypothesis that a significant amount of carbon has escaped from the martian atmosphere over time, resulting in preferential loss of the lighter isotope of carbon and the observed enrichment in <sup>13</sup>C (45). This implies that atmospheric escape has dominated over exchange with unfractionated surface reservoirs that exist in the crust or mantle.

## References and Notes

1. J. P. Grotzinger *et al.*, *Space Sci. Rev.* **170**, 5–56 (2012).
2. P. R. Mahaffy *et al.*, *Space Sci. Rev.* **170**, 401–478 (2012).
3. A Mars solar longitude of 180° represents the southern spring equinox, where the southern polar region would be covered with carbon dioxide ice.
4. T. Owen *et al.*, *J. Geophys. Res.* **82**, 4635–4639 (1977).
5. A. O. Nier, M. B. McElroy, *Science* **194**, 1298–1300 (1976).
6. M. D. Smith, M. J. Wolff, R. T. Clancy, S. L. Murchie, *J. Geophys. Res.* **114**, E00D03 (2009).
7. F. Billebaud *et al.*, *Planet. Space Sci.* **57**, 1446–1457 (2009).
8. G. Sindoni, V. Formisano, A. Geminale, *Planet. Space Sci.* **59**, 149–162 (2011).
9. V. A. Krasnopolsky, *Icarus* **190**, 93–102 (2007).
10. P. Hartogh *et al.*, *Astron. Astrophys.* **521**, L48 (2010).
11. P. Hartogh *et al.*, *Astron. Astrophys.* **521**, L49 (2010).
12. A. L. Sprague *et al.*, *Science* **306**, 1364–1367 (2004).
13. T. E. Economou, R. T. Pierrehumbert, paper presented at the 41st Lunar and Planetary Institute Science Conference, abstract 2179, The Woodlands, TX, 1 March 2010.
14. R. H. Becker, R. O. Pepin, *Earth Planet. Sci. Lett.* **69**, 225–242 (1984).
15. R. C. Wiens, R. H. Becker, R. O. Pepin, *Earth Planet. Sci. Lett.* **77**, 149–158 (1986).
16. K. Marti, J. S. Kim, A. N. Thakur, T. J. McCoy, K. Keil, *Science* **267**, 1981–1984 (1995).
17. H. C. Aoudjehane *et al.*, *Science* **338**, 785–788 (2012).



18. VPDB is a terrestrial isotopes standard.
19. P. B. Niles, W. V. Boynton, J. H. Hoffman, D. W. Ming, D. Hamara, *Science* **329**, 1334–1337 (2010).
20. V. A. Krasnopolsky, J. P. Maillard, T. C. Owen, R. A. Toth, M. D. Smith, *Icarus* **192**, 396–403 (2007).
21. D. D. Bogard, P. Johnson, *Science* **221**, 651–654 (1983).
22. R. H. Carr, M. M. Grady, I. P. Wright, C. T. Pillinger, *Nature* **314**, 248–250 (1985).
23. H. V. McSweeney Jr., *Meteoritics* **29**, 757–779 (1994).
24. U. Ott, *Geochim. Cosmochim. Acta* **52**, 1937–1948 (1988).
25. U. Ott, F. Begemann, *Meteoritics* **20**, 721 (1985).
26. S. V. S. Murty, R. K. Mohapatra, *Geochim. Cosmochim. Acta* **61**, 5417–5428 (1997).
27. D. D. Bogard, D. H. Garrison, *Meteorit. Planet. Sci.* **33** (suppl.), 19 (1998).
28. A. H. Treiman, J. D. Gleason, D. D. Bogard, *Planet. Space Sci.* **48**, 1213–1230 (2000).
29. T. Owen, A. Bar Nun, *AIP Conf. Proc.* **341**, 123–138 (1994).
30. T. D. Swindle, *AIP Conf. Proc.* **341**, 175 (1994).
31. T. D. Swindle, J. H. Jones, *J. Geophys. Res.* **102**, 1671 (1997).
32. Details of measurement procedures and treatment of uncertainties are provided in the supplementary materials on Science Online.
33. The turbomolecular pumps on SAM are expected to provide a more stable pressure of noble gas in the mass spectrometer ion source compared with the small ion pumps used on Viking.
34. C. R. Webster et al., *Science* **341**, 260–263 (2013).
35. A. J. T. Jull, C. J. Eastoe, S. Clout, *J. Geophys. Res.* **102**, 1663 (1997).
36. B. M. Jakosky, R. O. Pepin, R. E. Johnson, J. L. Fox, *Icarus* **111**, 271–288 (1994).
37. D. H. Garrison, D. D. Bogard, *Meteorit. Planet. Sci.* **35** (suppl.), A58 (2000).
38. D. D. Bogard, R. N. Clayton, K. Marti, T. Owen, G. Turner, *Space Sci. Rev.* **96**, 425–458 (2001).
39. R. C. Wiens, R. O. Pepin, *Geochim. Cosmochim. Acta* **52**, 295–307 (1988).
40. D. Bogard, F. Horz, *Meteoritics* **21**, 337 (1986).
41. R. O. Pepin, *Nature* **317**, 473–475 (1985).
42. R. O. Pepin, *Icarus* **111**, 289–304 (1994).
43. T. Owen, A. Bar-Nun, *Icarus* **116**, 215–226 (1995).
44. P. R. Mahaffy et al., *J. Geophys. Res. Planets* **105**, 15061–15071 (2000).
45. B. M. Jakosky, J. H. Jones, *Rev. Geophys.* **35**, 1–16 (1997).

# Supplementary Materials

www.sciencemag.org/cgi/content/full/341/6143/263/DC1

Materials and Methods

Tables S1 and S2

References (46, 47)

MSL Science Team Author List

18 March 2013; accepted 4 June 2013

10.1126/science.1237966

## Ice-Shelf Melting Around Antarctica

E. Rignot,<sup>1,2\*</sup> S. Jacobs,<sup>3</sup> J. Mouginot,<sup>1</sup> B. Scheuchl<sup>1</sup>

We compare the volume flux divergence of Antarctic ice shelves in 2007 and 2008 with 1979 to 2010 surface accumulation and 2003 to 2008 thinning to determine their rates of melting and mass balance. Basal melt of  $1325 \pm 235$  gigatons per year (Gt/year) exceeds a calving flux of  $1089 \pm 139$  Gt/year, making ice-shelf melting the largest ablation process in Antarctica. The giant cold-cavity Ross, Filchner, and Ronne ice shelves covering two-thirds of the total ice-shelf area account for only 15% of net melting. Half of the meltwater comes from 10 small, warm-cavity Southeast Pacific ice shelves occupying 8% of the area. A similar high melt/area ratio is found for six East Antarctic ice shelves, implying undocumented strong ocean thermal forcing on their deep grounding lines.

The Antarctic Ice Sheet and its 58-m sea level equivalent (1) is buttressed along most of its periphery by floating extensions of land ice called ice shelves and floating ice tongues (Fig. 1). Ice shelves cover an area  $>1.561$  million km<sup>2</sup>, comparable in size to the Greenland Ice Sheet, and fringe 75% of Antarctica's coastline while collecting 20% of its snow-fall over 11% of its area (2, 3). These features are nourished by the inflow of continental ice from grounded glaciers, surface accumulation, and freezing of marine ice on their undersides. They lose mass to iceberg calving and basal melting along with topside sublimation and wind drift. Ice shelves exert considerable control on glacier stability and Antarctic Ice Sheet mass balance (4–6) and play important roles in ocean stratification and bottom water formation (7).

The traditional view of ablation from Antarctic ice shelves has been that it occurs mostly by iceberg calving, with basal melting only contributing 10 to 28% of the total mass loss (3–6). Estimates of ice-shelf meltwater production derived from oceanographic data (8–10, e.g.) are impractical for synoptic circumpolar coverage. Numerical simulations of ice-ocean

interactions extend from individual ice shelves to circumpolar models at various resolutions, but comparisons with observations are limited, and estimates of total ice-shelf meltwater production have varied from 357 to 1600 gigatons per year ( $1 \text{ Gt} = 10^{12} \text{ kg}$ ) (3, 7, 11). Glaciological estimates have focused on few ice shelves (6, 12, 13) or near a fraction of glacier grounding lines (14) due to incomplete velocity and thickness mapping.

Here, we present more accurate, higher-resolution glaciological estimates of ice-shelf melting around the entire continent. At any point on an ice shelf of thickness  $H$  and velocity vector  $\mathbf{v}$ , the rate of ice-shelf thickening  $\partial H/\partial t$  equals the sum of net surface mass balance  $SMB$  minus net basal melting  $B$  minus the lateral divergence in volume flux  $H\mathbf{v}$  (15). A negative value of  $B$  indicates the freeze-on of marine ice. The calculation of volume flux divergence on a point per point basis yields the distribution of freeze/melt (Fig. 1). The integration of the total inflow and outflow within the ice-shelf perimeters yields the area-average melt rate and total meltwater production (Table 1).

For  $SMB$ , we use output products from the Regional Atmospheric and Climate Model RACMO2 (16), which is forced at the lateral boundary and sea surface by global reanalyses of the European Centre for Medium-Range Weather Forecasts. RACMO2 includes surface meltwater retention due to refreezing, evaporation, wind drift, and

sublimation. The products have been validated with field data and an error propagation analysis (17) to a precision of 7 to 25%, average 10%, depending on location. We use the average  $SMB$  for the years 1979 to 2010 to represent a longer-term state.

Ice-shelf thickness is from Operation IceBridge (OIB) (18, 19) and BEDMAP-2 (1) (fig. S1, supplementary materials). It combines direct measurements from radio-echo sounding, with indirect estimates from altimetry-derived ice-shelf surface elevation assuming hydrostatic equilibrium with a nominal precision of 15 to 50 m (20). Flux gates are selected at the location of Interferometric Synthetic Aperture Radar (InSAR)-derived grounding lines, which are more precise than those derived from photogrammetric techniques or visible imagery (21), with accompanying impacts on estimates of volume fluxes. Ice-front flux gates are at the seaward limit of the volume flux data, within 1 to 3 km of ice-front positions digitized from a 150-m spacing mosaic of Advanced Land Observing System (ALOS) Polarimetric SAR (PALSAR) data for the years 2007 and 2008.

Ice-shelf flow vector velocities are from InSAR data collected in 2007 and 2008 and processed at 450-m spacing (22). The average precision in speed is 4 m/year and  $1.7^\circ$  in direction (fig. S2). In the absence of vertical shear on floating ice, the surface-derived velocity is equivalent to a depth-averaged velocity. We surveyed 99.5% of Antarctic ice-shelf area in 2007 and 2008 (Table 1), or 1.554 million km<sup>2</sup>, excluding a few smaller ice shelves where ice thickness is not well known (table S1). Drainage boundaries between ice shelves, including the eastern and western Ross, are defined by flow vector direction. Ice rises and islands are excluded from the ice-shelf area estimates but included in the  $SMB$  calculation.

Ice-shelf thickening  $\partial H/\partial t$  for the period 2003 to 2008 is calculated using the procedure in (23), with an error dependent on firm depth corrections (fig. S3). The results are combined with  $SMB$  and the flux divergence to calculate  $B$ , with a precision dominated by uncertainties in

<sup>1</sup>Department of Earth System Science, University of California, Irvine, CA 92697, USA. <sup>2</sup>Jet Propulsion Laboratory, Pasadena, CA 91109, USA. <sup>3</sup>Lamont-Doherty Earth Observatory, Columbia University, Palisades, NY 10964, USA.

\*Corresponding author. E-mail: erignot@uci.edu

ice-front thickness and firm depth corrections (table S1). We also calculate the results for  $\partial H/\partial t = 0$ , i.e., no ice-shelf thickness change, to obtain a reference rate  $B_{ss}$  corresponding to the amount of freezing or melting that would be required to maintain an ice shelf in “steady state” for 2007 and 2008 (fig. S4).

The freeze/melt distribution confirms that basal melting is strongest near the grounding zones of major glaciers and along the ice fronts of some of the largest ice shelves, especially Ronne (Fig. 1). Ice-shelf melting decreases away from grounding lines and becomes negative (accretion of marine ice) on all large ice shelves and some smaller ice shelves. This general pattern of melting and freezing beneath ice shelves is well understood (4–6, 15) and is governed by the Coriolis-influenced transport and vertical mixing of ocean heat, the pressure dependence of the freezing point of seawater, and the sea floor and cavity morphology. On some large ice shelves, freezing is concentrated on the

western sides, consistent with an oceanic circulation during which seawater is first cooled, freshened, and made more buoyant by melting.

The highest melt rates are detected in the Southeast Pacific sector of the Antarctic Peninsula and West Antarctica, from the northern end of George VI to the western end of Getz Ice Shelf. On slow-moving to nearly stationary ice shelves like the Wilkins, George VI, Abbot, and Sulzberger, basal melting entirely consumes the inflow of individual glaciers within a few km of their grounding zones. High melt rates are also revealed in the grounding zones of the Amery, Moscow University, Shackleton, and Totten in East Antarctica.

In contrast, low melt rates are found under the largest ice shelves—for example, the Ross West—except near deep grounding lines. Maximum grounding-line depth is only 0.9 km under the Ross West but 2.1 km under the Filchner and Ronne, 1.8 km under the Ross East, and 2.4 km under the Amery (1). Each additional 100 m adds

0.076°C to the thermal driving of seawater that may have started out near the sea-surface freezing point. Differences in observed melt rate may also be accentuated by variations in flushing time and tidal activity (24).

Total ice inflow and outflow for each ice shelf is summarized in Fig. 1 and Table 1. Ice-front flux is a proxy for, but not identical to, iceberg calving, which occurs at irregular time intervals ranging from days to decades. The higher basal melting near some ice-shelf fronts (12, 25) results from stronger tidal currents and mixing, especially in combination with a shallow water column (24), as along the eastern front of Ronne [150 ± 50 m in (1) versus 350 ± 100 m for Ross or 500 ± 250 m for Filchner]. Ice-front fluxes may overestimate iceberg calving where near-ice-front melting is substantial and calving is infrequent; conversely, large icebergs may on average be thicker than the ice front, in which case ice-front fluxes underestimate calving.

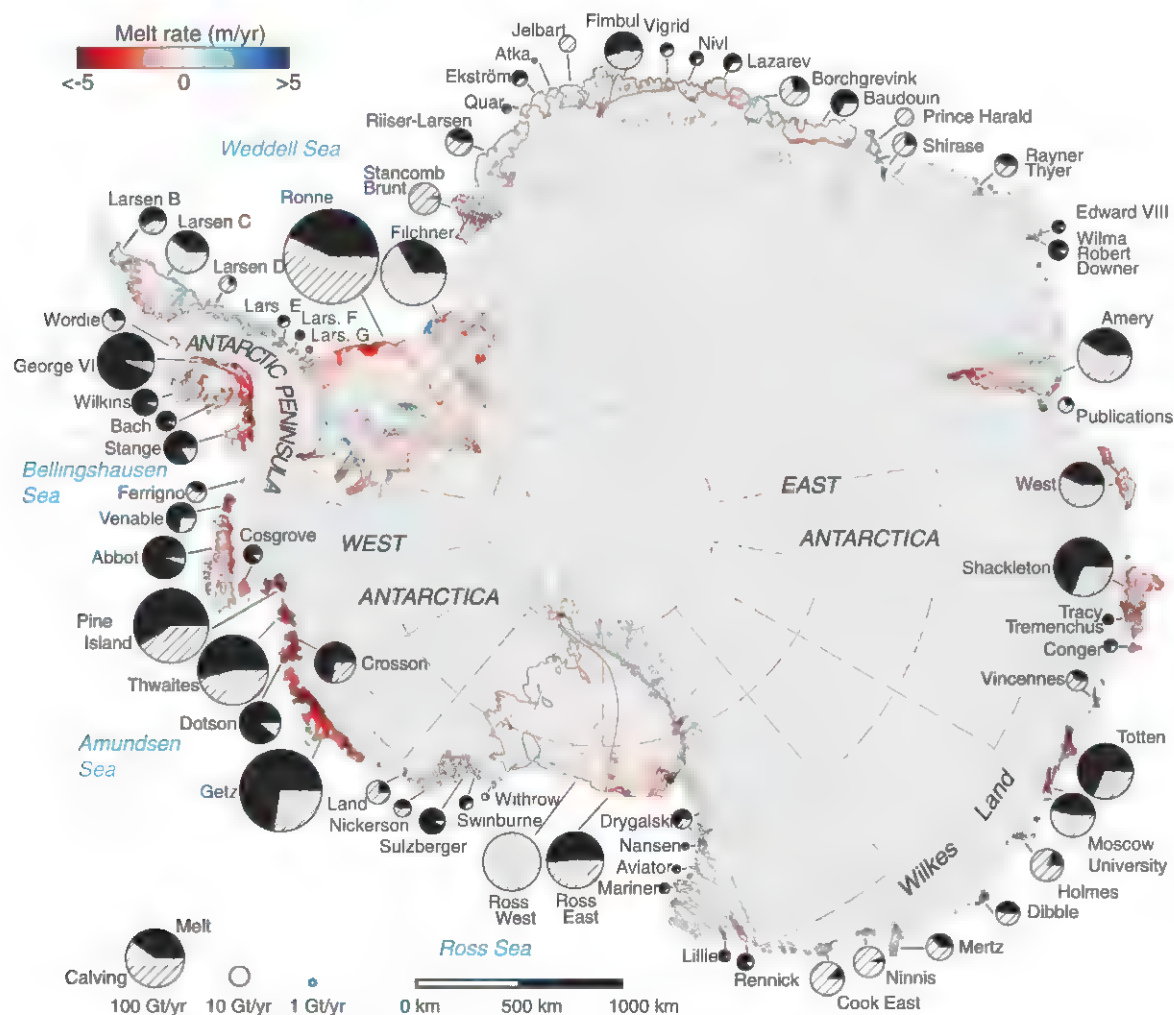


**Fig. 1. Basal melt rates of Antarctic ice shelves.** Color coded from  $<-5$  m/year (freezing) to  $>+5$  m/year (melting) and overlaid on a 2009 Moderate Resolution Imaging Spectroradiometer mosaic of Antarctica. Ice-shelf perimeters in 2007 and 2008, excluding ice rises and ice islands, are thin

black lines. Each circle graph is proportional in area to the mass loss from each shelf, in Gt/year, partitioned between iceberg calving (hatch fill) and basal melting (black fill). See Table 1 and table S1 for additional details on ice-shelf locations, areas, and mass balance components.



**Table 1. Meltwater production of Antarctic ice shelves, with ice shelves named in Fig. 1.** Areas in square kilometers exclude ice rises and islands. Grounding-line flux (GL), surface mass balance (SMB), ice-front (proxy for calving) flux (Ice Front), ice-shelf mass gain ( $\partial H/\partial t$  in water mass equivalent), and basal meltwater production in Gt/year, with area-average basal melt rate in meters of water per year indicated in parenthesis. Total Antarctica in the

last row includes nonsurveyed coastal sectors. Ice-shelf names are from United States Geological Survey and (3). Surveyed ice-shelf mass loss of  $287 \pm 89$  Gt/year in 2003 to 2008 ( $\partial H/\partial t$ ) is  $28 \pm 9\%$  higher than that required to maintain the ice shelves in steady state for 2003 to 2008. \*, Larsen B data (velocity, thickness) before the 2002 collapse; thinning rate from the remnant part of the ice shelf only. Additional details in table S1.

Name	Area km <sup>2</sup>	GL Gt/year	SMB Gt/year	Ice front Gt/year	$\partial H/\partial t$ Gt/year	Basal melt Gt/year (m/year)
Larsen G	412	$0.9 \pm 0.2$	$0.1 \pm 0$	$0.7 \pm 1$	$0.0 \pm 0$	$0.3 \pm 0.2$ ( $0.71 \pm 0.6$ )
Larsen F	828	$1.5 \pm 0.3$	$0.3 \pm 0.1$	$0.6 \pm 1$	$-0.7 \pm 0.5$	$1.2 \pm 0.4$ ( $1.4 \pm 0.5$ )
Larsen E	1,184	$3.6 \pm 0.7$	$0.4 \pm 0.1$	$1.5 \pm 1$	$1.1 \pm 0.7$	$1.4 \pm 1$ ( $1.2 \pm 0.9$ )
Larsen D	22,548	$18.5 \pm 4$	$9.8 \pm 2$	$6.3 \pm 1$	$20.5 \pm 14$	$1.4 \pm 14$ ( $0.1 \pm 0.6$ )
Larsen C	46,465	$29.6 \pm 3$	$23.8 \pm 4$	$31.3 \pm 3$	$1.4 \pm 67$	$20.7 \pm 67$ ( $0.4 \pm 1$ )
Larsen B*	6,755	$13.6 \pm 3$	$3.0 \pm 0.6$	$8.9 \pm 1$	$-4.5 \pm 13$	$12.2 \pm 14$ ( $1.8 \pm 2$ )
Wordie	277	$13.8 \pm 1$	$0.3 \pm 0$	$7.6 \pm 3$	$-0.1 \pm 0$	$6.5 \pm 3$ ( $23.6 \pm 10$ )
Wilkins	12,866	$7.8 \pm 2$	$8.3 \pm 2$	$0.7 \pm 0.4$	$-3.4 \pm 16$	$18.4 \pm 17$ ( $1.5 \pm 1$ )
Bach	4,579	$5.4 \pm 1$	$1.8 \pm 0.3$	$0.8 \pm 0.2$	$-4.0 \pm 0.3$	$10.4 \pm 1$ ( $2.3 \pm 0.3$ )
George VI	23,434	$68.2 \pm 5$	$12.7 \pm 2$	$5.7 \pm 1.2$	$-13.8 \pm 16$	$89.0 \pm 17$ ( $3.8 \pm 0.7$ )
Stange	8,027	$21.0 \pm 3$	$6.0 \pm 1$	$4.6 \pm 0.8$	$-5.6 \pm 5$	$28.0 \pm 6$ ( $3.5 \pm 0.7$ )
<b>Antarctic Peninsula</b>	<b>127,375</b>	<b><math>184 \pm 26</math></b>	<b><math>66 \pm 13</math></b>	<b><math>69 \pm 13</math></b>	<b><math>-9 \pm 74</math></b>	<b><math>191 \pm 80</math> (<math>1.5 \pm 0.6</math>)</b>
Ronne	338,887	$156.1 \pm 10$	$59.3 \pm 11$	$149.2 \pm 22$	$-47.4 \pm 22$	$113.5 \pm 35$ ( $0.3 \pm 0.1$ )
Ferrigno	117	$11.2 \pm 1$	$0.16 \pm 0$	$6.6 \pm 2$	$-0.3 \pm 0$	$5.1 \pm 2$ ( $43.4 \pm 17$ )
Venable	3,194	$14.6 \pm 2$	$3.5 \pm 1$	$6.5 \pm 1$	$-7.7 \pm 1$	$19.4 \pm 2$ ( $6.1 \pm 0.7$ )
Abbot	29,688	$34.0 \pm 4$	$25.0 \pm 5$	$2.4 \pm 0.5$	$4.7 \pm 18$	$51.8 \pm 19$ ( $1.7 \pm 0.6$ )
Cosgrove	3,033	$5.2 \pm 1$	$1.5 \pm 0.3$	$1.3 \pm 1.2$	$-3.1 \pm 2$	$8.5 \pm 2$ ( $2.8 \pm 0.7$ )
Pine Island	6,249	$126.4 \pm 6$	$4.6 \pm 0.9$	$62.3 \pm 5$	$-33.2 \pm 2$	$101.2 \pm 8$ ( $16.2 \pm 1$ )
Thwaites	5,499	$113.5 \pm 4$	$4.8 \pm 0.9$	$54.5 \pm 5$	$-33.7 \pm 3$	$97.5 \pm 7$ ( $17.7 \pm 1$ )
Crosson	3,229	$27.4 \pm 2$	$3.7 \pm 0.7$	$11.7 \pm 2$	$-19.2 \pm 1$	$38.5 \pm 4$ ( $11.9 \pm 1$ )
Dotson	5,803	$28.4 \pm 3$	$5.7 \pm 1$	$5.5 \pm 0.7$	$-16.6 \pm 2$	$45.2 \pm 4$ ( $7.8 \pm 0.6$ )
Getz	34,018	$96.7 \pm 5$	$34.2 \pm 7$	$53.5 \pm 2$	$-67.6 \pm 12$	$144.9 \pm 14$ ( $4.3 \pm 0.4$ )
Land	640	$14.5 \pm 1$	$0.8 \pm 0.1$	$12.2 \pm 1$	$-0.7 \pm 0.3$	$3.8 \pm 1$ ( $5.9 \pm 2$ )
Nickerson	6,495	$7.8 \pm 1$	$4.6 \pm 0.9$	$4.3 \pm 0.6$	$3.9 \pm 1$	$4.2 \pm 2$ ( $0.6 \pm 0.3$ )
Sulzberger	12,333	$15.1 \pm 2$	$8.2 \pm 2$	$1.0 \pm 0.2$	$4.1 \pm 2$	$18.2 \pm 3$ ( $1.5 \pm 0.3$ )
Swinburne	900	$4.9 \pm 0.4$	$0.9 \pm 0.2$	$1.5 \pm 0.3$	$0.6 \pm 0.2$	$3.8 \pm 0.5$ ( $4.2 \pm 0.6$ )
Withrow	632	$1.3 \pm 0.2$	$0.3 \pm 0.0$	$1.2 \pm 0.3$	$0.1 \pm 0.1$	$0.3 \pm 0.4$ ( $0.5 \pm 0.6$ )
Ross West	306,105	$73.0 \pm 4$	$33.5 \pm 6$	$100.4 \pm 8$	$7.6 \pm 17$	$-1.4 \pm 20$ ( $0.0 \pm 0.1$ )
<b>West Antarctica</b>	<b>756,822</b>	<b><math>730 \pm 47</math></b>	<b><math>191 \pm 36</math></b>	<b><math>494 \pm 57</math></b>	<b><math>-208 \pm 36</math></b>	<b><math>654 \pm 89</math> (<math>0.9 \pm 0.1</math>)</b>
Ross East	194,704	$56.1 \pm 4$	$31.0 \pm 6$	$45.9 \pm 4$	$-7.8 \pm 11$	$49.1 \pm 14$ ( $0.3 \pm 0.1$ )
Drygalski	2,338	$9.6 \pm 0.6$	$0.3 \pm 0.1$	$3.0 \pm 1$	$-0.8 \pm 0.4$	$7.6 \pm 1$ ( $3.3 \pm 0.5$ )
Nansen	1,985	$1.3 \pm 0.5$	$0.3 \pm 0.1$	$0.2 \pm 0.1$	$0.4 \pm 0.1$	$1.1 \pm 0.6$ ( $0.6 \pm 0.3$ )
Aviator	785	$1.1 \pm 0.2$	$0.2 \pm 0$	$0.2 \pm 0.1$	$-0.3 \pm 0.1$	$1.4 \pm 0.2$ ( $1.7 \pm 0.3$ )
Mariner	2,705	$2.5 \pm 0.4$	$1.1 \pm 0.2$	$0.6 \pm 0.2$	$0.6 \pm 0.3$	$2.4 \pm 0.6$ ( $0.9 \pm 0.2$ )
Lillie	770	$3.6 \pm 0.3$	$0.2 \pm 0$	$0.5 \pm 0.1$	$0.0 \pm 0$	$3.4 \pm 0.3$ ( $4.4 \pm 0.4$ )
Rennick	3,273	$4.8 \pm 1$	$0.7 \pm 0.1$	$0.8 \pm 0.2$	$-2.3 \pm 0.9$	$7.0 \pm 1$ ( $2.2 \pm 0.3$ )
Cook	3,462	$36.0 \pm 3$	$1.7 \pm 0.3$	$27.6 \pm 3$	$5.5 \pm 1$	$4.6 \pm 5$ ( $1.3 \pm 1$ )
Ninnis	1,899	$27.6 \pm 2$	$1.3 \pm 0.2$	$24.6 \pm 3$	$2.0 \pm 0.9$	$2.2 \pm 3$ ( $1.2 \pm 2$ )
Mertz	5,522	$20.0 \pm 1$	$3.6 \pm 0.7$	$12.0 \pm 2$	$3.6 \pm 1$	$7.9 \pm 3$ ( $1.4 \pm 0.6$ )
Dibble	1,482	$12.5 \pm 1$	$1.5 \pm 0.3$	$8.2 \pm 0.9$	$-2.3 \pm 0.7$	$8.1 \pm 1$ ( $5.5 \pm 0.9$ )
Holmes	1,921	$26.0 \pm 2$	$2.8 \pm 0.5$	$24.7 \pm 4$	$-2.5 \pm 1$	$6.7 \pm 4$ ( $3.5 \pm 2$ )
Moscow Univ.	5,798	$52.3 \pm 1$	$4.7 \pm 0.9$	$29.6 \pm 3$	$-0.1 \pm 3$	$27.4 \pm 4$ ( $4.7 \pm 0.8$ )
Totten	6,032	$71.0 \pm 3$	$6.2 \pm 1$	$28.0 \pm 2$	$-14.0 \pm 2$	$63.2 \pm 4$ ( $10.5 \pm 0.7$ )
Vincennes	935	$12.7 \pm 1$	$0.5 \pm 0.1$	$6.8 \pm 1$	$1.3 \pm 0.6$	$5.0 \pm 2$ ( $5.3 \pm 2$ )
Conger/Glenzer	1,547	$1.7 \pm 0.4$	$0.9 \pm 0.2$	$1.1 \pm 0.8$	$-2.1 \pm 1$	$3.6 \pm 1$ ( $2.3 \pm 0.9$ )
Tracy/Tremenchus	2,845	$0.6 \pm 0.4$	$1.0 \pm 0.2$	$0.2 \pm 0.1$	$-1.7 \pm 2$	$3.0 \pm 2$ ( $1.5 \pm 0.7$ )
Shackleton	26,080	$55.0 \pm 4$	$16.2 \pm 3$	$30.3 \pm 3$	$-31.7 \pm 14$	$72.6 \pm 15$ ( $2.8 \pm 0.6$ )
West	15,666	$41.9 \pm 4$	$6.9 \pm 1$	$32.6 \pm 7$	$-11.1 \pm 7$	$27.2 \pm 10$ ( $1.7 \pm 0.7$ )
Publications	1,551	$5.8 \pm 0.8$	$0.4 \pm 0.1$	$5.2 \pm 1$	$-0.5 \pm 0.8$	$1.5 \pm 2$ ( $1.0 \pm 1$ )
Amery	60,654	$56.0 \pm 0.5$	$8.5 \pm 2$	$50.4 \pm 8$	$-21.4 \pm 21$	$35.5 \pm 23$ ( $0.6 \pm 0.4$ )
Wilma/Robert/Downer	858	$10.3 \pm 0.5$	$0.6 \pm 0.1$	$0.8 \pm 0.4$	$0.0 \pm 0$	$10.0 \pm 0.6$ ( $11.7 \pm 0.7$ )
Edward VIII	411	$4.1 \pm 0.8$	$0.4 \pm 0.1$	$0.3 \pm 0.1$	$0.0 \pm 0$	$4.2 \pm 0.8$ ( $10.2 \pm 2$ )

continued on next page

Table 1 continued

Name	Area km <sup>2</sup>	GL Gt/year	SMB Gt/year	Ice front Gt/year	$\partial H/\partial t$ Gt/year	Basal melt Gt/year (m/year)
Edward VIII	411	4.1 ± 0.8	0.4 ± 0.1	0.3 ± 0.1	0.0 ± 0	4.2 ± 0.8 (10.2 ± 2)
Rayner/Thyer	641	14.2 ± 1	0.3 ± 0.1	7.8 ± 0.6	0.0 ± 0	6.7 ± 1 (10.5 ± 2)
Shirase	821	15.0 ± 1	0.4 ± 0.1	9.6 ± 1	0.0 ± 0	5.7 ± 1 (7.0 ± 2)
Prince Harald	5,392	8.3 ± 1	4.1 ± 0.8	10.3 ± 2	4.0 ± 2	-2.0 ± 3 (-0.4 ± 0.6)
Baudouin	32,952	22.0 ± 3	8.4 ± 2	6.5 ± 1	9.8 ± 11	14.1 ± 12 (0.4 ± 0.4)
Borchgrevink	21,580	19.6 ± 3	6.1 ± 1	17.5 ± 3	0.7 ± 4	7.5 ± 6 (0.3 ± 0.3)
Lazarev	8,519	3.7 ± 0.6	2.0 ± 0.4	3.1 ± 1	-3.6 ± 2	6.3 ± 2 (0.7 ± 0.2)
Nivl	7,285	3.9 ± 0.8	1.8 ± 0.3	1.3 ± 0.4	0.6 ± 1	3.9 ± 2 (0.5 ± 0.2)
Vigrid	2,089	2.7 ± 0.4	0.4 ± 0.1	2.0 ± 0.4	-2.0 ± 0.4	3.2 ± 0.7 (1.5 ± 0.3)
Fimbul	40,843	24.9 ± 4	12.7 ± 2	18.2 ± 2	-4.0 ± 7	23.5 ± 9 (0.6 ± 0.2)
Jelbart	10,844	9.9 ± 1	4.9 ± 0.9	8.8 ± 2	6.9 ± 2	-1.0 ± 3 (-0.1 ± 0.3)
Atka	1,969	0.9 ± 0.2	0.8 ± 0.1	1.0 ± 0.2	1.1 ± 0.2	-0.5 ± 0.4 (-0.2 ± 0.2)
Ekstrom	6,872	4.1 ± 0.8	2.6 ± 0.5	2.3 ± 0.6	0.0 ± 0	4.3 ± 2 (0.6 ± 0.2)
Quar	2,156	1.0 ± 0.2	0.5 ± 0.1	0.6 ± 0.1	-0.5 ± 0.4	1.4 ± 0.5 (0.7 ± 0.2)
Riiser-Larsen	43,450	21.5 ± 3	12.7 ± 2	12.1 ± 2	13.4 ± 8	8.7 ± 9 (0.2 ± 0.2)
Brunt/Stancomb	36,894	20.3 ± 3	11.4 ± 2	28.1 ± 4	2.6 ± 4	1.0 ± 7 (0.03 ± 0.2)
Filchner	104,253	97.7 ± 6	13.4 ± 2	82.8 ± 4	-13.6 ± 7	41.9 ± 10 (0.4 ± 0.1)
<b>East Antarctica</b>	<b>669,781</b>	<b>782 ± 80</b>	<b>174 ± 33</b>	<b>546 ± 70</b>	<b>-70 ± 34</b>	<b>480 ± 116 (0.7 ± 0.2)</b>
<b>Total surveyed</b>	<b>1,553,978</b>	<b>1,696 ± 146</b>	<b>430 ± 81</b>	<b>1,089 ± 139</b>	<b>-287 ± 89</b>	<b>1,325 ± 235 (0.85 ± 0.1)</b>
<b>Total Antarctica</b>	<b>1,561,402</b>	<b>2,048 ± 149</b>		<b>1,265 ± 141</b>		<b>1,500 ± 237</b>

The total ice-shelf grounding-line inflow of  $1696 \pm 146$  Gt/year combined with an *SMB* input of  $430 \pm 81$  Gt/year is partitioned into an ice-front flux of  $1,089 \pm 139$  Gt/year and a basal meltwater production of  $1,325 \pm 235$  Gt/year. Basal melting thus accounts for  $55 \pm 10\%$  of ice-shelf mass ablation. The corresponding area-average melt rate of  $85 \pm 15$  cm/year is three times as large as the average *SMB* on ice shelves ( $28 \pm 5$  cm) and five times the average *SMB* on grounded ice sheet ( $16 \pm 1$  cm) (16), illustrating the considerable importance of ocean interactions in freshwater transfers between the ice and ocean.

The grounding-line flux of all surveyed ice shelves accounts for  $83 \pm 7\%$  of the total ice discharge into the Southern Ocean (Table 1). Total Antarctic grounded ice discharge (26) is  $352 \pm 30$  Gt/year higher than our grounding-line flux because of additional discharge from smaller ice shelves and ice walls that terminate in the ocean (27). An equal partitioning of these missing areas between calving and basal melting (see supplementary materials) would increase in situ meltwater production to  $1500 \pm 237$  Gt/year and ice-front flux to  $1265 \pm 139$  Gt/year.

The comparison of basal melting *B* (Fig. 1) with steady state melting  $B_{ss}$  (fig. S4, Table 1, and table S1) shows that many ice shelves are near equilibrium ( $B \sim B_{ss}$ ), whereas some are thickening ( $B < B_{ss}$ ) and others are thinning ( $B > B_{ss}$ ). High basal melting is therefore not synonymous with thinning. Ice shelves with high melt rates can be in a state of mass balance, but meltwater production is  $28 \pm 9\%$  higher than required to maintain the ice shelves in overall steady state ( $1037 \pm 218$  Gt/year). Ice shelves in the Amundsen Sea sector (Pine Island to Getz) contribute 59% of the  $287 \pm 89$  Gt/year imbalance, an attrition rate twice

that of their glacier source regions over the same time period (26). Similarly, the total imbalance of all Antarctic ice shelves combined is more than twice that of the grounded ice (26).

The ratio of calving to melting averages  $0.45 \pm 0.3$ , but exhibits considerable regional variability (Table 1), with area-average melt rates varying from negative to  $> 40$  m/year. This wide range reflects diverse ocean environments, which include seawater temperature, the depths of troughs and sills that influence the access of oceanic heat to ice-shelf cavities, and the sea-ice formation and drifts resulting from atmospheric forcing.

Large ice shelves generate a disproportionately small portion of the total ice-shelf meltwater despite high production rates in their deep grounding zones and along lengthy ice fronts. The four giants with areas  $> 100,000$  km<sup>2</sup> (Ross East, Ross West, Filchner, and Ronne) cover 61% of the total ice-shelf area but contribute only 15% of the meltwater at an average rate of 13 cm/year. The low melt rates result from the relatively weak ocean heat source provided by cold shelf waters, in turn leading to substantial marine ice accretion (28). Despite areas 3 to 10 times as large as the Getz, none of the big four ice shelves produce as much meltwater, with the Ross West contributing no net melt. Meltwater from the Southeast Pacific-Antarctic sector (George VI through Getz) accounts for 48% of the total meltwater over only 8% of the area, with the Getz being the largest meltwater source in Antarctica during the study period. *B* averages 5.1 m/year in this region, from a maximum of 43 m/year under the short Ferrigno Glacier tongue to a minimum of 1.8 m/year beneath the Abbot. That area-average rate may seem low

for a warm-cavity Southeast Pacific ice shelf, but the moderate-sized, shallow-draft Abbot (29) ranks eighth overall in meltwater production, while maintaining a positive mass balance ( $B < B_{ss}$ ).

Meltwater production from several small East Antarctic ice shelves in the Wilkes Land sector is larger than expected. Area-average melt rates from Dibble through Vincennes (4 to 11 m/year) are comparable to Amundsen Sea ice-shelf rates from Crosson through Land (4 to 11 m/year), whereas meltwater produced by Shackleton and West (73 and 27 Gt/year, respectively) rivals that from Thwaites and Sulzberger (98 and 18 Gt/year, respectively). Except for the region from  $140^\circ$  to  $150^\circ$ W where Mertz and Ninnis melting is dominated by shelf waters, oceanographic data are sparse along the Wilkes Land coastline. "Modified" warm deep water at a temperature near  $0^\circ$ C has been reported 40 km south of the continental shelf break northeast of Totten (30). By analogy with observations in the Amundsen Sea, our results suggest the presence of seawater at similar temperatures under several East Antarctic ice shelves. Even  $0^\circ$  seawater at outer continental shelf depths could expose ice shelves with deep grounding lines like the Totten (2.2 km), Moscow (2.0 km), and Shackleton (1.8 km) to temperatures more than  $3^\circ$ C above their melting points. To evaluate the impact of these warm deep waters on ice-shelf melting, more information is needed about their spatial and temporal variability on the outer shelf and links through glacially scoured troughs to the vulnerable glacier grounding lines.

Our glaciological estimates are generally consistent with recent results from high-resolution ocean models in the Amundsen, Bellingshausen,



and Weddell Seas (29, 31–33) (see supplementary materials), but total melting of 10 of the larger ice shelves is notably less here than in circumpolar models (7, 11). Discrepancies between model results and observations have been attributed to deficiencies in atmospheric forcing, the representation of sea-ice cover, the smoothing of bottom topography, and assumptions regarding cavity shape. Some models yield annual cycles and decadal variability (29) that can now be compared for specific periods with glaciological measurements, which need to be extended in time.

Our results indicate that basal melting accounts for a larger fraction of Antarctic ice-shelf attrition than previously estimated. These improved glaciological estimates provide not only more accurate and detailed reference values for modeling but also a baseline for similar future studies. Ice-shelf meltwater production exhibits a complex spatial pattern around the continent, with an outsized contribution of smaller, fast-melting ice shelves in both West and East Antarctica. Warm-cavity ice shelves along the Southeast Pacific coastline, predicted and observed to be sensitive to ocean warming and circulation strength (9, 34), were thinning rapidly in 2003 to 2008 (23). Nearly half of the East Antarctic ice shelves were also thinning, some due to probable exposure to “warm” seawater, with connections to ice drainage basins grounded below sea level.

Continued observations of ice-shelf velocity and thickness change, along with more detailed information on cavity shape, seafloor topography, and atmospheric and oceanic forcing variability are critical to understand the temporal variability and evolution of Antarctic ice shelves. Continued warming of the ocean will slowly increase ice-

shelf thinning, but if major shifts in sea ice cover and ocean circulation tip even large ice-shelf cavities from cold to warm (35), there could be major changes in ice shelf and thus ice-sheet mass balance.

#### References and Notes

1. P. Fretwell *et al.*, *The Cryosphere* 7, 375–393 (2013).
2. C. W. Swinbank, *Satellite Image Atlas of Glaciers of the World: Antarctica*, R. S. Williams, J. G. Ferrigno, Eds (USGS Prof. Paper 1386-B, 1988).
3. N. I. Barkov, *Ice Shelves of Antarctica* (New Delhi, NY, Amerind Publishing Company, 1985).
4. R. LeB. Hooke, *Principles of Glacier Mechanics* (Cambridge University Press, Cambridge, 2005).
5. K. M. Cuffey, W. S. B. Paterson, *The Physics of Glaciers* (Elsevier, Burlington, MA, ed. 4, 2010).
6. S. S. Jacobs *et al.*, *J. Glaciol.* 38, 375 (1992).
7. H. H. Hellmer, *Geophys. Res. Lett.* 31, L10307 (2004).
8. A. Jenkins, S. S. Jacobs, *J. Geophys. Res.* 113, (C4), C04013 (2008).
9. S. S. Jacobs, A. Jenkins, C. F. Giulivi, P. Dutieux, *Nature Geosci.* 4, 519–523 (2011).
10. A. Foldvik, T. Gammelsrød, E. Nygaard, S. Osterhus, *J. Geophys. Res. Oceans* 106, 4463 (2001).
11. R. Timmermann, Q. Wang, H. H. Hellmer, *Ann. Glaciol.* 53, 303–314 (2012).
12. I. Joughin, L. Padman, *Geophys. Res. Lett.* 30, 1477 (2003).
13. J. Wen *et al.*, *J. Glaciol.* 56, 81–90 (2010).
14. E. Rignot, S. S. Jacobs, *Science* 296, 2020–2023 (2002).
15. A. Jenkins, C. S. M. Doake, *J. Geophys. Res.* 96, 791 (1991).
16. J. T. M. Lenaerts *et al.*, *J. Geophys. Res.* 117, D05108 (2012).
17. E. Rignot *et al.*, *Nat. Geosci.* 1, 106–110 (2008).
18. C. Atten, IceBridge MCoRDS L2 Ice Thickness. Boulder, Colorado, USA: NASA DAAC at the National Snow and Ice Data Center (2010).
19. D. D. Blankenship, S. Kempf, D. Young, IceBridge HiCARS 2 L2 Geo. located Ice Thickness. Boulder, Colorado, USA: NASA DAAC at the National Snow and Ice Data Center (2012).
20. J. A. Griggs, J. L. Bamber, *J. Glaciol.* 57, 485–498 (2011).
21. E. Rignot, J. Mouginot, B. Scheuchl, *Geophys. Res. Lett.* 38, L10504 (2011).
22. E. Rignot, J. Mouginot, B. Scheuchl, *Science* 333, 1427–1430 (2011).
23. H. D. Pritchard *et al.*, *Nature* 484, 502–505 (2012).
24. K. Makinson *et al.*, *Geophys. Res. Lett.* 38, L06601 (2011).
25. H. J. Horgan, R. T. Walker, S. Anandakrishnan, R. B. Alley, *J. Geophys. Res.* 116, C02005 (2011).
26. A. Shepherd *et al.*, *Science* 338, 1183–1189 (2012).
27. S. Neshyba, E. G. Josberger, *J. Phys. Oceanogr.* 10, 1681–1685 (1980).
28. K. Grosfeld *et al.*, *Antarct. Res. Ser.* 75, 319–339 (1998).
29. M. P. Schodlok, D. Menemenlis, E. Rignot, M. Studinger, *Ann. Glaciol.* 53, 156–162 (2012).
30. G. D. Williams *et al.*, *Deep Sea Res. Part II Top. Stud. Oceanogr.* 58, 1194–1210 (2011).
31. P. R. Holland, A. Jenkins, D. Holland, *Geophys. Res. Lett.* 115, (C5), C05020 (2010).
32. L. Padman *et al.*, *J. Geophys. Res.* 117, C01010 (2012).
33. P. R. Holland *et al.*, *Geophys. Res. Lett.* 36, L11604 (2009).
34. P. R. Holland, A. Jenkins, D. M. Holland, *J. Clim.* 21, 2558–2572 (2008).
35. H. H. Hellmer *et al.*, *Nature* 485, 225–228 (2012).

**Acknowledgments:** We thank three anonymous reviewers for their constructive criticism of the manuscript. This work was performed at the University of California, Irvine, and at the Jet Propulsion Laboratory, California Institute of Technology, under grants from NASA's Cryospheric Science Program and Operation IceBridge (OIB) and at the Lamont-Doherty Earth Observatory of Columbia University under grants from the National Science Foundation and the National Oceanic and Atmospheric Administration.

#### Supplementary Materials

[www.sciencemag.org/cgi/content/full/science.1235798/DC1](http://www.sciencemag.org/cgi/content/full/science.1235798/DC1)  
Supplementary Text  
Figs. S1 to S4  
Tables S1 and S2  
References (36–58)

29 January 2013; accepted 31 May 2013  
Published online 13 June 2013;  
10.1126/science.1235798

## Lethal Aggression in Mobile Forager Bands and Implications for the Origins of War

Douglas P. Fry<sup>1,2\*</sup> and Patrik Söderberg<sup>1,3</sup>

It has been argued that warfare evolved as a component of early human behavior within foraging band societies. We investigated lethal aggression in a sample of 21 mobile forager band societies (MFBS) derived systematically from the standard cross-cultural sample. We hypothesized, on the basis of mobile forager ethnography, that most lethal events would stem from personal disputes rather than coalitional aggression against other groups (war). More than half of the lethal aggression events were perpetrated by lone individuals, and almost two-thirds resulted from accidents, interfamilial disputes, within-group executions, or interpersonal motives such as competition over a particular woman. Overall, the findings suggest that most incidents of lethal aggression among MFBS may be classified as homicides, a few others as feuds, and a minority as war.

A controversy exists regarding mobile forager band societies (MFBS) and warfare. Field researchers who have worked

with MFBS generally report that warfare is absent or rudimentarily developed (1–6). Fry (7) compared MFBSs with complex and equestrian

an foragers and found that most MFBS (62%) were nonwarring, whereas all of the complex and equestrian societies made war. On the other hand, Wrangham and Glowacki [(8), p. 7] developed a chimpanzee-based lethal raiding model, asserting that “humans evolved a tendency to kill members of other groups,” and they provided ethnographic quotations on MFBS to illustrate the model. They [(8), p. 8] define war as when “coalitions of members of a group seek to inflict bodily harm on one or more members of another group; ‘groups’ are independent political units.” Bowles (9) examined war deaths in eight societies, six of which were MFBS, and reported the occurrence of war in all eight societies, which he takes as confirmation that war has been pervasive during human evolution.

<sup>1</sup>Peace, Mediation and Conflict Research, Åbo Akademi University in Vasa, Post Office Box 311, FIN-65101, Vasa, Finland.

<sup>2</sup>Bureau of Applied Research in Anthropology, School of Anthropology, Post Office Box 210030, Tucson, AZ 85721–0030, USA. <sup>3</sup>Developmental Psychology, Åbo Akademi University in Vasa, Post Office Box 311, FIN-65101, Vasa, Finland.

\*Corresponding author. E-mail: dfry@abo.fi

There are two likely explanations for such divergent interpretations about warfare and MFBS: differences in how warfare is defined and differences in sampling procedure and composition (7, 8). Recognizing that definitional opinions differ, rather than making an a priori determination regarding which events are classified as manslaughter, homicide, feud, or war, we instead consider the salient characteristics of each and every actual event involving lethal aggression in a systematically derived, representative sample of MFBS.

There are numerous reasons to predict a paucity of warfare among MFBS (see supplementary materials). (i) In MFBS, group size is too small to support warfare. (ii) MFBS have egocentric social networks with descent generally figured bilaterally through both parental lines. This does not facilitate coalitional alliance formation useful in war. (iii) Group composition fluctuates over time, resulting in kinship and social networks that cut across different groups,

a factor that dampens intergroup hostility. (iv) MFBS tend not to be segmented into subgroups. In terms of residence, MFBS tend to be multi-local, not patrilocal, thus lacking a residential pattern known to facilitate coalitions among male kin useful for war. (v) The social order is egalitarian and leadership is lacking; no one has the authority to order others to fight. (vi) Foraging areas are large, population densities low, and resources spread-out, making defense of territory difficult or impossible. (vii) Boundaries often are controlled socially through use-requests and permission-granting. (viii) Typical spoils of war—material goods or stored food—are largely lacking, and the necessity of mobility makes the capture and containment of individuals against their will (e.g., slaves or brides) impractical (and runs counter to the MFBS ethos of egalitarianism). (ix) Conflicts within and between groups are easily handled by separation and other conflict-resolution mechanisms. On the basis of these foregoing characteristics, we

would expect lethal aggression in MFBS to be mostly interpersonal, not intergroup. Additionally, in mammals the killing of conspecifics is an atypical and infrequent form of aggression compared to displays, noncontact threats, and restrained aggression, so perhaps also for humans the development of an evolutionary model based on restraint as a widely documented phenomenon across species, rather than on rare killing behavior, merits consideration (10).

We extracted a subsample of purely MFBS ( $n = 21$ ) from the standard cross-cultural sample (SCCS). To circumvent sampling bias, rather than self-selecting cases, we derived the sample of MFBS based on the published rating criteria of others researchers (11, 12). During data collection, we used only the principal authority sources (PAS) as the earliest, high-quality ethnographic descriptions available (12). We considered every instance of lethal aggression reported for these 21 MFBS (13).

The 21 MFBS produced a total of 148 lethal aggression events. The median number was 4 (mean = 7.05; SD = 14.64), with a range from 0 to 69. One society, the Tiwi of Australia, had an exceptionally large number of lethal events ( $n = 69$ ). If the Tiwi case is removed, the median number of lethal events for the remaining 20 societies drops to 3.5, the mean is almost cut in half (mean = 3.95; SD = 3.69), and the range is reduced to 0 to 15.

Of 135 lethal events with unambiguous perpetrator and victim information, 55% consisted of one killer and one victim. In 23% of the lethal events, more than one person participated in killing a single individual, and in 22% of the events, more than one person participated in killing more than one person (Fig. 1). In only one lethal event (0.7%), did a single killer dispatch more than one person (table S4, case 18), and the two victims were children. Tiwi society reflects a different pattern wherein 44% of the lethal events involved one killer and one victim, whereas the corresponding figure for the other 20 societies combined was 64% (supplementary text).

Thirty-six percent of the lethal events took place within the local band; for example, between brothers, father and son, mother and child, in-laws, husbands and wives, companions, friends, clan “brothers,” neighbors, and so on (table S2). Six percent of all incidents involved husbands killing wives. In most lethal events (85%), the killers and victims were members of the same society. The remaining lethal aggression events involved persons from outside the society, such as shipwreck victims, colonists, missionaries, or neighboring indigenous cultures. Almost all of the killers were male, whether they acted alone or with others. Females were the killers or co-perpetrators in only 4% of the events.

The reasons for the lethal events varied. Given that most lethal aggression involved one killer and one victim, the large number of personal motives for killing is not surprising (Table 1 and

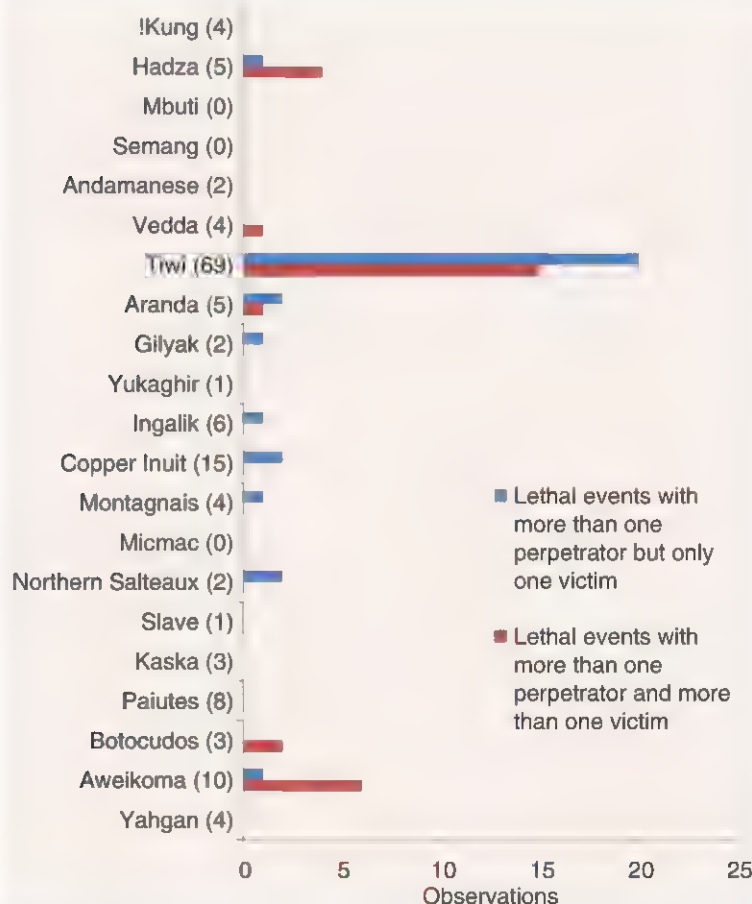


**Fig. 1. Lethal aggression events with multiple perpetrators in 21 MBFS.** The distribution of all lethal events that involved multiple perpetrators is shown, based on whether there was a single victim (31 events) or multiple victims (29 events), out of a grand total of 148 lethal events. The figure reflects how the Tiwi are more violent than the other MFBS. Nearly half of the sample societies (10 of 21) had no lethal events perpetrated by two or more persons. Three societies had no lethal events at all. For each society, the total number of lethal events is in parentheses.



table S3). Specifically, many lethal disputes involved two men competing over a particular woman (sometimes the wife of one of them), revenge homicide exacted by family members of a victim (often aimed at the specific person responsible for the previous killing), and interpersonal quarrels of various kinds; for instance, stealing of honey, insults or taunting, incest, self-defense or the protection of a loved-one, and so on. Additionally, in some killing events, another person or persons supported a companion who acted out of personal, not group, motives, such as when a friend assisted a husband in killing his wife's lover (see table S4, case 109).

About one third of the lethal events involved disputes between people of different groups (Table 1). However, three-quarters (38 of 50) of intergroup disputes took place among the Tiwi alone. The percentage of intergroup disputes for the Tiwi exceeded 50% of their events, whereas the corresponding percentage for the other twenty societies was only about 15%. Another feature of the Tiwi data is the regular occurrence of strings of killings. Thirty-nine percent (27 of 69) of Tiwi lethal events occurred in seven separate strings (table S4, cases 129 to 131, 133 to 139, 140 to 141 and 145, 142 to 144, 146 to 149, 150 to 153, and 156 to 158), whereas only two strings of killings occurred in the other 20 societies (table S4, cases 10 to 13 and 82 to 89).

The findings suggest that MFBS are not particularly warlike if the actual circumstances of lethal aggression are examined. Fifty-five percent of the lethal events involved a sole perpetrator killing only one individual (64% if the atypical Tiwi are removed). One-person-killing-

one-person reflects homicide or manslaughter, not coalitional killings or war. Additionally, 36% of all lethal events occurred within the same local group (62% if the atypical Tiwi are removed), and violence within a local group is not coalitional war. Only 15% of the lethal events occurred across societal lines. Some such events might fall within a definition of war, whereas others might not (such as when shipwreck survivors were killed). Finally, very few lethal disputes were over resources. Overall, a consideration of reasons for lethal aggression reveals that most cases stemmed from personal motives consistent with homicide and, in some cases, family feuds, but much less often with lethal aggression between political communities, or warfare (supplementary text).

Approximately half of the societies had no lethal events that involved more than one perpetrator. This observation is incongruent with assertions by Bowles (9) and Pinker (14) that war is prevalent in MFBS or by Wrangham and Glowacki (8) that humans have an evolved tendency to form coalitions to kill members of neighboring groups. Additionally, two or more persons killing a third person might or might not occur in the context of a coalition against another group or war. In some instances, motives such as sexual jealousy (table S4, e.g., cases 29 and 109) or avenging the murder of a family member (table S4, e.g., case 157) are clearly personal rather than stemming from hypothesized general hostility toward other groups. Most mammalian aggression also is between individuals. A different evolutionary perspective supported by comparative mammalian data, game

theory on the evolutionary logic of fighting, and the observation that killing is an exceptional event in human societies leads to the counter-hypothesis that lethal behavior has been strongly selected against, not favored, in comparison to more restrained conflict behavior (7, 10, 15).

Taken together, the current findings contradict recent assertions that MFBS regularly engage in coalitional war against other groups (8), that "chronic raiding and feuding characterize life in a state of nature" [(14), p. xxiv], or that MFBS war deaths are substantial in recent millennia and in the Pleistocene (9) (supplementary text). Perhaps discrepancies between the foregoing propositions and the current findings can be accounted for by proposing that self-selection of ethnographic material may have exaggerated war (10). Additionally, methodological factors such as relying heavily on only a few secondary sources (8), or estimating war mortality on the basis of genocidal massacres and murders of indigenous peoples by armed ranchers and settlers (9), can lead to misimpressions in comparison to the use of systematic sampling procedures, reliance on primary ethnographic data, and a focus on the specific circumstances of lethal aggression cases in MFBS (7, 10).

In conclusion, when all cases are examined for a systematically drawn sample of MFBS, most incidents of lethal aggression can aptly be called homicides, a few others feud, and only a minority warfare. The findings do not lend support to the coalitional model. The predictions are substantiated that MFBS, as a social type, possess many features that make warfare unlikely. The actual reasons for lethal aggression are most often interpersonal, and consequently, the particulars of most of the lethal events in these societies do not conform to the usual conceptualization of war.

**Table 1. Reasons for lethal aggression, from the personal to the communal.** The atypical Tiwi findings are shown separately, followed by the other societies minus the Tiwi ( $n = 20$ ), and the entire sample ( $n = 21$ ), all in number of cases (with percentages in parentheses). A more detailed version of the table with case numbers for lethal aggression events is presented in table S3.

Reason	Tiwi only		All others		Total sample	
<b>Interpersonal events</b>	<b>24</b>	<b>(34.8%)</b>	<b>50</b>	<b>(63.3%)</b>	<b>74</b>	<b>(50.0%)</b>
Revenge against a particular killer(s)	9	(13.0%)	8	(10.1%)	17	(11.5%)
Over a particular woman	8	(11.6%)	6	(7.6%)	14	(9.5%)
Over a particular man	0	(0.0%)	1	(1.3%)	1	(0.7%)
Husband kills wife	2	(2.9%)	7	(8.9%)	9	(6.1%)
Wife kills husband	0	(0.0%)	0	(0.0%)	0	(0.0%)
Miscellaneous interpersonal disputes*	5	(7.2%)	28	(35.4%)	33	(22.3%)
<b>Interfamilial feud</b>	<b>0</b>	<b>(0.0%)</b>	<b>6</b>	<b>(7.6%)</b>	<b>6</b>	<b>(4.1%)</b>
<b>Within-group execution</b>	<b>0</b>	<b>(0.0%)</b>	<b>3</b>	<b>(3.8%)</b>	<b>3</b>	<b>(2.0%)</b>
<b>Execution of outsiders</b>	<b>4</b>	<b>(5.8%)</b>	<b>3</b>	<b>(3.8%)</b>	<b>7</b>	<b>(4.7%)</b>
<b>Intergroup events</b>	<b>38</b>	<b>(55.1%)</b>	<b>12</b>	<b>(15.2%)</b>	<b>50</b>	<b>(33.8%)</b>
Over borders/resources (e.g., fruit tree)	0	(0.0%)	2	(2.5%)	2	(1.4%)
Theft of women from another group	0	(0.0%)	2	(2.5%)	2	(1.4%)
Interclan revenge-seeking	17	(24.6%)	0	(0.0%)	17	(11.5%)
During a general fight	4	(5.8%)	0	(0.0%)	4	(2.7%)
Miscellaneous intergroup disputes*	17	(24.6%)	8	(10.1%)	25	(16.9%)
<b>Accident</b>	<b>3</b>	<b>(4.3%)</b>	<b>3</b>	<b>(3.8%)</b>	<b>6</b>	<b>(4.1%)</b>
<b>Starvation cannibalism</b>	<b>0</b>	<b>(0.0%)</b>	<b>2</b>	<b>(2.5%)</b>	<b>2</b>	<b>(1.4%)</b>
<b>Grand total</b>	<b>69</b>	<b>(100%)</b>	<b>79</b>	<b>(100%)</b>	<b>148</b>	<b>(100%)</b>

\*For a listing of miscellaneous events, see table S3.

## References and Notes

1. E. Leacock, *Curr. Anthropol.* **19**, 247–275 (1978).
2. E. R. Service, *The Hunters* (Prentice-Hall, Englewood Cliffs, NJ, 1966).
3. J. Steward, in *Man the Hunter*, R. Lee, I. DeVore, Eds. (Aldine, Chicago, 1968), pp. 321–334.
4. R. Lee, R. Daly, in *The Cambridge Encyclopedia of Hunters and Gatherers*, R. B. Lee, R. Daly, Eds. (Cambridge Univ. Press, Cambridge, 1999), 1–19.
5. R. Tonkinson, in *Keeping the Peace*, G. Kemp, D. P. Fry, Eds. (Routledge, New York, 2004), pp. 89–104.
6. R. Tonkinson, in *War, Peace, and Human Nature: Convergence of Evolutionary and Cultural Views*, D. P. Fry, Ed. (Oxford Univ. Press, New York, 2013), pp. 262–277.
7. D. P. Fry, *The Human Potential for Peace* (Oxford Univ. Press, New York, 2006).
8. R. W. Wrangham, L. Glowacki, *Hum. Nat.* **23**, 5–29 (2012).
9. S. Bowles, *Science* **324**, 1293–1298 (2009).
10. D. P. Fry, in *War, Peace, and Human Nature: Convergence of Evolutionary and Cultural Views*, D. P. Fry, Ed. (Oxford Univ. Press, New York, 2013), pp. 1–21.
11. G. Murdock, *Ethnology* **6**, 109–236 (1967).
12. D. White, *Behav. Sci. Res.* **23**, 1–145 (1989).
13. Materials and Methods are available as supplementary materials on Science Online.
14. S. Pinker, *The Better Angels of Our Nature* (Viking, New York, 2011).

15. J. Maynard Smith, G. Price, *Nature* **246**, 15–18 (1973).

**Acknowledgments:** Some of the data reported here were collected during research funded by the NSF (grant 03-13670). We are grateful to the Svenska Kulturfonden for assisting

with the costs of publication. The data reported in this study are located in the supplementary materials.

#### Supplementary Materials

www.sciencemag.org/cgi/content/full/341/6143/270/DC1  
Material and Methods

Supplementary Text  
Tables S1 to S4  
References (16–127)

25 January 2013; accepted 10 June 2013  
10.1126/science.1235675

# Interactions of Multisensory Components Perceptually Rescue Túngara Frog Mating Signals

R. C. Taylor<sup>1</sup> and M. J. Ryan<sup>2,3\*</sup>

Sexual signals are often complex and perceived by multiple senses. How animals integrate signal components across sensory modalities can influence signal evolution. Here we show that two relatively unattractive signals that are perceived acoustically and visually can be combined in a pattern to form a signal that is attractive to female túngara frogs. Such unanticipated perceptual effects suggest that the evolution of complex signals can occur by alteration of the relationships among already-existing traits.

Human perception of stimuli in multiple sensory modalities can positively influence signal detection, selective attention, learning, and memory (1). One example is “hearing lips and seeing voices” in the McGurk effect (2), which provided the foundation for speech auditory-visual research (3). Studies of multimodal communication in animals have often asked whether individual signal components in different sensory modalities are redundant or carry different information (4), but few studies have investigated how specific interactions influence signal perception (5).

Female túngara frogs base their mate choices on male mating calls. Specifically, males produce calls consisting of a whine alone or they may add up to seven chucks; they do not produce only chucks (6). Females exhibit phonotaxis (movement toward a call, a bioassay of call recognition and preference) to a whine only, but exhibit a fivefold preference for calls with a whine-chuck over a whine only [ $N = 3662$  (11); see also Fig. 1A]. We tested female mate preferences in a series of two-choice tests. Synthetic male vocalizations were broadcast from two speakers, one of which was paired with a robotic frog that provided the visual stimulus of a calling male. Females were released equidistant from the two speakers (with a 60° separation relative to the female release point) and allowed to choose a stimulus. Because our experimental configuration differed from those of previous experiments, we replicated some studies and obtained similar

results (Fig. 1, A, B, and D). Females were tested only once.

The acoustic component of a frog’s mating call is its most distinguishing feature, but visual

cues are also associated with the sexual display. Male frogs have inflatable vocal sacs that shuttle air to and from the lungs while calling. Similar to the movement of lips during human speech (2), they are a biomechanical consequence of the sound production system (7), but, as with lips and speech, they can also influence the perception of the call (8, 9). We have shown previously that female túngara frogs prefer a multimodal signal (a call associated with a robotic frog) to a call by itself (10), a result reconfirmed here (Fig. 1D).

In túngara frogs, the temporal relationship between acoustic components influences the signal’s attractiveness (11). When the chuck in a whine-chuck call is displaced by 500 ms, the call becomes merely as attractive as a whine only (Fig. 1B) and less attractive than a normal whine-chuck (Fig. 1C). The temporal relationship between the acoustic and visual components of the signal also influences the signal’s attractiveness

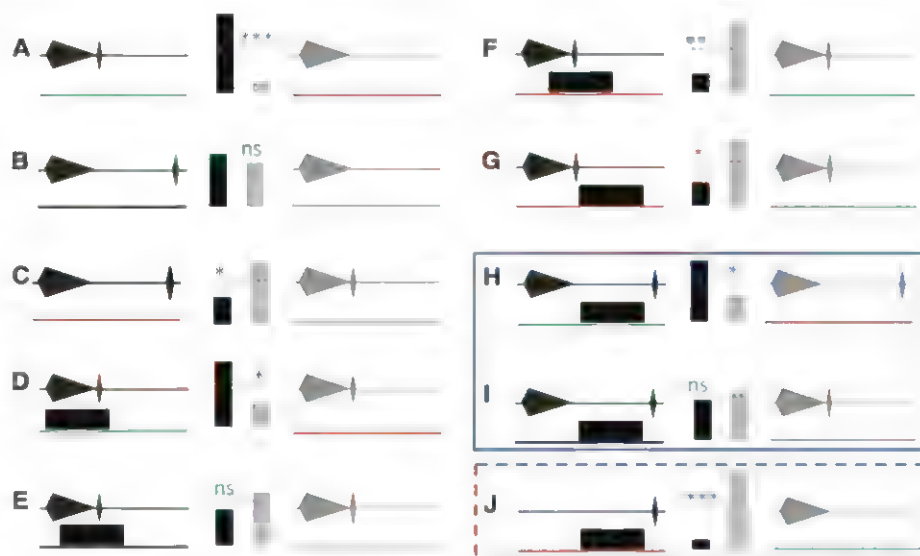


**Fig. 1. Preference responses.** Each portion of the figure illustrates the acoustic components of the túngara frog mating call: a whine only [(A, B, and J), right gray], a chuck only [(J), left black], or a whine-chuck (all other calls). The natural whine-chuck is depicted in (A), left black; (C), right gray; (D to G), all acoustic signals; and (I), right gray. The rectangle represents the inflation-deflation cycle of the robofrog’s vocal sac and its temporal relationship to the call [(D) to (J), left black]. The x axis represents 1000 ms, green indicates the significantly preferred stimulus, and red indicates the unpreferred stimulus. In each of the 10 experiments [(A) to (J)], 20 females were given a choice between the signal in black versus the signal in gray. The vertical black and gray bars represent the number of females that chose the respective signal, and the blue dashed horizontal lines represent the null hypothesis of equal preference. Experiments highlighted in the solid blue box are tests of the perceptual rescue versus template-matching hypotheses, and those in the dashed blue box are the test of the component substitution hypothesis. The results of binomial tests are noted as \*\*\* =  $P < 0.001$ , \*\* =  $P < 0.01$ , \* =  $P < 0.05$ , ns (not significant) =  $P > 0.05$ . The exact  $P$  values for each experiment are as follows: (A)  $P = 0.0003$ , (B)  $P = 0.744$ , (C)  $P = 0.019$ , (D)  $P = 0.034$ , (E)  $P = 0.323$ , (F)  $P = 0.0049$ , (G)  $P = 0.019$ , (H)  $P = 0.039$ , (I)  $P = 0.583$ , (J)  $P = 0.0001$ .

<sup>1</sup>Department of Biology, Salisbury University, Salisbury, MD 21801, USA. <sup>2</sup>Section of Integrative Biology, University of Texas, Austin, TX 78712, USA. <sup>3</sup>Smithsonian Tropical Research Institute, Post Office Box 0843-03092, Balboa, Ancón, Republic of Panama.

\*Corresponding author. E-mail: mryan@utexas.edu



[fig. 1, E to G, from (12)]. When the acoustic and visual cues are offset by 100 ms, the visual cue no longer adds to the attractiveness of the acoustic cue (Fig. 1E). When the visual cue is displaced further in time, 200 ms after the call's onset (Fig. 1F) or immediately after the call's offset (Fig. 1G), the manipulated multimodal signals are both significantly less attractive than the call alone (12). Thus, displacement of the visual cue can reverse the valence of the multimodal signal (Fig. 1, F and G).

Two hypotheses may explain why the acoustic (chuck) and visual (vocal sac) cues lose salience when temporally displaced from the whine. The template-matching hypothesis predicts that females have an internal neural template of the species' call that facilitates recognition (13); disrupting components of mating signals will disrupt their recognition by females. An alternative hypothesis, which we term perceptual rescue, posits that stimulus saliency is influenced by the relative and not the absolute relationships of signal components to one another. If so, a temporally disrupted and less attractive stimulus could be rescued by strategic association with another less attractive stimulus, causing females to bind these components into the percept of a more attractive mating signal. Perceptual rescue predicts more flexibility in signal recognition than template matching.

We tested the perceptual rescue hypothesis against the mutually exclusive template-matching hypothesis [in the sense of "strong inference" (14)]. Specifically, we asked whether placing a visual cue between two separated acoustic cues would cause the components to be bound into one coherent signal. To do this, we placed the vocal sac inflation from the relatively unattractive whine-chuck-sac (Fig. 1G, left black) into the gap between the whine and the chuck (Fig. 1B, left black). This generated a whine followed by the vocal sac inflation-deflation, which in turn was followed by a chuck 500 ms after the whine's offset (Fig. 1H, left black). This multimodal signal was competed against the unimodal whine-gap-chuck, the same acoustic stimulus but lacking a visual stimulus between the whine and the chuck.

Fourteen of 20 females preferred the multimodal signal to the unimodal signal [mid-value  $P$  reported throughout (15, 16),  $P = 0.039$ , Fig. 1H]. Thus, adding the visual cue to the gap between the whine and the chuck, which is equivalent to adding the chuck to the end of the temporally displaced visual cue, rescued the perceptual effects of these stimuli; it made this stimulus complex more attractive. Further, the addition of the visual cue restored the signal's attractiveness to that of a normal whine-chuck, also predicted by the perceptual rescue hypothesis (9 responses to the multimodal signal, 11 to the unimodal,  $P = 0.41$ , Fig. 1I).

These results reject the hypothesis that the negative influence of temporally displaced components on the signal's attractiveness (Fig. 1, B and C, and E to G) was due to these stimuli not matching a conspecific call template. Rather, these

data support the hypothesis that temporally disjunct stimuli can be linked into a common percept of a mating call by their strategic placement in time, even when the resulting stimulus complex has never been experienced by females in nature.

One explanation for our results is that the displaced vocal sac causes the whine and displaced chuck to be perceptually bound. An alternative, the component substitution hypothesis, posits that the vocal sac inflation substitutes for the whine, creating the context for perceiving the chuck as part of the mating signal (i.e., "whine-chuck") and making the whine itself irrelevant. This is not the case. Females significantly preferred a whine to a vocal sac inflation followed by a chuck (sac-chuck) ( $P < 0.0002$ , Fig. 1J). These results further support our interpretation of perceptual binding.

What is the mechanistic basis of perceptual rescue? Humans can group streams of speech into perceptual units, and when sound is interrupted, a continuity illusion can be generated by introducing broadband noise into silent gaps (17). Although one study in frogs failed to find a continuity illusion in the auditory channel (18), our results are consistent with a continuity-type illusion that combines sensory modalities. Thus, one possible mechanism for perceptual rescue is that the presence of the visual cue generates a multisensory continuity illusion.

Although túngara frogs do not produce dissociated acoustic and visual signal components, these manipulations are not as ecologically irrelevant as they might seem. Females are challenged by an auditory world similar to the cocktail party problem in humans (19). At their breeding choruses, they need to perceptually bind the whine and chuck, and assignment of the two acoustic components to their sources is not always accurate (20). The cross-modal interactions we reveal here suggest that the problem might be even more challenging when auditory and visual scene analyses are combined.

These dynamic and context-dependent interactions among multimodal signal components could form a basis for signal recognition, but it would be radically different from the standard template-matching model (13). Our study suggests a need to reconsider the neural basis by which animals recognize signals, to account for these cognitive and perceptual biases that lead to the emergence of hidden preferences. Emergent properties arising from interactions among sensory modalities are not restricted to the recognition of communication signals. In chicks, odor and color can interact to generate an aversive response that does not occur with either component in isolation (21). In this domain as well, there is a psychological response that is hidden when only isolated stimuli are encountered.

Our findings also have implications for understanding receiver psychology (22) and specifically how perceptual processes can drive the evolution of complex signal phenotypes. The interactions we report could facilitate signal evolu-

tion with only a few key changes. Different components of a complex phenotype need not arise simultaneously and de novo but could result from temporal or spatial shifts in previously incoherent traits. Put another way, perceptual integration in a multisensory universe may yield emergent psychological percepts that provide the basis for positive selection of complex signals. This type of unanticipated perceptual bias could be responsible for the evolution of some of the extreme and elaborate signals that evolve under sexual selection by mate choice (23, 24).

## References and Notes

1. L. E. Bahrick, R. Lickliter, R. Flom, *Curr. Dir. Psychol. Sci.* **13**, 99 (2004).
2. H. McGurk, J. MacDonald, *Nature* **264**, 746 (1976).
3. J. Driver, *Nature* **381**, 66 (1996).
4. S. R. Partan, P. Marler, *Am. Nat.* **166**, 231 (2005).
5. E. Hebets, D. Papaj, *Behav. Ecol. Sociobiol.* **57**, 197 (2005).
6. M. Griddi-Papp, A. S. Rand, M. J. Ryan, *Nature* **441**, 38 (2006).
7. G. B. Pauly, X. E. Bernal, A. S. Rand, M. J. Ryan, *Physiol. Biochem. Zool.* **79**, 708 (2006).
8. P. M. Narins, W. Hödl, D. S. Grabul, *Proc. Natl. Acad. Sci. U.S.A.* **100**, 577 (2003).
9. R. C. Taylor, B. Buchanan, J. Doherty, *Anim. Behav.* **74**, 1753 (2007).
10. R. C. Taylor, B. A. Klein, J. Stein, M. J. Ryan, *Anim. Behav.* **76**, 1089 (2008).
11. W. Wilczynski, S. A. Rand, M. J. Ryan, *Anim. Behav.* **58**, 841 (1999).
12. R. C. Taylor, B. A. Klein, J. Stein, M. J. Ryan, *J. Exp. Biol.* **214**, 815 (2011).
13. P. Marler, *J. Neurobiol.* **33**, 501 (1997).
14. J. R. Platt, *Science* **146**, 347 (1964).
15. A. Agresti, *Stat. Med.* **20**, 2709 (2001).
16. A. Agresti, *An Introduction to Categorical Data Analysis* (Wiley-Blackwell, New York, 2007).
17. A. Bregman, *Auditory Scene Analysis: The Perceptual Organization of Sound* (MIT Press, Cambridge, MA, 1994).
18. F. Seeba, J. J. Schwartz, M. A. Bee, *Anim. Behav.* **79**, 1317 (2010).
19. M. A. Bee, C. Micheyl, *J. Comp. Psychol.* **122**, 235 (2008).
20. H. E. Farris, M. J. Ryan, *Nat. Commun.* **2**, 410 (2011).
21. C. T. Rowe, T. Guilford, *Nature* **383**, 520 (1996).
22. T. Guilford, M. Dawkins, *Anim. Behav.* **42**, 1 (1991).
23. M. J. Ryan, *Integr. Comp. Biol.* **51**, 756 (2011).
24. M. J. Ryan, M. E. Cummings, *Annu. Rev. Ecol. Syst.*, in press.

**Acknowledgments:** We are grateful to the NSF (grants IBN 0517328, IBN 0078150, and IOS 1120031) and the Clark Hubbs Regents Professorship (M.J.R.) for funding and the Smithsonian Tropical Research Institute for logistical support. We thank E. Balaban for helpful discussion and H. Farris, S. Partan, S. Pika, G. Rosenthal, and three anonymous reviewers for their comments on the manuscript. We thank B. Klein and Moe, Incorporated for design and fabrication of the robotic frogs. We are especially grateful to the interns who assisted in data collection. All research reported here complied with IACUC protocols from Salisbury University, the University of Texas, and the Smithsonian Tropical Research Institute. We obtained all required permits from the Government of Panama. Data will be archived in the Dryad Data Repository at [dx.doi.org/10.5061/dryad.pk85](http://dx.doi.org/10.5061/dryad.pk85).

## Supplementary Materials

[www.sciencemag.org/cgi/content/full/science.1237113/DC1](http://www.sciencemag.org/cgi/content/full/science.1237113/DC1)  
Materials and Methods

26 February 2013; accepted 8 May 2013  
Published online 6 June 2013,  
10.1126/science.1237113

# Loss of Function of the Melanocortin 2 Receptor Accessory Protein 2 Is Associated with Mammalian Obesity

Masato Asai,<sup>1,2</sup> Shwetha Ramachandrapa,<sup>3</sup> Maria Joachim,<sup>1</sup> Yuan Shen,<sup>1</sup> Rong Zhang,<sup>1</sup> Nikhil Nuthalapati,<sup>1</sup> Visali Ramanathan,<sup>1</sup> David E. Strohlic,<sup>1</sup> Peter Ferket,<sup>4</sup> Kirsten Linhart,<sup>1,\*</sup> Caroline Ho,<sup>1</sup> Tatiana V. Novoselova,<sup>5</sup> Sumedha Garg,<sup>3</sup> Martin Ridderstråle,<sup>6</sup> Claude Marcus,<sup>7</sup> Joel N. Hirschhorn,<sup>1,8</sup> Julia M. Keogh,<sup>3</sup> Stephen O'Rahilly,<sup>3</sup> Li F. Chan,<sup>5</sup> Adrian J. Clark,<sup>5</sup> I. Sadaf Farooqi,<sup>3,†</sup> Joseph A. Majzoub<sup>1,†</sup>

Melanocortin receptor accessory proteins (MRAPs) modulate signaling of melanocortin receptors in vitro. To investigate the physiological role of brain-expressed melanocortin 2 receptor accessory protein 2 (MRAP2), we characterized mice with whole-body and brain-specific targeted deletion of *Mrap2*, both of which develop severe obesity at a young age. *Mrap2* interacts directly with melanocortin 4 receptor (Mc4r), a protein previously implicated in mammalian obesity, and it enhances Mc4r-mediated generation of the second messenger cyclic adenosine monophosphate, suggesting that alterations in Mc4r signaling may be one mechanism underlying the association between *Mrap2* disruption and obesity. In a study of humans with severe, early-onset obesity, we found four rare, potentially pathogenic genetic variants in *MRAP2*, suggesting that the gene may also contribute to body weight regulation in humans.

Membrane-expressed G protein-coupled receptors (GPCRs) modulate cellular responses to numerous physiological stimuli. The melanocortin receptors (MCRs) are a subfamily of GPCRs that mediate signaling in response to the pro-opiomelanocortin-derived peptides, adrenocorticotrophic hormone (ACTH), and  $\alpha$ -melanocyte-stimulating hormone ( $\alpha$ MSH) and their competitive antagonists, agouti and agouti-related protein. The MCRs mediate a diverse range of physiological functions. MC1R is involved in skin pigmentation, MC2R plays a critical role in the hypothalamic-pituitary-adrenal axis, MC3R and MC4R are involved in energy homeostasis, and MC5R is implicated in exocrine function (1).

There is increasing recognition that accessory proteins can modulate GPCR trafficking, as well as ligand binding and signaling (2). An accessory

protein for MC2R, MC2R accessory protein (MRAP), is required for the trafficking of MC2R to the surface of adrenal cells and for signaling in response

to ACTH (3, 4). Loss of either MC2R or MRAP in humans causes severe resistance to ACTH, with resulting glucocorticoid deficiency (5, 6).

All mammals have a paralogous gene, *MRAP2*, which, like *MC3R* and *MC4R*, is predominantly expressed in the brain (7), most prominently in the pons and cerebellum but also in regions involved in energy homeostasis, such as the hypothalamus and brainstem (fig. S1, A to C). Within the paraventricular nucleus of the hypothalamus (PVN), *Mrap2* and *Mc4r* mRNAs are coexpressed in many cells (fig. S1D). We hypothesized that *Mrap2* might modulate signaling through a MCR and potentially affect energy homeostasis. We therefore performed targeted deletion of *Mrap2* in mice using Cre-lox-mediated excision of the 100-bp exon 3 [which encodes the highly conserved transmembrane domain (7)] to create mice with normal levels of an mRNA predicted to encode a truncated protein that includes the first 55 amino acids of *Mrap2*, with the transmembrane domain replaced by 11 aberrant amino acids specified by the out-of-frame exon 4, followed by a stop codon (fig. S1, E to H). Normal levels of the mutant mRNA indicate preservation of *Mrap2*-containing neurons in null mice, although these neurons probably do not express the predicted mutant protein because mutant *Mrap2* mRNA, but not

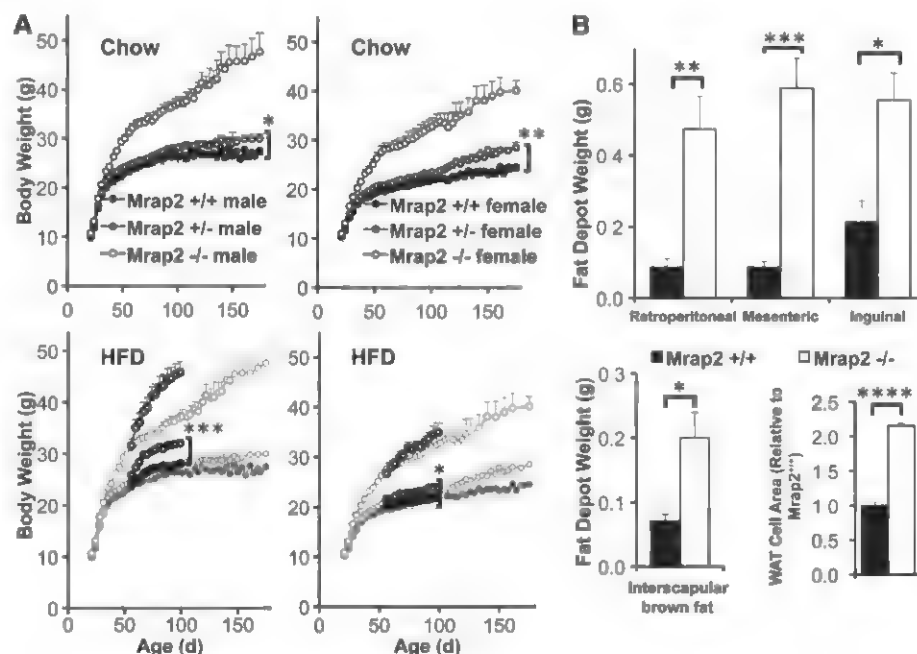


**Fig. 1. Phenotype of *Mrap2*<sup>-/-</sup> mice.** (A) Weight curves for *Mrap2*<sup>+/+</sup> versus *Mrap2*<sup>+/-</sup> versus *Mrap2*<sup>-/-</sup> mice on standard-chow (Chow, top: male  $n = 9$  versus 28 versus 15 mice, female  $n = 12$  versus 18 versus 10 mice) or high-fat diets (HFD; ages 56 to 95 days, bottom: superimposed on standard-chow curves: male  $n = 10$  versus 8 versus 10 mice; female  $n = 7$  versus 12 versus 7 mice). For both genders, the weight curves of *Mrap2*<sup>+/+</sup> and *Mrap2*<sup>+/-</sup> mice on standard chow differ significantly at older ages (161 to 175 days) and at younger ages (56 to 95 days) on a high-fat diet.  $*P = 0.02$ ,  $**P = 0.001$ ,  $***P = 0.0003$ . (B) Fat depots on standard-chow diet. (Top) White adipose tissue (WAT) weights in *Mrap2*<sup>+/+</sup> versus *Mrap2*<sup>-/-</sup> (males and females, ages 117 to 122 days,  $n = 5$  versus 4 mice, respectively). (Bottom left) Brown adipose tissue (BAT) weight in *Mrap2*<sup>+/+</sup> versus *Mrap2*<sup>-/-</sup> mice (males and females, ages 117 to 122 days,  $n = 5$  versus 4 mice). (Bottom right) WAT cell size in *Mrap2*<sup>+/+</sup> versus *Mrap2*<sup>-/-</sup> mice (females, 50 cells counted from each mouse).  $*P = 0.009$ ,  $**P = 0.003$ ,  $***P = 0.0003$ ,  $****P < 0.00001$ .

<sup>1</sup>Division of Endocrinology, Department of Medicine, Boston Children's Hospital, Harvard Medical School, 300 Longwood Avenue, Boston, MA 02115, USA. <sup>2</sup>Departments of Pathology, Endocrinology and Diabetes, Nagoya University Graduate School of Medicine, 65 Tsurumai-cho, Showa-ku, Nagoya 466-8550, Japan. <sup>3</sup>University of Cambridge Metabolic Research Laboratories and National Institute for Health Research (NIHR) Cambridge Biomedical Research Centre, Institute of Metabolic Science, Addenbrooke's Hospital, Cambridge CB2 0QQ, UK. <sup>4</sup>Prestige Department of Poultry Science, North Carolina State University, Raleigh, NC 27695, USA. <sup>5</sup>William Harvey Research Institute, Centre for Endocrinology Queen Mary, University of London Barts and The London School of Medicine and Dentistry, London EC1M 6BQ, UK. <sup>6</sup>Department of Clinical Sciences, Lund University, Malmö, Sweden, and Steno Diabetes Center, DK-2820 Gentofte, Denmark. <sup>7</sup>Department for Clinical Science, Intervention and Technology, Karolinska Institute, Division of Pediatrics, National Childhood Obesity Centre, S-141 86 Stockholm, Sweden. <sup>8</sup>Department of Genetics, Harvard Medical School and Broad Institute, Cambridge, MA 02142, USA.

\*Present address: Department of Internal Medicine, KH Salem, University of Heidelberg, 69120 Heidelberg, Germany.

†Corresponding author. E-mail: joseph.majzoub@childrens.harvard.edu (J.A.M.); tsf20@cam.ac.uk (I.S.F.).



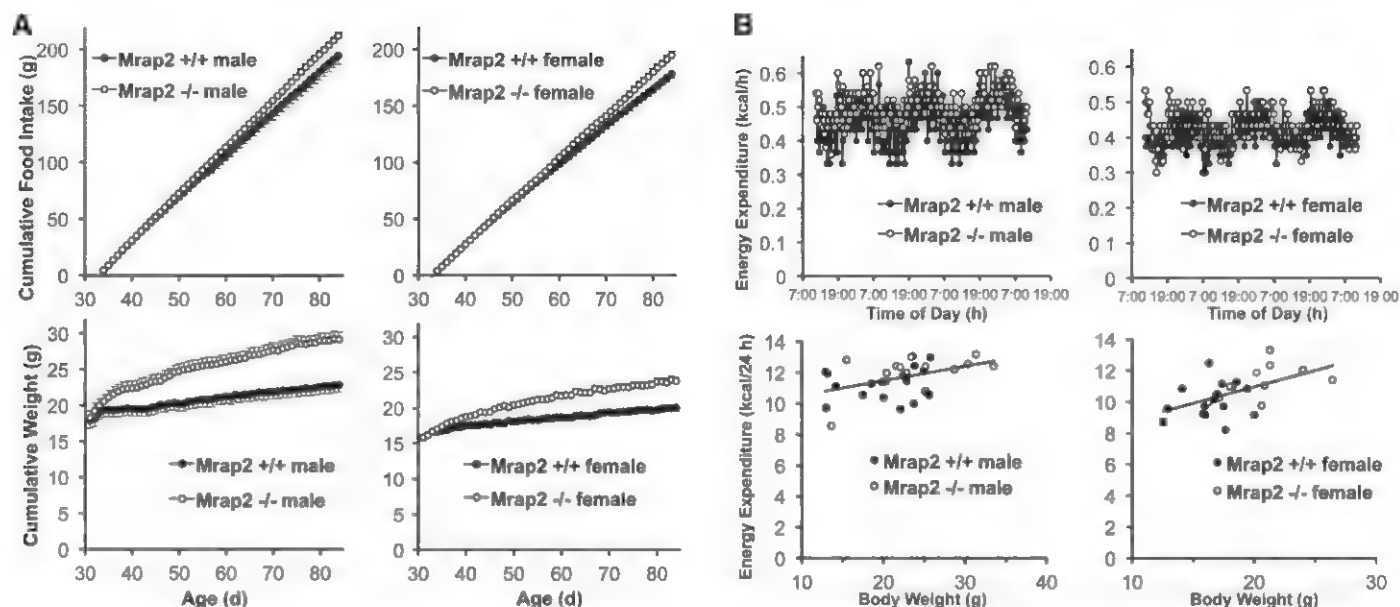


**Fig. 2. Energy balance in *Mrap2*<sup>-/-</sup> mice.** (A) Cumulative food intake (top) and weight (bottom) in ad libitum-fed *Mrap2*<sup>+/+</sup> versus *Mrap2*<sup>-/-</sup> males ( $n = 10$  versus 11 mice) and females ( $n = 11$  versus 8 mice). (B) Energy expenditure in ad libitum-fed *Mrap2*<sup>+/+</sup> versus *Mrap2*<sup>-/-</sup> mice. (Top) Continuous measurement over 3 days, males ( $n = 3$  versus 4 mice), females ( $n = 4$  versus

3 mice), ages 30 to 34 days. (Bottom) Body weight versus energy expenditure, integrated over 24 hours, males ( $n = 18$  versus 14 mice, ages 30 to 45 days), females ( $n = 16$  versus 11 mice, ages 30 to 42 days). Analysis with ANCOVA showed no differences between genotypes (males,  $P = 0.38$ ; females,  $P = 0.67$ ).

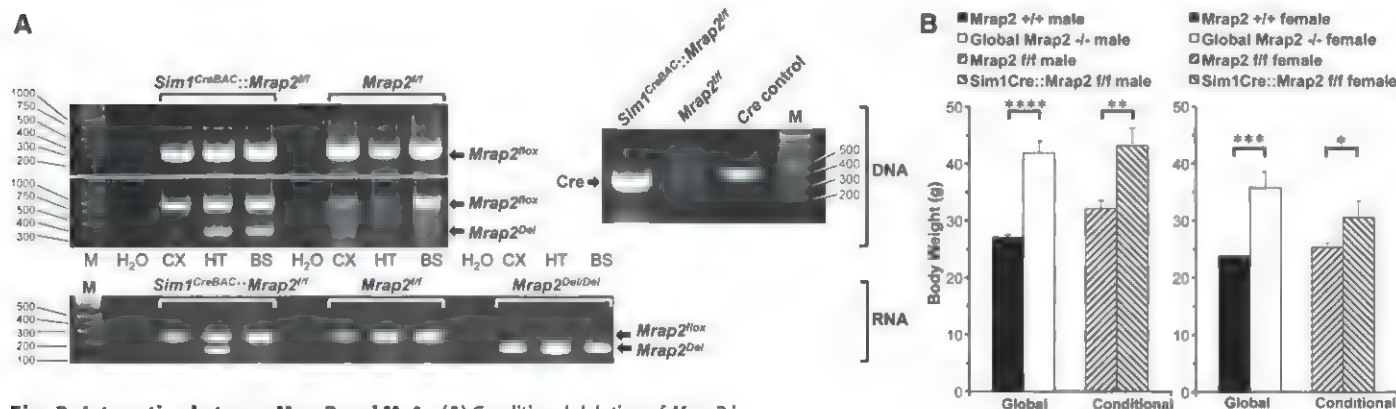
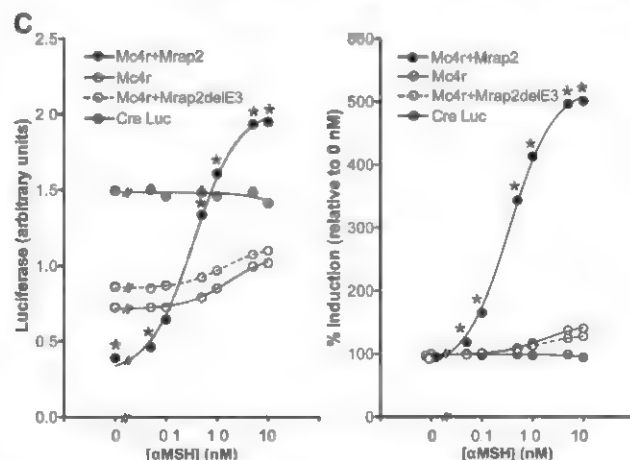


**Fig. 3. Interaction between *Mrap2* and *Mc4r*.** (A) Conditional deletion of *Mrap2* in *Sim1* neurons. (Top right) Cre DNA analysis by means of polymerase chain reaction (PCR). HT DNA from *Sim1*<sup>CreBAC</sup>::*Mrap2*<sup>flf</sup> mice contains *Cre* (374 bp), but from *Mrap2*<sup>flf</sup> mice does not. Molecular weight marker (M) is shown on right (base pairs). (Top left) *Mrap2* DNA analysis in *Sim1*<sup>CreBAC</sup>::*Mrap2*<sup>flf</sup> and *Mrap2*<sup>flf</sup> mice by means of PCR. Both genotypes contain floxed, intact *Mrap2* DNA in CX, HT, and BS (314 bp in top electropherogram, and 1013 bp in bottom electropherogram, and molecular weight markers on left). Only *Sim1*<sup>CreBAC</sup>::*Mrap2*<sup>flf</sup> mice contain *Mrap2*<sup>Del</sup> (400 bp, bottom electropherogram), and only in HT and BS, but not in CX, which is consistent with fluorescent reporter data (fig. S3A). No PCR products are present without added DNA (H<sub>2</sub>O). (Bottom) *Mrap2* mRNA expression in *Sim1*<sup>CreBAC</sup>::*Mrap2*<sup>flf</sup> and *Mrap2*<sup>flf</sup> mice by means of reverse transcriptase (RT)-PCR. Both genotypes express floxed, intact *Mrap2* mRNA in CX, HT, and BS (247 bp). Only *Sim1*<sup>CreBAC</sup>::*Mrap2*<sup>flf</sup> mice express *Mrap2*<sup>Del</sup> mRNA (147 bp), and only in HT. Global *Mrap2*<sup>Del/Del</sup> mice express *Mrap2*<sup>Del</sup> mRNA in all three sites. (B) Body weights of *Mrap2*<sup>+/+</sup> (male  $n = 6$  mice, female  $n = 11$  mice), *Mrap2*<sup>-/-</sup> (male  $n = 11$  mice, female  $n = 7$  mice), *Mrap2*<sup>flf</sup> (male  $n = 8$  mice, female  $n = 12$  mice), and conditional *Sim1*<sup>CreBAC</sup>::*Mrap2*<sup>flf</sup> (male  $n = 8$  mice, female  $n = 7$  mice) mice, all age 133 days. \* $P = 0.04$ , \*\* $P = 0.007$ , \*\*\* $P = 0.0002$ , \*\*\*\* $P < 0.0001$ . (C) Effect of *Mrap2* on *Mc4r* signaling. (Left) Level of cAMP reporter activity (CRE Luc) in CHO cells alone or cotransfected with *Mc4r*, with or without *Mrap2* or the *Mrap2* knock-out construct, *Mrap2*<sup>delE3</sup>, 5 hours after exposure to 0 to 10 nM  $\alpha$ MSH ( $n = 3$  mice per group). (Right) cAMP activity of these same constructs, expressed as percent induction after 0 to 10 nM  $\alpha$ MSH, relative to 0 nM  $\alpha$ MSH. \* $P < .0001$ , *Mc4r*+*Mrap2* versus *Mc4r* at same [ $\alpha$ MSH], by means of analysis of variance. For most data points, error bars are obscured by symbols.



protein, is present in cells transfected with the same *Mrap2* mutant construct used to create the null mice (fig. S1I).

*Mrap2*-null mice appeared normal at birth, with normal weight gain and post-weaning food intake during early life (0 to 32 days and 23 to 32 days, respectively), although young *Mrap2*<sup>-/-</sup> male mice trended toward greater weight and food intake with advancing age (fig. S1J). However, null mice of both genders gradually became extremely obese on a diet of regular chow ad libitum (figs. 1A and S2A). Heterozygous mice were significantly heavier than were wild-type animals on standard chow (160 to 175 days; males, *Mrap2*<sup>+/-</sup> 26.0 ± 0.4 g, *Mrap2*<sup>+/-</sup> 29.9 ± 0.9 g; females, *Mrap2*<sup>+/-</sup> 24.5 ± 0.9 g, *Mrap2*<sup>+/-</sup> 28.1 ± 0.7 g), and at younger ages (56 to 95 days) on a high-fat diet (Fig. 1A). In addition, *Mrap2*<sup>+/-</sup> mice had increased length (fig. S1K) and percent of weight due to fat and decreased percent of weight due to lean mass (fig. S1L). Both genders of *Mrap2*<sup>+/-</sup> mice had increased visceral adiposity, greater than twice the normal white adipose tissue cell size, enlarged brown adipose tissue depots, normal liver histology on a regular chow diet, but much greater hepatic steatosis as compared with those of wild-type mice on a high-fat diet (Fig. 1B and fig. S2, A and B). Adult *Mrap2*-null mice had, as expected, elevated leptin concentrations corresponding to their increased fat mass, which normalized to diet-induced weight normalization (fig. S2C). Obese adult mice had normal fasting insulin (fig. S2D) and normal tolerance to intraperitoneal glucose injection (fig. S2E). *Mrap2* has been postulated to play a role in the adrenal response to ACTH (8). We therefore measured diurnal rhythmicity and stress responsiveness of the adrenal axis in *Mrap2*-null mice, which were normal (fig. S2F). Thyroid hormone levels were also normal (table S1). Epinephrine and norepinephrine excretion were reduced in male *Mrap2*<sup>+/-</sup> mice only (fig. S2G), but *Ucp1* mRNA concentrations increased appropriately in both genders of null mice after exposure to 4°C for 18 hours (fig. S2H). Hypothalamic *AgRP* mRNA concentration was reduced in *Mrap2*-null mice, whereas *Pomc* mRNA was normal (fig. S2I).

To characterize the mechanisms underlying the obesity in these mice, we measured food in-

take under a variety of conditions. At 42 (fig. S2J) and 84 (fig. S2K) days of age, when *Mrap2*<sup>+/-</sup> mice were clearly overweight, no difference in food intake was detected between the two genotypes when analyzed over a 4-day interval. Obesity was not caused by more efficient absorption of calories in null mice (fig. S2L). Only when monitored daily over 50 days (ages 34 to 84 days) was a subtle increase in cumulative food intake discernable in the null animals (Fig. 2A), with the onset of obesity preceding hyperphagia (Fig. 2A and fig. S2M). To further understand the contribution of hyperphagia to obesity in *Mrap2*<sup>+/-</sup> mice, we limited their food intake to that amount consumed by their normal siblings (pair feeding). Even when fed the same amount of chow, null mice gained more weight than did wild-type mice (fig. S2, N and O). Only when the amount of food intake in null mice was further restricted to 10% (females) and 13% (males) less than that of wild-type mice was there equivalent weight gain (fig. S2P) in the two genotypes. To determine whether the late-onset hyperphagia in *Mrap2*<sup>+/-</sup> mice (Fig. 2A) could simply be the consequence of an increased body mass at this older age caused by a separate metabolic defect, we switched null mice to ad libitum access to chow after 40 days of restricted feeding (fig. S2P, upward arrow). During the first 24 hours of ad libitum feeding, food intake almost doubled in null mice (from 2.9 ± 0.1 to 5.6 ± 0.5 g/day in males, and from 2.8 ± 0.1 to 5.3 ± 0.2 g/day in females), with a corresponding marked increase in body weight. Thus, hyperphagia develops in an age-dependent manner in older mice, independent of body weight. Consistent with this, young (age 38 to 45 days) *Mrap2*<sup>+/-</sup> mice had an intact anorectic response to the MCR (Mc4r and Mc3r) agonist, MTII (fig. S2Q), corresponding to their normal ad libitum food intake at this age.

We hypothesized that young *Mrap2*<sup>+/-</sup> mice might display abnormal energy expenditure because obesity develops early during ad libitum feeding before the onset of hyperphagia, persists in mutant mice pair-fed to a normal dietary intake, and is abolished only by underfeeding. To explore this, we measured energy expenditure and respiratory exchange ratio (RER) with indirect calorimetry, as well as locomotor activity and core

body temperature, in young (30 to 45 days of age) wild-type and *Mrap2*-null mice, just as their weights began to diverge (Fig. 2A). Surprisingly, the wild-type and mutant mice had indistinguishable 24-hour total energy expenditure, as analyzed by means of analysis of covariance (ANCOVA) (Fig. 2B) (9). There were also no differences between *Mrap2*<sup>+/-</sup> and *Mrap2*<sup>-/-</sup> mice in RER (fig. S2R), locomotor activity (fig. S2S), or core body temperature at 22°C (fig. S2T), with both genotypes exhibiting the expected increase in all three parameters during the active night period. After exposure to 4°C for 18 hours, null and wild-type mice became significantly hypothermic to the same extent (fig. S2T).

Because (i) MRAP is essential for signaling through MC2R (3, 4), (ii) MRAP's paralog, *Mrap2*, is expressed principally in the brain, and (iii) Mc2r's paralog, Mc4r, has a key role in energy balance in *Sim1*-containing neurons (10), we asked whether deletion of *Mrap2* causes obesity in part by altering signaling through centrally expressed Mc4r. We created a *Sim1*<sup>Cre</sup>::*Mrap2*<sup>fllox/fllox</sup> mouse with conditional deletion of *Mrap2* exclusively in these neurons and expression of *Mrap2*<sup>Del</sup> mRNA only in hypothalamus and not cerebral cortex or brainstem (Fig. 3A and fig. S3A). Like global null mice, conditional mutants were similarly obese (Fig. 3B), and pair-feeding to a normal dietary intake only partially reversed their obesity (fig. S3B).

If *Mrap2* facilitates the action of Mc4r, then Mc4r deficiency should create an equivalent or more severe obesity phenotype than does *Mrap2* deficiency, depending on the degree to which *Mrap2* interferes with Mc4r function. Supporting this, *Mrap2*<sup>+/-</sup> mice of both genders were less obese than either *Mc4r*<sup>+/-</sup> or doubly heterozygous mice (fig. S3C). The differences between *Mc4r*<sup>+/-</sup> and doubly heterozygous mice were not statistically significant, although the latter trended toward being heavier. Among homozygous knockouts, those with Mc4r deficiency alone were more obese than those with *Mrap2* deficiency alone (fig. S3C). The mice in which *Mc4r* was knocked out were more obese than were mice with deletion of both *Mc4r* and *Mrap2* (in males, with a trend in females), suggesting that *Mrap2* may promote weight gain through both Mc4r-dependent and -independent actions.

To determine whether mouse *Mrap2* and Mc4r can interact directly, we coimmunoprecipitated transiently expressed, N-terminally Myc-tagged *Mrap2* and N-terminally green fluorescent protein-tagged Mc4r in Chinese hamster ovary (CHO) cells (devoid of endogenous *Mrap2*, *Mrap2*, and MCRs). We found that mouse *Mrap2* and Mc4r interact (fig. S3D), which is consistent with previous data (7). We next investigated the impact of *Mrap2* on Mc4r (Fig. 3C) and Mc3r (fig. S3E) signaling. The combined expression of Mc4r and *Mrap2* in CHO cells suppressed basal cyclic adenosine monophosphate (cAMP)-dependent protein kinase (PKA) signaling compared with Mc4r alone (Fig. 3C, left), as previously reported with the human orthologs (7). But in contrast to that

**Table 1. MRAP2 variants detected in obese subjects and controls.**

MRAP2 variant	Subjects with variant	Subject sex/ age/BMI/ BMI SDS*	Controls with variant	MAF†: European American	MAF†: African American	***PolyPhen-2 prediction‡
E24X	1/488	M/19/63/4.7	0/488	0.000% (0/8600)	0.000% (0/4406)	Damaging
N88Y	1/376	M/11/29.6/3.3	0/376	0.000% (0/8600)	0.000% (0/4406)	Possibly damaging
L115V	1/488	M/5/24/4.2	0/488	0.012% (1/8600)	0.000% (0/4406)	Benign
R125C	1/488	F/8/29/3.5	0/488	0.047% (4/8600)	0.045% (2/4406)	Possibly damaging

\*Subject sex (male, M; female, F)/age (years)/body mass index (BMI) (kilograms per square meter)/standard deviation score (SDS).

†MAF, minor allele frequency; available at the National Heart, Lung, and Blood Institute exome variant server: <http://evs.gs.washington.edu/EVS>.

‡PolyPhen-2; available at <http://genetics.bwh.harvard.edu/pph2>.



report (which used NDP-MSH), we found that  $\alpha$ MSH caused a fivefold increase above basal PKA activity (Fig. 3C, right) compared with less than a twofold increase with Mc4r alone or Mc4r plus the *Mrap2*-null construct, *Mrap2<sup>delE3</sup>* (our in vitro model for in vivo disruption of *Mrap2*). The presence of *Mrap2* increased signaling through Mc3r at the two highest  $\alpha$ MSH doses (fig. S3E). These findings suggest *Mrap2* may alter signaling through Mc4r and perhaps other receptors.

To investigate whether alterations in MRAP2 are associated with human obesity, we sequenced the coding region and intron/exon boundaries of *MRAP2* in obese and control individuals from the Genetics of Obesity Study (GOOS) cohort (11) and the Swedish obese children's cohort (12). Four rare heterozygous variants that were absent from cohort-specific controls and 1000 genomes (Table 1) were found in unrelated, nonsyndromic, severely obese individuals, with all but one variant in the C-terminal region of the protein (fig. S4). In three of these subjects, no pathogenic variants were found in the coding region or intron/exon boundaries of all known nonsyndromic human obesity genes (table S2). Only one of the variants (E24X) is clearly disruptive, and overall, few rare variants were found in the obese cohorts, indicating that if *MRAP2* mutations contribute to severe human obesity, they do so rarely.

We have found that global or brain-specific inactivation of *Mrap2* causes obesity in mice and

that rare heterozygous variants in *MRAP2* are associated with early-onset, severe obesity in humans. The mechanism (or mechanisms) by which *Mrap2* exerts its effects on body weight regulation remain to be firmly established but likely involve altered signaling through Mc4r and perhaps other MCRs. Under conditions comparable with those we describe, in which *Mrap2* greatly enhances cAMP signaling through Mc4r, Sebag *et al.* (13) have found that the zebrafish ortholog of *Mrap2* (*zMRAP2b*) similarly affects *zMC4R* signaling. This evolutionary conservation, plus the extreme disease phenotype caused by loss of *Mrap2* function, supports the importance of *Mrap2* in vertebrate biology.

## References and Notes

1. R. D. Cone, *Endocr. Rev.* **27**, 736–749 (2006).
2. D. L. Hay, D. R. Poyner, P. M. Sexton, *Pharmacol. Ther.* **109**, 173–197 (2006).
3. P. M. Hinkle, J. A. Sebag, *Mol. Cell. Endocrinol.* **300**, 25–31 (2009).
4. S. N. Cooray, A. J. Clark, *Mol. Cell. Endocrinol.* **331**, 215–221 (2011).
5. L. A. Metherell *et al.*, *Nat. Genet.* **37**, 166–170 (2005).
6. L. F. Chan, L. A. Metherell, A. J. Clark, *Eur. J. Pharmacol.* **660**, 171–180 (2011).
7. L. F. Chan *et al.*, *Proc. Natl. Acad. Sci. U.S.A.* **106**, 6146–6151 (2009).
8. J. A. Sebag, P. M. Hinkle, *Sci. Signal.* **3**, ra28 (2010).
9. M. H. Tschöp *et al.*, *Nat. Methods* **9**, 57–63 (2012).
10. N. Balthasar *et al.*, *Cell* **123**, 493–505 (2005).
11. S. Farooqi, S. O'Rahilly, *Endocr. Rev.* **27**, 710–718 (2006).

12. L. E. Johansson *et al.*, *PLoS ONE* **4**, e5327 (2009).
13. J. A. Sebag *et al.*, *Science* **341**, 278 (2013).

**Acknowledgments:** We thank T. Nguyen for DNA analysis; H. Feldman and A. Fleisch for statistical advice; M. Mucahey for thyroid assays; H. Turkova for catecholamine assays; S. Cabi for creating the software program used to analyze calorimetry data; M. Geibel for bioinformatics analyses; and D. Margulies, B. Lowell, J. Flier, and Boston Children's Hospital Endocrinology Division scientists for helpful discussions. We are indebted to the patients and their families for their participation and to the physicians involved in GOOS and the Swedish obese children's cohort study. This work was supported by grants from the National Institutes of Health, including NIH30-HD18655 (J.A.M.), the Timothy Murphy Fund (J.A.M.), the National Alliance for Research on Schizophrenia and Depression (M.A.), the Wellcome Trust (I.S.F. and S.O'R.), the Medical Research Council (I.S.F. and L.F.C. (grant no. G0802796)), the NIHR Cambridge Biomedical Research Centre (I.S.F. and S.O'R.), and R01DK075787 (J.N.H.). S.O'R. is a paid Scientific Adviser for Pfizer in the area of cardiometabolic disease. Until 2010, J.A.M. was on the Board of, and was a paid Scientific Advisor for, Correlagen Diagnostics, a company whose projects included molecular diagnostic tests related to obesity. The authors (M.A., J.A.M., Boston Children's Hospital) have filed a patent application related to modulating *Mrap2* to alter growth.

## Supplementary Materials

www.sciencemag.org/cgi/content/full/341/6143/275/DC1  
Materials and Methods  
Figs. S1 to S4  
Tables S1 to S3  
References (14–19)

20 November 2012; accepted 13 June 2013  
10.1126/science.1233000

# Developmental Control of the Melanocortin-4 Receptor by MRAP2 Proteins in Zebrafish

Julien A. Sebag,<sup>1\*</sup> Chao Zhang,<sup>1\*</sup> Patricia M. Hinkle,<sup>2</sup> Amanda M. Bradshaw,<sup>1</sup> Roger D. Cone<sup>1†</sup>

The melanocortin-4 receptor (MC4R) is essential for control of energy homeostasis in vertebrates. MC4R interacts with melanocortin receptor accessory protein 2 (MRAP2) in vitro, but its functions in vivo are unknown. We found that MRAP2a, a larval form, stimulates growth of zebrafish by specifically blocking the action of MC4R. In cell culture, this protein binds MC4R and reduces the ability of the receptor to bind its ligand,  $\alpha$ -melanocyte-stimulating hormone ( $\alpha$ -MSH). A paralog, MRAP2b, expressed later in development, also binds MC4R but increases ligand sensitivity. Thus, MRAP2 proteins allow for developmental control of MC4R activity, with MRAP2a blocking its function and stimulating growth during larval development, whereas MRAP2b enhances responsiveness to  $\alpha$ -MSH once the zebrafish begins feeding, thus increasing the capacity for regulated feeding and growth.

**T**he melanocortin-4 receptor (MC4R), a G protein-coupled receptor (GPCR), plays a central role in energy homeostasis (1–4)

and somatic growth (1, 2, 5). Mutations in the gene encoding MC4R are the most common monogenic cause of severe early-onset obesity in humans (1). In the zebrafish, as in mammals, MC4R is prominently involved in the regulation of energy homeostasis and somatic growth (6). Dominant negative mutations in MC4R are a natural cause of increased growth rate and final size in some teleost species (5). An artificially induced increase in MC4R activity early in the development of the zebrafish embryo causes a

decrease in growth, a decrease in growth hormone gene expression, and a compensatory increase in growth hormone-releasing hormone (*ghrh*) gene expression (6), thus providing quantitative assays for MC4R activity in vivo. The melanocortin receptors have been shown to interact with the melanocortin receptor accessory proteins MRAP1 and MRAP2 (7–13), which are single-transmembrane proteins that form unusual antiparallel homo- and heterodimers (7–9). Whereas MRAP1 is essential for adrenocorticotrophic hormone receptor (MC2R) trafficking to the plasma membrane, ligand binding, and downstream signaling (7, 8, 11), the functions of MRAP2 remain unclear. In the zebrafish, MRAP2 exists in two isoforms, a and b (14). Here, we investigated the role of MRAP2a and MRAP2b in the regulation of MC4R activity in vivo in the zebrafish and in vitro in human embryonic kidney (HEK) 293T cells.

We first characterized the distribution and developmental expression kinetics of *mc4r*, *mrap2a*, and *mrap2b* gene expression in the zebrafish embryo at 1, 2, 3, or 4 days post-fertilization (dpf) by reverse transcription polymerase chain reaction (RT-PCR) (Fig. 1A). *mc4r* and *mrap2a* mRNA were detectable from 1 dpf and their expression increased every day until 4 dpf, whereas *mrap2b* was hardly detectable. To identify the larval tissue distribution of *mrap2* mRNAs, we performed whole-mount in situ hybridization on zebrafish embryos at 5 dpf. *mrap2a* was ubiquitously ex-

<sup>1</sup>Department of Molecular Physiology and Biophysics, Vanderbilt University School of Medicine, Nashville, TN 37232, USA. <sup>2</sup>Department of Pharmacology and Physiology, School of Medicine and Dentistry, University of Rochester Medical Center, Rochester, NY 14642, USA.

\*These authors contributed equally to this work.

†Corresponding author. E-mail: roger.cone@vanderbilt.edu

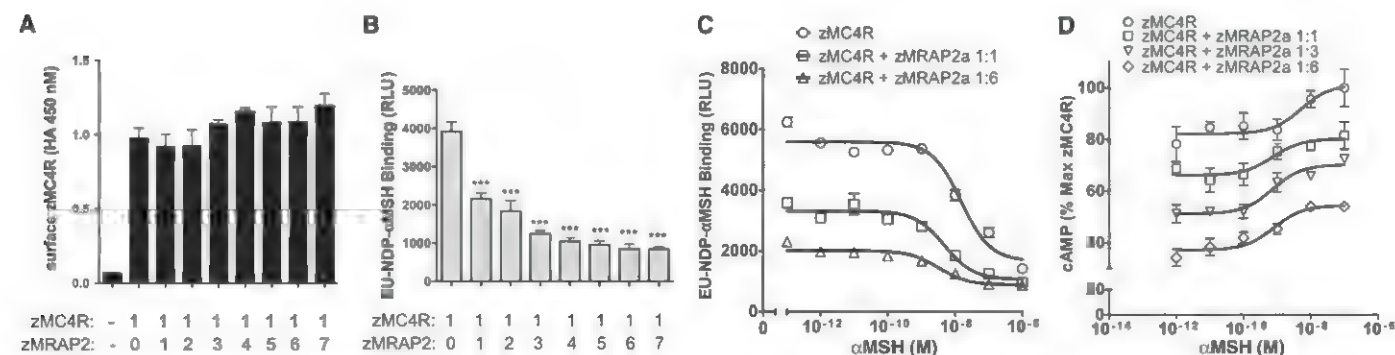
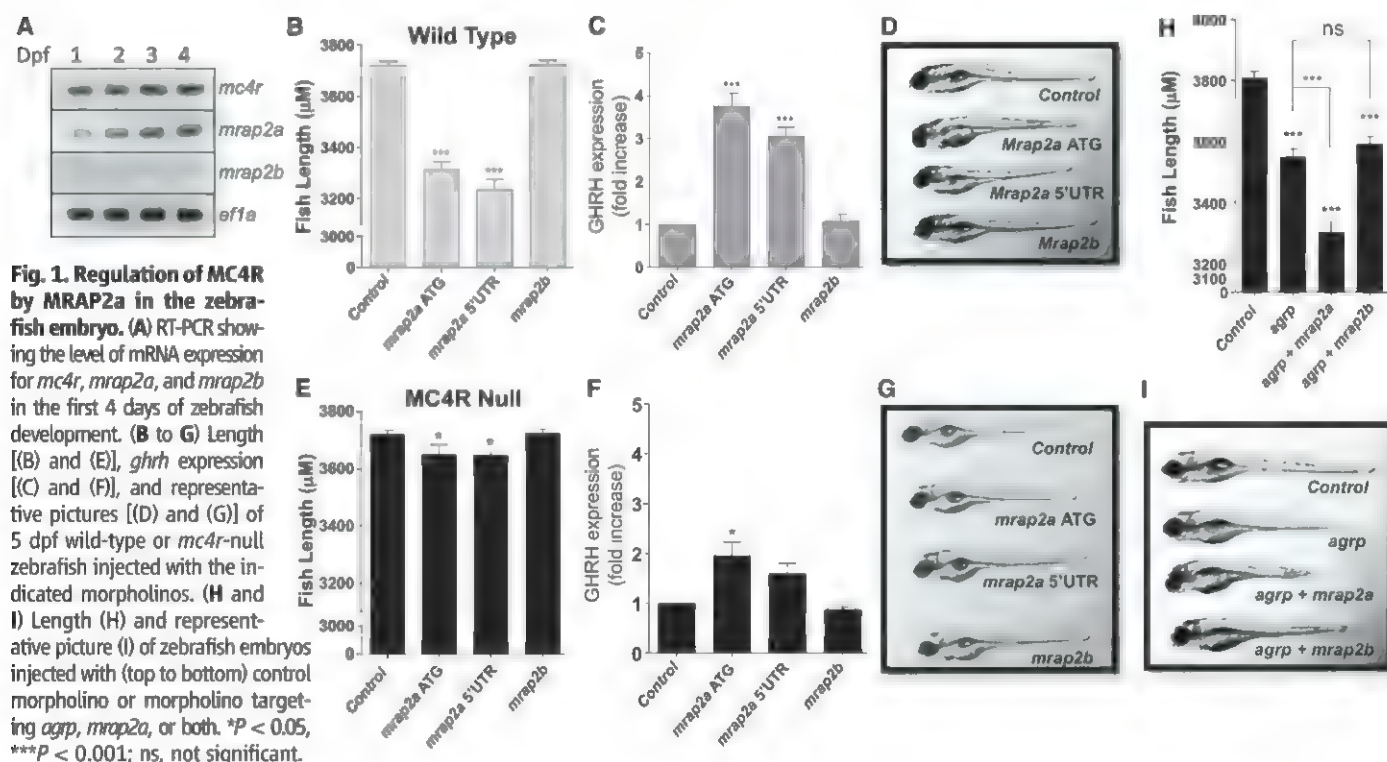
pressed, whereas no *mrp2b*-specific staining was detected (fig. S1).

To determine whether MRAP2a was modulating MC4R in vivo, we knocked down *mrp2a* expression by using two distinct antisense morpholino oligonucleotides targeting two different sites of the *mrp2a* transcript. Relative to fish injected with a nontargeting morpholino, embryos injected with either of the *mrp2a* morpholinos showed a significant decrease in linear growth [11% with the morpholino targeting the start of the coding sequence, ATG, and 13% with the morpholino targeting the 5' untranslated region (5'UTR)] (Fig. 1, B and D) and a factor of 3 to 4 increase in *ghrh* expression (Fig. 1C), consistent with an increase in MC4R activity. In

contrast, when the same experiment was conducted in *mc4r*-null fish, only a small decrease in linear growth and small increase in *ghrh* were observed (Fig. 1, E to G). The specificity of the morpholinos was demonstrated by inhibition of a green fluorescent protein reporter plasmid containing the target sequence, and by the rescue of both length and *ghrh* expression phenotype by co-injection of *mrp2a* mRNA lacking the morpholino target sequences (fig. S2, A to C). Overall, these results indicate that MRAP2a suppresses MC4R signaling in the larval zebrafish. The use of morpholinos to down-regulate *mrp2b* did not have any impact on the size of the zebrafish or *ghrh* expression, regardless of genotype (Fig. 1); this result was

expected because *mrp2b* is not expressed in the embryo.

We previously reported that MC4R is constitutively inhibited by high levels of agouti-related protein (AgRP), the endogenous MC4R inverse agonist, in the zebrafish embryo (6). To determine whether both AgRP and MRAP2a contribute to the silencing of MC4R, we injected wild-type zebrafish zygotes with control morpholinos or morpholinos targeting *agrp* alone, *agrp* and *mrp2a*, or *agrp* and *mrp2b*. As previously reported, *agrp* morpholino caused a measurable decrease (7%) in fish growth by increasing MC4R activity, as measured at 5 dpf (6). When co-injected, *agrp* and *mrp2a* morpholinos caused a more profound impairment of growth (13%) than *agrp* morpholino



petition binding assay in HEK293T cells transfected with *mc4r* without or with *mrp2a* at *mc4r*/*mrp2a* ratios of 1:1 or 1:6. (D) Concentration-response curves of  $\alpha$ -MSH-induced cAMP production in HEK293T cells expressing the CRE-luciferase reporter, *mc4r*, and different amounts of *mrp2a*. \*\*\* $P < 0.001$ .

petition binding assay in HEK293T cells transfected with *mc4r* without or with *mrp2a* at *mc4r*/*mrp2a* ratios of 1:1 or 1:6. (D) Concentration-response curves of  $\alpha$ -MSH-induced cAMP production in HEK293T cells expressing the CRE-luciferase reporter, *mc4r*, and different amounts of *mrp2a*. \*\*\* $P < 0.001$ .



alone (Fig. 1, H and I), which suggests that AGRP and MRAP2a both participate in keeping MC4R inactive in the zebrafish embryo. Co-injection of *agrp* and *mrp2b* morpholinos had the same effect as *agrp* alone.

We next investigated the mechanism by which MRAP2a regulates MC4R. Surface expression of MC4R at the plasma membrane of transfected HEK293T cells was not changed by MRAP2a expression (Fig. 2A). However, because the number of receptors at the plasma membrane may not reflect the number of receptors that are competent to bind ligand and signal, we measured the effect of MRAP2a on the density of high-affinity binding sites for the MC4R agonist NDP- $\alpha$ -MSH. MRAP2a caused up to an 80% decrease in europium-labeled NDP- $\alpha$ -MSH binding to MC4R (Fig. 2B). MRAP2a did not significantly change the affinity of MC4R for  $\alpha$ -MSH, as measured in a competition binding assay (median inhibitory concentration  $IC_{50} = 45 \pm 15$  nM) (Fig. 2C). These results suggest that MRAP2a reduces ligand binding by decreasing the number of binding sites but not by altering affinity. Both constitutive activity and  $\alpha$ -MSH-inducible activity were suppressed in parallel by increasing expression of MRAP2a (Fig. 2D), which suggests that MRAP2a stabilizes an inactive conformation of MC4R. We performed a coimmunoprecipitation assay and found that MC4R and MRAP2a are part of the same complex; a large fraction of the receptor copurified with MRAP2a (fig. S3A), and conversely, a large fraction of MRAP2a coprecipitated with MC4R (fig. S3B).

As mentioned previously, the zebrafish has two *mrp2* genes, *mrp2a* and *mrp2b*. As shown above, *mrp2b* expression was barely detectable in the embryo (Fig. 1A). To determine whether its expression increased later in the life of the zebrafish, we harvested RNA from the brain of adult fish and measured the expression of *mc4r*, *mrp2a*, and *mrp2b*, using RT-PCR and quantitative PCR (qPCR). The expression of all three genes increased in the adult brain relative to embryos (Fig. 3, A and B). Most notably, the expression of *mrp2b* increased in the adult by a factor of 10, raising the possibility that MRAP2b regulates MC4R function in the adult fish.

MRAP2 expression in the mouse is also not seen during embryogenesis and appears only after birth, reaching maximal levels close to the time of weaning, at day 18 (Fig. 3C). This suggests a conservation of the expression kinetics for the mouse MRAP2 and teleost MRAP2b proteins. In contrast to MRAP2a, which had no effect on the trafficking of MC4R, MRAP2b caused a modest increase in MC4R surface expression in transfected HEK293T cells (Fig. 3D). MRAP2b also caused a dose-dependent increase in maximal binding, probably due to the increased number of MC4 receptors at the cell surface; however, MRAP2b did not change the affinity of MC4R for  $\alpha$ -MSH ( $IC_{50} = 50 \pm 15$  nM) (Fig. 3E).

Remarkably, MRAP2b suppressed the constitutive activity of MC4R by 93% and shifted the

dose-response curve for agonist, increasing  $\alpha$ -MSH potency by a factor of 17 (MC4R alone, median effective concentration  $EC_{50} = 140 \pm 60$  nM; MC4R + MRAP2b,  $EC_{50} = 8.3 \pm 1.7$  nM). MRAP2b also amplified the maximal cAMP response to  $\alpha$ -MSH stimulation, from a factor of 1.5 in its absence to a factor of 17.5 in its presence. The mouse MRAP2 replicated all of the signaling effects caused by MRAP2b on the zebrafish MC4R (Fig. 3F), thereby confirming that MRAP2b is the homologous isoform to the mammalian MRAP2. After expression in HEK293T cells, a coimmunoprecipitation assay showed that MC4R copurified with MRAP2b (fig. S4A) and that MRAP2b copurified with MC4R (fig. S4B), which suggests that those proteins are in the same complex.

For MRAP2a or MRAP2b to have direct effects on the pharmacology and physiology of MC4R in vivo, they must be expressed in the same cells. We used in situ hybridization to localize *mc4r* and *mrp2* mRNAs in adult zebrafish brain slices. *mc4r* and *mrp2a* were largely colocalized, as were *mc4r* and *mrp2b* (fig. S5). This result supports the concept that the diverse effects of MRAP2s on MC4R signaling observed in vitro are relevant in vivo and may play a major role in energy homeostasis.

The broad tissue expression of MRAP2 proteins in vertebrates, and our observation that *mrp2a* blockade continues to have a small effect in *mc4r*

mutant fish, together suggest that the MRAP2 proteins regulate multiple GPCRs. Nonetheless, the MRAP2-GPCR interaction appears highly selective. MRAP2a and MRAP2b did not modify zebrafish MC3R signaling (fig. S7A), and mouse MRAP2 had no effect on the function of the mouse corticotropin-releasing hormone 1 and 2 receptors or the mouse neuropeptide Y2 and Y5 receptors (fig. S7, B to E). A small change in efficacy was observed in the presence of MRAP2 at the mouse glucagon-like peptide-1 receptor and  $\beta_2$ -adrenergic receptor (fig. S7, F and G).

Our findings reveal a new level of complexity in the regulation of MC4R signaling by uncovering the ability of MRAP2 proteins to modify the pharmacology and physiology of MC4R in zebrafish. The zebrafish MC4R displays an atypical signaling profile with very high constitutive activity and a modest cyclic adenosine monophosphate (cAMP) response to its agonist  $\alpha$ -MSH. In the embryo, the MC4R inverse agonist AgRP is expressed at a high level (6). We show here that *mrp2a* is also expressed in the embryo and inhibits MC4R signaling. AgRP and MRAP2a collaborate to stabilize MC4R in an inactive state, inhibiting both constitutive activity and ligand-induced signaling, and thus maximizing growth during the larval period.

*mrp2b* is expressed at high levels only in adult fish, where it could act to reduce the constitutive activity of MC4R and simultaneously

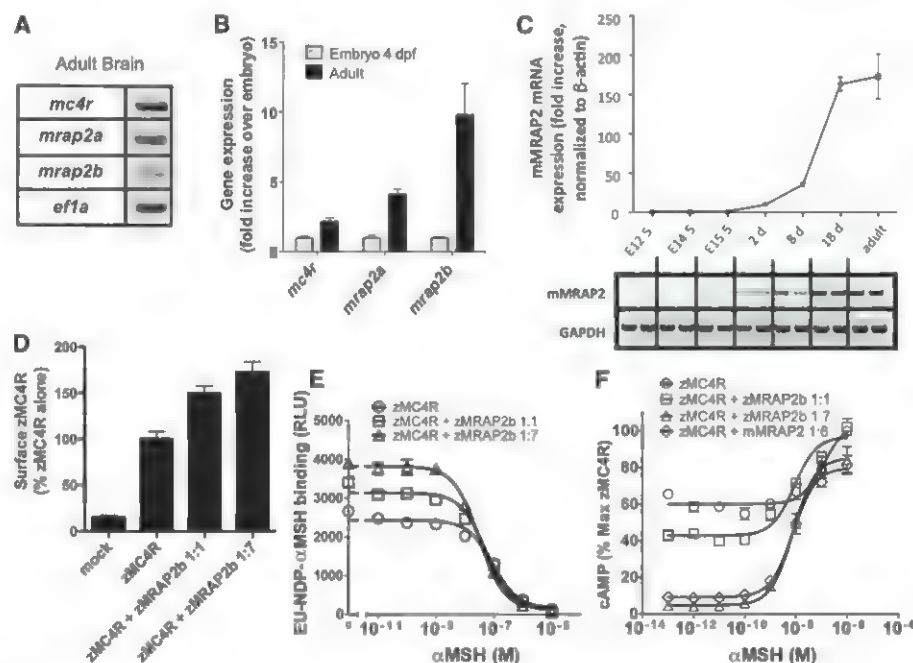


**Fig. 3. Regulation of MC4R by MRAP2b.** (A) RT-PCR depicting the expression of *mc4r*, *mrp2a*, *mrp2b*, and the housekeeping gene *ef1a* in zebrafish adult brain. (B) qPCR measuring the change in expression of *mc4r*, *mrp2a*, and *mrp2b* in the adult brain relative to the 4 dpf embryo. (C) qPCR (top) and RT-PCR (bottom) depicting the expression of mouse MRAP2 at different embryonic and postnatal stages; E, embryonic day. (D) Surface expression of MC4R measured by whole-cell ELISA in nonpermeabilized HEK293T cells transfected with *mc4r* and different amounts of *mrp2b*. (E) Competition binding assay in HEK293T cells transfected with *mc4r* alone or with *mrp2b* at the indicated ratio. (F) Concentration-response curves of  $\alpha$ -MSH-induced cAMP production in HEK293T cells transfected with *mc4r* and the indicated amount of *mrp2b* or mouse MRAP2. \*\*\* $P < 0.001$ .

sensitizes the receptor to agonist. In this manner, MRAP2b would convert the adult zebrafish MC4R from a constitutively active to a ligand-dependent receptor. Additionally, *mrp2b* expression kinetics matches that of the mouse MRAP2 and is functionally homologous. MRAP2a and MRAP2b proteins share a strong homology with each other and with mammalian MRAP2 in most of the N-terminal region and the transmembrane domain, whereas the N-terminal 15 amino acids and C terminus of these proteins are vastly divergent (fig. S6). Interestingly, the N-terminal and transmembrane domain of MRAP1 are sufficient for full activity of the mammalian MC2R (15). The first 15 amino acids of MRAP2a and MRAP2b could thus represent an important regulatory region of MRAP2s, possibly responsible for the differential regulation of MC4R.

During zebrafish embryonic development, all the energy consumed is obtained from the yolk sac. Our findings suggest that the embryo benefits from having MC4R locked in an inactive state by the joint actions of AgRP and MRAP2a. Activation of MC4R at this stage would slow the rapid maturation to the mobile free-feeding juvenile stage reached at 5 dpf. Upon maturation and depletion of the yolk sac, the zebrafish must regulate nutrient intake. Appropriate behavioral response to diurnal, seasonal, and other inputs requires a functional adipostat and energy balance sensor. This

switch is aided by MRAP2b, which forms a complex with MC4R and renders it highly sensitive to  $\alpha$ -MSH.

MRAP2 introduces a previously unappreciated level of complexity in the control of MC4R, with developmentally regulated paralogs in the fish that can either inhibit (MRAP2a) or stimulate (MRAP2b) ligand-mediated receptor activation (fig. S8). A component of this complexity is retained in mammals: Asai *et al.* (16) show that, like MRAP2b, mouse MRAP2 expression is activated proximal to weaning and increases the responsiveness of MC4R to  $\alpha$ -MSH. Their observation that MRAP2 deletion causes an obesity syndrome in the mouse can likely be attributed, in part, to reduced function of MC4R (16). However, given the ubiquitous expression of MRAP2 proteins, we hypothesize that these proteins also modulate the activity of GPCRs and perhaps other membrane proteins as well.

#### References and Notes

1. I. S. Farooqi *et al.*, *N. Engl. J. Med.* **348**, 1085–1095 (2003).
2. D. Huszar *et al.*, *Cell* **88**, 131–141 (1997).
3. C. Vaisse, K. Clement, B. Guy-Grand, P. Froguel, *Nat. Genet.* **20**, 113–114 (1998).
4. G. S. Yeo *et al.*, *Nat. Genet.* **20**, 111–112 (1998).
5. K. P. Lampert *et al.*, *Curr. Biol.* **20**, 1729–1734 (2010).
6. C. Zhang, P. M. Forlano, R. D. Cone, *Cell Metab.* **15**, 256–264 (2012).

7. J. A. Sebag, P. M. Hinkle, *Proc. Natl. Acad. Sci. U.S.A.* **104**, 20244–20249 (2007).
8. J. A. Sebag, P. M. Hinkle, *J. Biol. Chem.* **284**, 22641–22648 (2009).
9. J. A. Sebag, P. M. Hinkle, *Sci. Signal.* **3**, ra28 (2010).
10. P. M. Hinkle *et al.*, *Eur. J. Pharmacol.* **660**, 94–102 (2011).
11. L. A. Metherell *et al.*, *Nat. Genet.* **37**, 166–170 (2005).
12. L. F. Chan *et al.*, *Proc. Natl. Acad. Sci. U.S.A.* **106**, 6146–6151 (2009).
13. S. Roy, M. Rached, N. Gallo-Payet, *Mol. Endocrinol.* **21**, 1656–1669 (2007).
14. M. J. Agulleiro *et al.*, *Mol. Cell. Endocrinol.* **320**, 145–152 (2010).
15. J. A. Sebag, P. M. Hinkle, *J. Biol. Chem.* **284**, 610–618 (2009).
16. M. Asai *et al.*, *Science* **341**, 275–278 (2013).

**Acknowledgments:** Supported by NIH grants DK075721 and DK070332 (R.D.C.), DK19974 (P.M.H.), and F23DK091055 (J.A.S.); United States–Israel Binational Agricultural Research and Development Fund (BARD) research grant 15-4489-12 (R.D.C. and C.Z.); and Vanderbilt Diabetes Research and Training Center grant DK020593 (R.D.C.). All data and methods are publicly available in the supplementary materials.

#### Supplementary Materials

[www.sciencemag.org/cgi/content/full/341/6143/278/DC1](http://www.sciencemag.org/cgi/content/full/341/6143/278/DC1)  
Materials and Methods  
Figs. S1 to S8  
References (17–19)

20 November 2012; accepted 20 June 2013  
10.1126/science.1232995

## Pandoraviruses: Amoeba Viruses with Genomes Up to 2.5 Mb Reaching That of Parasitic Eukaryotes

Nadège Philippe,<sup>1,2\*</sup> Matthieu Legendre,<sup>1\*</sup> Gabriel Dautre,<sup>1</sup> Yohann Couté,<sup>3</sup> Olivier Poirot,<sup>1</sup> Magali Lescot,<sup>1</sup> Defne Arslan,<sup>1</sup> Virginie Seltzer,<sup>1</sup> Lionel Bertaux,<sup>1</sup> Christophe Bruley,<sup>3</sup> Jérôme Garin,<sup>3</sup> Jean-Michel Claverie,<sup>1†</sup> Chantal Abergel<sup>1†</sup>

Ten years ago, the discovery of Mimivirus, a virus infecting *Acanthamoeba*, initiated a reappraisal of the upper limits of the viral world, both in terms of particle size (>0.7 micrometers) and genome complexity (>1000 genes), dimensions typical of parasitic bacteria. The diversity of these giant viruses (the Megaviridae) was assessed by sampling a variety of aquatic environments and their associated sediments worldwide. We report the isolation of two giant viruses, one off the coast of central Chile, the other from a freshwater pond near Melbourne (Australia), without morphological or genomic resemblance to any previously defined virus families. Their micrometer-sized ovoid particles contain DNA genomes of at least 2.5 and 1.9 megabases, respectively. These viruses are the first members of the proposed “Pandoravirus” genus, a term reflecting their lack of similarity with previously described microorganisms and the surprises expected from their future study.

The serendipitous discovery of the first giant DNA virus Mimivirus (1, 2), initially misinterpreted as a Gram-positive parasitic bacterium, challenged criteria and protocols historically established to separate viruses from cellular organisms (3–5). It was then realized that virus particles could be large enough to be visible under light microscope and contain DNA genomes larger in size (>1 Mb) and gene contents

(>1000) than those of bacteria. In the past decade, several Mimivirus relatives have been fully characterized, including the largest known viral genome of *Megavirus chilensis* (1.259 Mb encoding 1120 proteins) (6–8). The study of this new family of viruses (referred to as “Megaviridae”) revealed distinctive features concerning the virion structure and core delivery mechanism (9, 10), transcription signaling (11–13), and protein trans-

lation (14, 15). In particular, seven virus-encoded amino acid–transfer RNA (tRNA) ligases (8) and other enzymes thought to be the hallmark of cellular organisms were found in these viruses (16, 17). Their study also led to the discovery of “virophages” that replicate within the virion factory of the Megaviridae (18–20).

After our discovery of *M. chilensis* with laboratory-grown *Acanthamoeba* for amplification, we searched for new giant viruses in sediments where *Acanthamoeba* are more prevalent than in the water column (21, 22). We identified samples demonstrating strong cellular lytic activity. Some of these cocultures revealed the intracellular multiplication of particles larger than that of the previously isolated Megaviridae, albeit without their icosahedral appearance. As the multiplication of these particles was found to be insensitive to antibiotics, they were retained for further investigation.

Parasite 1 originated from the superficial marine sediment layer (~10 m deep) taken at the mouth of the Tunquen river (coast of central

<sup>1</sup>Structural and Genomic Information Laboratory, UMR 7256 CNRS Aix-Marseille Université, 163 Avenue de Luminy, Case 934, 13288 Marseille cedex 9, France. <sup>2</sup>Laboratory of Molecular Biophysics, Department of Cell and Molecular Biology, Uppsala University, Husargatan 3 (Box 596), SE-751 24 Uppsala, Sweden. <sup>3</sup>CEA, IRTSV, Biologie à Grande Echelle, INSERM, U1038, Université Joseph Fourier Grenoble 1, F-38054 Grenoble, France.

\*These authors contributed equally to this work.  
†Corresponding author. E-mail: [chantal.abergel@igs.cnrs-mrs.fr](mailto:chantal.abergel@igs.cnrs-mrs.fr) (C.A.); [jean-michel.claverie@univ-amu.fr](mailto:jean-michel.claverie@univ-amu.fr) (J.-M.C.)



Chile). Parasite 2 originated from mud taken at the bottom of a shallow freshwater pond near Melbourne, Australia. After amplification on *Acanthamoeba* cultures, both parasites became observable by optical microscopy as a lawn of ovoid particles 1  $\mu\text{m}$  in length and 0.5  $\mu\text{m}$  in diameter (Fig. 1A). Observations by transmission electron microscopy revealed characteristic ultrastructural features (Fig. 1) common to both parasites. Despite their identical appearance, the micro-organisms showed different global protein contents when profiled by electrophoresis (Fig. 1C). Anticipating the demonstration of their viral nature, parasites 1 and 2 will henceforth be referred to as *Pandoravirus salinus* and *Pandoravirus dulcis*.

To distinguish whether the parasites were cellular or viral in nature, we imaged their propagation in axenic *Acanthamoeba* cultures over an entire multiplication cycle, starting from purified particles. The replication cycle of *Pandoravirus* in *Acanthamoeba castellanii* lasts from 10 to 15 hours and is initiated by the internalization of individual particles via phagocytic vacuoles. The particles then empty the content of their internal compartment into the *Acanthamoeba* cytoplasm through their apical pore. The internal lipid membrane delimiting the particle core fuses with the vacuole membrane (Fig. 1, D and E), creating a channel through which the particle proteins and DNA content can be delivered, a process reminiscent of the one used by Mimivirus (19). This fusion process leads to a bona fide “eclipse” phase whereby the content of the particle becomes invisible once delivered into the cytoplasm. Two to 4 hours later, the host nucleus undergoes major reorganization initiated by the loss of its spherical appearance. Whereas the electron-dense nu-

cleolus becomes paler and progressively vanishes, the nuclear membrane develops multiple invaginations, resulting in the formation of numerous vesicles (fig. S1). Peroxisome-like crystalline structures appear at the periphery of the deliquescent nucleus and progressively vanish during the particles’ maturation process (fig. S1). Eight to 10 hours after infection, the cells become rounded and lose their adherence, and new particles appear at the periphery of the region formerly occupied by the nucleus (Fig. 1F and fig. S1). Unlike eukaryotic DNA viruses and phages, which first synthesize and then fill their capsids, the tegument and internal compartment of the *Pandoravirus* particles are synthesized simultaneously, in a manner suggestive of knitting, until the particles are fully formed and closed. Curiously, particle synthesis is initiated and proceeds from the ostiole-like apex (Fig. 2). No image suggestive of division (binary fission) was obtained during ultrastructural study of particle multiplication in *A. castellanii*. The replicative cycle ends when the cells lyse to release about a hundred particles. The replication cycles of *P. salinus* and *P. dulcis* exhibit the same stages and characteristics.

We sequenced the genome of both parasites, starting from DNA prepared from purified particles. For *P. salinus*, a 2,473,870-base pair (bp) sequence was assembled as a single contig through a combination of Illumina, 454-Roche, and PacBio approaches. The sequence coverage (11,164, 67, and 41 for the above platforms, respectively) was quite uniform, except for 50 kb at the 3’ extremity of the contig where it was 10 times as high, hinting at the presence of unresolved terminal repeats. Using a combination of polymerase chain reaction (PCR) primers targeting sequences expected to arise from tandem or head-to-tail repetitions, we

found evidence of at least six additional tandem terminal copies, raising the lowest estimate of the *P. salinus* total genome size to 2.77 Mb. The same approach was used to sequence the *P. dulcis* genome. The combination of the Illumina, 454-Roche, and PacBio data sets resulted in the assembly of a 1,908,524-bp sequence with an average coverage of 3,112, 62, and 133, respectively. Again, a higher coverage over 20 kb at the 3’ end of this contig hinted at the presence of two tandem terminal repeats. At strong variance with the previously sequenced *Acanthamoeba* giant viruses and most intracellular bacteria, the two *Pandoravirus* genomes are GC-rich ( $G + C = 61.7$  and  $63.7\%$  for *P. salinus* and *P. dulcis*, respectively), with a noticeable difference between the predicted protein-coding and noncoding regions ( $64\%$  versus  $54\%$  for *P. salinus*). Such a high GC content remains below the extreme values reached by herpesviruses ( $G + C > 70\%$ ) (23). At a packing density typical of bacterial nucleoid ( $0.05$  to  $0.1$  bp/nm<sup>3</sup>), a 2.8-Mb DNA molecule would easily fit into the volume ( $\approx 75 \times 10^6$  nm<sup>3</sup>) of the ovoid *P. salinus* particle.

We identified 2556 putative protein-coding sequences (CDSs) in the *P. salinus* 2.47-Mb unique genome sequence (considering a single terminal repeat) and 1502 for the *P. dulcis* 1.91-Mb genome. The alignment of the two genomes with Nucmer (24) showed a quasiperfect colinearity, solely interrupted by the presence of four large genomic segments specific to *P. salinus* (fig. S2). These additional segments mostly account for the size difference between the two genomes, indicating that the global gene content of *P. dulcis* is merely a subset of that of *P. salinus*. We thus focused our detailed analysis on the *P. salinus* genomic sequence.

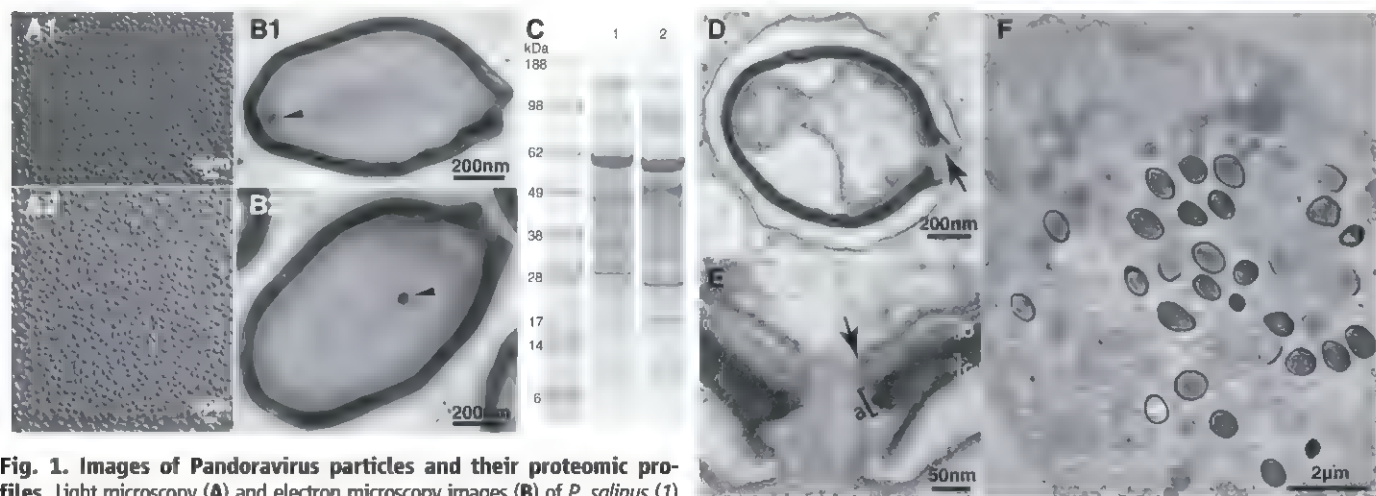


**Fig. 1. Images of *Pandoravirus* particles and their proteomic profiles.** Light microscopy (A) and electron microscopy images (B) of *P. salinus* (1) and *P. dulcis* (2) purified particles. (C) Electrophoresis profiles of *P. salinus* (lane 1) and *P. dulcis* (lane 2) extracted proteins. (D) Internalized *P. salinus* particle in the host vacuole. Once fused with the vacuole membrane (arrow), the virion internal membrane creates a continuum with the host cytoplasm. The particles are wrapped into a  $\sim 70$ -nm-thick tegument-like envelope consisting of three layers. (E) Magnified image of the opened ostiole-like apex: from the inside out, a layer of light density of unknown composition ( $\sim 20$  nm, marked “a”), a dark layer comprising a dense mesh of fibrils ( $\sim 25$  nm, marked

“b”), and an external layer of medium density ( $\sim 25$  nm, marked “c”). This tegument-like envelope is interrupted by the ostiole-like pore measuring  $\sim 70$  nm in diameter. Inside the particle, the lipid membrane encloses a diffuse interior devoid of visible substructure, except for a spherical area of electron-dense material (50 nm in diameter, arrowhead) seen episodically but in a reproducible fashion. (F) Ultrathin section of an *Acanthamoeba* cell filled with *P. salinus* at various stages of maturation.

The 2556 *P. salinus* predicted proteins ranged from 26 to 2367 residues [with 2364 CDSs longer than 150 nucleotides (nt)], with an average of 258 residues. The distance between consecutive CDSs was short (233 nt on average), resulting in a coding density of 80% (Fig. 3). A gene density of one protein-coding gene per kilobase is typical of both prokaryotic organisms and large double-stranded DNA (dsDNA) viruses. A comprehensive search of the National Center for Biotechnology Information nonredundant database (NR) (25) for homologs to the 2556 CDSs returned only 401 significant matches (E-value  $\leq 10^{-5}$ ) (15.7%) (fig. S3), of which 215 (53.6%) primarily resulted from the sole presence of uninformative ankyrin, MORN, and F-box motifs. The large number of open reading frames (ORFs) containing these repeats is accounted for by few families of paralogs, most likely generated by local gene duplications. The largest duplications “hot spots” coincide with four regions of the *P. salinus* genome with no equivalent in the *P. dulcis* genome (fig. S2). We used the ankyrin, MORN, and F-box signatures (26) to mask *P. salinus* predicted protein sequences, reducing to 186 (7%) the CDSs significantly similar to NR entries (table S1). Their best matches were distributed between eukaryotes ( $n = 101$ ), bacteria ( $n = 43$ ), and viruses ( $n = 42$ ) (fig. S3). The phylogenetic distribution of these matches, together with their low similarity levels (38% of identical residues across the best matching segment on average), indicates that no microorganism closely related to *P. salinus* has ever been sequenced. A similar result was obtained in comparisons against the environmental database (env\_nr, 25), with only eight unique significant matches out of 341 (333 matching in NR). Only 17 *P. salinus* CDSs have their closest homolog (34% identical residues in average) within the Megaviridae, indicating that *P. salinus* has no particular phylogenetic affinity with the clade grouping the other known Acanthamoeba-infecting

viruses. Similarly, only 92 (50 after masking) *P. salinus* CDSs (3.6% of the predicted CDSs) have an Amoebozoa protein as their closest homolog, indicating that lateral gene transfers between *P. salinus* and its host rarely occur. The high percentage (93%) of CDSs without recognizable homolog (ORFans), the alien morphological features displayed by *P. salinus*, and its atypical replication process raised the concern that the translation of its genes into proteins might not obey the standard genetic code, hence obscuring potential sequence similarities. This concern was addressed by Nano-liquid chromatography–tandem mass spectrometry (LC-MS/MS) proteomic analysis of purified *P. salinus* particles.

The ion-mass data were interpreted in reference to a database that includes the *A. castellanii* (27) and the *P. salinus* predicted protein sequences. A total of 266 proteins were identified on the basis of at least two different peptides. Fifty-six of them corresponded to *A. castellanii* proteins presumably associated with the *P. salinus* particles, and 210 corresponded to predicted *P. salinus* CDSs. These identifications demonstrate that *P. salinus* uses the standard genetic code, legitimizing our gene predictions. Furthermore, of the 210 *P. salinus*-encoded proteins detected in its particle, only 42 (20%) exhibit a homolog in NR (table S2) (BlastP, E-value  $< 10^{-5}$ ), while the rest (80%) do not. The proportion of NR-matching sequences is thus similar among experimentally validated proteins and the theoretical proteome (Fisher's exact test,  $P > 0.07$ ). This result validates the unprecedented proportion of ORFans in the *P. salinus* genome and confirms its large evolutionary distance from known microorganisms. Finally, 195 (93%) of the proteins identified in the *P. salinus* particles have a homolog encoded in the *P. dulcis* genome, predicting that the composition of the two virions is globally similar, even though variations in their protein sequences produce different proteomic profiles (Fig. 1C).

The functional annotation of *P. salinus*-predicted proteins was complemented by motif searches (26) and three-dimensional-fold recognition programs (28). The failure to detect components of the basic cellular functions—i.e., protein translation, adenosine 5'-triphosphate generation, and binary fission (3, 5)—confirmed the viral nature of Pandoraviruses. *P. salinus* possesses none of the ribosome components (RNAs and proteins) and no enzyme from the glycolysis pathway or the Krebs cycle. Our search was similarly unsuccessful for homologs of cell division-related proteins such as FtsZ (29), tubulin (30), or components of the alternative ESCRT system (31). *P. salinus* thus lacks most of the hallmark components of cellular organisms, including those retained in the most reduced intracellular parasites (5).

Nonetheless, the *P. salinus* genome exhibited 14 of the 31 genes most consistently present in large dsDNA viruses [i.e., “core” genes (32)] (table S3). We identified three of the nine most conserved (type I) core genes (including a DNA polymerase and four copies of virion packaging adenosine triphosphatase). We also identified four out of the eight type II (lesser conserved) core genes (including the two subunits of the ribonucleotide reductase) and 7 of the 14 type III core genes (including an mRNA-capping enzyme and three subunits of the DNA-dependent RNA polymerase). Yet, *P. salinus* lacks several core genes that encode components essential to DNA replication such as DNA ligases, topoisomerases, and the DNA sliding clamp (Proliferating Cell Nuclear Antigen). This already suggests that, in contrast to the largest known viruses, replication of Pandoraviruses requires host functions normally segregated in the nucleus. Another notable absence is that of a gene encoding a major capsid protein, a hallmark of all large eukaryotic dsDNA viruses, except for the Poxviruses which, like *P. salinus* and *P. dulcis*, lack icosahedral symmetry. Nor does *P. salinus* possess a homolog

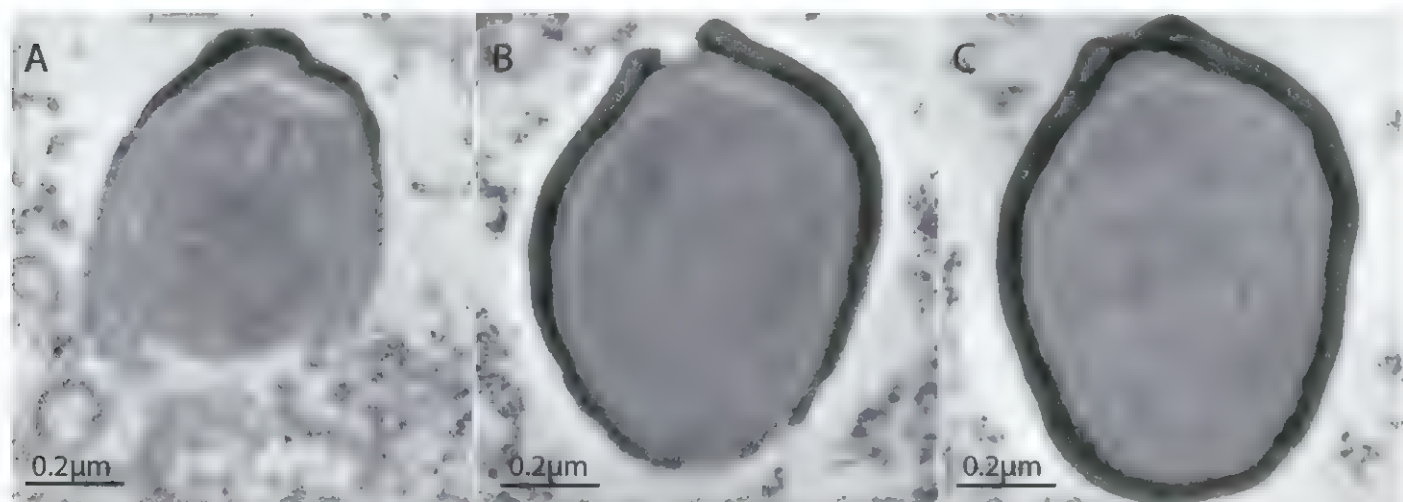


**Fig. 2. Electron microscopy images of ultrathin sections of *P. salinus*.** (A to C) Three stages of maturation are presented, illustrating the progressive knitting together of the particles starting from the apex and ending up as mature virions fully encased in their tegument-like envelope.



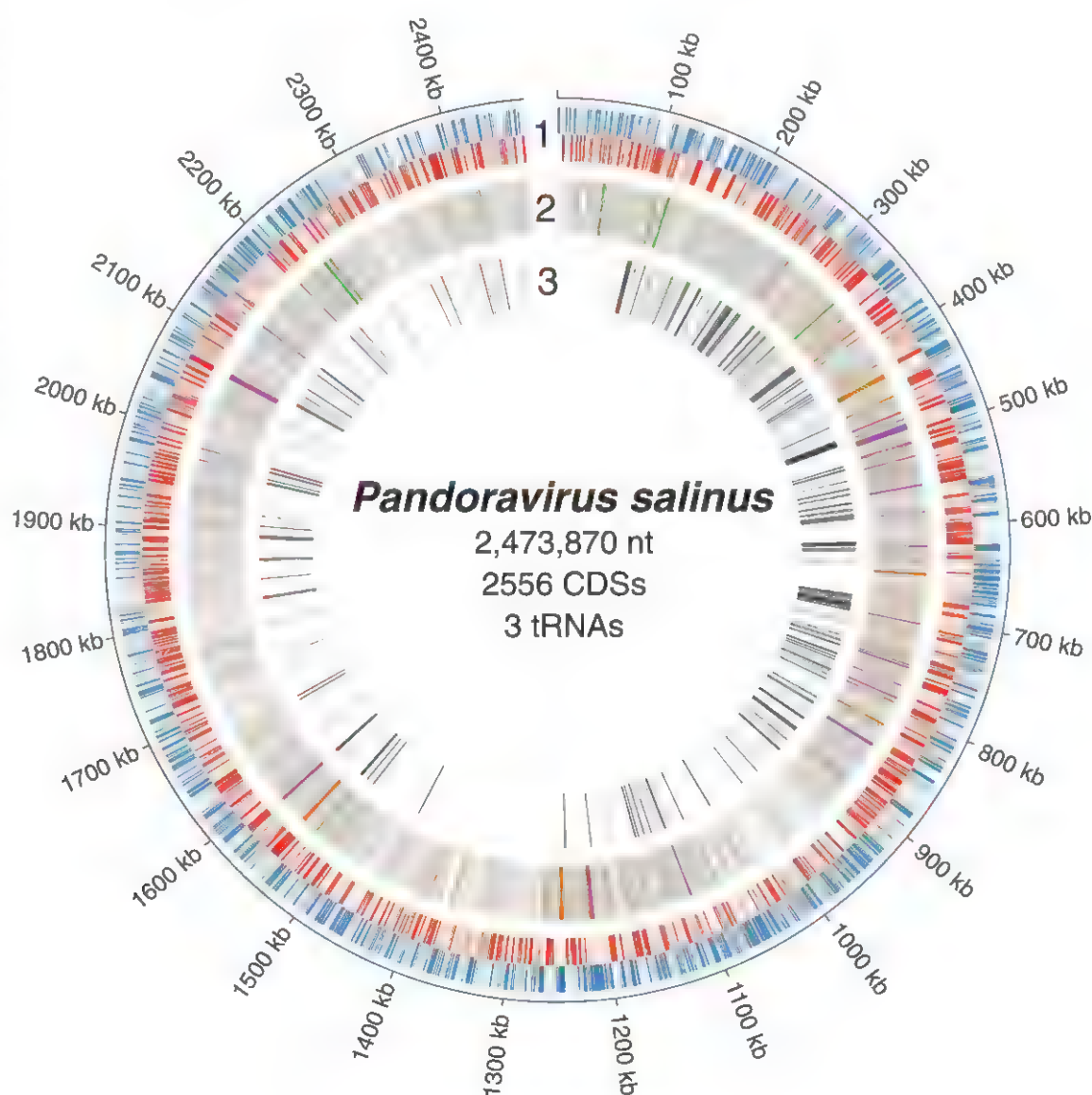
of the vaccinia scaffolding protein D13, which is structurally similar to the double-barreled capsid protein found in icosahedral dsDNA viruses (33).

Despite lacking several of the large dsDNA virus core genes (table S3), *P. salinus* remains typically virus-like by possessing a large fraction of enzymes involved in DNA processing (including replication, transcription, repair, and nucleotide synthesis) (table S1). Its 54 DNA-processing proteins include three enzymes that have no known homolog in viruses: a *p*-aminobenzoic acid synthase, a dihydroneopterin aldolase, and a hydroxymethylpterin-pyrophosphokinase (HPPK). Transcription is represented by four RNA polymerase subunits, two copies of VLTF3-like gene transcription factors, an SII-like transcription elongation factor, and a DEAD-like helicase. Besides DNA-processing proteins, we identified 82 proteins involved in miscellaneous cellular functions, none of which related to a specific feature of the Pandoravirus replication cycle. We identified several components of the ubiquitin-dependent pro-

tein degradation pathway, and various hydrolases and proteases, kinases, and phosphatases, likely to interfere with the host metabolism, as well as four fascin-domain-containing proteins potentially involved in the formation of intracytoplasmic substructures. We also identified two amino acid-tRNA ligases, one for tyrosine (TyrRS) and the other for tryptophan (TrpRS). Before this study, the presence of virally encoded amino acid-tRNA ligases was a hallmark of the Megaviridae (6–8) and their closest known relative *Cafeteria roenbergensis* virus (CroV) (34). However, the TyrRS and TrpRS encoded by the Pandoraviruses are much closer to their *Acanthamoeba* homologs (57 and 58% identity, respectively) than to their Megaviridae counterparts, arguing against a common viral ancestry for these genes (fig. S4). *P. salinus* also possesses few other translation-related genes: a eIF4E translation initiation factor, a SUA5-like tRNA modification enzyme, and three tRNAs (tRNA<sup>Pro</sup>, tRNA<sup>Met</sup>, and tRNA<sup>Trp</sup>).

Consistent with the subcellular location of their replication, the cytoplasmic large DNA viruses (e.g., Megaviridae, Poxviridae, and Iridoviridae) lack spliceosomal introns. Even the nucleus-dependent Chloroviruses (e.g., PBCV-1) have only few small introns (35). Unexpectedly, 16 of the 186 (~9%) *P. salinus* CDSs with database homologs contain one or more introns (table S4). These introns are 138 nt long on average, bear no resemblance with group I or group II self-splicing introns and, once validated by reverse transcriptase-PCR, were found to be precisely delineated by a 5'-GT and 3'-AG dinucleotide. These spliceosomal introns are most likely excised from the *P. salinus* transcripts by the cellular U2-dependent splicing machinery, which strongly suggests that at least part of the *P. salinus* genome is transcribed within the host nucleus. Fourteen out of the 39 identified introns (36%) remained in frame with the flanking coding regions and exhibited a similar GC content, making their computational detection impossible for ORFs

**Fig. 3. Structure of the *P. salinus* genome.** Specific features are marked on concentric circles using Circos (43) as follows: 1, CDSs positions on the direct (blue) and reverse (red) strands. 2, CDSs with a best match within eukaryotes (in orange), bacteria (in green), and viruses (in purple). CDSs with MORN repeats, ankyrin repeats, and F-box domain motifs are shown in white; CDSs with no match are shown in gray. 3, CDSs identified in the proteome of purified *P. salinus* particles.



without database homologs. The introns that were not in frame exhibited a GC content 10% lower than that of their flanking exons. A comprehensive transcriptome analysis will be required to identify all the intron-containing genes potentially representing around 10% of the predicted genes, as estimated from the few that exhibit database homologs. Finally, as in other large DNA viruses (2, 8, 34), a handful of essential DNA synthesis enzymes contain inteins: one in the largest RNA polymerase subunit and the small ribonucleoside reductase (RNR) subunit, and two in the large RNR subunit and the DNA polymerase. The *P. salinus* small RNR subunit and the DNA polymerase genes are interrupted by both inteins and introns (fig. S5).

To quantitatively analyze the proteomic content of the *P. salinus* particles, we first scrutinized the most abundant proteins, searching for a candidate capsid-like protein. Two prominent proteins with molecular masses of ~60 kD were

visible (Fig. 1C). However, the most abundant of these does not resemble any known protein, whereas the second protein is similar to a conserved Megaviridae protein, albeit of unknown function (table S2). Furthermore, Pandoravirus-encoded transcription machinery was completely absent in the particle, in contrast to Mimivirus and other viruses that replicate in the cytoplasm (16). Together with the presence of spliceosomal introns, this finding confirms that the host nucleus is actively involved in the early stage of the Pandoravirus replication cycle, before decaying at a later stage. The proteomic data also confirmed four splice junction predictions (table S4). Finally, 56 low-abundance *A. castellanii* proteins were detected in the proteome of the particles (table S2). Because Pandoraviruses replicate in the host cytoplasm, but not inside a well-defined cellular substructure, these Acanthamoeba proteins may be randomly packaged into the virion as simple bystanders.

The discovery of Mimivirus, followed by the characterization over the past decade of other Megaviridae exhibiting slight increments in genome sizes, suggested that the maximum viral genome size possible was about 1.3 Mb and 1200 genes, a genetic complexity already larger than that of many parasitic bacteria. Meanwhile, the discovery of viruses with smaller genomes, but sharing several features previously thought to be specific to the Megaviridae (2, 8, 18, 36), indicated a phylogenetic continuity between the giant viruses and other dsDNA viruses (5, 8, 34). This conceptual framework is challenged by the Pandoraviruses that have genomes twice as large as, and lack any phylogenetic affinity with, previously described virus families (Fig. 4). Indeed, the Pandoravirus genome size exceeds that of parasitic eukaryotic microorganisms, such as *Encephalitozoon* species (37, 38).

Because more than 93% of Pandoraviruses genes resemble nothing known, their origin

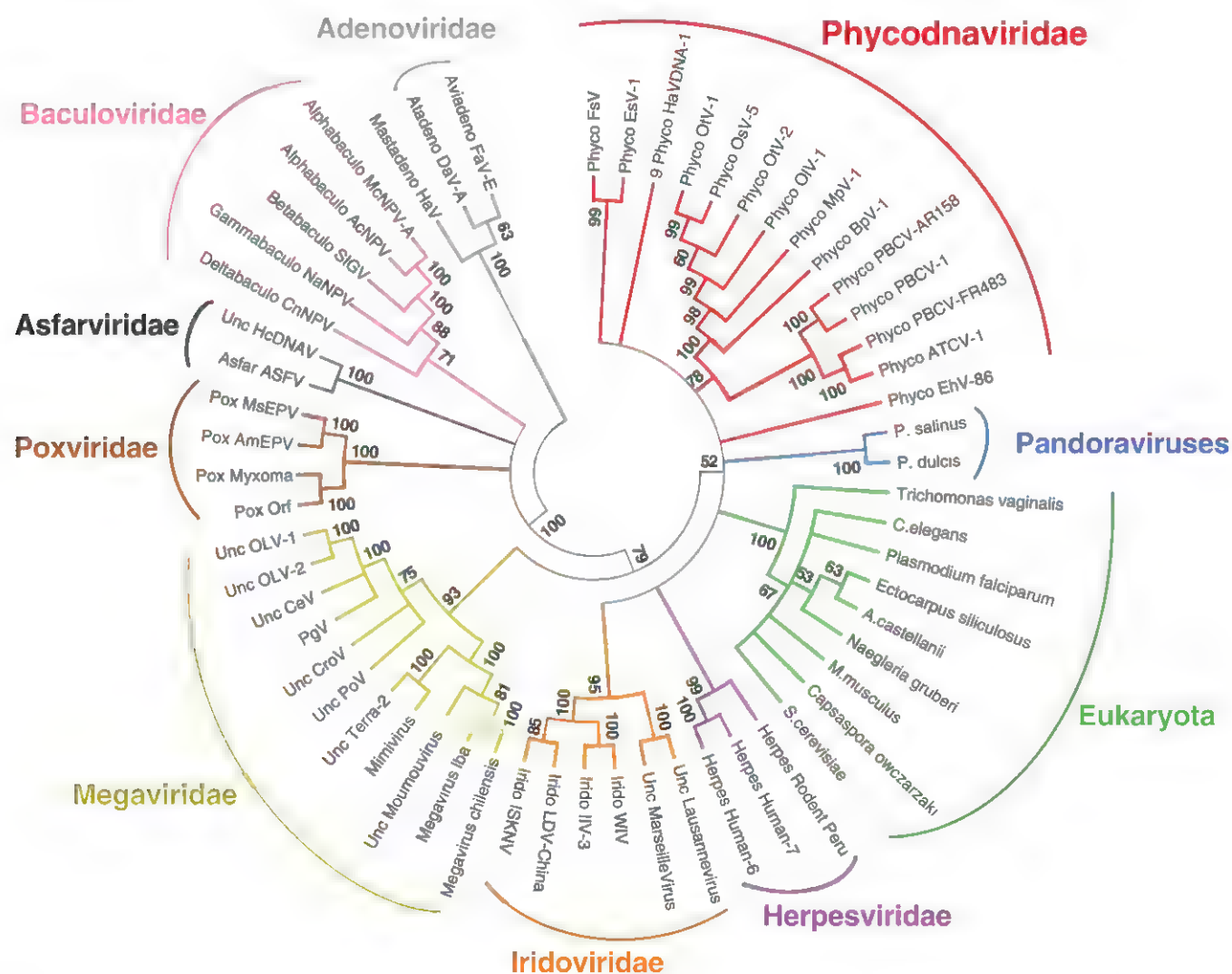


**Fig. 4. Phylogenetic analysis of the B-family DNA polymerase.** A multiple alignment of 59 viral DNA polymerase B sequences (472 ungapped positions) was computed with the default options of the MAFFT server (44). The neighbor-joining (midpoint rooted) tree was built with

the JTT substitution model. The parameter of heterogeneity among sites was estimated ( $\alpha = 1.04$ ), and 100 bootstrap resamplings were computed. The tree was collapsed for bootstrap values <50 and drawn with MEGA5 (45).



cannot be traced back to any known cellular lineage. However, their DNA polymerase does cluster with those of other giant DNA viruses, suggesting the controversial existence of a fourth domain of life (fig. S6) (1, 5, 39, 40). The absence of Pandoravirus-like sequences from the rapidly growing environmental metagenomic databases suggests either that they are rare or that their ecological niche has never been prospected. However, the screening of the literature on Acanthamoeba parasites does reveal that Pandoravirus-like particles had been observed 13 years ago (41, 42), although not interpreted as viruses. This work is a reminder that our census of the microbial diversity is far from comprehensive and that some important clues about the fundamental nature of the relationship between the viral and the cellular world might still lie within unexplored environments.

## References and Notes

- B. La Scola et al., *Science* **299**, 2033 (2003).
- D. Raoult et al., *Science* **306**, 1344–1350 (2004).
- A. Lwoff, *J. Gen. Microbiol.* **17**, 239–253 (1957).
- J.-M. Claverie, C. Abergel, *Trends Genet.* **26**, 431–437 (2010).
- J.-M. Claverie, C. Abergel, *Adv. Virus Res.* **85**, 25–56 (2013).
- P. Colson et al., *Genome Biol. Evol.* **3**, 737–742 (2011).
- N. Yoosuf et al., *Genome Biol. Evol.* **4**, 1324–1330 (2012).
- D. Arslan, M. Legendre, V. Seltzer, C. Abergel, J.-M. Claverie, *Proc. Natl. Acad. Sci. U.S.A.* **108**, 17486–17491 (2011).
- C. Xiao et al., *PLoS Biol.* **7**, e92 (2009).
- N. Zauberman et al., *PLoS Biol.* **6**, e114 (2008).
- K. Suhre, S. Audic, J.-M. Claverie, *Proc. Natl. Acad. Sci. U.S.A.* **102**, 14689–14693 (2005).
- D. Byrne et al., *Genome Res.* **19**, 1233–1242 (2009).
- M. Legendre et al., *Genome Res.* **20**, 664–674 (2010).
- C. Abergel, J. Rudinger-Thirion, R. Giegé, J.-M. Claverie, *J. Virol.* **81**, 12406–12417 (2007).
- S. Jeudy, C. Abergel, J.-M. Claverie, M. Legendre, *PLoS Genet.* **8**, e1003122 (2012).
- J.-M. Claverie, C. Abergel, H. Ogata, *Curr. Top. Microbiol. Immunol.* **328**, 89–121 (2009).
- F. Placente et al., *J. Biol. Chem.* **287**, 3009–3018 (2012).
- B. La Scola et al., *Nature* **455**, 100–104 (2008).
- J. M. Claverie, C. Abergel, *Annu. Rev. Genet.* **43**, 49–66 (2009).
- C. Desnues et al., *Proc. Natl. Acad. Sci. U.S.A.* **109**, 18078–18083 (2012).
- D. A. Månson, T. A. Paget, *J. Eukaryot. Microbiol.* **53**, S12–S14 (2006).
- H. Liu et al., *Korean J. Parasitol.* **44**, 117–125 (2006).
- A. Dolan, et al., *J. Virol.* **72**, 2010–2021 (1998).
- S. Kurtz et al., *Genome Biol.* **5**, R12 (2004).
- E. W. Sayers et al., *Nucleic Acids Res.* **40**, D13–D25 (2012).
- M. Punta et al., *Nucleic Acids Res.* **40**, D290–D301 (2012).
- M. Clarke et al., *Genome Biol.* **14**, R11 (2013).
- J. Shi, T. L. Blundell, K. Mizuguchi, *J. Mol. Biol.* **310**, 243–257 (2001).
- D. W. Adams, J. Errington, *Nat. Rev. Microbiol.* **7**, 642–653 (2009).
- M. T. Cabeen, C. Jacobs-Wagner, *Annu. Rev. Genet.* **44**, 365–392 (2010).
- R. Y. Samson, S. D. Bell, *Trends Microbiol.* **17**, 507–513 (2009).
- L. M. Iyer, L. Aravind, E. V. Koonin, *J. Virol.* **75**, 11720–11734 (2001).
- J. K. Hyun et al., *J. Virol.* **81**, 11075–11083 (2007).
- M. G. Fischer, M. J. Allen, W. H. Wilson, C. A. Suttle, *Proc. Natl. Acad. Sci. U.S.A.* **107**, 19508–19513 (2010).
- L. M. Iyer, S. Balaji, E. V. Koonin, L. Aravind, *Virus Res.* **117**, 156–184 (2006).
- H. Ogata et al., *ISME J.* **5**, 1143–1151 (2011).
- N. Corradi, J. F. Pombert, L. Farinelli, E. S. Didier, P. J. Keeling, *Nat. Commun.* **1**, 77 (2010).
- J. F. Pombert et al., *Proc. Natl. Acad. Sci. U.S.A.* **109**, 12638–12643 (2012).
- D. Moreira, P. López-García, *Nat. Rev. Microbiol.* **7**, 306–311 (2009).
- J.-M. Claverie, H. Ogata, *Nat. Rev. Microbiol.* **7**, 615, author reply 615 (2009).
- P. Scheid, B. Hauröder, R. Michel, *Parasitol. Res.* **106**, 1371–1377 (2010).
- R. Hoffmann, R. Michel, K.-D. Müller, E. N. Schmid, *Endocytobiosis Cell Res.* **12**, 185 (1998).
- M. Krzyminski et al., *Genome Res.* **19**, 1639–1645 (2009).
- K. Katoh, H. Toh, *Brief. Bioinform.* **9**, 286–298 (2008).
- K. Tamura et al., *Mol. Biol. Evol.* **28**, 2731–2739 (2011).

**Acknowledgments:** We thank S. Faugeron and R. Finke from the Estación de Investigaciones Marinas in Chile for help during the sampling expedition. We also thank J. Hajdu for invaluable support and J.-P. Chauvin and A. Aouane for expert assistance on the Institut de Biologie du Développement de Marseille Luminy imagery facility, as well as A. Bernadac and A. Kosta from the Institut de Microbiologie de la Méditerranée. We thank E. Fabre and V. Schmidt for technical assistance, and P. Bonin and R. Claverie for helpful discussions. This work was supported by Centre National de la Recherche Scientifique, Institut National de la Santé et de la Recherche Médicale, Centre de l'Energie Atomique, and Agence National pour la Recherche (ANR-BLAN08-0089, ANR-09-GENM-032-001, and ANR-10-INBS-08-01). The sampling expedition was sponsored by the ASSEMBLE grant 227799. The genome sequences of *P. salinus* and *P. dulcis* have been deposited in GenBank (accession numbers KC977471 and KC977470, respectively). The mass spectrometry proteomics data have been deposited to the ProteomeXchange Consortium (<http://proteomecentral.proteomexchange.org>) via the PRIDE partner repository with the data set identifier PXD000213 and DOI 10.6019/PXD000213.

## Supplementary Materials

[www.sciencemag.org/cgi/content/full/341/6143/281/DC1](http://www.sciencemag.org/cgi/content/full/341/6143/281/DC1)  
Materials and Methods  
Figs. S1 to S6  
Tables S1 to S5  
References (46–59)

15 April 2013; accepted 13 June 2013  
10.1126/science.1239181

# Sept4/ARTS Regulates Stem Cell Apoptosis and Skin Regeneration

Yaron Fuchs,<sup>1</sup> Samara Brown,<sup>1</sup> Travis Gorenc,<sup>1</sup> Joe Rodriguez,<sup>1</sup> Elaine Fuchs,<sup>2\*</sup> Hermann Steller<sup>1\*</sup>

Adult stem cells are essential for tissue homeostasis and wound repair. Their proliferative capacity must be tightly regulated to prevent the emergence of unwanted and potentially dangerous cells, such as cancer cells. We found that mice deficient for the proapoptotic *Sept4/ARTS* gene have elevated numbers of hair follicle stem cells (HFSCs) that are protected against apoptosis. *Sept4/ARTS*<sup>−/−</sup> mice display marked improvement in wound healing and regeneration of hair follicles. These phenotypes depend on HFSCs, as indicated by lineage tracing. Inactivation of XIAP, a direct target of ARTS, abrogated these phenotypes and impaired wound healing. Our results indicate that apoptosis plays an important role in regulating stem cell-dependent regeneration and suggest that this pathway may be a target for regenerative medicine.

The ability of stem cells (SCs) to self-renew and differentiate enables them to replace cells that die during tissue homeostasis or upon injury. Elevated SC numbers might be desirable, at least transiently, to enhance tissue repair (1, 2). However, a large SC pool may potentially increase the risk of cancer (3).

One major mechanism that eliminates undesired and dangerous cells is apoptosis (4). Relatively little is known about the role of apoptosis in controlling SC numbers and its possible effect on SC-dependent regeneration. Apoptosis is executed by caspases that are negatively regulated by IAPs (inhibitor of apoptosis proteins) (5, 6). The best-studied mammalian IAP is XIAP (7). In cells destined to die, IAPs are inactivated by specific antagonists (8, 9). One mammalian IAP antagonist is ARTS, a splice variant of the mam-

malian gene *Septin4* (*Sept4*) (10, 11). Deletion of the *Sept4/ARTS* gene results in increased numbers of hematopoietic stem and progenitor cells and elevated XIAP levels. This causes increased apoptotic resistance and accelerated tumor development (12). Here, we report crucial roles of XIAP and *Sept4/ARTS* in regulating hair follicle stem cell (HFSC) apoptosis and show that apoptotic alterations have profound consequences for wound healing and regeneration.

Hair follicles cycle between phases of growth (anagen), destruction (catagen), and rest (telogen). This process requires distinct populations of HFSCs that reside within the bulge (13–16). ARTS was the only *Sept4* isoform detected in HFSCs (fig. S1, A to C). To investigate the consequences of ARTS deficiency, we examined bulge HFSCs with specific bulge markers (CD34 and K15)

Hair follicles cycle between phases of growth (anagen), destruction (catagen), and rest (telogen). This process requires distinct populations of HFSCs that reside within the bulge (13–16). ARTS was the only *Sept4* isoform detected in HFSCs (fig. S1, A to C). To investigate the consequences of ARTS deficiency, we examined bulge HFSCs with specific bulge markers (CD34 and K15)

<sup>1</sup>Strang Laboratory of Apoptosis and Cancer Biology, Howard Hughes Medical Institute, The Rockefeller University, New York, NY 10065, USA. <sup>2</sup>Laboratory of Mammalian Cell Biology and Development, Howard Hughes Medical Institute, The Rockefeller University, New York, NY 10065, USA.

\*Corresponding author. E-mail: [steller@rockefeller.edu](mailto:steller@rockefeller.edu) (H.S.); [fuchslb@rockefeller.edu](mailto:fuchslb@rockefeller.edu) (E.F.)

as well as Sox9, which, depending on the hair follicle phase, labels HFSCs and/or progeny. Although *Sept4/ARTS*<sup>-/-</sup> hair follicles had bulges with overall normal morphology, fluorescence-activated cell sorting (FACS) revealed that within the  $\alpha 6^+ \beta 1^+$  population of skin epithelial progenitors there were more than twice as many CD34<sup>+</sup> cells in *Sept4/ARTS*<sup>-/-</sup> as in the wild type (Fig. 1, A and B, and fig. S1D). Similarly, for the *Tg(Krt1-15-EGFP)2Cot/J* reporter mouse, which specifically marks K15<sup>+</sup> bulge and hair germ cells (17), the numbers of K15-GFP<sup>+</sup>  $\alpha 6^{\text{hi}}$  cells were elevated when backskin hair follicles lacked *Sept4/ARTS* (Fig. 1, C and D).

ARTS-dependent differences were even more striking in tailskin (fig. S2). At 8 weeks of age, *Sept4/ARTS*<sup>-/-</sup> tailskin hair follicles displayed an expanded epithelial strand populated by K15<sup>+</sup> and Sox9<sup>+</sup> cells (fig. S2). In normal backskin

follicles, this strand forms during mid- to late catagen phase, when most matrix cells have died and only a small number of outer root sheath (ORS) cells remain (18). Because ARTS is a proapoptotic protein, the elongated epithelial strand suggested that more ORS cells survive catagen when ARTS is absent.

To test whether ARTS affects the survival of skin progenitors, we cultured CD34<sup>+</sup>Sca1<sup>+</sup> and CD34<sup>+</sup>Sca1<sup>+</sup> keratinocytes from telogen-phase backskins and evaluated their colony-forming efficiency ( $\geq 2$  cells per colony) and cell number. *Sept4/ARTS*<sup>-/-</sup> HFSCs generated  $\sim 2.5$  times as many colonies as wild-type HFSCs (fig. S3A). Moreover, the number of cells within these colonies was significantly higher (fig. S3C). By contrast, epidermal keratinocytes were unaffected (fig. S3, B and D). We also examined the proliferation rates of HFSCs and of other skin cells, and

found no effect of *Sept4/ARTS* (fig. S3, E to K). These findings suggest that loss of ARTS protects HFSCs against apoptosis.

In wild-type catagen follicles, a new bulge is formed from CD34<sup>+</sup> HFSCs along the upper ORS, whereas surviving CD34<sup>+</sup> ORS cells form the new hair germ (18). Both wild-type and *Sept4/ARTS*<sup>-/-</sup> hair follicles formed new bulges (fig. S4, A and B). Apoptotic cells are rarely seen in telogen or anagen but are prevalent in catagen (19). Therefore, we surmised that the pronounced epithelial strand seen in *Sept4/ARTS*<sup>-/-</sup> hair follicles might reflect enhanced apoptotic resistance of HFSCs. To test this hypothesis, we examined apoptosis in the first catagen phase [postnatal day 16 (P16)] and found a striking decrease of cell death in *Sept4/ARTS*<sup>-/-</sup> mice (Fig. 1E and fig. S4, C and D). These results suggest that in *Sept4/ARTS*<sup>-/-</sup> mice, more ORS HFSCs are spared during catagen, thereby yielding a larger HFSC pool. Because there is only a single bulge at this stage, it also explains why the bulge region appeared larger in P21 *Sept4/ARTS*<sup>-/-</sup> hair follicles (Fig. 1A).

In contrast to backskin, tailskin had CP3<sup>+</sup> (cleaved caspase3<sup>+</sup>) cells in the bulge of what appeared to be late catagen-phase wild-type hair follicles (Fig. 1F and fig. S4E). Furthermore, these CD34<sup>+</sup>K15<sup>+</sup> bulge cells displayed membrane blebbing, nuclear condensation, and TUNEL (terminal deoxynucleotidyl transferase-mediated deoxyuridine triphosphate nick end labeling), indicating that they were bona fide apoptotic cells (fig. S4E). This suggests that HFSC apoptosis can occur within the bulge of tailskin hair follicles.

Next, we examined whether deletion of *Sept4/ARTS* protects HFSCs from staurosporine- and etoposide-induced apoptosis in vitro. Relative to wild-type HFSCs, *Sept4/ARTS*<sup>-/-</sup> HFSCs displayed a marked decrease in apoptotic markers (Fig. 1G). Because *Sept4/ARTS*<sup>-/-</sup> HFSCs are resistant to apoptosis, we examined whether they have greater capacity to cope with stress by culturing HFSCs without sustaining feeder cells. In contrast to wild-type HFSCs, *Sept4/ARTS*<sup>-/-</sup> HFSCs exhibited an increase in cell number, reaching confluence under conditions that severely hindered the growth of control cells (fig. S5). Collectively, these results reveal an important physiological function of *Sept4/ARTS* for HFSC apoptosis in response to stress.

HFSCs do not contribute to normal epidermal homeostasis. However, in response to wounding, they participate in repopulating the epidermis (20, 21). Because *Sept4/ARTS*<sup>-/-</sup> HFSCs are protected against cell death, we investigated whether they have enhanced capacity for tissue repair. Full-thickness excision wounds (1 cm<sup>2</sup>) were generated on the dorsal skins of 8- and 15-week-old mice and monitored for wound coverage. In 8-week-old *Sept4/ARTS*<sup>-/-</sup> mice, the wound size was reduced by 80% after only 5 days, whereas in wild-type mice the wound size was reduced by only 10% (Fig. 2A and fig. S6A). Accelerated healing was seen at all time points. In 15-week-old mice, healing was generally slower, but again

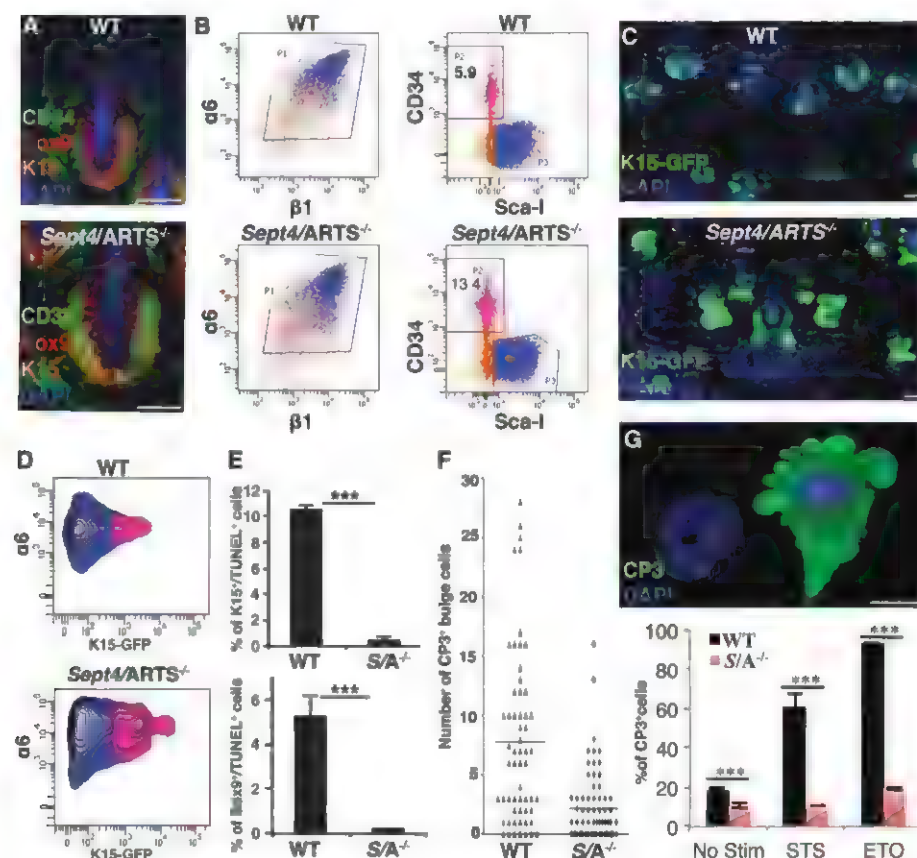


**Fig. 1. *Sept4/ARTS*<sup>-/-</sup> mice display HFSCs that are resistant to apoptosis.** (A) Dorsal whole mounts (DWMs) stained for CD34, K15, Sox9, and 4',6-diamidino-2-phenylindole (DAPI) at P21. WT, wild type. (B) FACS analysis of dorsal skins assessing the percentage of bulge HFSCs within control (WT) and *Sept4/ARTS*<sup>-/-</sup> skins. Equivalent numbers of FACS-purified  $\alpha 6^+ \beta 1^+$  progenitors were resorted for CD34<sup>+</sup>Sca1<sup>+</sup> (pink,  $\alpha 6^+ \beta 1^+ \text{CD}34^+ \text{Sca}1^+$ ; blue,  $\alpha 6^+ \beta 1^+ \text{CD}34^+ \text{Sca}1^+$ ; orange,  $\alpha 6^+ \beta 1^+ \text{CD}34^+ \text{Sca}1^+$ ). Data shown are from four mice combined and sorted together. Experiments were repeated four times independently ( $n > 11$ ,  $P < 0.001$ ). (C) DWM images of control and *Sept4/ARTS*<sup>-/-</sup>; *Tg(Krt1-15-EGFP)2Cot/J* reporter skins. (D) FACS analyses of  $\alpha 6^+ \text{K}15^+$  cells from control and *Sept4/ARTS*<sup>-/-</sup>; *Tg(Krt1-15-EGFP)2Cot/J* reporter skins. (E) Quantifications of K15<sup>+</sup>TUNEL<sup>+</sup> and Sox9<sup>+</sup>TUNEL<sup>+</sup> cells during first catagen (P16). S/A<sup>-/-</sup> denotes *Sept4/ARTS*<sup>-/-</sup>. (F) Quantifications of CD34<sup>+</sup>CP3<sup>+</sup> HFSCs in control and *Sept4/ARTS*<sup>-/-</sup> tailskin hair follicles. Horizontal line defines average. (G) Top: Z-stack of control cultured HFSCs undergoing apoptosis in vitro. Bottom: Percentage of sorted HFSCs (CD34<sup>+</sup>Sca1<sup>+</sup>) placed into culture that are CP3<sup>+</sup> with and without staurosporine (STS) and etoposide (ETO) treatment. Scale bars, 100  $\mu\text{m}$  (A), 20  $\mu\text{m}$  (C), 10  $\mu\text{m}$  (G). \*\*\* $P < 0.001$ .



**Fig. 2. Loss of *Sept4/ARTS* function accelerates wound healing and improves skin regeneration.** (A and B) Reepithelialization dynamics of skins at different times PWI. Excision wounds (1 cm<sup>2</sup>) were inflicted on dorsal skin of 8-week-old [(A), *n* = 12] or 15-week-old mice [(B), *n* = 8]. Percentage of wound coverage was calculated versus original wound size. D denotes day PWI. (C) Hematoxylin and eosin staining of full-thickness excision wounds of 8-week-old mice, 18 days PWI. Hair follicle formation within the wound bed is observed in *Sept4/ARTS*<sup>-/-</sup> mice. (D to F) HFSC niches within regenerated hair follicles are positive for CD34, K15, and Sox9. (D) Regenerated hair follicle displays a HFSC niche positive for K15 and Sox9. (E) Zoom-in of the HFSC niche in (D). (F) Regenerated hair follicle niche is positive for CD34. (G and H) Immunofluorescence for PCNA (G) and Ki67 (H), indicating proliferative activity within the regenerated hair follicle niche of *Sept4/ARTS*<sup>-/-</sup> mice. Scale bars, 500 μm (C), 50 μm (D), 20 μm [(E), (F), and (G)], 10 μm (H).

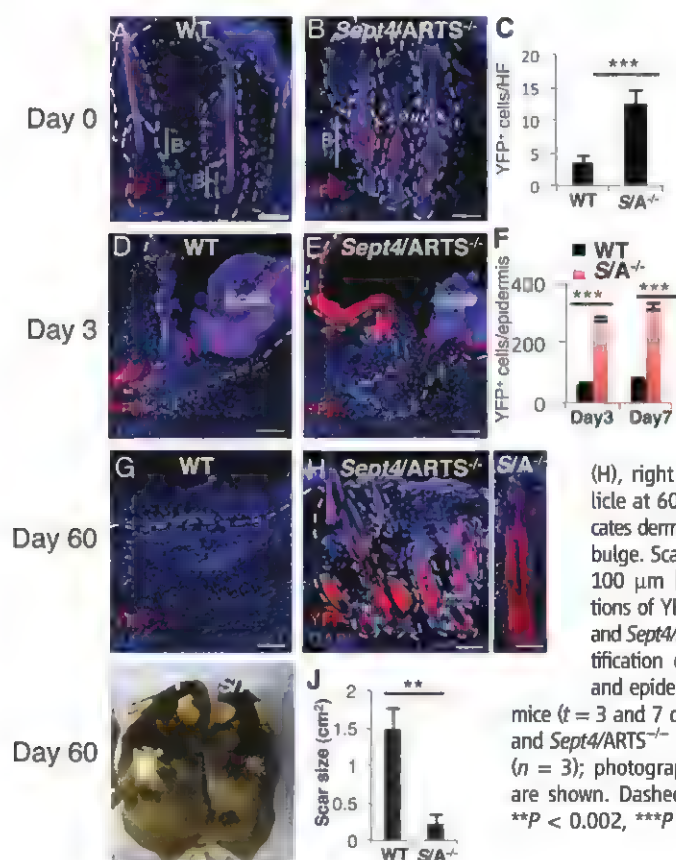
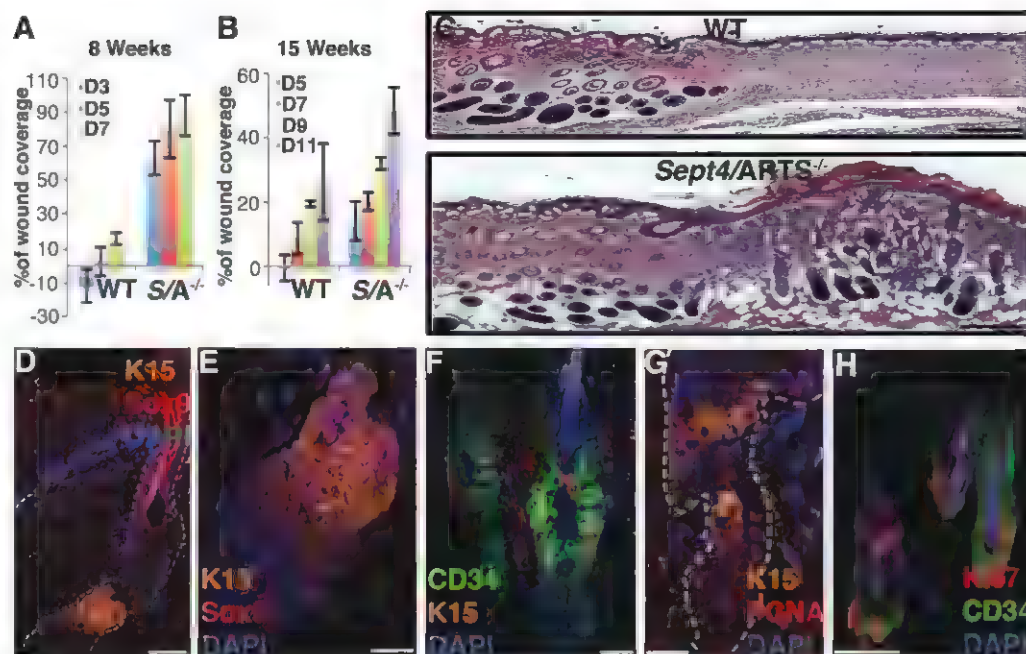


**Fig. 3. *Sept4/ARTS*<sup>-/-</sup> HFSCs are responsible for enhanced tissue regeneration.** (A to H) Reporter expression was induced from P20 to P25 [(A) to (F)] or from P45 to P50 [(G) and (H)], and wounding was executed at P26 or P56, respectively (see fig. S7). Skins were analyzed at *t* = 0, 3, 7, 18, and 60 days PWI. WT [(A), (D), (G)], and *Sept4/ARTS*<sup>-/-</sup> [(B), (E), (H)] lineage tracings are shown at *t* = 0, 3, and 60 days.

(H), right panel: Close-up of hair follicle at 60 days PWI. Dashed line indicates dermis-epidermis border; B denotes bulge. Scale bars, 50 μm [(A), (B), (G)], 100 μm [(D), (E), (H)]. (C) Quantifications of YFP<sup>+</sup> cells in hair follicles of WT and *Sept4/ARTS*<sup>-/-</sup> mice (*t* = 0). (F) Quantification of YFP<sup>+</sup> cells in hair follicles and epidermis of WT and *Sept4/ARTS*<sup>-/-</sup> mice (*t* = 3 and 7 days). (I and J) Scar size of WT and *Sept4/ARTS*<sup>-/-</sup> mice at 60 days PWI (2 cm<sup>2</sup>) (*n* = 3); photograph (I) and quantification (J) are shown. Dashed line indicates scar border. \*\**P* < 0.002, \*\*\**P* < 0.001.

*Sept4/ARTS*<sup>-/-</sup> mice were more efficient in wound repair (Fig. 2B).

By 18 days post-wound infliction (PWI), 1-cm<sup>2</sup> wounds of 8-week-old wild-type and *Sept4/*

*ARTS*<sup>-/-</sup> mice had healed. Histological analyses revealed that in contrast to wild-type mice, high numbers of hair follicles were seen in the wound beds of *Sept4/ARTS*<sup>-/-</sup> skins, which

sometimes appeared hyperplastic but otherwise appeared relatively normal (Fig. 2, C to H). Long after wild-type HFSCs had returned to quiescence, some *Sept4/ARTS*<sup>-/-</sup> HFSCs were still proliferative, as indicated by PCNA (proliferating cell nuclear antigen) and Ki67 staining (Fig. 2, G and H, and fig. S6B). Together, these results suggest that the enhanced survival of HFSCs in *Sept4/ARTS*<sup>-/-</sup> mice is responsible for accelerated repair and hair follicle regeneration in response to injury.

To examine the contribution of HFSCs to accelerated wound healing in *Sept4/ARTS*<sup>-/-</sup> mice, we used *Tg(Krt1-15-cre/PGR)22Cot; Rosa26-YFP* reporter mice. When induced by RU486, this reporter specifically activates Cre in HFSCs, and thereafter they and their progeny are marked by yellow fluorescent protein (YFP) (22). *Sept4/ARTS*<sup>-/-</sup> follicles displayed about 3.5 times as many YFP-marked HFSCs at *t* = 0 (Fig. 3, A to C, and fig. S7, A and B). By *t* = 3 days and *t* = 7 days after wounding, 4 to 5 times as many YFP<sup>+</sup> cells were present in the upper hair follicles and epidermis of *Sept4/ARTS*<sup>-/-</sup> skin (Fig. 3, D to F, and fig. S7, C and D). Enhanced repair was also observed when *Sept4/ARTS*<sup>-/-</sup> mice were lineage-marked and wounded during the protracted second telogen (fig. S7, E to G). Moreover, in contrast to wild-type regeneration, *Sept4/ARTS*<sup>-/-</sup> HFSC progeny remained in the skin epidermis at 2 months PWI, and the scars of *Sept4/ARTS*<sup>-/-</sup> were significantly smaller (Fig. 3, G to J). Taken together, these results suggest that apoptosis-impaired *Sept4/ARTS*<sup>-/-</sup> HFSCs are functional and robustly contribute to healing and hair follicle regeneration.

XIAP is a direct downstream target for the proapoptotic activity of ARTS (11, 12, 23, 24).

XIAP<sup>-/-</sup> mice are viable and do not display overt phenotypes (7, 25). However, microarray and chromatin immunoprecipitation sequencing analyses indicate that XIAP is expressed throughout skin epithelium, including the bulge (26). Because ARTS can promote ubiquitination and degradation of XIAP (27, 28), we compared XIAP protein levels in wild-type and *Sept4/ARTS*<sup>-/-</sup> HFSCs. In wild-type mice, anti-XIAP immunolabeling was detected in bulge HFSCs, sebaceous glands, and dermal papillae (Fig. 4, A and B, and fig. S8). Most notable, however, was the striking increase of XIAP in tailskin *Sept4/ARTS*<sup>-/-</sup> HFSCs (Fig. 4B and fig. S9A).

To determine the biological role of elevated XIAP in *Sept4/ARTS*<sup>-/-</sup> hair follicles, we generated double knockout *Sept4/ARTS*<sup>-/-</sup>;XIAP<sup>-/-</sup> (SX<sup>-/-</sup>) animals and examined them for wound repair and hair follicle regeneration. Intriguingly, loss of XIAP function abolished the enhanced reepithelialization of *Sept4/ARTS*<sup>-/-</sup> mice. In addition, wound repair in SX<sup>-/-</sup> mutants was markedly delayed relative to the wild type (Fig. 4C). XIAP<sup>-/-</sup> single mutants were severely compromised in wound repair (Fig. 4C and fig. S9B). Taken together, these results demonstrate a critical physiological role of XIAP in wound healing. Moreover, because ARTS was unable to stimulate healing in the absence of XIAP, this suggests that XIAP is a major target for the proapoptotic activity of ARTS in this system (11, 12).

To investigate whether XIAP participates in wound healing by suppressing apoptosis, we analyzed the cell death sensitivity of CD34<sup>+</sup> HFSCs

from SX<sup>-/-</sup> mutants. In contrast to *Sept4/ARTS*<sup>-/-</sup> (CD34<sup>+</sup>) HFSCs, SX<sup>-/-</sup> HFSCs exhibited significantly increased apoptosis (Fig. 4D and fig. S10). XIAP directly inhibits caspases and contains a RING domain required for E3 ligase activity (29). To address its importance for SC apoptosis, we analyzed XIAP<sup>ΔRING</sup> mice, in which the XIAP RING domain was deleted (7). CD34<sup>+</sup> SCs from *Sept4/ARTS*<sup>-/-</sup>;XIAP<sup>ΔRING</sup> (SX<sup>ΔRING</sup>) and SX<sup>-/-</sup> mice had virtually identical phenotypes (Fig. 4D). Finally, inactivation of XIAP also impaired the growth of CD34<sup>+</sup> HFSCs in vitro (fig. S10). Together, these results show that XIAP is a physiological downstream target for the proapoptotic and regenerative activity of *Sept4/ARTS* in skin, and that XIAP RING function is required for the antiapoptotic activity of XIAP in HFSCs.

Our findings reveal the importance of apoptosis in regulating hair follicle homeostasis and wound repair, and the nonredundant functions of ARTS and XIAP in this process. At the surface, our results may appear at odds with a previously reported role of apoptosis in promoting skin wound healing, which was ascribed to mitogenic signaling by apoptotic cells (30). However, depending on the point of interference in the apoptotic pathway, the outcome for mitogenic signaling can vary considerably (31). Furthermore, our studies suggest that ARTS and XIAP function specifically in regulating apoptosis of progenitors in the hair follicle, but not in more differentiated skin cells. Therefore, targeting these genes is very different from a general inhibition of effector caspases in differentiated skin cells. Our results suggest

that targeting apoptotic pathways in HFSCs may have therapeutic benefits to promote wound healing and regeneration.

## References and Notes

1. I. L. Weissman, *Science* **287**, 1442–1446 (2000).
2. S. Rafii, D. Lyden, *Nat. Med.* **9**, 702–712 (2003).
3. Y. C. Hsu, E. Fuchs, *Nat. Rev. Mol. Cell Biol.* **13**, 103–114 (2012).
4. Y. Fuchs, H. Steller, *Cell* **147**, 742–758 (2011).
5. M. Gyrd Hansen, P. Meier, *Nat. Rev. Cancer* **10**, 561–574 (2010).
6. E. Kuranaga, M. Miura, *Trends Cell Biol.* **17**, 135–144 (2007).
7. A. J. Schile, M. García-Fernández, H. Steller, *Genes Dev.* **22**, 2256–2266 (2008).
8. S. Kornbluth, K. White, *J. Cell Sci.* **118**, 1779–1787 (2005).
9. A. Bergmann, A. Y. Yang, M. Srivastava, *Curr. Opin. Cell Biol.* **15**, 717–724 (2003).
10. S. Larisch et al., *Nat. Cell Biol.* **2**, 915–921 (2000).
11. Y. Gottfried, A. Rotem, R. Lotan, H. Steller, S. Larisch, *EMBO J.* **23**, 1627–1635 (2004).
12. M. García-Fernández et al., *Genes Dev.* **24**, 2282–2293 (2010).
13. E. Fuchs, *Nature* **445**, 834–842 (2007).
14. S. J. Morrison, A. C. Spradling, *Cell* **132**, 598–611 (2008).
15. C. A. Jahoda, A. M. Christiano, *Cell* **146**, 678–681 (2011).
16. W. M. Woo, A. E. Oro, *Cell* **146**, 334 (2011).
17. R. J. Morris et al., *Nat. Biotechnol.* **22**, 411–417 (2004).
18. Y. C. Hsu, H. A. Pasolli, E. Fuchs, *Cell* **144**, 92–105 (2011).
19. S. Müller-Röver et al., *J. Invest. Dermatol.* **117**, 3–15 (2001).
20. M. Ito et al., *Nat. Med.* **11**, 1351–1354 (2005).
21. I. Brownell, E. Guevara, C. B. Bai, C. A. Loomis, A. L. Joyner, *Cell Stem Cell* **8**, 552–565 (2011).
22. M. Ito et al., *Nature* **447**, 316–320 (2007).
23. J. C. Reed, *Cancer Cell* **3**, 17–22 (2003).
24. E. C. LaCasse et al., *Oncogene* **27**, 6252–6275 (2008).
25. H. Harlin, S. B. Refey, C. S. Duckett, T. Lindsten, C. B. Thompson, *Mol. Cell Biol.* **21**, 3604–3608 (2001).
26. W. H. Lien et al., *Cell Stem Cell* **9**, 219–232 (2011).
27. J. B. Garrison et al., *Mol. Cell* **41**, 107–116 (2011).
28. N. Edson et al., *Cell Death Differ.* **19**, 356–368 (2012).
29. S. Fulda, D. Vucic, *Nat. Rev. Drug Discov.* **11**, 109–124 (2012).
30. F. Li et al., *Sci. Signal.* **3**, ra13 (2010).
31. A. Bergmann, H. Steller, *Sci. Signal.* **3**, re8 (2010).

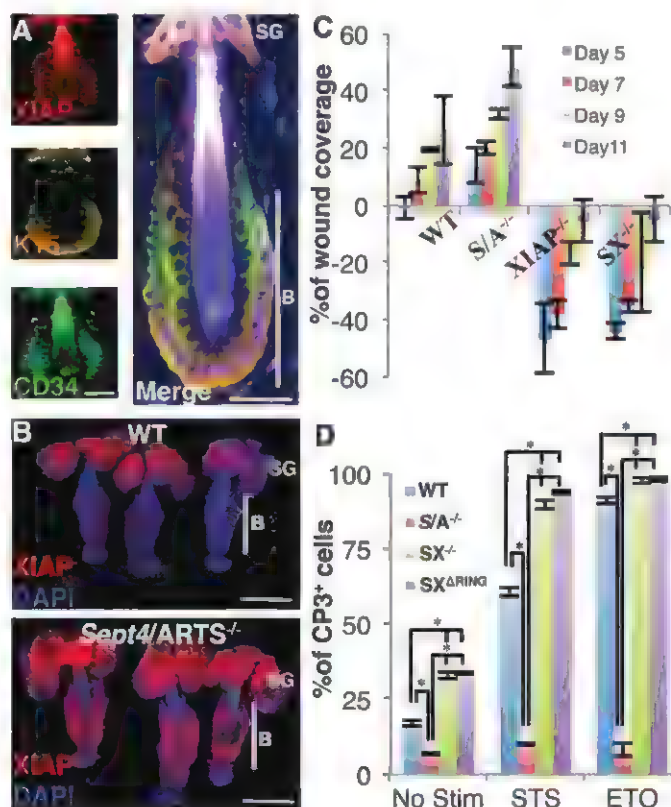
**Acknowledgments:** We apologize to colleagues whose contributions we could not adequately cite because of space constraints. We thank B. Keyes, Y. C. Hsu, N. Stokes, and I. Shachrai for discussion, advice, and technical assistance; S. Mazel, X. Li, S. Semova, and S. Tadesse for FACS sorting; the Comparative Biology Center (AAALAC-accredited) for health care to our mice; and members of the Steller lab H. S. and E. F. are Investigators of the Howard Hughes Medical Institute. Supported by NIH grants R01GM60124 (H.S.) and R01AR050452 (E.F.). The *Sept4/ARTS* and XIAP mouse mutant strains used in this study are available from the Rockefeller University to academic groups through a materials transfer agreement and to for-profit groups through a license.

## Supplementary Materials

www.sciencemag.org/cgi/content/full/science.1233029/DC1  
Materials and Methods  
Figs. S1 to S10  
References (32–35)

21 November 2012; accepted 13 June 2013  
Published online 20 June 2013;  
10.1126/science.1233029

**Fig. 4. XIAP is required for proper wound healing.** (A) Immunofluorescence indicates that XIAP protein is present in dorsal telogen bulge (P20) hair follicles. (B) Immunofluorescence indicates increased XIAP in *Sept4/ARTS*<sup>-/-</sup> tailskin hair follicles. B denotes bulge; SG, sebaceous gland. (C) Wound coverage dynamics in WT, S/A<sup>-/-</sup>, XIAP<sup>-/-</sup>, and SX<sup>-/-</sup> mice at various times PWI, as described in Fig. 3A (*n* = 8). (D) Quantifications of WT, S/A<sup>-/-</sup>, SX<sup>-/-</sup>, and SX<sup>ΔRING</sup> CD34<sup>+</sup>CP3<sup>+</sup> HFSCs. Scale bars, 20 μm (A), 100 μm (B). *P* < 0.001.





# How the Red Queen Drives Terrestrial Mammals to Extinction

Tiago B. Quental<sup>1\*</sup> and Charles R. Marshall<sup>2\*</sup>

Most species disappear by the processes of background extinction, yet those processes are poorly understood. We analyzed the evolutionary dynamics of 19 Cenozoic terrestrial mammalian clades with rich fossil records that are now fully extinct or in diversity decline. We find their diversity loss was not just a consequence of “gamblers ruin” but resulted from the evolutionary loss to the Red Queen, a failure to keep pace with a deteriorating environment. Diversity loss is driven equally by both depressed origination rates and elevated extinction rates. Although we find diversity-dependent origination and extinction rates, the diversity of each clade only transiently equaled the implied equilibrium diversity. Thus, the processes that drove diversity loss in terrestrial mammal clades were fundamentally nonequilibrium and overwhelmed diversity-dependent processes.

The majority of all species that have ever lived are now extinct (1), yet we know little about the dynamics of extinction. Most prior work has examined the mechanisms and selectivity of mass extinctions (2), although mass extinctions only account for a minority of extinctions in the history of life. To examine the dynamics of background extinction, we analyzed the generic diversity trajectories of 19 Cenozoic terrestrial mammalian families with excellent fos-

sil records. To qualify for analysis, each family had to be monophyletic and have at least 100 genus occurrences (average = 419), a total diversity of at least five genera, a longevity of at least eight stratigraphic stages, and an average preservation potential of at least 0.6 per genus per stage (average = 0.89) (see supplementary materials). We only analyzed Cenozoic clades to avoid any complicating factors that might have been introduced by the end-Cretaceous mass extinction event.

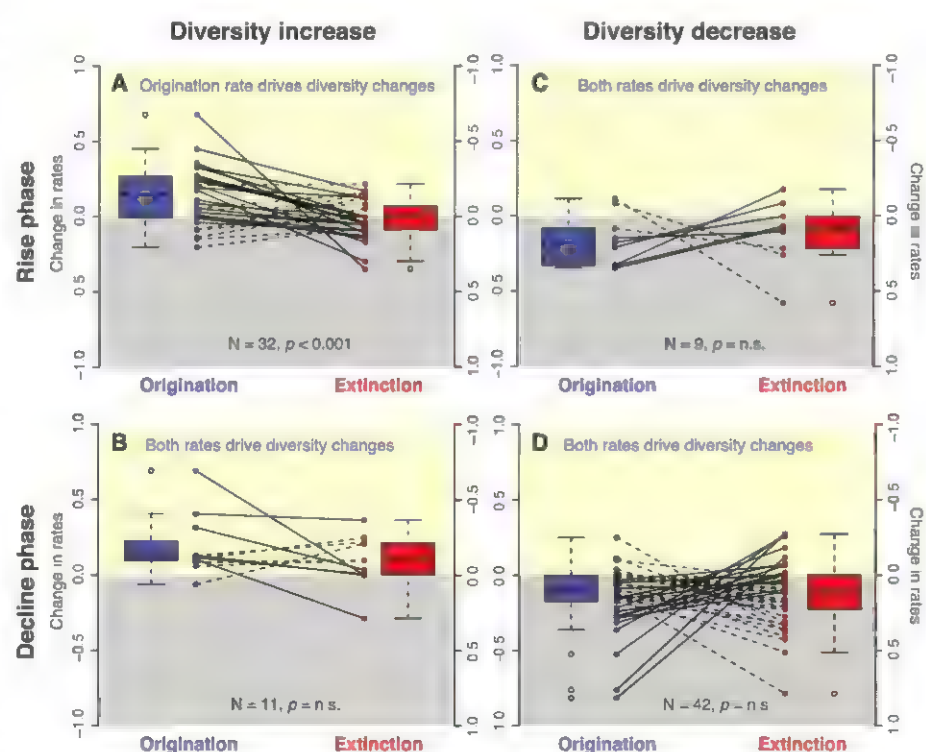
We first tested the hypothesis that the observed diversity trajectories were a consequence of the loss to the Red Queen, that is, an evolutionary loss driven by the deterioration of the environment (3–6), against the alternative hy-

pothesis that the waxing and waning in the clades’ diversity was random, the evolutionary equivalent of “gamblers ruin” (7–9). If the rise and fall in diversity was deterministic, then we would expect the longevity of the clades to be shorter than if their diversity trajectories were due to stochastic fluctuations in intrinsically constant rates of origination and extinction, where diversity would have simply drifted up and then down. Indeed, this is what we find: On average, the longevity of the clades are too short to simply be the result of stochastic processes [figs. S3 and S4; see also (10)], suggesting a deterministic component to the diversity dynamics.

Although the exact causes of the decline are hard to determine, we were able to characterize the dynamics responsible for the diversity trajectories. Quantitative analysis revealed four generalities. First, on average the duration of the rise phase is statistically indistinguishable from the duration of the decline phase—the diversity trajectories are temporally symmetrical [see (10) for how we dealt with clades that are not extinct]. A similar pattern has also been observed in Paleozoic marine invertebrates (11).

Second, both the per-genus origination rates and the extinction rates exhibit diversity dependence [fig. S8 and table S2; see also (10)]: When diversity increased, origination rates dropped and extinction rates increased. Thus, these mammalian clades exhibit the macroevolutionary equivalent of MacArthur and Wilson’s (12) model for diversity change during island colonization. In

**Fig. 1. Changes in per-genus origination and extinction rates for events of increasing and decreasing diversity within the rise and decline phases of mammalian diversity trajectories.** Increases in diversity during the rise phases (A) are mostly controlled by increases in the per-genus origination rate (the change in the origination rate is significantly larger than the change in the extinction rate,  $N = 32$ ,  $V$  (test statistic) = 438,  $P = 0.00071$ , Wilcoxon rank paired test). In contrast, increases in the per-genus origination rates and decreases in the per-genus extinction rates contribute equally to increases in diversity during the decline phases (B) (the magnitude of these changes is not significantly different,  $N = 11$ ,  $V = 44$ ,  $P = 0.3652$ , Wilcoxon rank paired test). Decreases in the per-genus origination rates and increases in the per-genus extinction rates also contribute equally to decreases in diversity during both rise (C) and decline (D) phases (the magnitude of these changes is not significantly different,  $N = 9$ ,  $V = 18$ ,  $P = 0.6523$ , Wilcoxon rank paired test, for the rise phases, and  $N = 42$ ,  $V = 512$ ,  $P = 0.4571$ , Wilcoxon rank paired test, for the decline phases). Changes in rates and diversity were measured between adjacent stages (fig. S5). The changes in the per-genus origination and extinction rates for each stage are connected by a line, and each pair constituted a replicate in the Wilcoxon rank paired test. Solid lines indicate that change in origination rate is more important than change in extinction rate in driving diversity change; dashed lines, that change in extinction is more important. The box-



plots show the median and first and third quartiles of the data. The whiskers indicate the datum still within 1.5 interquartile range defined by the first and third quartiles. n.s., not significant.

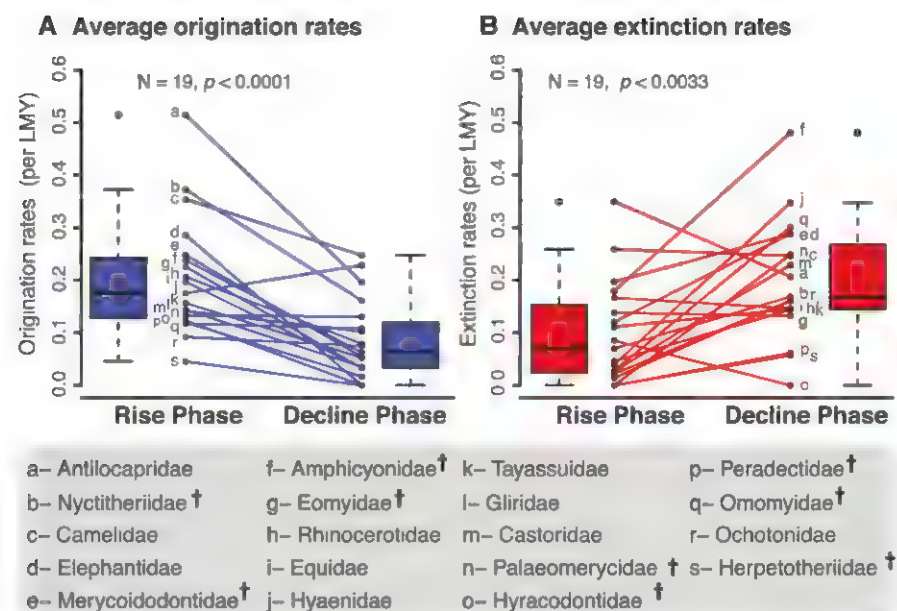


**Fig. 2. Origination rates decrease and extinction rates increase as the mammalian clades age.** There is a significant and roughly equal change in the average per-genus origination (A) and the average per-genus extinction (B) rates between the diversity-rise and the diversity-decline phases across the 19 families analyzed. Each pair of values corresponds to one of the analyzed families. For origination,  $N = 19$ ,  $V = 184$ ,  $P = 0.000053$ , Wilcoxon rank paired test; for extinction,  $N = 19$ ,  $V = 25$ ,  $P = 0.0033$ , Wilcoxon rank paired test. The crosses in the legend identify extinct clades. LMV, lineage million years.

both scenarios, the existence of diversity-dependent rates implies that each island (in MacArthur and Wilson's model) or clade (in the macroevolutionary equivalent of their model) has an equilibrium diversity, the diversity at which the origination rate equals the extinction rate. Diversity dependence in origination rates, but not in extinction rates, has also been reported in Cenozoic North American mammals [(13), but see (14)].

Third, we unexpectedly find that, during the decline phase, decreases in the per-genus origination rate are just as important as increases in the per-genus extinction rate in driving the observed diversity losses (Fig. 1). In fact, on average the initial origination rate is of a similar magnitude to the final extinction rate, and the final origination rate is as low as the initial extinction rate (Fig. 2). Most discussions of clade extinction focus only on the processes and rates of extinction and seldom consider the possibility that diversity can also be lost because of a failure to replace extinct taxa. However, Bambach *et al.* (15) showed that the loss in generic diversity in the end-Devonian and end-Triassic mass extinctions was primarily driven by a lack of origination. Similarly, Van Valen (3) noted that the decline in generic diversity of perissodactyl mammals was largely due to a drop in origination rate. The causes of a failure to originate, the evolutionary sterility that we call the Entwines effect (16), are not understood and require more attention.

Last, on average the overall diversity trajectories were more influenced by changes in origination rate than by changes in extinction rate

(fig. S6). This disparity is due to the fact that changes in origination rate dominated the diversification phases of the diversity trajectories (Fig. 1), whereas changes in origination and extinction rates contributed equally during the decline phases. Similarly, Gilinsky and Bambach (17) found that family diversity within marine orders and sub-orders was largely driven by changes (decreases) in family origination rates.

The simplest way of modeling these observed diversity dynamics is with the macroevolutionary equivalent of MacArthur and Wilson's model (12). However, this model leads to logistic diversification with a stable equilibrium diversity and thus requires modification to accommodate diversity loss. Whereas Whittaker *et al.* (18) provides a qualitative modification of the model that incorporates the formation and ultimate demise of oceanic islands with the extinction of their terrestrial biotas, we quantitatively extended MacArthur and Wilson's framework to incorporate loss to the Red Queen by adding in a temporal decay in the intrinsic diversification rate, the diversification rate at the inception of the clade. We achieved this by decreasing the intrinsic origination rate and increasing the intrinsic extinction rate at constant rates with time (10), which translates into a constant rate of decay in the expected equilibrium diversity (Fig. 3 and eq. S13). Thus, under this model the expected equilibrium diversity steadily decays to zero and then becomes increasingly negative, driving the clade to extinction.

We began with a slow rate of decay in the intrinsic diversification rate (from 0.03% to 0.3%

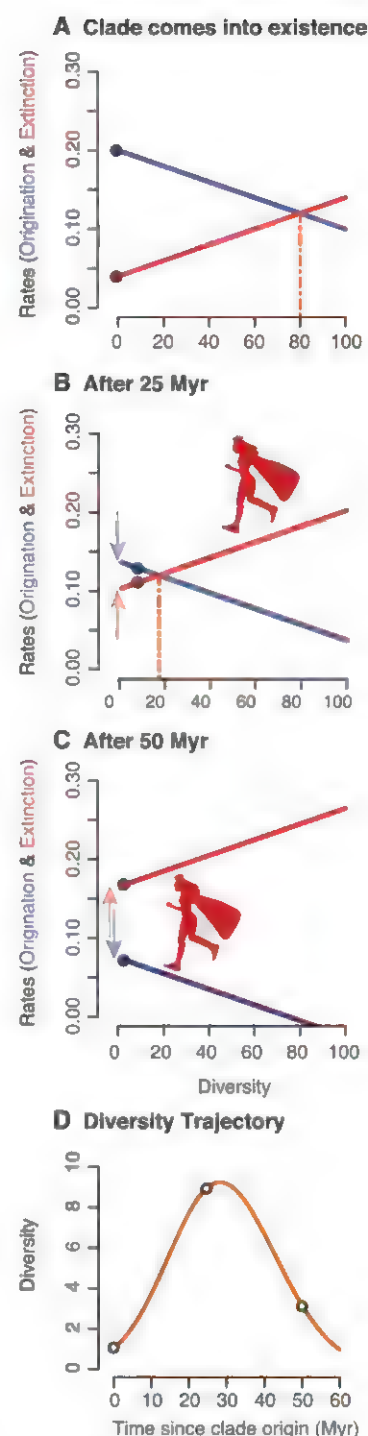


**Fig. 3. How a clade loses to the Red Queen via a decay in its intrinsic per-genus rate of diversification.** (A to C) The change of the intrinsic origination and extinction rates (shown by the arrows); the decay of the equilibrium diversity (shown by the moving position of the dashed orange line); and the realized per-genus origination (blue points) and per-genus extinction (red points) rates at different times in its history. (D) The diversity trajectory generated by the diversity dynamics shown in (A) to (C). Light blue points show the diversity for the time points shown in (A) to (C). The graphs depict solution to eqs. S10, S11, and S17 (10). The running Red Queen symbolizes the deterioration of the environment. Myr, million years.



per million years) but could not generate diversity trajectories with temporally symmetrical waxing and waning phases nor the switch in the magnitudes of the initial origination and extinction rates with their final rates (10). Instead, clades quickly reached equilibrium diversity and then slowly rode the decaying equilibrium diversity down to extinction—the decline phase was longer than the diversification phase, and the final origination and extinction rates remained at intermediate values between the high initial origination rate and the low initial extinction rate, rather than switching in value.

The only way to accommodate the observed diversity dynamics is if the intrinsic diversification rate (and thus the equilibrium diversity) deteriorated sufficiently fast. For example, when we modeled the decay in the intrinsic diversification at a rate of ~3% per million years, the clade was left with a standing diversity that increasingly lagged behind the equilibrium diversity as the clade went extinct (Fig. 3C). This resulted in the switching in the values of the initial and final per-genus origination and extinction rates and led to a sufficiently negative diversification rate during the clade's decline to produce the temporally symmetric waxing and waning phases of diversity change.

An unexpected consequence of the rapid decline in the per-genus rate of diversification is that a clade's diversity only transiently equals the equilibrium diversity. In contrast, in typical diversity-dependent models, species diversity remains at or close to the equilibrium diversity after the initial radiation, even when the equilibrium diversity decays with time, for example, as in Whittaker *et al.*'s modeling of the disappearance of islands through erosion (18, 19). Under our model, the diversification phase involves a gain toward an equilibrium diversity, as in standard logistic growth. However, as diversity increases, the equilibrium diversity is decaying in response to an already deteriorating environment, and the clade reaches its peak diversity at an equilibrium value less than the initial equilibrium diversity. Then, as the clade moves into the decline phase, the decay in its intrinsic rate of diversification leads to a sufficiently rapid decrease in its equilibrium diversity that the clade's realized diversity increasingly lags behind the decaying equilibrium diversity (Fig. 3). Thus, although diversity dependence in the per-genus origination and extinction rates plays a role in determining the duration of the clade's history, the diversity dynamics is dominated by the decay in the intrinsic diversification rates, not by the diversity-dependent equilibrium processes.

The secondary role that diversity-dependent rates of origination and extinction play in the diversity dynamics of the mammalian clades in decline offers a resolution to a debate in the paleontological literature, where diversity dependence has been proposed (13, 20) but where the evidence of equilibrium is scarce (21–23). In our model, the mechanism of diversity dependence is decoupled from the ultimate factors that deter-

mine the clades' fates: the deterioration of their environment. Our results suggest that diversity dependence plays a role in diversity dynamics similar to the role that friction plays in the dynamics of motion—although it must be accounted for in the dynamics of diversity change, the dominant forces of diversity change lie beyond the existence of diversity dependence.

## References and Notes

1. D. M. Raup, *Science* **231**, 1528–1533 (1986).
2. R. K. Bambach, *Annu. Rev. Earth Planet. Sci.* **34**, 127–155 (2006).
3. L. M. Van Valen, *Evol. Theory* **1**, 1–30 (1973).
4. We used Van Valen's original definition of the Red Queen as a measure of environmental deterioration regardless of the role that biotic and abiotic factors might have played in that deterioration (3). More recently, some have restricted the meaning of the Red Queen to biotic factors (5, 6), using the term Court Jester for abiotic factors (5, 6).
5. A. D. Barnosky, *J. Vertebr. Paleontol.* **21**, 172–185 (2001).
6. M. J. Benton, *Science* **323**, 728–732 (2009).
7. D. M. Raup, S. J. Gould, T. J. M. Schopf, D. S. Simberloff, *J. Geol.* **81**, 525–542 (1973).
8. The idea that the major patterns in Phanerozoic diversity change could be attributed to purely stochastic process was later rejected (9).
9. S. M. Stanley, P. W. Signor III, S. Lidgard, A. F. Karr, *Paleobiology* **7**, 115–127 (1981).
10. Material and methods and supplementary materials can be found on Science Online.
11. M. Foote, *Paleobiology* **33**, 517–529 (2007).
12. R. H. MacArthur, E. O. Wilson, *The Theory of Island Biogeography* (Princeton Univ. Press, Princeton, NJ, 1967).
13. J. Alroy, *Paleogeogr. Palaeoclimatol. Palaeoecol.* **127**, 285–311 (1996).

14. J. Alroy, in *Speciation and Patterns of Diversity*, R. Butlin, J. Bridle, D. Schluter, Eds. (Cambridge Univ. Press, Cambridge, 2009), pp. 301–323.
15. R. K. Bambach, A. H. Knoll, S. Wang, *Paleobiology* **30**, 522–524 (2004).
16. In J. R. R. Tolkien's Middle Earth [J. R. R. Tolkien, *The Lord of the Rings* (Mariner Books, Boston, 2012)], the Ents lost their wives and thus had no means of regenerating their race, hence the term the Entwives effect.
17. L. Gilinsky, R. K. Bambach, *Paleobiology* **13**, 427–445 (1987).
18. R. J. Whittaker, K. A. Triantis, R. J. Ladle, *J. Biogeogr.* **35**, 977–994 (2008).
19. In Whittaker *et al.*'s model (18), their time axis is on a log scale.
20. J. J. Sepkoski Jr., *Paleobiology* **7**, 36–53 (1984).
21. M. J. Benton, B. C. Emerson, *Paleontology* **50**, 23–40 (2007).
22. S. M. Stanley, *Paleobiology* **33** (suppl.), 1–55 (2007).
23. S. M. Stanley, *Paleobiology* **34**, 1–21 (2008).

**Acknowledgments:** We thank all those who generated the mammal data as well as those who entered the data into the Paleobiology Database, especially J. Alroy, K. Behrensmeyer, A. Turner, M. Uhen, and M. Carrano. This is the Paleobiology Database publication number 178. We thank S. Finnegan, H. Morlon, and S. P. Quek for discussion. T.B.Q. thanks Fundação de Amparo à Pesquisa do Estado de São Paulo (2012/04072-3) and USP for funding. All of the data are available from the Paleobiology Database (<http://pa.eodb.org>).

## Supplementary Materials

[www.sciencemag.org/cgi/content/full/science.1239431/DC1](http://www.sciencemag.org/cgi/content/full/science.1239431/DC1)  
Materials and Methods  
Figs. S1 to S8  
Tables S1 and S2  
References (24–35)

22 April 2013; accepted 5 June 2013  
Published online 20 June 2013;  
10.1126/science.1239431

# Exceptional Convergence on the Macroevolutionary Landscape in Island Lizard Radiations

D. Luke Mahler,<sup>1\*</sup> Travis Ingram,<sup>2</sup> Liam J. Revell,<sup>3</sup> Jonathan B. Losos<sup>2</sup>

G. G. Simpson, one of the chief architects of evolutionary biology's modern synthesis, proposed that diversification occurs on a macroevolutionary adaptive landscape, but landscape models are seldom used to study adaptive divergence in large radiations. We show that for Caribbean *Anolis* lizards, diversification on similar Simpsonian landscapes leads to striking convergence of entire faunas on four islands. Parallel radiations unfolding at large temporal scales shed light on the process of adaptive diversification, indicating that the adaptive landscape may give rise to predictable evolutionary patterns in nature, that adaptive peaks may be stable over macroevolutionary time, and that available geographic area influences the ability of lineages to discover new adaptive peaks.

The concept of a macroevolutionary adaptive landscape—a multivariate phenotype surface on which species evolve up local adaptive peaks—has guided thinking about adaptive radiation since G. G. Simpson proposed it in

1944 (1–4). Although influential as a metaphor, Simpson's landscape has only rarely been applied to study large adaptive radiations in nature. Moreover, when applied the macroevolutionary landscape generally has been invoked to describe evolutionary dynamics within a single lineage in a particular ecological setting. In recent years, however, a number of studies have suggested that entire evolutionary radiations can exhibit phenotypic convergence when they diversify in similar environments (5–10). To the extent that such

<sup>1</sup>Center for Population Biology, University of California Davis, Davis, CA 95616, USA. <sup>2</sup>Department of Organismic and Evolutionary Biology, Harvard University, Cambridge, MA 02138, USA. <sup>3</sup>Department of Biology, University of Massachusetts Boston, Boston, MA 02125, USA.

\*Correspondence to: [lmahler@ucdavis.edu](mailto:lmahler@ucdavis.edu)

“replicated adaptive radiations” exist (11), they suggest not only that diversification over macroevolutionary time scales may be surprisingly deterministic but also that ecological factors can give rise to highly similar adaptive landscapes in geographically distinct regions (1, 2, 12).

Laboratory investigations of microbial divergence (13) and computer simulation studies (1) both suggest that stable adaptive landscapes can generate predictable evolutionary patterns, but testing this hypothesis in naturally evolving radiations requires the comparison of adaptive landscapes over macroevolutionary time scales. Investigations of this type require a two-step process in which we first test the hypothesis that radiations are more convergent than expected by chance (11), and then we ask if this convergence has resulted from diversification on similar macroevolutionary landscapes.

We used this approach to study the putative replicated adaptive radiations (2, 14) of *Anolis* lizards (anoles) on Caribbean islands. On each island in the Greater Antilles (Cuba, Hispaniola, Puerto Rico, and Jamaica), anoles have independently evolved a similar set of habitat specialists termed “ecomorphs” (such as “twig” or “grass-bush”) (14, 15). Each ecomorph is composed of morphologically and behaviorally similar species that occupy similar microhabitats. Prior studies have documented that members of the same ecomorph category from different islands cluster morphologically, providing evidence for repeated

instances of convergent evolution (16). However, these analyses omitted an important dimension of the anole radiations: so-called “unique” species that evolved a morphology and ecology not found on other islands (14, 15). The number of unique species varies among islands, from none on Puerto Rico to 14 on Cuba, and they collectively constitute approximately 20% of Greater Antillean *Anolis* diversity. Thus, although repeated evolution of the ecomorphs has been demonstrated, whether the anole radiations themselves are convergent remains an open question.

Thus, we began by asking whether the four Greater Antillean anole faunas exhibit exceptional species-for-species matching (2); i.e., greater pairwise phenotypic similarity between species on different islands than expected by chance, when the full ecomorphological diversity of lineages is considered. We compiled phylogenetic and phenotypic data for 100 of 119 Greater Antillean *Anolis* species, representing the diversity of both the ecomorph and unique species. We tested for species-for-species matching among islands using a phylogenetic comparative analysis of species similarity in a four-dimensional principal components morphospace generated from 11 traits important for niche partitioning in *Anolis*, including body size, limb and tail lengths, and adhesive toepad lamella number (14, 17). We measured the among-island Euclidean distance between each species and its nearest neighbor from each other

island in morphospace, and assessed whether the average among-island distance for anoles was lower than expected by chance via comparison to a phylogenetic null distribution (18). We simulated null morphospaces using the empirical maximum clade credibility (MCC) phylogeny from a Bayesian analysis of mitochondrial DNA and evolutionary models that account for temporal and among-trait evolutionary rate variation (17, 19). We repeated the analysis across a Bayesian posterior tree sample, obtaining qualitatively identical results (18). These analyses provide strong evidence for exceptional species-for-species matching among island anole faunas: Most species on each island are more morphologically similar to species from other islands than expected by chance ( $P = 0.003$ ; Fig. 1A).

Next, we investigated whether a macroevolutionary model involving convergent shifts to common peaks on a Simpsonian landscape can explain the evolution of remarkably similar faunas on these four Caribbean islands. We applied a new method (SURFACE) to infer the history of adaptive diversification in anoles using a phylogeny and phenotypic data. This method fits a model of adaptive radiation in which lineages may undergo shifts to adaptive peaks on a macroevolutionary landscape without reference to a priori hypotheses specifying which lineages correspond to particular peaks (18, 20). In this model, lineages may undergo shifts to otherwise unoccupied peaks or to those shared with other lineages, which gives us the ability to explicitly model the macroevolutionary convergence of independent lineages in a common phenotype space. Starting with an Ornstein-Uhlenbeck model (21, 22) in which all species are attracted to a single adaptive peak in trait space, SURFACE uses a stepwise model selection procedure based on the finite-samples Akaike information criterion ( $AIC_c$ ) (23, 24) to fit increasingly complex multippeak models. At each step, a new peak shift is added to the branch of the phylogeny that most improves model fit across all traits, and shifts are added until none result in further improvement. To identify convergence, the method then evaluates whether the  $AIC_c$  score is further improved by permitting these independent lineages to shift toward shared adaptive peaks rather than requiring each to occupy a unique peak. We compared the convergent landscape model to several alternatives, including three variants of the “early burst” model of adaptive radiation, which features a diversity-dependent decline in evolutionary rate but does not explicitly model adaptation or convergence on a macroevolutionary landscape (17, 19).

A Simpsonian model of peak shifts on a shared macroevolutionary adaptive landscape best explains the evolution of ecomorphological traits in Greater Antillean *Anolis*. Convergence of lineages to shared adaptive peaks was the dominant mode of macroevolutionary trait change for these replicated island radiations: A landscape model with explicit convergence was strongly favored over the best non-convergent landscape model ( $\Delta AIC_c = 162.6$ ;

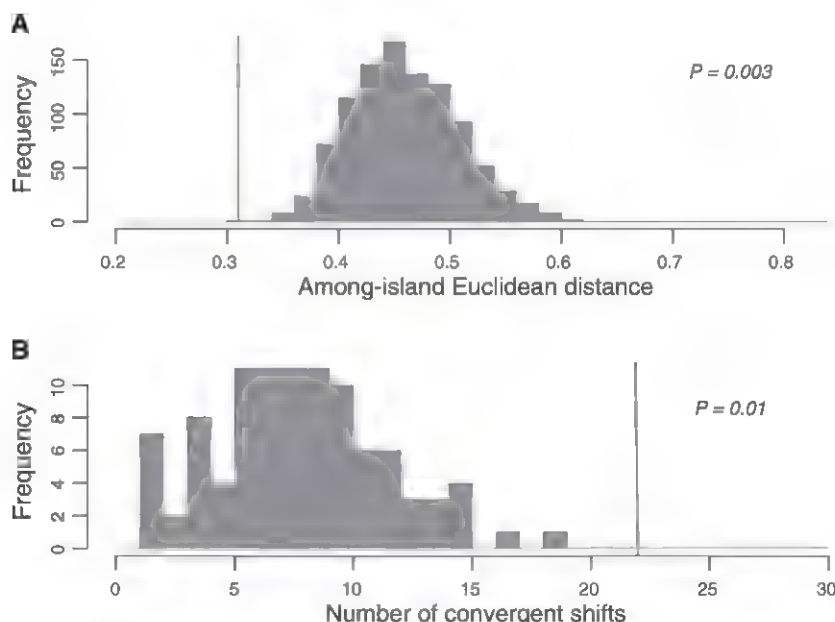


**Fig. 1. Morphological similarity among Greater Antillean *Anolis* faunas is due to exceptional convergence.** (A) Anole species are more similar to their closest matches from other islands than expected by chance. The vertical line indicates the average distance separating each Greater Antillean species from the most morphologically similar species on other islands (among-island Euclidean distance); the histogram depicts a null distribution of the same scores calculated from 999 data sets generated by evolutionary simulation. (B) The great inter-island similarity (low distance) results from an exceptionally large number of convergent shifts to shared peaks on a macroevolutionary adaptive landscape during anole diversification. Here, the vertical line depicts the number of convergent peak shifts detected for Greater Antillean anoles, and the histogram depicts a null distribution of convergent shifts detected from 99 simulated data sets.



fig. S2), and even more strongly favored over models without peaks ( $\Delta AIC_c \geq 279.3$ ; fig. S2). Peak shifts on the adaptive landscape were common as anoles diversified (29 lineage-specific shifts), with 76% of shifts involving convergence in morphospace (Figs. 1B and 2 and Table 1). The estimated landscape contained 15 adaptive peaks, with 8 occupied by more than one lineage. These convergent peaks attracted 2.8 lineages on average, and all but one hosted lineages from multiple islands. Overall, the number of convergent adaptive peak shifts was significantly greater than expected by chance ( $P = 0.01$ ; Fig. 1B), and these shifts account for the exceptional similarity among island faunas (18). The number and position of peak shifts varied across 100 phylogenies, but the number of convergent shifts was similar for all trees (Table 1). Species traditionally grouped in the same ecomorph class (14–16) tended to be attracted toward the same adaptive peak (fig. S4).

Our comparison of macroevolutionary models suggests that the adaptive landscape plays an important role in shaping parallel diversification. The only model to account for the observed convergence of entire island anole faunas was a Simpsonian model (3, 5, 20–22), in which lineages experience selection toward common peaks on the adaptive landscape (fig. S1). Fitted peaks on the anole landscape correspond to trait combinations that have been shown experimentally to be adaptive for microhabitat partitioning (14) (fig. S4). Although it is possible that evolutionary constraints may play a role in shaping whole-fauna convergence, in the case of anoles the evidence points to a dominant role for selection. The *Anolis* radiation unfolded over tens of millions of years (14), a time scale over which constraints on the production of variation are unlikely to be maintained, especially for quantitative traits (25). Constraint seems an even less likely culprit considering that diverse radiations of Central and South American *Anolis*, which occur in ecologically different communities, exhibit many morphologies not seen in Caribbean forms (26), strongly suggesting that repeated Greater Antillean convergence is not due to intrinsic limits on morphological variation.

Replication of adaptive radiations is readily attainable in simple systems over short time scales (2, 13), but convincing examples at a grander macroevolutionary scale have so far been lacking. Why this is the case is not yet clear, but our results argue against the possibility that the temporal lability of adaptive landscapes precludes faunal convergence over long time scales. The Greater Antillean anole radiation is old (with a minimum age of 30 to 40 million years) (14), and most ecomorphological diversity among anoles arose long ago (17) (Fig. 2), suggesting not only that the adaptive landscape for anoles is similar across islands but also that it is relatively static in its principal features (14, 27). Stable landscapes are further indicated by the similarity of adaptive peaks discovered by anole lineages from different islands, which would be highly unlikely if adaptive landscapes were themselves highly labile (3, 27). It

remains to be seen whether this stability is a general feature of adaptive radiation, but our observations support the hypothesis that stable macroevolutionary landscapes underlie the common pattern of long-term phenotypic stasis in both fossil and comparative data sets (28, 29).

Although convergence is the most conspicuous feature of Greater Antillean anole radiations, the island faunas are far from identical. Most no-

tably, we found evidence for a number of non-convergent shifts to island-specific peaks. However, such peaks are occupied only on the larger islands of Hispaniola and Cuba, a predicted “area effect” from adaptive radiation theory (1). Larger areas provide greater opportunities for diversification (1, 30), which may permit lineages to more fully explore the macroevolutionary landscape and discover peaks not reached on smaller islands (1).

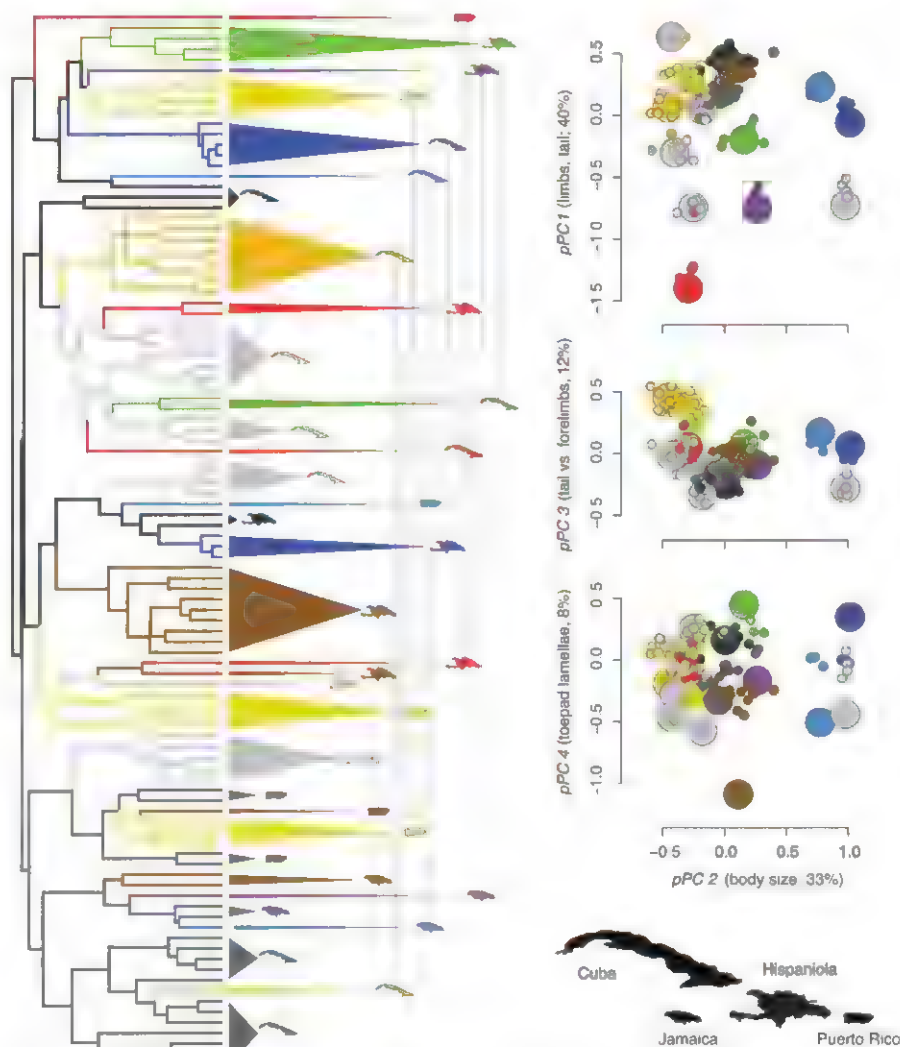


**Fig. 2. Phenotypic convergence on the macroevolutionary adaptive landscape in island radiations of Greater Antillean *Anolis*.** MCC phylogeny (left panel), painted to depict the estimated phylogenetic history of adaptive peak shifts. Branches and island silhouettes representing geographic location are colored according to adaptive peak. Convergent peaks are colored and are connected by solid lines; with one exception, these peaks attract lineages from multiple islands. Nonconvergent peaks are light gray (single-island radiations), or black or dark gray (radiations that spread to multiple islands; these islands are connected by dashed lines). Right panels show that anole species (small circles) cluster near their inferred adaptive peak (large circles) in morphospace, especially for pPCs 1 to 3 (primary trait correlations and variance explained are reported in the axis labels). Inferred convergent peaks broadly correspond to *Anolis* ecomorph classes, a consistent finding across phylogenies, although specific peak assignments vary from tree to tree (18) (fig. S4). In the MCC estimate plotted here, grass-bush specialists are attracted to dark or light yellow peaks. Larger and smaller twig specialists occur on purple and red peaks, respectively. Green peaks contain trunk-crown specialists, and brown peaks contain trunk-ground specialists. Dark blue peaks contain large crown-giant anoles; light blue peaks contain smaller giant anoles. A single dark gray peak contains additional trunk-ground and trunk-crown species; although similar because of inherited ancestral condition rather than convergence in this reconstruction phenotypically similar species on this peak occur on three different islands.

**Table 1. SURFACE convergence parameters estimated using the MCC tree, as well as 100 trees from the Bayesian posterior probability distribution of *Anolis* phylogeny.**

	MCC phylogeny	Mean (SD) for 100 sampled phylogenies
Adaptive peak shifts	29	25.7 (2.1)
Convergent adaptive peak shifts	22	20.2 (1.9)
Adaptive peaks	15	12.7 (1.4)
Convergent adaptive peaks	8	7.2 (0.97)
Convergence fraction (convergent peak shifts/total peak shifts)	0.76	0.79 (0.045)
Average number of lineages converging to each shared adaptive peak	2.8	2.8 (0.30)
Fraction of convergent peaks with lineages from multiple islands	0.88	0.94 (0.074)

Anoles have diversified into many more species on the larger islands (14, 31). Given the number of convergent and unique adaptive peak shifts that have occurred across the Greater Antilles in anoles, the area effect hypothesis predicts that all endemic unique peaks should occur on Cuba and Hispaniola, as observed (18) (fig. S3). Thus, in this system, even the apparently contingent evolution of unique ecomorphologies may be, to some extent, predictable—in this case a result of the speciation-area relationship (30).

Gould famously argued that evolution over long time scales is “utterly unpredictable and quite unrepeatable” (32, p. 14) due to historical contingency. Widespread convergence among entire faunas of Greater Antillean *Anolis* refutes Gould’s claim and shows that adaptation can overcome the influence of chance events on the course of evolution. Our demonstration of deterministic convergence on a macroevolutionary adaptive landscape complements studies of diversification in species numbers in showing that many features of large-scale radiations may be surprisingly predictable. A recent analysis discovered that both island diversification rate and standing species richness in Greater Antillean anoles could be predicted from island size and time since colonization (31). In cichlids, whether colonizing lineages will radiate in African lakes can be predicted from the intrinsic traits of the colonist and the ecological opportunities provided by the new habitat (33). Together, these studies suggest that the primary aspects of evolutionary radiation—adaptation and the proliferation of species—may in some cases be largely deterministic.

#### References and Notes

- S. Gavrilets, A. Vose, *Proc. Natl. Acad. Sci. U.S.A.* **102**, 18040–18045 (2005).
- D. Schluter, *The Ecology of Adaptive Radiation* (Oxford Univ. Press, Oxford, 2000).
- G. G. Simpson, *Tempo and Mode in Evolution* (Columbia Univ. Press, New York, 1944).
- E. I. Svensson, R. Calsbeek, Eds., *The Adaptive Landscape in Evolutionary Biology* (Oxford Univ. Press, Oxford, 2012).
- B. Frédérich, L. Sorenson, F. Santini, G. J. Slater, M. E. Alfaro, *Am. Nat.* **181**, 94–113 (2013).
- R. Gillespie, *Science* **303**, 356–359 (2004).
- T. J. Givnish, in *The Biology of Biodiversity*, M. Kato, Ed. (Springer-Verlag, Tokyo, 1999), pp. 67–90.
- M. Muschick, A. Indermaur, W. Salzburger, *Curr. Biol.* **22**, 2362–2368 (2012).
- M. L. J. Stifassny, A. Meyer, *Sci. Am.* **280**, 64–69 (1999).

- K. A. Young, J. Snoeks, O. Seehausen, *PLoS ONE* **4**, e4740 (2009).
- Past studies of convergence between species-rich radiations have been selective in scope and have not compared entire radiations. Even lineages diversifying randomly under genetic drift will generate many convergent pairs (34), as will radiations adapting on a labile macroevolutionary landscape (27). Much of the diversity unsampled by past studies may be nonconvergent, so that different radiations may share many convergent species pairs while being unexceptionally similar at the whole-radiation scale.
- M. L. Cody, H. A. Mooney, *Annu. Rev. Ecol. Syst.* **9**, 265–321 (1978).
- R. Kassen, *Ann. N. Y. Acad. Sci.* **1168**, 3–22 (2009).
- J. B. Losos, *Lizards in an Evolutionary Tree: Ecology and Adaptive Radiation of Anoles* (Univ. of California Press, Berkeley, CA, 2009).
- E. E. Williams, in *Lizard Ecology: Studies of a Model Organism*, R. B. Huey, E. R. Pianka, T. W. Schoener, Eds. (Harvard Univ. Press, Cambridge, MA, 1983), pp. 326–370.
- J. B. Losos, T. R. Jackman, A. Larson, K. de Queiroz, L. Rodríguez-Schettino, *Science* **279**, 2115–2118 (1998).
- D. L. Mahler, L. J. Revell, R. E. Glor, J. B. Losos, *Evolution* **64**, 2731–2745 (2010).
- Information on materials and methods is available as supplementary material on Science Online.

- L. J. Harmon *et al.*, *Evolution* **64**, 2385–2396 (2010).
- T. Ingram, D. L. Mahler, *Methods Ecol. Evol.* **4**, 416–425 (2013).
- M. A. Butler, A. A. King, *Am. Nat.* **164**, 683–695 (2004).
- T. F. Hansen, *Evolution* **51**, 1341 (1997).
- M. E. Alfaro *et al.*, *Proc. Natl. Acad. Sci. U.S.A.* **106**, 13410–13414 (2009).
- G. H. Thomas, R. P. Freckleton, *Methods Ecol. Evol.* **3**, 145–151 (2012).
- G. L. Conte, M. E. Arnegard, C. L. Peichel, D. Schuster, *Proc. Biol. Sci.* **279**, 5039–5047 (2012).
- G. Pinto, D. L. Mahler, L. J. Harmon, J. B. Losos, *Proc. Biol. Sci.* **275**, 2749–2757 (2008).
- T. F. Hansen, in *The Adaptive Landscape in Evolutionary Biology*, E. Svensson, R. Calsbeek, Eds. (Oxford Univ. Press, Oxford, 2012), pp. 205–226.
- S. Estes, S. J. Arnold, *Am. Nat.* **169**, 227–244 (2007).
- J. C. Uyeda, T. F. Hansen, S. J. Arnold, J. Pienaar, *Proc. Natl. Acad. Sci. U.S.A.* **108**, 15908–15913 (2011).
- Y. Kisel, T. G. Barraclough, *Am. Nat.* **175**, 316–334 (2010).
- D. L. Rabosky, R. E. Glor, *Proc. Natl. Acad. Sci. U.S.A.* **107**, 22178–22183 (2010).
- S. J. Gould, *Wonderful Life: The Burgess Shale and the Nature of History* (Norton, New York, 1989).
- C. E. Wagner, L. J. Harmon, O. Seehausen, *Nature* **487**, 366–369 (2012).
- C. T. Stayton, *J. Theor. Biol.* **252**, 1–14 (2008).

**Acknowledgments:** We thank G. Bradburd, C. Davis, L. Harmon, and F. Jenkins for discussion and advice; the National Evolutionary Synthesis Center and NSF for financial support; and three anonymous reviewers for insightful feedback. Data are archived in Dryad (<http://datadryad.org>, doi: 10.5061/dryad.9g182).

#### Supplementary Materials

[www.sciencemag.org/cgi/content/full/341/6143/292/DC1](http://www.sciencemag.org/cgi/content/full/341/6143/292/DC1)  
Materials and Methods  
Figs. S1 to S9  
Tables S1 to S5  
References (35–42)  
Author Contributions

5 November 2012; accepted 5 June 2013  
10.1126/science.1232392

## Predicting and Manipulating Cardiac Drug Inactivation by the Human Gut Bacterium *Eggerthella lenta*

Henry J. Haider,<sup>1</sup> David B. Gootenberg,<sup>1</sup> Kelly Chatman,<sup>1</sup> Gopal Sirasani,<sup>2</sup> Emily P. Balskus,<sup>2</sup> Peter J. Turnbaugh<sup>1\*</sup>

Despite numerous examples of the effects of the human gastrointestinal microbiome on drug efficacy and toxicity, there is often an incomplete understanding of the underlying mechanisms. Here, we dissect the inactivation of the cardiac drug digoxin by the gut Actinobacterium *Eggerthella lenta*. Transcriptional profiling, comparative genomics, and culture-based assays revealed a cytochrome-encoding operon up-regulated by digoxin, inhibited by arginine, absent in nonmetabolizing *E. lenta* strains, and predictive of digoxin inactivation by the human gut microbiome. Pharmacokinetic studies using gnotobiotic mice revealed that dietary protein reduces the in vivo microbial metabolism of digoxin, with significant changes to drug concentration in the serum and urine. These results emphasize the importance of viewing pharmacology from the perspective of both our human and microbial genomes.

**H**umans are home to large and diverse microbial communities, the most abundant of which resides in the gastrointestinal tract. Recent studies have highlighted the clinical relevance of the biotransformations catalyzed by

the human gut microbiome, including alterations to the bioavailability, activity, and toxicity of therapeutic drugs (1, 2). Although >40 drugs are metabolized by the gut microbiome, little is known about the underlying mechanisms. This



knowledge is critical to enable the rational design of pharmaceutical or dietary interventions.

The inactivation of the cardiac drug digoxin provides a promising starting point for understanding microbial drug metabolism. Digoxin and other cardiac glycosides have been widely used for hundreds of years to treat heart failure and arrhythmias. Therapeutic effects are accomplished indirectly when inhibition of the  $\text{Na}^+/\text{K}^+$  ATPase in cardiac myocytes raises the intracellular  $\text{Ca}^{2+}$  concentration (3). Digoxin has a narrow therapeutic range (0.5 to 2.0 ng/ml) (3), and some patients excrete the inactive digoxin metabolite, dihydrodigoxin, in which the lactone ring is reduced (fig. S1A) (4). This modification disrupts ring planarity, which is thought to shift positioning within the binding pocket of the  $\text{Na}^+/\text{K}^+$  ATPase, resulting in decreased target affinity (5). Coadministration of broad-spectrum antibiotics increases serum digoxin (4), and *Eggerthella lenta* reduces digoxin in vitro (6). Before this work, the molecular mechanism of digoxin reduction and the factors that alter microbial drug inactivation in vivo were unknown.

We confirmed that *E. lenta* DSM2243, the type strain, reduces digoxin in vitro (7) and that

arginine inhibits this reaction (Fig. 1A). The growth of *E. lenta* DSM2243 was stimulated by arginine supplementation (Fig. 1A and fig. S2), indicative of using the arginine dihydrolase pathway for adenosine 5'-triphosphate (ATP) (8). Citrulline (an intermediate upstream of ATP production) stimulated growth, whereas ornithine (an end product) did not (figs. S2 and S3).

*E. lenta* cultures were grown anaerobically in rich medium supplemented with low and high levels of arginine (0.25% and 1.25%, respectively) in the presence or absence of digoxin (10  $\mu\text{g}/\text{ml}$ ), and we performed RNA sequencing (RNA-Seq) on the resultant cellular biomass (figs. S4 to S6 and table S1). A two-gene operon was highly up-regulated after exposure to digoxin during exponential growth (>100-fold) (Fig. 1B and tables S2 and S3). These two genes, referred to here as the cardiac glycoside reductase (*cgr*) operon (gene labels: *cgr1* and *cgr2*), encode proteins that are homologous to bacterial cytochromes and are therefore potentially capable of using digoxin as an alternative electron acceptor. Incubation of *E. lenta* with multiple cardiac glycosides and their reduced forms revealed that the *cgr* operon is broadly responsive to compounds with an  $\alpha,\beta$ -unsaturated butyrolactone ring (figs. S7 to S9 and table S5).

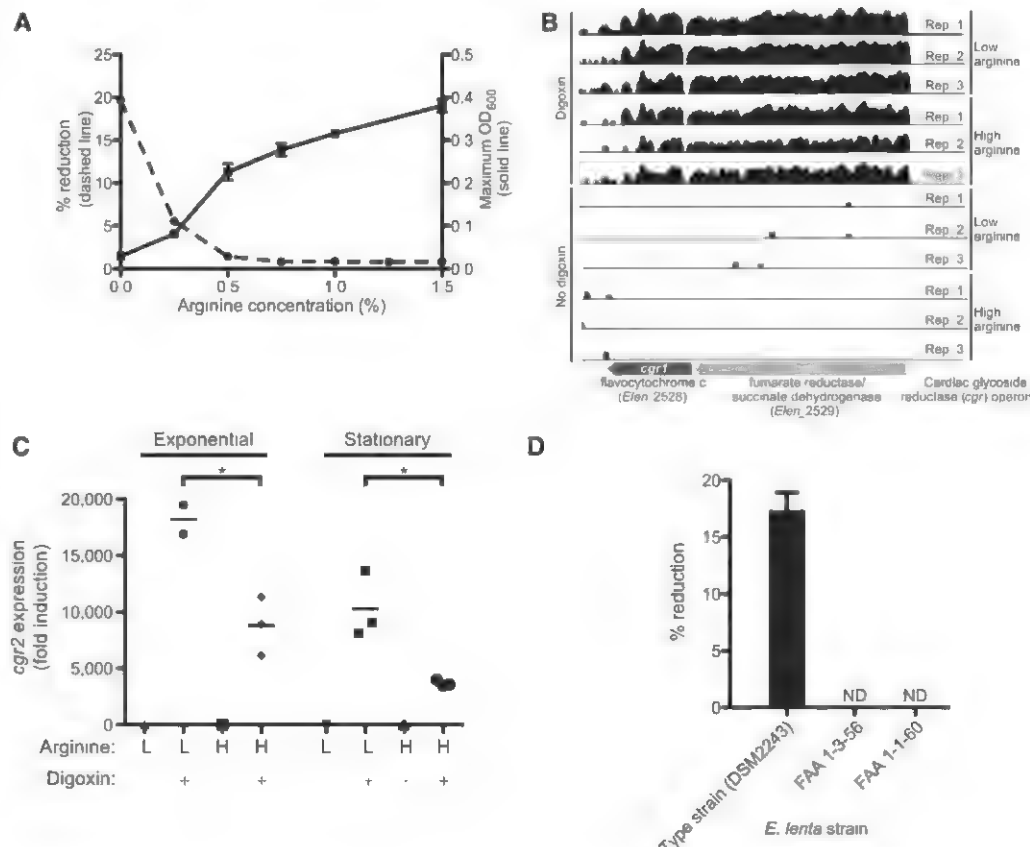
Digoxin induction was increased in low-arginine conditions during both its exponential and stationary phases, relative to cultures exposed to high levels of arginine (fig. S10, A and B). *cgr* induction by digoxin and the growth phase-

dependent effects exerted by arginine were confirmed on independent samples using quantitative reverse transcription polymerase chain reaction (QRT-PCR) (Fig. 1C, fig. S10C, and table S4). Unlike arginine, ornithine did not repress *cgr2* expression (fig. S11). These results are consistent with the hypothesis that arginine represses *cgr* operon expression and thereby inhibits digoxin reduction.

Next, we tested three strains of *E. lenta* (DSM2243, FAA 1-3-56, and FAA 1-1-60) (9, 10) for digoxin reduction; the type strain was the sole strain capable of digoxin reduction in vitro (Fig. 1D). Comparative genomics revealed that the type strain was nearly indistinguishable from the other two strains when common marker genes were used (fig. S12). Reciprocal BLASTP comparisons of all protein-coding sequences of the three fully sequenced *E. lenta* strains revealed that the type strain shared 79.4% and 90.5% of its proteome with strains FAA 1-3-56 and FAA 1-1-60, respectively (fig. S12). The *cgr* operon was unique to the type strain (table S6); furthermore, the two nonreducing *E. lenta* strains were missing three genomic loci, which were also up-regulated by digoxin, and are predicted to encode membrane transporters for the uptake of small molecules and glycosides (fig. S13). Arginine did not significantly decrease the expression level of these transporters (fig. S14).

Strain-level variation provides an explanation for the difficulties in predicting dihydrodigoxin levels in cardiac patients by the presence or ab-

**Fig. 1. Discovery of a bacterial operon induced by digoxin.** (A) Arginine stimulates the growth of *E. lenta* DSM2243 in vitro while blocking the reduction of digoxin. Maximum optical density (absorbance) at 600 nm ( $\text{OD}_{600}$ ) (solid line; values are means  $\pm$  SEM;  $n = 3$ ) and digoxin percentage reduction efficiency (dashed line; values are means;  $n = 2$ ) after 48 hours of growth. (B) RNA-Seq profiles of the *cgr* operon are shown with and without digoxin during exponential growth in medium containing low or high arginine. The height is proportional to the natural log of the number of unambiguous sequencing reads mapped to each base. (C) *cgr2* transcription as determined by QRT-PCR. Asterisks indicate statistical significance by Student's *t* test ( $P < 0.05$ ). Horizontal lines are means;  $n = 2$  to 3. (D) Identification of two strains of *E. lenta* incapable of reducing digoxin. Values are means  $\pm$  SEM;  $n = 3$ . ND, no reduction detected.



sence of *E. lenta* (6, 11). We used quantitative PCR (QPCR) to measure the abundance of the *cgr* operon relative to the *E. lenta* 16S ribosomal RNA (rRNA) gene (the “*cgr* ratio”) in microbial community DNA from 20 unrelated healthy people, along with ex vivo digoxin reduction assays. The results stratified our cohort into low reducers ( $12.82 \pm 10.68\%$  reduction;  $n = 6$ ) and high reducers ( $96.25 \pm 7.69\%$  reduction;  $n = 14$ ) (Fig. 2A). The *cgr* ratio was significantly increased for the high reducers ( $1.058 \pm 0.562$ ) when compared with low reducers ( $0.425 \pm 0.582$ ;  $P < 0.05$ , Student's *t* test) (Fig. 2B and fig. S15). Linear regression of reduction efficiency with the *cgr* ratio revealed a significant correlation ( $R^2 = 0.22$ ,  $P < 0.05$ ), whereas the abundance of *E. lenta* failed to predict the extent of reduction ( $R^2 = 0.06$ ,  $P = 0.30$ ). The optimal *cgr* ratio cutoff (0.6) predicted digoxin reduction efficiency with a sensitivity of 86%, specificity of 83%, and precision of 92%.

Coculture of *E. lenta* with the fecal microbiome enhanced the efficiency of digoxin reduction. Each low-reducing fecal sample was incubated with the type (reducing) and FAA 1-3-56 (nonreducing) strains of *E. lenta*. The communities incubated with the type strain reduced more digoxin ( $95.39 \pm 2.41\%$ ) than the type strain alone ( $68.91 \pm 7.70\%$ ;  $P < 0.05$ , Mann-Whitney *U* test) (Fig. 2C). The *cgr* ratio was significantly elevated after coculture (Fig. 2D) and was tightly

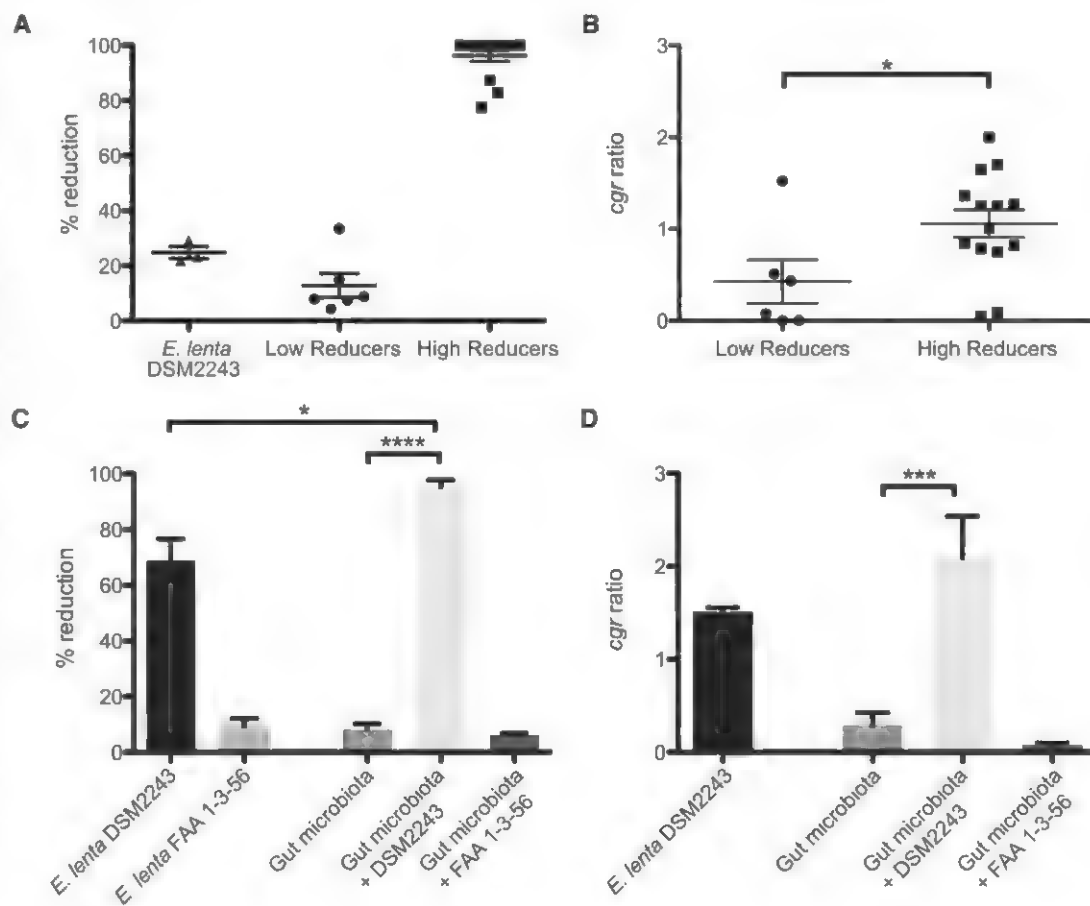
linked to reduction efficiency ( $R^2 = 0.74$ ,  $P < 0.0001$ ). An explanation for the observed microbial synergy is that the fastidious growth of *E. lenta* is promoted by growth factors supplied by the gut microbiota, a phenomena that is known to affect the metabolism of environmental pollutants by soil microbial communities (12), along with competition for arginine that boosts digoxin reduction by *E. lenta*. Consistent with these hypotheses, the abundance of the *E. lenta* type strain was significantly increased in the presence of a complex microbial community ( $1.6e6 \pm 4.8e5$  versus  $1.8e5 \pm 8.4e3$  in isolation;  $P < 0.05$ , Mann-Whitney test), and arginine supplementation suppressed the reduction of digoxin during coculture (fig. S16).

Diet could also explain interindividual variations in digoxin reduction. In vitro growth of *E. lenta* showed that, although arginine stimulated cell growth, it decreased *cgr* operon expression and prevented the conversion of digoxin to dihydrodigoxin (Fig. 1, A and C, and fig. S10). These observations led us to hypothesize that increased consumption of dietary protein, and the corresponding increase in arginine, would inhibit the in vivo reduction of digoxin by *E. lenta*. Germ-free adult male Swiss-Webster mice were colonized with the type strain before being fed diets differing only in the amount of total protein ( $n = 5$  mice/group) (tables S7 and S8 and fig. S17A). *E. lenta* colonized mice fed both diets

(fig. S18A) and exhibited high levels of expression of the *cgr* operon (fig. S18B). Quantification of serum and urine digoxin (7) revealed significant increases in mice fed the high-protein diet, indicative of suppressed digoxin reduction by *E. lenta* (Fig. 3, A and B). These trends were also consistent with fecal analysis of samples from each group of mice 4 to 16 hours after digoxin administration (Fig. 3). We also confirmed that the high-protein diet significantly elevated the amino acids in the distal small intestine (7), which resulted in a fold increase of  $1.71 \pm 0.06$  ( $P < 0.001$ , Wilcoxon test) (tables S9 and 10).

We controlled for the indirect effects of host diet and colonization that might alter digoxin pharmacokinetics irrespective of reduction by *E. lenta*. Germ-free mice were colonized with either the digoxin-reducing type strain or the nonreducing FAA 1-3-56 strain and subsequently fed the same two diets (fig. S17B). As seen before, we detected colonization with both strains, high-*cgr* operon expression, and elevated serum and urine digoxin on the high-protein diet for mice colonized with the type strain (Fig. 3, C and D, and fig. S18, C and D). Diet did not significantly affect the serum or urine digoxin levels of mice colonized with the nonreducing strain (Fig. 3, C and D). Serum digoxin was significantly lower in mice colonized with the type strain fed the 0% protein diet, relative to those colonized with the nonreducing strain ( $4.91 \pm 1.56$  ng/ml vs.

**Fig. 2. A microbial biomarker predicts the inactivation of digoxin.** (A) Liquid chromatography–mass spectrometry (LC-MS) was used to quantify digoxin reduction in the fecal microbiomes of 20 unrelated individuals. (B) The *cgr* ratio was significantly different between low and high reducers. Data represent QPCR with the *cgr2* gene, and *E. lenta*-specific 16S rDNA primers (table S4). (C) Five low-reducing fecal microbial communities were incubated for 5 days in the presence or absence of *E. lenta* DSM2243 or FAA 1-3-56. LC-MS was used to quantify the completion of digoxin reduction. Supplementation with the nonreducing strain of *E. lenta* did not significantly affect digoxin reduction efficiency. (D) The *cgr* ratio was obtained for each of the low-reducing microbial communities after incubation. Outliers were identified using Grubbs' test ( $P < 0.01$ ) and removed. Values are means  $\pm$  SEM. Points in (A) and (B) represent biological replicates. Asterisks indicate statistical significance by Student's *t* test (\* $P < 0.05$ ; \*\*\* $P < 0.001$ ; \*\*\*\* $P < 0.0001$ ).





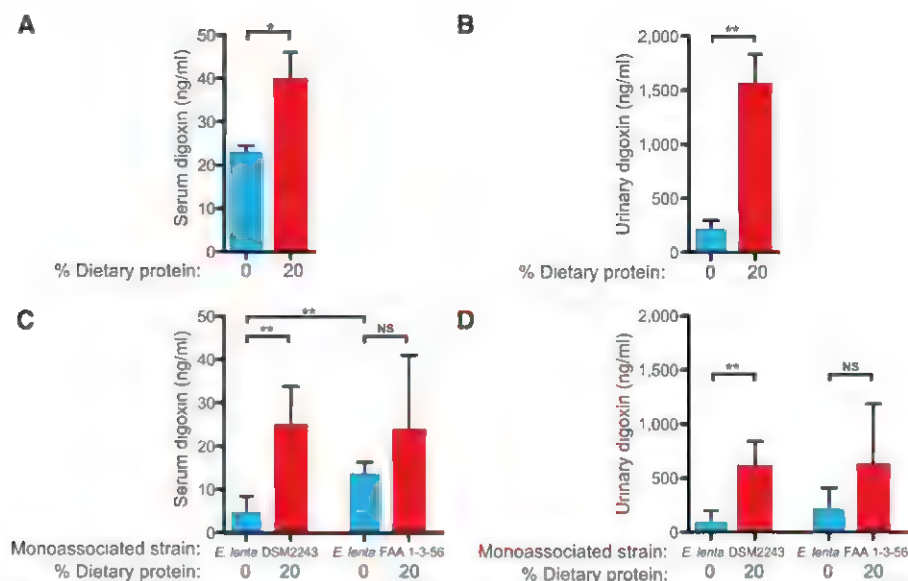


**Fig. 3. Dietary protein blocks the inactivation of digoxin.** Serum (A) and urinary (B) digoxin levels from the type strain experiment. Fecal digoxin levels showed a consistent trend: the mean area under the curve was 6.226 ng digoxin per hour per ml in germ-free mice, 3.576 for mice fed the 0% protein diet, and 6.364 for mice fed the 20% protein diet. Serum (C) and urinary (D) digoxin levels from each group. Digoxin levels were quantified by enzyme-linked immunosorbent assay (ELISA) (7). Values are means  $\pm$  SEM. Asterisks indicate statistical significance by Student's *t* test (\**P* < 0.05; \*\**P* < 0.01). *n* = 4 to 5 mice per group. NS, not significant.

$13.8 \pm 1.25$ ; *P* < 0.01, Student's *t* test) (Fig. 3C). Together, these results suggest that the enhanced free amino acids available to *E. lenta* inhibited the activity of the *cgr* operon and increased the bioavailability of digoxin.

An expanded model of digoxin pharmacokinetics is now emerging: Colonization by distinct strains of *E. lenta*, microbial interactions, and host diet act together to influence drug levels (fig. S19). Follow-up studies in cardiac patients are necessary to determine whether rapid QPCR-

based biomarker assessments of the gut microbiome can guide dosage regimes. It may also be possible to provide dietary guidelines or supplements that prevent microbial drug metabolism. More broadly, our results emphasize that a comprehensive view of pharmacology includes the structure and activity of our resident microbial communities and a deeper understanding of their interactions with each other, with their host habitat, and with the nutritional milieu of the gastrointestinal tract.

## References and Notes

1. H. J. Haider, P. J. Turnbaugh, *Science* **336**, 1253–1255 (2012).
2. B. D. Wallace *et al.*, *Science* **330**, 831–835 (2010).
3. L. S. Goodman *et al.*, *Goodman & Gilman's the Pharmacological Basis of Therapeutics* (McGraw-Hill, New York, ed. 12, 2011).
4. J. Lindenbaum, D. G. Rund, V. P. Butler Jr., D. Tse-Eng J. R. Saha, *N. Engl. J. Med.* **305**, 789–794 (1981).
5. C. D. Farr *et al.*, *Biochemistry* **41**, 1137–1148 (2002).
6. J. F. Dobkin, J. R. Saha, V. P. Butler Jr., H. C. Neu, J. Lindenbaum, *Science* **220**, 325–327 (1983).
7. Materials and methods are available as supplementary materials on Science Online.
8. J. F. Sperry, T. D. Wilkins, *J. Bacteriol.* **127**, 780–784 (1976).
9. E. Saunders *et al.*, *Stand. Genomic Sci.* **1**, 174–182 (2009).
10. K. E. Nelson *et al.*, *Science* **328**, 994–999 (2010).
11. V. I. Mathan, J. Wiederman, J. F. Dobkin, J. Lindenbaum, *Gut* **30**, 971–977 (1989).
12. X. Maymó-Gatell, Y. Chien, J. M. Gossett, S. H. Zinder, *Science* **276**, 1568–1571 (1997).

**Acknowledgments:** B. Budnik and S. Trauger for liquid chromatography–mass spectrometry (LC-MS) analyses; V. Yeliseyev, A. Liou, and R. Carmody for mouse studies; C. Reardon and C. Daly for sequencing support; C. Maurice, L. David, R. Dutton, B. Wolfe, J. Button, M. Elliot, Y. Falanga, R. Losick, A. Murray, and B. Stern for helpful discussions. Mouse experiments were done with the generous support of the Harvard Digestive Diseases Center and the University of North Carolina gnotobiotic cores. This work was supported by grants from the NIH (P50 GM068763) and the Harvard Digestive Diseases Center (2P30DK034854-26). H.J.H. is supported by the Canadian Institutes of Health Research (MFE-112991). RNA-Seq data are deposited in the Gene Expression Omnibus (GEO) database (accession GSE43919).

## Supplementary Materials

www.sciencemag.org/cgi/content/full/341/6143/295/DC1  
Materials and Methods  
Figs. S1 to S19  
Tables S1 to S10  
References (13–25)

30 January 2013; accepted 14 June 2013  
10.1126/science.1235872

**DIGITAL HD VIDEO CONTROLLER**

Easy to use, fast live images, brilliant results—microscope users achieve all of this and more with the new Leica MC120 HD and MC170 HD cameras. The new high-performance cameras provide high speed, precise images in real time at a rate of up to 30 frames per second. They are directly connectable to an HD monitor as a stand-alone solution or to a computer via USB interface. While the 2.5 megapixel Leica MC120 HD is ideal for almost all microscopic applications, the Leica MC170 HD with a resolution of 5 megapixels is especially well suited for acquiring the finest details at low magnifications. For fast documentation or hands-on training the user can record brilliant full HD movie clips as MP4. Images and movies are easily, cost-effectively stored with high quality onto a portable SD-card. The infrared remote control allows direct and convenient control of all camera parameters such as brightness, gain, and contrast of the image as well as white balance operations, changing to other camera modes, and image capture.

**Leica Microsystems**

For info: 800-248-0123 | [www.leica-microsystems.com](http://www.leica-microsystems.com)

**EVAPORATORS**

The third generation Acid-Resistant EZ-2 Plus Evaporator uses inert- and corrosion-proof materials to enable it to withstand up to 6N Hydrochloric acid, 70% Nitric acid, and most acid chlorides including thionyl chloride. These strongly acidic materials can be routinely removed from samples without any loss of performance or long-term deterioration in the system. Acid resistant components in the Acid-Resistant EZ-2 Plus include a PTFE coated evaporation chamber, a glass condenser, and all metallic parts that come into contact with removed solvent, which are manufactured from acid resistant Hasteloy C steel. The innovative design of the Acid-Resistant EZ-2 Plus presents real advantages for all scientists and engineers tasked with removing both regular solvents and strongly acidic chemicals. Intuitive controls and large LCD display provide ease of use comparable to a typical rotary evaporator yet the Acid-Resistant EZ-2 Plus can process many more samples per unit time.

**Genevac**

For info: +44-(0)-1473-240000 | [www.genevac.com](http://www.genevac.com)

**DIGITAL SLIDE SCANNER**

Axio Scan.Z1 is an automated microscope system that allows researchers to digitalize fixed tissue sections and cytologic specimens in brightfield and fluorescence. Thanks to the tray concept, Axio Scan.Z1 captures the entire specimen area of the microscope slide—including the edge. Just a few minutes later, the self-calibrating automated slide scanner presents specimens on high-quality virtual slides. Up to 100 microscope slides can be digitalized at a time. For fluorescence applications, filter wheels switch wavelengths in just 50 ms. Sensitive cameras and maximally corrected optics achieve optimal image quality. The Colibri.2 ultraviolet-free LED light source and a focus finder with oblique illumination, the Ring Aperture Contrast, ensure maximum protection for the sample. Axio Scan.Z1 is operated by ZEN imaging software from Carl Zeiss. ZEN allows users either to work with predefined recording parameters automatically or to select all settings individually.

**Carl Zeiss**

For info: 800-233-2343 | [www.zeiss.com/micro](http://www.zeiss.com/micro)

**MULTISAMPLE HOMOGENIZER**

The Multi-Prep Laboratory Homogenizing System makes multisample homogenizing simple. This compact, benchtop unit was designed with decades of homogenizing experience and was created to address the challenges and rigorous nature of multisample homogenization. The Multi-Prep's unique automated system improves lab productivity by homogenizing up to six samples at a time quickly and with ease. All samples are homogenized simultaneously in mere seconds, ensuring accurate homogenizing speed and results. Precision crafted 316 Stainless Steel Multi-Prep Sample Probes deliver accurate and quick homogenizing results that are superior to plastic disposable generators while still addressing the concerns of avoiding cross contamination. Their multipack design means a clean, durable multisample probe can be used each and every time. Typical run time is mere seconds. The short sample runtime coupled with the ability to process six samples per cycle can result in 300 homogenized samples per hour.

**ProScientific**

For info: 203-267-4600 | [www.proscientific.com](http://www.proscientific.com)

**PLATE HEATER**

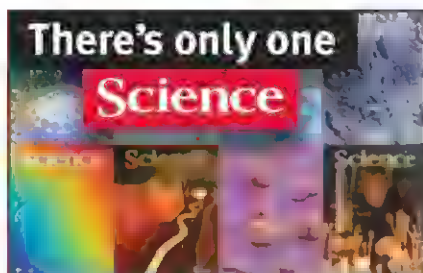
The new Plate Heater is designed specifically for cell biologists who require accurate and precise temperature control for plates in laminar flow hoods. The new Plate Heater has been developed to solve issues associated with short-term assay incubations in a laminar flow hood environment. The Plate Heater has a defined temperature range suitable for cell biology use (ambient + 5°C to 50°C) and maintains a consistent temperature across its surface ensuring all cells, no matter where their location on the plate, are incubated at the same temperature. Furthermore, the unit also incorporates a lid to help maintain a stable temperature, even when being used inside a laminar flow hood. These features make the Plate Heater ideal for cell-based and biochemical applications where consistent temperature control is important, such as incubating cell-based assays in microplates, trypsinising cells in cell culture T-flasks, or even generating reproducible 3-D cell cultures with the RAFT (Real Architecture for 3D Tissue) System.

**TAP Biosystems**

For info: +44-(0)-1763-227333 | [www.tapbiosystems.com](http://www.tapbiosystems.com)

Electronically submit your new product description or product literature information! Go to [www.sciencemag.org/products/newproducts.dtl](http://www.sciencemag.org/products/newproducts.dtl) for more information. Newly offered instrumentation, apparatus, and laboratory materials of interest to researchers in all disciplines in academic, industrial, and governmental organizations are featured in this space. Emphasis is given to purpose, chief characteristics, and availability of products and materials. Endorsement by Science or AAAS of any products or materials mentioned is not implied. Additional information may be obtained from the manufacturer or supplier.





## Science Careers Advertising

For full advertising details, go to ScienceCareers.org and click For Employers, or call one of our representatives.

**Tracy Holmes**  
Worldwide Associate Director  
Science Careers  
Phone: +44 (0) 1223 326525

### THE AMERICAS

E-mail: [advertise@sciencecareers.org](mailto:advertise@sciencecareers.org)  
Fax: 202-289-6742

**Tina Burks**  
East Coast/West Coast/South America  
Phone: 202-326-6577

**Marci Gallun**  
Midwest/Canada  
Phone: 202-326-6582

**Candice Nulsen**  
Corporate  
Phone: 202-256-1528

**Online Job Posting Questions**  
Phone: 202-312-6375

### EUROPE / INDIA / AUSTRALIA / NEW ZEALAND / REST OF WORLD

E-mail: [ads@science-int.co.uk](mailto:ads@science-int.co.uk)  
Fax: +44 (0) 1223 326532

**Axel Gesatzki**  
Phone: +44 (0)1223 326529

**Kelly Grace**  
Phone: +44 (0) 1223 326528

### JAPAN

**Yuri Kobayashi**  
Phone: +81-(0)90-9110-1719  
E-mail: [ykobayas@aaas.org](mailto:ykobayas@aaas.org)

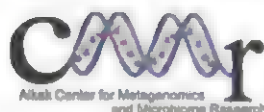
### CHINA / KOREA / SINGAPORE / TAIWAN / THAILAND

**Ruolei Wu**  
Phone: +86-1367-1015-294  
E-mail: [rwu@aaas.org](mailto:rwu@aaas.org)

All ads submitted for publication must comply with applicable U.S. and non-U.S. laws. Science reserves the right to refuse any advertisement at its sole discretion for any reason, including without limitation for offensive language or inappropriate content, and all advertising is subject to publisher approval. Science encourages our readers to alert us to any ads that they feel may be discriminatory or offensive.



ScienceCareers.org



## Department of Molecular Virology and Microbiology

The Alkek Center for Metagenomics and Microbiome Research (CMMR) and the Department of Molecular Virology and Microbiology at Baylor College of Medicine seek to fill (3) tenure track faculty positions at the ASSISTANT PROFESSOR level. We are seeking investigators with promising track records who are emphasizing Microbiome Research in humans and/or model systems. While specific research interests may vary, preferred candidates will be pursuing studies in host-microbe interactions, mucosal immunology, cell signaling, metabolomics and/or other 'multi-omic' related strategies and analyses.

At Baylor College of Medicine (BCM), you will find a unique collaborative spirit, a dedication to excellence in patient care and an environment that surpasses its reputation as a research powerhouse and educational giant. BCM is located in the heart of the Texas Medical Center (TMC), the largest incorporated medical center in the world with more than 42 member institutions in 100 buildings. The CMMR is building a highly collaborative environment where exciting advances in our understanding of how microbes impact human health and disease will result from synergistic interactions between collaborating faculty, clinicians, centers and institutions. This position features a competitive start-up package and laboratory/office space and will leverage the facilities and resources located in the CMMR and at BCM/TMC, including the Baylor College of Medicine Human Genome Sequencing Center, one of the three NHGRI-funded Large Scale Sequencing Centers with production scale platforms for the latest generation sequencing technologies.

Successful candidates will synergize with our strengths in metagenomics research to delve into the mechanisms by which microbes impact human health. They will maintain an outstanding research program that focuses on solving core problems in this area, and have a commitment to excellence in teaching. Required qualifications include a Ph.D. and a recognized reputation for innovative scholarship, a distinguished track record for research support and publications, leadership experience of students and trainees, and continued faculty development.

Applicants should submit a cover letter, a curriculum vitae including a publication list, a statement of research accomplishments and future research plans, a description of teaching experience and philosophy, and the names and addresses of three potential referees to the address or email below by **September 13, 2013**. **Search Committee, Alkek Center for Metagenomics and Microbiome Research, Baylor College of Medicine, One Baylor Plaza BCM MS385, Houston, Texas 77030; Telephone: 713-798-5867; email: [bcm-mvm-facultypos1@bcm.edu](mailto:bcm-mvm-facultypos1@bcm.edu).**

*Baylor College of Medicine is an Equal Opportunity, Affirmative Action and Equal Access Employer.*



## PRESIDENT TUCSON, ARIZONA

The Research Corporation for Science Advancement (RCSA) invites applications for the position of President. The President reports to the Board of Directors and will carry out responsibilities of chief executive officer. RCSA is the oldest foundation in the United States devoted wholly to science and its mission is to support the pursuit of high-potential early-stage scientific research. It focuses on providing catalytic funding for highly innovative research that will have a lasting impact on science and society. Its historic emphasis is on the physical sciences and closely related fields.

The President will join RCSA at an exciting time. Having recently celebrated its centennial, the organization is engaged in strategic planning to identify ways of amplifying its impact. The President will lead the completion of the plan and drive its implementation. The President will oversee the Foundation's science programs and peer review process, enhance relationships with external communities, and steward the organization's resources. RCSA seeks an innovative and visionary leader with a deep history of scientific excellence and demonstrated management skills and financial acumen.

Inquiries, nominations, and applications should be sent in confidence to: **John Muckle, Principal, Isaacson, Miller at [RCSA@imsearch.com](mailto:RCSA@imsearch.com).**



## Neuroscience Faculty Positions

The California Institute of Technology invites applications for tenure-track professorial positions in the Division of Biology and Biological Engineering. We are searching for talented investigators in **Molecular, Cellular, and Systems Neuroscience**. Successful applicants are expected to develop an innovative research program and should have a commitment to teaching. Preference will be given to candidates at the Assistant Professor level. Initial appointments at the assistant professor level are for four years, and are contingent upon completion of the Ph.D. degree.

Please submit an on-line application at <http://biology.caltech.edu/Positions> and include a brief cover letter, curriculum vitae, relevant publications, and a description of proposed research. Instructions will be given for submission of letters of reference when you apply on-line. The **application deadline is October 31, 2013**. Applicants must be prepared to attend a recruiting symposium at Caltech on January 9-10, 2014.

*The California Institute of Technology is an Equal Opportunity/Affirmative Action Employer. Women, minorities, veterans, and disabled persons are encouraged to apply.*

# UNIVERSITY OF Nebraska Medical Center

With the recent opening of the Stanley M. Truhlsen Eye Institute, the Department of Ophthalmology and Visual Sciences at the University of Nebraska Medical Center in Omaha, NE is seeking to expand its research faculty. Candidates for **Assistant Professor** should have a strong record of scholarly activity with evidence of initial research funding success. Candidates for **Associate or Full Professor** should have a strong, well-funded eye research program with qualifications appropriate to appointment level. Research interests should complement strengths of existing faculty in retinal diseases, neuroscience, stem cells, corneal diseases, glaucoma, cataract, and lens. Approaches of particular interest include epigenetics, pharmacogenomics, imaging, expertise with zebra fish or mouse as model animal systems, and ocular drug delivery.

Interested candidates should submit their curriculum vitae and statement of research interests by email to: **Wallace Thoreson, Ph.D., Vice Chair for Research (wbthores@unmc.edu)**. The successful candidate will have a primary appointment in the Department of Ophthalmology and Visual Sciences and may also have secondary appointments with other departments.

*UNMC is an Equal Opportunity Employer.*



## CHUGAI PHARMABODY RESEARCH PTE. LTD.

Chugai Pharmabody Research Pte. Ltd. ("CPR") was established in **Singapore** as a wholly-owned subsidiary of Chugai Pharmaceutical Co., Ltd (Chugai) in January 2012 and started operations on July 2, 2012. Located at Biopolis in Singapore, it aims to generate new antibody drugs based on Chugai's proprietary antibody engineering technology.

We are inviting talented and highly motivated individuals with postdoctorate qualifications to join us as postdoc **Researchers**.

### Job Requirements

You must have completed and be awarded with a PhD Degree in Science or Technology (not in the process of achieving it). You must be able to demonstrate technical expertise in areas which may include molecular biology, cell biology, protein chemistry, protein engineering and pharmacology as evidenced by projects, presentations, or peer-reviewed scientific publications. You will have a strong advantage if you possess prior work experience in antibody drug discovery work, coupled with strong interpersonal, team working and communication skills.

If you are interested to join us as a postdoc Researcher, please visit our website (Careers Page) at <http://www.chugai-pharmabody.com/> for more information and application procedure.

*We regret that only shortlisted candidates will be notified.*



### Senior Researcher positions (2) and Post-Doc fellowships (3)

Self-assembling peptides/Nanofabrication - Glycosaminoglycans/Bioimaging/Nanocharacterization

The 3B's Research Group (Uminho), lead by Prof Rui L Reis, a member of the ICVS/3B's Lab, is one of the most productive European groups in *Tissue Engineering and Regenerative Medicine (TERM)*. Its facilities are also the HQ of the European Institute of Excellence on TERM. 3B's possesses state of the art labs to perform chemical synthesis, materials processing, *in vitro* (stem) cell culture and *in vivo* animal testing. The group is composed by ~125 researchers (~20 Nationalities) and is responsible for >30ME (20ME UMinho) of funding. 3B's is now running one of the largest European University based projects in the field of **Nanomedicine - POLARIS** (~3.15ME of EC funding). It counts with the collaboration of 4 Institutions: **University of Strathclyde** (Prof Rein V Ultp), **University College Dublin** (Prof Kenneth Dawson), **Max Planck Institute for Intelligent Systems** (Prof. Joachim P. Spatz), and **Chalmers University of Technology** (Prof. Fredrik Hook), where the selected researchers may spend some periods. We are now opening 2 Senior Researcher and 3 Post-Doc positions on:

- 1) Self-assembling peptides for nanomedicine. **Senior** (#SR1-POL).
- 2) Fabrication and characterization of nanobiomaterials. **Senior** (#SR2-POL).
- 3) Surface models to study glycan-protein/glycan-glycan interactions. **Post-Doc** (#PD1-POL).
- 4) Synthesis of carbohydrates for bioimaging of cells and tissues. **Post-Doc** (#PD2-POL).
- 5) Nanobiomaterials for preventing hospital acquired infections. **Post-Doc** (#PD3-POL).

Successful candidates should possess PhD in Chemistry, Physics, Materials Engineering, Biomedical Engineering, Biotechnology or similar fields (all pos); experience in self-assembling systems (pos. 1); nanofabrication / nanocharacterization (pos. 2, 5); protein-glycan interactions (pos. 3); glycan synthesis (pos. 4); a research profile supported by publications in high impact journals (all pos); and experience in the supervision of MSc/PhD students (pos. 1, 2).

Candidates for SR positions will have a starting grant of 1800 \$1E/month (tax-free) for 6 months and the possibility to be integrated in the staff as assistant researchers (contracts, gross salary 3191 \$2E/month, 14 months/year) after this initial period. Post-Doc grants correspond to a monthly stipend of 1495\$ (tax-free) for 1 year with the possibility of renewal until the end of the project.

Applications (indicating the ref. # of the position) including a motivation letter, copy of the proof of academic degree and detailed CV, should be submitted until **2<sup>nd</sup> of August 2013**, by e-mail to [info@3bs.uminho.pt](mailto:info@3bs.uminho.pt) or by ordinary mail to:

A/C Prof Rui L. Reis  
3B's Research Group - University of Minho  
AvePark, Zona Industrial da Gandra  
4806-909 Taipas - Guimarães, Portugal



For more info on the 3B's Research Group visit: [www.3bs.uminho.pt](http://www.3bs.uminho.pt) or call +351253510810

## University of Lethbridge



School of Graduate Studies

The Alberta Terrestrial Imaging Centre (ATIC) at the University of Lethbridge undertakes a concentrated effort towards the advancement of scientific knowledge in remote sensing. The Centre places special emphasis on imaging spectroscopy and LiDAR, applying research and development to the monitoring of natural resources and the environment.

**The ATIC, the Faculty of Arts & Science, and the School of Graduate Studies at the University of Lethbridge invite applications for:**

### 2 MSc Studentships

L DAR based environmental modeling  
Forest ecosystem modeling

**Dr. C. Hopkinson**  
**Dr. D. Peddle**

### 2 PhD Studentships

L DAR based environmental modeling  
Vegetation health monitoring

**Dr. C. Hopkinson**  
**Dr. C. Coburn**

### 2 Post Doctoral Fellowships

L DAR based environmental modeling  
Terrestrial or atmospheric remote sensing

**Dr. C. Hopkinson**  
**Dr. Karl Staenz**

Applicants to the above positions/studentships should clearly specify which project they are applying and submit a curriculum vitae, a letter of application outlining research experiences and aspirations, and the names and contact information for at least three referees to [trevor.armstrong@uleth.ca](mailto:trevor.armstrong@uleth.ca) by September 10, 2013.

**The University of Lethbridge offers Masters and Doctoral studentship/ assistantship opportunities in a range of multi-disciplinary areas in the Sciences.**

**For more information, contact the School of Graduate Studies:**

[www.uleth.ca/graduatestudies](http://www.uleth.ca/graduatestudies)  
Phone: 403 329-5194  
Email: [sgs.nqj@res@uleth.ca](mailto:sgs.nqj@res@uleth.ca)



# Women in Science Booklet

Science and the L'Oréal Foundation present



Read inspiring profiles of women  
making a difference in biology.

**Free download at**  
**[ScienceCareers.org/LOrealWIS](http://ScienceCareers.org/LOrealWIS)**



OREGON  
HEALTH & SCIENCE  
UNIVERSITY

### Cardiac Electrophysiology/Molecular Physiology

Oregon Health & Science University (OHSU) Department of Physiology and Pharmacology and the Knight Cardiovascular Institute invite applications for a tenure-track faculty position from individuals with training in Bioengineering, Biophysics or Physiology who are interested in investigating the **molecular basis of cardiac arrhythmias**. The successful candidate will join a multidisciplinary, translational research team comprising basic science and clinical faculty focused on the underlying mechanisms of arrhythmia development and generation, with the aim of developing novel therapeutic approaches. Preference will be given to candidates for the position of **Assistant Professor**, but exceptional candidates for the position of **Associate and Full Professor** will also be considered. We seek an individual who will develop an independent research program, contribute to the teaching of medical and graduate students and interact with investigators studying cardiovascular and reproductive biology, drug metabolism, signal transduction, ion channel biology and G-protein coupled receptors. OHSU offers a highly interactive research environment and superb opportunities for career development in a spectacular Pacific Northwest setting. The recent founding of the Knight Cardiovascular Institute offers an opportunity to be a part of the development of this new, multidisciplinary translational research effort.

OHSU values a diverse and culturally competent workforce. Candidates should model a positive attitude regarding diversity and inclusion while ensuring service delivery is provided in a culturally competent manner. Individuals who promote diversity and a culture of inclusion are encouraged to apply. OHSU provides reasonable accommodations for applicants with disabilities. We are proud to be an equal opportunity, affirmative action organization.

A completed application should consist of the following: curriculum vitae, a brief summary of research accomplishments, an outline of future research plans, and three letters of recommendation. The successful candidate will have a Ph.D. in a relevant discipline and a track record of independent publications and funding. Applications and letters of reference may be sent electronically to: **Beth Habecker, Ph.D., Department of Physiology & Pharmacology, Oregon Health & Science University, [habecker@ohsu.edu](mailto:habecker@ohsu.edu).**



UNIVERSITY OF SOUTH ALABAMA  
**MITCHELL**  
CANCER INSTITUTE

### Abraham A. Mitchell Chair Urologic Oncology

The highly qualified candidate for this position at the University of South Alabama Mitchell Cancer Institute will be a clinically active physician-scientist with appropriate training and experience, exemplary credentials in clinical urologic oncology, and an established, well-funded basic/translational research program focused on urologic cancers. The ideal candidate additionally will have demonstrated leadership potential and business acumen, as responsibilities of the position will include leading the development of an entrepreneurial, financially sound, translational research-focused department of urologic oncology that brings specialized clinical services and clinical trials to the patients of the Gulf coastal region and beyond.

Applications are to be e-mailed to: [sallen@usouthal.edu](mailto:sallen@usouthal.edu) by **August 30, 2013**.

*USA is an Affirmative Action and Equal Opportunity Employer.*

## CAREER TRENDS

Running  
Your Lab



Science Careers

[ScienceCareers.org/booklets](http://ScienceCareers.org/booklets)

These materials are brought to you by the AAAS Science & Business Office

Download your free copy today at  
**ScienceCareers.org/booklets**

### Chair, Department of Pathology and Laboratory Medicine

Rutgers New Jersey Medical School invites applicants for the position of Chair of the Department of Pathology and Laboratory Medicine.

We are seeking an individual with strong leadership qualities and a record of accomplishment as a clinician and researcher to head a department with a faculty with broad expertise in both basic science and the clinical sciences. The department's clinical activities include Surgical Pathology, Autopsy Pathology, Neuropathology, Molecular Diagnostics, Clinical Hematology and Hematopathology, Blood Bank, Microbiology, Chemistry, and Immunology and Serology. Departmental research is concentrated in the areas of immunology, cancer biology and HIV. In addition, the department has major teaching responsibilities in the New Jersey Medical School and the Graduate School of Biomedical Sciences, and an ACGME-accredited training program in Anatomic and Clinical Pathology. The successful candidate should be a leader in the field of Pathology with a national and international reputation with clinical and basic science expertise and be able to integrate both into a cohesive department excelling in research, education and clinical service.

Interested individuals should send a curriculum vitae or letter of inquiry to

Soly Baredes, MD, Chair, Search Committee for Chair,  
Department of Pathology & Laboratory Medicine  
c/o Michael Petti, Executive Assistant to the Dean  
Rutgers New Jersey Medical School  
185 South Orange Avenue, MSB C-671  
Newark, NJ 07101-1709  
Email: [pettome@njms.rutgers.edu](mailto:pettome@njms.rutgers.edu)

Unless confidentiality is requested in writing, information regarding applicants and nominees must be released upon request. Finalists cannot be guaranteed confidentiality.

Please note that effective July 1, 2013, as a result of the New Jersey Medical and Health Sciences Restructuring Act, several units from the former University of Medicine and Dentistry of New Jersey (UMDNJ) are now part of Rutgers Biomedical and Health Sciences (RBHS). For the purposes of payroll and benefits administration, the above position is a legacy UMDNJ position at Rutgers, and is eligible for benefits associated with legacy UMDNJ positions.

Rutgers, the State University of New Jersey, is an Equal Opportunity / Affirmative Action employer, and is compliant with the Americans with Disabilities Act (ADA). For more information, please visit <http://jobs.rutgers.edu/TheRUCommitment.htm>.

**RUTGERS**

New Jersey Medical School





## AAAS is here – helping scientists achieve career success.

Every month, over 400,000 students and scientists visit ScienceCareers.org in search of the information, advice, and opportunities they need to take the next step in their careers.

A complete career resource, free to the public, *Science Careers* offers a suite of tools and services developed specifically for scientists. With hundreds of career development articles, webinars and downloadable booklets filled with practical advice, a community forum providing answers to career questions, and thousands of job listings in academia, government, and industry, *Science Careers* has helped countless individuals prepare themselves for successful careers.

As a AAAS member, your dues help AAAS make this service freely available to the scientific community. If you're not a member, join us. Together we can make a difference.

To learn more, visit [aaas.org/plusyou/sciencecareers](http://aaas.org/plusyou/sciencecareers)





## AAAS is here – promoting universal science literacy.

In 1985, AAAS founded Project 2061 with the goal of helping all Americans become literate in science, mathematics, and technology. With its landmark publications *Science for All Americans* and *Benchmarks for Science Literacy*, Project 2061 set out recommendations for what all students should know and be able to do in science, mathematics, and technology by the time they graduate from high school. Today, many of the state standards in the United States have drawn their content from Project 2061.

Every day Project 2061 staff use their expertise as teachers, researchers, and scientists to evaluate textbooks and assessments, create conceptual strand maps for educators, produce groundbreaking research and innovative books, CD-ROMs, and professional development workshops for educators, all in the service of achieving our goal of universal science literacy.

As a AAAS member, your dues help support Project 2061 as it works to improve science education. If you are not yet a AAAS member, join us. Together we can make a difference.

To learn more, visit [aaas.org/plusyou/project2061](http://aaas.org/plusyou/project2061)





**Download  
your free copy  
today.**

**ScienceCareers.org/booklets**



From technology specialists to patent attorneys to policy advisers, learn more about the types of careers that scientists can pursue and the skills needed in order to succeed in nonresearch careers.



**Your  
career  
is our  
cause.**

Get help  
from the  
experts.

**www.  
sciencecareers.org**

- Job Postings
- Job Alerts
- Resume/CV Database
- Career Advice
- Career Forum



**Stop searching  
for a job;  
start your career.**



**www.ScienceCareers.org**

#### MARKETPLACE

ProMab Biotechnologies, Inc.

**Ascites Production  
\$20 - \$30 / Mouse**

UP TO 100,000 MICE / YEAR

**1-866-339-0871**

www.ProMab.com | info@promab.com

Widely  
Recognized  
Original &  
Guaranteed

**KlenTaq1™** 8¢/u  
Truncated  
Taq DNA  
Polymerase  
Withstand 99°C

e-mail: order@JEMBIO.com www.JEMBIO.com  
Call: JEM BIO Home of KlenTaq-S  
Ph: 1-866-493-3464 Fax: 636-465-3979



# STAY INFORMED! STAY CONNECTED!

Get more from your AAAS membership

Are you currently registered to receive e-mails from AAAS and *Science*?

E-mail is the primary way that AAAS communicates with our members about AAAS programs, new member benefits, invitations to special events, and, of course, the latest news and research being published in *Science*.

Sign up today to receive e-mails from AAAS and ensure that you are getting the most out of your membership and *Science* subscription.\*

To get started visit: [promo.aaas.org/stayconnected](http://promo.aaas.org/stayconnected)

You'll need your AAAS Member number. Find it above your name on your *Science* mailing label.

Don't miss a thing. Sign up for e-mail communications from AAAS today!







# By your side since 1962

One company, one family of trusted brands. Here to support your research.

As your research needs evolve, we evolve to meet them. We continuously innovate high-quality solutions for every lab and every application, building from technology chosen by scientists for up to 50 years. And we're staffed to support your success, with 3,000 technical sales, service, and support professionals ready to assist you.

Invitrogen™

Applied Biosystems®

Gibco®

Molecular Probes®

Novex™

Ambion®

Ion Torrent™

Find the most cited life science brands at  
[lifetechnologies.com/trustedbrands](http://lifetechnologies.com/trustedbrands)

*life*  
technologies™

©2013 Life Technologies Corporation. All rights reserved. The trademarks mentioned herein are the property of Life Technologies Corporation and/or its affiliate(s) or their respective owners. C005619 0613